Microchip HPLC: Experimental investigation of separation efficiency, column characteristics, and coupling with mass spectrometry

Dissertation

zur

Erlangung des Doktorgrades

der Naturwissenschaften

(Dr. rer. nat.)

dem

Fachbereich Chemie

der Philipps-Universität Marburg

vorgelegt von

Dipl.-Chem. Stephanie Jung

aus Dillenburg/Hessen

Marburg an der Lahn 2012

Vom Fachbereich Chemie der Philipps-Universität Marburg (Hochschulkennziffer: 1180) als Dissertation am 23.08.2012 angenommen.

Erstgutachter: Prof. Dr. Ulrich Tallarek

Zweitgutachter: Prof. Dr. Andreas Seubert

Tag der mündlichen Prüfung: 04.10.2012

Die vorliegende Arbeit wurde in der Zeit von August 2008 bis Juli 2012 am Fachbereich Chemie der Philipps-Universität Marburg unter der Leitung von Herrn Prof. Dr. Ulrich Tallarek angefertigt.

In den folgenden Artikeln wurden Teile dieser Dissertation bereits veröffentlicht:

Jung, S.; Ehlert, S.; Mora, J.-A.; Kraiczek, K.; Dittmann, M.; Rozing, G.P.; Tallarek, U. *J. Chromatogr. A* **2007**, *1172*, 25-39. „Packing density, permeability, and separation efficiency of packed microchips at different particle-aspect ratios."

Jung, S.; Höltzel, A.; Ehlert, S.; Mora, J.-A.; Kraiczek, K.; Dittmann, M.; Rozing, G.P.; Tallarek, U. *Anal. Chem.* **2009**, *81*, 10193-10200. „Impact of Conduit Geometry on the Performance of Typical Particulate Microchip Packings."

Jung, S.; Ehlert, S.; Pattky, M.; Tallarek, U. *J. Chromatogr. A* **2010**, *1217*, 696-704. „Determination of interparticle void volume in packed beds via intraparticle Donnan exclusion."

Jung, S.; Effelsberg, U.; Tallarek, U. *J. Chromatogr. A* **2011**, *1218*, 1611-1619. „Microchip electrospray: Cone-jet stability analysis for water-acetonitrile and water-methanol mobile phases."

Jung, S.; Stoeckel, D.; Tallarek, U. *J. Sep. Sci.* **2011**, *34*, 800-805. „Fast, accurate, and convenient analysis of bed densities and for columns packed with fine reversed-phase particles."

Jung, S.; Effelsberg, U.; Tallarek, U. *Anal. Chem.* **2011**, *83*, 9167-9173. „Microchip electrospray: Improvements in Spray and Signal Stability during Gradient Elution by an Inverted Postcolumn Makeup Flow."

Dank

Zuerst möchte ich Herrn Prof. Dr. Ulrich Tallarek für die Übergabe dieser interessanten und abwechslungsreichen Aufgabenstellung sowie für zahlreiche konstruktive Gespräche und Ideen während der Promotionszeit danken. Ebenfalls danke ich ihm für seine Begeisterung für die Forschung und die Unterstützung, wodurch die Ergebnisse dieser Arbeit bereits erfolgreich in Fachzeitschriften veröffentlicht und auf internationalen Konferenzen präsentiert werden konnten.

Herrn Prof. Dr. Andreas Seubert danke ich für die Übernahme des Koreferates und die gute Zusammenarbeit während der Praktikumsbetreuung.

Prof. Dr. Gerhart Hilt und Prof. Dr. Bernhard Roling danke ich, dass Sie sich bereit erklärt haben an der Prüfungskommission teilzunehmen.

Ein ganz besonderer Dank geht an Jose-Angel Mora, Karsten Kraiczek, Uwe Effelsberg und Monika Dittmann von Agilent Technologies, die durch Geschenke in Form von Kapillaren, Mikrochips, HPLC-Säulen und anderen Kleinteilen maßgeblich zur Durchführung der Experimente beigetragen haben. Jose und Uwe danke ich ebenfalls für jede Menge Zeit, die sie geopfert haben, wenn ich Fragen zu Hard- und Software von Agilent Technologies hatte, die über das Wissen eines Service-Technikers hinaus gingen.

Dear colleagues, many special thanks for: Coffee, cake, beer, different advices of how-to-use-HPLC-grade-ethanol, fruitful discussions, helping hands, enjoyable company, superfluous knowledge, excellent working atmosphere, confusion and chaos disrupted by tidiness and spruceness.

Herzlichen Dank an Alexandra Höltzel, die es viel Zeit und Mühe gekostet hat, meine Texte zu korrigieren und zu verbessern, was entscheidend zu den Veröffentlichungen beigetragen hat.

Meinem Mann Wolf Schorn, meinen Eltern, der Familie, Schatzi, Häschen, Mausi, Bärli, Lollilü, Sonnenschein und allen anderen guten Freunden DANKE für die Unterstützung, ein großartiges Miteinander, viel Spaß und immer wieder Motivation.

Abbreviations and Symbols

α	Selectivity
ACN	Acetonitrile
$[A_m]$	Concentration of the analyte A in the mobile phase
APCI	Atmospheric pressure chemical ionisation
$[A_s]$	Concentration of the analyte A in the stationary phase
A_S	Asymmetry factor
β	Phase ratio
C8	Octyl-
C18	Octadecyl-
c_m	Concentration in the mobile phase
CRM	Charged residue model
c_s	Concentration in the stationary phase
d	Diameter
D_{ax}	Axial dispersion coefficient
δ_{EDL}	Electric double layer thickness
d_h	Hydraulic diameter
D_m	Molecular diffusion coefficient (in bulk mobile phase)
d_p	Particle diameter
d_{pore}	Pore diameter
d_S	SAUTER mean diameter
ε_0	Vacuum permittivity
ε_{inter}	Interparticle porosity
ε_{intra}	Intraparticle porosity

ε_r	Relative permittivity
ε_{total}	Total porosity
ESI	Electrospray ionisation
η	Dynamic viscosity
f	Shape factor that quantifies dispersion
F	FARADAY constant
FA	Formic acid
f_{KC}	KOZENY-CARMAN factor
F_V	Volumetric flow rate
FWHM	Full width at half maximum
γ	Obstruction factor or activity coefficient, as indicated
GC	Gas chromatography
h	Reduced plate height or transverse length, as indicated
H	Plate height
HETP	Height equivalent to a theoretical plate
HILIC	Hydrophilic interaction liquid chromatography
i.d.	Inner diameter
IC	Ion chromatography
IEM	Ion evaporation model
IEX	Ion exchange chromatography
ISEC	Inverse size-exclusion chromatography
k_0	shape factor
k	retention factor
K	Equilibrium constant
κ	Electrical conductivity
κ_D	DARCY permeability
K_C	NERNST partition coefficient

l	Length
λ_D	DEBYE length
λ_i	Coefficient in A term
L_{bed}	Length of the packed bed
L_C	Column length
m/z	Mass-to-charge ratio
MeOH	Methanol
MS	Mass spectrometry
M_W	Molecular weight
μ	Hydraulic tortuosity factor
μ_c	Standard chemical potential of cation
N_m	Number of molecules in the mobile phase
NP	Normal phase
N_s	Number of molecules in the stationary phase
ν	Reduced velocity or kinematic viscosity, as indicated
o.d.	Outer diameter
ω	Coefficient in C term
p	Pressure
pH	Potential Hydrogen
ϕ	Potential
ϕ_D	DONNAN potential
ϕ_S	Surface potential
psd	Particle size distribution
r_C	Column or capillary radius
R	Gas constant or Resolution, as indicated

Re	REYNOLDs number
ρ	Density of fluid or ratio of solid core to particle radius, as indicated
r_{meso}	Mesopore radius
r_p	Particle radius
r_{pore}	Pore radius
SEC	Size-exclusion chromatography
σ	Standard deviation
Sv	Specific surface area (surface-to-volume-ratio)
t	Time
T	Temperature
t^+	Transference number of cation
t_0	Column dead time
t_e	Electrical relaxation time
T_f	Tailing factor
t_h	Hydrodynamic time
t_m	Time that an analyte spends in the mobile phase
t_R	Retention time
Tris	Tris(hydroxymethyl)aminomethane
t_s	Time that an analyte spends in the stationary phase
u_0	Linear velocity
V_0	Retention volume of a dead time marker
V_{inter}	Interparticle void volume
V_{intra}	Intraparticle void volume
V_m	Mobile phase volume
V_R	Retention volume
V_s	Stationary phase volume

V_{total}	Total column void volume
w	Peak width or channel width, as indicated
W	Electrical potential energy or Water, as indicated
X	Gravity of a chromatographic zone
ζ	Zeta potential
z_i	Valency of ionic species i

Zusammenfassung

Die vorliegende Arbeit beschäftigt sich mit verschiedenen Aspekten, welche die chromatographische Effizienz in der miniaturisierten HPLC beeinflussen. Zur Optimierung der Trennleistung in Nano- und Mikrochip-Trennformaten sind verschiedene Parameter von Relevanz: Reduktion von Peakdispersion, Minimierung von externen Säulenvolumina, Optimierung von Packprozeduren, um möglichst hohe Packungsdichten in den chromatographischen Partikelfestbetten zu erreichen, und Optimierung der Betriebsbedingungen.

Für die Abschätzung von Qualität und Leistungsvermögen einer mit Partikeln gepackten Trennsäule ist die interpartikuläre Porosität ε_{inter} ein wichtiger Indikator. Niedrige interpartikuläre Säulenvolumina und Porositäten tragen entscheidend zur Effizienz (durch eine Verringerung der interpartikulären Abstände) und zur Stabilität einer Packung bei. Eine präzise Messung dieser Werte ist somit nicht nur für die Beurteilung der Trennqualität einer Säule von Bedeutung, sondern auch für die Validierung von Packprozessen. Zwei unabhängige chromatographische Methoden zur Bestimmung von ε_{inter}, welche zum einen auf inversem Größenausschluss und zum anderen auf DONNAN-Ausschluss basieren, werden in *Kapitel 1, Teil A* und *Teil B* untersucht. Im Speziellen wird ihre Anwendbarkeit auf verschiedene chromatographische Materialien getestet. In *Kapitel 1, Teil A – Determination of the interparticle void volume in packed beds via intraparticle DONNAN exclusion* – wurden die interpartikulären Volumina und Porositäten von Silikakapillaren bestimmt. Die Kapillaren besaßen einen Innendurchmesser von 75 µm und wurden mit Partikeln aus einer Suspension gepackt. Zur Bestimmung wurden die Methoden des elektrostatischen (DONNAN) Ausschlusses und der inversen Größenausschlusschromatographie (inverse size-exclusion chromatography, ISEC) verwendet. Vollständiger DONNAN-Ausschluss eines kleinen nicht-retardierten gleichionischen Ladungsträgers aus dem intrapartikulären Porenvolumen der Trennsäule wurde durch sorgfältiges Anpassen der Ionenstärke der mobilen Phase erreicht. In diesem Fall bestand der Ladungsträger aus Nitrationen, welche sich in Bezug auf die negative Ladung an der Oberfläche der kieselgelbasierten Partikel gleichionisch verhalten. Die Anwendbarkeit der Methode wurde für Kieselgelpartikel (Nucleosil 100-5 und Nucleosil 1000-5), Umkehrphasen (Hypersil MOS 3 µm und Hypersil MOS 10 µm) und starke Kationenaustauschermaterialien (Spherisorb SCX 3 µm) mit verschiedenen Partikelgrößen und intrapartikulären Porengrößen bestimmt. Tris-HCl Pufferlösungen wurden verwendet um

die Überlappungsintensität der intrapartikulären elektrischen Doppelschichten (electric double layer, EDL) zu manipulieren und das Maß des gleichionischen Ausschlusses in Abhängigkeit der intrapartikulären Porengröße (Nucleosil 100-5 gegenüber Nucleosil 1000-5 Partikel) zum einen und der Oberflächenladung (Hypersil MOS 3 µm gegenüber Spherisorb SCX 3 µm Partikel) zum anderen zu bestimmen. Ergänzend zu diesen Experimenten wurden ε_{inter}-Werte mit der in der Chromatographie bereits etablierten Methode des inversen Größenausschlusses gemessen. Zu diesem Zweck wird eine Reihe von Polymerstandards von definiertem Molekulargewicht in Dichlormethan gelöst und auf die Trennsäule gegeben. Die Elutionsvolumina der Polymerstandards beschreiben eine bimodale Verteilungskurve innerhalb der Grenzen der Permeation des totalen Säulenvolumens und des Ausschlusses aus dem intrapartikulären Porenraum der Trennsäule. Die für ε_{inter} erhaltenen Werte mittels DONNAN-Ausschluss stimmen gut mit den Werten der ISEC für alle verwendeten Trennsäulen überein. Einschränkungen in der Anwendbarkeit der beiden Methoden treten erst dann auf, wenn die beiden Ausschlussprinzipien, d.h. elektrostatischer (DONNAN-) Ausschluss und mechanischer Ausschluss, ebenfalls zwischen den Partikeln auftreten. Im Falle des DONNAN-Ausschlusses heißt das, dass eine EDL Überlappung zwischen individuellen Partikeln der Packung auftritt und im Falle der ISEC, dass die interpartikulären Poren zu klein werden, um die Polymerknäuel ungehindert passieren zu lassen. Die Bestimmung der interpartikulären Porosität ist ebenfalls nicht möglich, wenn die intrapartikulären Porendurchmesser so groß werden, dass vollständiger elektrostatischer und Größenausschluss nicht mehr realisierbar sind.

In *Kapitel 1, Teil B – Fast, accurate, and convenient analysis of bed densities for columns packed with fine reversed-phase particles* – wurde die DONNAN-Ausschlussmethode zur Porositätsbestimmung auf kommerziell erhältliche analytische HPLC Säulen von Agilent Technologies übertragen. Die Säulen waren mit kleinen Umkehrphasenpartikeln unterschiedlicher nomineller Größe (1.8, 2.7, 3.5 und 5 µm) und unterschiedlicher Konstruktion (vollporös und core-shell) gepackt. Die experimentell erhaltenen Daten ließen erkennen, dass mit der Methode auch an einem kommerziellen LC-Apparat eine hohe Wiederholpräzision erzielt werden konnte. Die durch das Ausschlussprinzip bedingten sehr kleinen Nitratkonzentrationen konnten mit einer Standarddetektionszelle erfasst werden. Ein ausgeprägtes Plateau am Fuß der Elutionskurve bei niedrigen Pufferkonzentrationen weist auf eine EDL Überlappung in den intrapartikulären Mesoporen hin, wodurch gleichionische Spezies vollständig vom intrapartikulären Porenraum ausgeschlossen werden. Das Elutionsvolumen der gleichionischen Ladungsträger entspricht unter diesen Bedingungen dem

interpartikulären Volumen der Trennsäule. Die DONNAN-Ausschlussmethode eignete sich für alle vermessenen kommerziellen Trennsäulen, die unter anderem mit 2.7 µm core-shell und 1.8 µm vollporösen Partikeln gepackt waren. Die DONNAN-Ausschlussmethode stellte sich im Allgemeinen als eine schnelle, akkurate und leicht anwendbare Methode zur Bestimmung der interpartikulären Säulenvolumina und Porositäten verschiedener stationärer Phasen mit unterschiedlicher Oberflächenchemie (Umkehrphasen-, Kieselgel- und Kationenaustauscher-material), Partikelkonstruktion (vollporös und core-shell) und Partikelgröße (1.8–5 µm) heraus.

Die Elutionsvolumina im Falle hoher Pufferkonzentrationen nähern sich asymptotisch einer Grenze, die dem totalen Porenvolumen der Trennsäule entspricht. Allerdings wird, bedingt durch den langsamen Abfall der EDL Schichtdicke über eine große Spanne an Ionenstärken, auch noch bei hohen Pufferkonzentrationen ein merklicher Ausschluss aus Teilen der Mesoporen beobachtet. Diese Beobachtung unterstützt die Aussage, dass kleine Ionen nicht für eine akkurate Bestimmung des Totvolumens einer Säule geeignet sind,[1] solange das genaue Ausmaß eines möglichen elektrostatischen Ausschlusses aus Teilen des intrapartikulären Porenvolumens nicht bekannt ist.

Die chromatographische Effizienz ist beschränkt durch Bandenverbreiterungsprozesse auf Grund hydrodynamischer Dispersion, welche ihrerseits durch die Mikrostruktur der Säulenpackung bestimmt wird. Bedingt durch die Herstellungsprozesse ist die Querschnittsgeometrie von Trennkanälen in mikrofluidischen Systemen sehr häufig nicht-zylindrisch. Die nicht-zylindrische Kanalgeometrie beeinflusst die axiale Dispersion, die mit größer werdender Abweichung von zylindrischer Geometrie (über quadratische zu rechteckiger und halbkreisförmiger Geometrie) ansteigt.[2] Zusätzlich sind die in nicht-zylindrischen Formaten vorhandenen Ecken schwieriger dicht zu packen. Die sphärischen Partikel können die Spitzen der Eckregionen nicht vollständig ausfüllen. Die einzelnen Beiträge, welche die ungleichmäßige Strömungsverteilung und damit die Dispersion erhöhen, sind stark von der Packungsdichte und dem Verhältnis von Kanal zu Partikelgröße in

[1] Ein detaillierter Übersichtsartikel über die verschiedenen existierenden Methoden in der Chromatographie zur Bestimmung des Totvolumens einer Trennsäule wurde veröffentlicht von C.A. Rimmer, C.R. Simmons und J.G. Dorsey in J. Chromatogr. A 965 (2002) 219-232.

[2] Quantitative numerische Analysen der hydrodynamischen Dispersion in Druckfluss-betriebenen Festbetten wurden für Kanäle von zylindrischer, quadratischer, rechteckiger und halbkreisförmiger Geometrie von Khirevich *et al*. durchgeführt. Die Autoren fanden, dass die axiale Dispersion mit steigender Abweichung von der zylindrischen Geometrie ebenfalls anstieg. Die Eckregionen in nicht-zylindrischen Geometrien führen zur Ausbildung von Kanälen mit bevorzugter Strömung. Außerdem sind die charakteristischen Distanzen, die für die laterale Equilibrierung der Lösungsmittelmoleküle zurückgelegt werden müssen, größer. [S. Khirevich, A. Höltzel, D. Hlushkou, U. Tallarek, Anal. Chem. 79 (2007) 9340-9349].

gepackten Mikrochips abhängig.[3] In *Kapitel 2 – Impact of Conduit Geometry on the Performance of Typical Particulate Microchip Packings* – wurde die axiale Dispersion der leeren sowie der gepackten Mikrochipkanäle chromatographisch bestimmt. Die aus Polyimid hergestellten HPLC/UV Mikrochips enthielten einen Trennkanal mit unterschiedlicher Kanalgeometrie. Es wurden Trennkanäle mit trapezoidalem, quadratischem und gaußförmigem Kanalquerschnitt vermessen.

Die Dispersion in den Leerkanälen spiegelt die Symmetrie der jeweiligen Kanalquerschnittsgeometrie wider. Die höchste Symmetrie besitzen die quadratischen Mikrochipkanäle. Daraus resultieren im Vergleich zu den trapezoidalen und gaußförmigen Kanälen ein gleichmäßigeres Flussprofil und eine gleichmäßigere Strömungsverteilung. Die Ungleichmäßigkeit der Strömungsverteilung steigt mit sinkender Querschnittssymmetrie. Dies ist auf die wachsende Distanz zurückzuführen, die vom Analyten durch laterale Diffusion durch die verschiedenen Geschwindigkeitszonen des Flussprofils zurückgelegt werden muss, um die konstante mittlere Dispersionsrate von axialem Dispersions- zu molekularem Diffusionskoeffizienten im Langzeitlimit zu erreichen. Mikrochipkanäle von gaußförmiger Geometrie zeigten die größte axiale Dispersion. Die kontinuierlich steigende laterale Diffusionslänge im gaußförmigen Profil geht mit größeren Reibungswiderständen im oberen, schmaleren Teil des Kanalquerschnitts einher, woraus ein größerer Geschwindigkeitsunterschied zwischen dem oberen und dem unteren Teil resultiert. Dadurch erhöht sich die benötigte Zeit um das laterale Äquilibrium zu erreichen und eine größere axiale Dispersion wird beobachtet.

Die realisierten Packungsdichten in den Mikrochipkanälen erwiesen sich als abhängig vom Verhältnis der Kanal- zu Partikelgröße (particle-aspect ratio). Mit 3 µm großen Partikeln konnten für alle verwendeten Kanalformen hohe Packungsdichten erzielt werden. Im Falle der mit 5 µm großen Partikeln gepackten Betten wurden eher lose Packungen erhalten. Es wurden steigende ε_{inter} Werte von 0.40 für gaußförmige über 0.41 für trapezoidale bis 0.42 für quadratische Kanäle ermittelt. Dieser Trend ist auf die Anzahl und die Form der Ecken der verschiedenen Kanalquerschnitte zurückzuführen.

Die beobachteten Trenneffizienzen der 3 µm Packungen geben die Dispersionseigenschaften in den Leerkanälen wider. Das Dispersionsverhalten der gepackten 5 µm Betten spiegelt jedoch deren jeweilige Packungsdichte wider. Die Effizienz der

[3] Trapezoidale Mikrochips wurden bezüglich ihrer Packungsdichten, der Beziehung von Druckabfall und Flussrate, ihrer hydraulischen Permeabilität und der chromatographischen Effizienz untersucht. Es wurde eine starke Abhängigkeit der Packungsdichten und der chromatographischen Effizienz vom Verhältnis der Kanalbreite zur Partikelgröße gefunden. Die Ergebnisse wurden veröffentlicht unter: S. Jung, S. Ehlert, J.-A. Mora, K. Kraiczek, M. Dittmann, G.P. Rozing, U. Tallarek, J. Chromatogr. A 1216 (2009) 264-273.

Gaußkanäle gepackt mit 5 µm großen Partikeln ist vergleichbar mit der Effizienz der trapezoidalen Trennkanäle. Die höhere Packungsdichte der Packung im Gaußkanal gleicht die schlechteren Dispersionseigenschaften durch die niedrigere Symmetrie der Kanalgeometrie, welche bei den Leerkanalmessungen beobachtet wurden, aus. Die quadratischen Trennkanäle verlieren ihren Vorteil der geringeren Dispersion auf Grund der höheren Symmetrie durch die lose Packungsstruktur. Die Partikel können nicht dicht genug in die Eckregionen gepackt werden, woraus eine höhere Dispersion bzw. schlechtere Effizienz resultiert.

Die Ergebnisse der Dispersionsstudie zeigen, dass die Querschnittsgeometrie der Trennkanäle die Effizienz auf verschiedene Weisen beeinflusst, jedoch immer abhängig vom Größenverhältnis von Kanalbreite zu Partikeldurchmesser ist.

In *Kapitel 3* wird der Einfluss von sich graduell ändernder Lösungsmittel-zusammensetzung, wie es bei Gradientenelution der Fall ist, auf den Elektrosprayprozess untersucht. Elektrosprayionisation (ESI) ist zu einer Standardkopplungstechnik von HPLC mit Massenspektrometrie (MS) herangewachsen. Idealerweise liefert eine Ionenquelle konstant über die gesamte Analysendauer die maximale Anzahl an Ionen. In der ESI ist die Ionenproduktionsrate direkt gekoppelt mit der Spraystabilität. Diese wiederum ist abhängig von verschiedenen Faktoren, wie der angelegten Potentialdifferenz, der Entfernung zwischen Emitter und MS Einlass, der Flussrate und der Zusammensetzung der versprühten Lösung. HPLC-MS Analysen, welche Gradientenelution benutzen, werden üblicherweise ohne Rückmeldung über die aktuelle Leistung des Elektrosprayprozesses durchgeführt. Die Potentialdifferenz, welche jedoch zu Beginn einer Gradientenelution die maximale Ionenproduktion gewährleistet, kann für die Zusammensetzung der versprühten Lösung am Ende des Gradientenlaufs nicht mehr geeignet sein, um optimale Ausbeute zu erzielen. Die Änderungen in der Zusammensetzung der Lösung während einer Gradientenelution gehen mit wechselnden physikalisch-chemischen Eigenschaften einher, die den Operationsmodus des Elektrosprays beeinflussen.

In *Kapitel 3, Teil A – Microchip electrospray: Cone-jet stability analysis for water–acetonitrile and water–methanol mobile phases* – werden Lösungsmittelgemische, welche häufig in Umkehrphasen HPLC eingesetzt werden, auf ihr Vermögen, einen stabilen Cone-Jet Modus auszubilden, untersucht. Die eingesetzten mobilen Phasen bestehen aus Wasser–Acetonitril und Wasser–Methanol Gemischen, deren Leitfähigkeit mithilfe von Ameisensäure variiert wird. Für die experimentelle Durchführung wird ein kommerziell erhältliches Mikrochip HPLC/ESI-MS System von Agilent Technologies verwendet. Um die online-Aufzeichnung des Emitterstroms zu ermöglichen, wurde der ChipCube modifiziert und ein

Oszilloskop angeschlossen. Die Charakterisierung des Elektrosprays erfolgte über die Frequenzanalyse des Emitterstroms und über die Auswertung des Spraykegels mit einer im ChipCube integrierten Kamera. Es wurden verschiedene Spraymodi und deren Stabilitätsbereiche mit besonderem Schwerpunkt auf dem stabilen Cone-Jet Modus analysiert. Der stabile Cone-Jet Modus liefert einen relativ großen und stabilen Stromfluss und produziert kleinere Primärtropfen, wodurch er zu dem favorisierten Spraymodus für die Anwendung in der Massenspektrometrie wird.

Bei niedrigem Wassergehalt in den mobilen Phasen ist der Stabilitätsbereich des Cone-Jet Modus durch die Leitfähigkeit limitiert: Unterhalb eines kritischen Leitfähigkeitswertes ist die Geschwindigkeit der Ladungstrennung und damit die Tropfenbildungsrate zu gering, um einen stabilen Cone-Jet Modus auszubilden. Mit steigender Leitfähigkeit der mobilen Phase verschiebt sich der Stabilitätsbereich des Cone-Jet Modus zu größerem organischem Anteil im Lösungsmittelgemisch. Bedingt durch die größere Leitfähigkeit von Wasser–Methanol Gemischen verglichen mit Wasser–Acetonitril Gemischen, sind die Stabilitätsbereiche des Cone-Jet Modus von Wasser–Methanol Gemischen größer, reichen zu höheren Anteilen an organischem Zusatz im Gemisch und tolerieren niedrigere Flussraten.

Enthalten die versprühten Lösungen große Wasseranteile und besitzen eine hohe Leitfähigkeit, so können die elektrostatischen Anziehungskräfte der Zusatzelektrode im ChipCube auf den Flüssigkeitsjet nicht mehr vernachlässigt werden. Der Flüssigkeitsjet wird Richtung Zusatzelektrode abgelenkt, wodurch der stabile Cone-Jet Modus übersprungen wird und der Pulsating Cone-Jet Modus direkt in den Multi-Jet Modus übergeht. Wird der Wasseranteil in der mobilen Phase zu hoch (> 85%) kann selbst bei moderaten Leitfähigkeiten (bei niedrigem Ameisensäureanteil im Eluenten) kein stabiler Cone-Jet Modus mehr ausgebildet werden. Die hohe Oberflächenspannung des Wassers verhindert ein gleichmäßiges pulsationsfreies Aufbrechen des Flüssigkeitsmeniskus. Die hohe Permittivität des Wassers destabilisiert den Kegel im stabilen Cone-Jet Modus. Diesem Effekt kann durch Senken des Gasflusses und der Temperatur im Elektrosprayinterface entgegengewirkt werden. Die Flüssigkeitsverdampfung wird reduziert, wodurch sich das Kegelvolumen vergrößert und der Kegel im Cone-Jet Modus stabilisiert wird.

In diesem Teil der Arbeit wurde deutlich gemacht, dass der Stabilitätsbereich des stabilen Cone-Jet Modus während einer Gradientenelution leicht durchkreuzt werden kann, auf Grund der starken Änderungen der Leitfähigkeit und der Oberflächenspannung der versprühten mobilen Phase. In *Kapitel 3, Teil B – Microchip electrospray: Improvements in*

spray and signal stability during gradient elution by an inverted post-column make-up flow – wird der Einfluss der Eluentzusammensetzung auf die Stabilität des Elektrosprays und die MS Detektion anhand von Infusions- und Injektionsexperimenten untersucht. Der in diesem Teil der Arbeit verwendete Mikrochip war mit einer Anreicherungssäule, einer Trennsäule und einem make-up-flow (MUF) Kanal ausgestattet. Es wurden zwei Nanopumpen verwendet; eine lieferte die mobile Phase zur Trennsäule, die zweite war mit dem MUF Kanal verbunden und pumpte Lösungsmittel mit exakt inverser Zusammensetzung zur mobilen Phase im Trennkanal. Die beiden Lösungsmittelflüsse wurden am Ende der Trennsäule und des MUF Kanals, aber noch vor der ESI Spitze, zusammengeführt, so dass die versprühte Lösung von gleichbleibender Zusammensetzung auch während eines Gradientenlaufs war. Die Signalintensitäten des Massenspektrometers wurden sowohl ohne als auch mit Benutzung des MUF Kanals für verschiedene Zusammensetzungen der mobilen Phase aufgezeichnet. Ohne Kompensation der physikalisch-chemischen Eigenschaften der versprühten Lösung mit Hilfe des MUFs wurde der stabile Cone-jet Modus als stabilster Elektrospraymodus für eine HPLC-MS Analyse ausgemacht. Obwohl die absoluten Signalintensitäten des stabilen Cone-jet Modus geringer waren, als die, die im Pulsating Cone-jet Modus beobachtet wurden, war die beobachtete Stabilität des Elektrosprays deutlich größer. Die bessere Stabilität führte zu wesentlich kleineren Standardabweichungen der Absolutintensitäten und gewährleistete somit ein zuverlässigeres MS Signal.

Ohne Kompensation der Zusammensetzung veränderten sich die Elektrospraykonditionen und das MS Signal bei konstanter Emitterspannung mit dem Wasseranteil im Eluenten während der Gradientenelution. Die unter diesen Bedingungen aufgezeichneten Chromatogramme zeigten stark variierende Peakparameter. In nachfolgenden Experimenten wurden die Änderungen in der Zusammensetzung der mobilen Phase während der Gradientenelution mit Hilfe des MUFs ausgeglichen. In den Kompensationsexperimenten reduzierten sich die Schwankungen der Peakparameter von einem Faktor von bis zu 8.3 ohne Kompensation zu einem Faktor von ~ 1.6. Die bessere Spray- und Signalstabilität mit der MUF Kompensation führte zu deutlich geringeren Fehlern in der Analytquantifizierung. Der Einfluss der Mischkammer der beiden Lösungsmittelströme nach der Trennsäule auf die Bandenverbreiterung stellte sich als vernachlässigbar gegenüber den Einflüssen des gepackten Bettes und der externen Bandenverbreiterung im MS dar.

In dieser Arbeit konnte gezeigt werden, dass für den Erhalt der optimalen Trenneffizienz mit Mikrochip HPLC/ESI-MS Systemen nicht nur die Packungsdichte der chromatographischen Festbetten, sondern auch die Kanalgeometrie der mikrofluidischen

Trennkanäle und die Elektrospraykonditionen während der Trennung und Detektion entscheidend sind. Es ist wichtig, Packprozeduren für die auf Grund ihrer Kanalgeometrie und der verwendeten Materialien von Mikrochips schwer zu packenden Kanäle zu optimieren, um möglichst dicht gepackte chromatographische Festbetten zu erhalten. Dabei spielen das Verhältnis der Kanalgröße zu Partikelgröße und die Anzahl der vorhandenen Eckregionen sowie deren Form in den nicht-zylindrischen Kanälen eine Rolle. Der Einfluss des Elektrospraymodus auf die Signalintensität und -stabilität kann nicht vernachlässigt werden. Um die während einer Gradientenelution auftretenden Änderungen des Elektrospraymodus und damit schwankenden Signalparameter während der Analyse zu vermeiden, konnte erfolgreich ein post-column make-up-flow in den Mikrochip integriert werden. Dieser kompensierte die dynamischen Änderungen der physikalisch-chemischen Eigenschaften der mobilen Phase und trug somit entscheidend zu stabilen Detektionsbedingungen bei. Die Trenneffizienz der chromatographischen Trennsäule wurde durch den MUF nicht beeinflusst. Der post-column MUF verbessert die Analytdetektion ohne die Trenneffizienz herabzusetzen und steigert somit die Leistungsfähigkeit von HPLC/ESI-MS Systemen, welche für viele pharmazeutische und industrielle Anwendungen eingesetzt werden.

Introduction

1.1 Historical development

In the beginning of the 20th century particularly organic chemistry and its techniques already had become well established. Investigation of natural substances was still in its infancy and the key features were isolation of natural substances from the accompanying material and purification from other similar compounds present together with the targeted substance. The usually employed techniques like extraction, distillation, and crystallization were time-consuming, expensive, and required large amounts of starting material. From the 1930s onwards the development of chromatography and its associated techniques changed this situation and the way how investigations of complex natural substances were carried out [1].

Precursors to chromatography were developed prior to 1900, but these investigations did not proceed further. The beginning of chromatography took place in the early 1900s when Mikhail TSWETT invented classical column chromatography and demonstrated its ability to separate different plant extracts [2]. He packed long tubes with fine powder of a porous adsorbent and flushed these columns with a stream of solvent eluting the injected sample and separating its components in the process. In his lifetime TSWETT's achievements were not appreciated by most of his peers who criticized both his results and his claims that chromatography is a superior separation technique which can provide compounds as pure as crystallization [1]. KUHN and LEDERER in Heidelberg returned to the isolation of plant constituents two decades later [3]. In the course of this study KUHN and BROCKMANN recognized the need for more reproducible and also more selective adsorbents that were specially tuned for specific separation problems. This recognized demand for uniform and reproducible adsorbents later led to the first materials standardized in terms of adsorption strength and describes the first attempt towards reproducible separations [3].

Liquid partition chromatography was developed by A. J. P. MARTIN and R. L. M. SYNGE and first described in 1941 [4]. The importance of the work of MARTIN and SYNGE was that, by introducing partitioning as the basis of separation, it made chromatography a linear process in which retention characteristics were – within a certain range – independent of the sample size. Thus, MARTIN and SYNGE were able to present a mathematical treatment of the theory of chromatography including the theoretical plate concept [4].

After these early approaches, applications of liquid chromatography appeared more rapidly between 1960 and 1970 when high-performance liquid chromatography (HPLC) was developed as an analytical tool in addition to gas chromatography (GC). At this time GC dominated the analytical field, being driven by the needs of the petrochemical industry [3]. In 1965, Csaba HORVÁTH developed the first modern liquid chromatograph. The stationary phase consisted of impermeable glass beads of about 40 µm diameter and narrow particle size distribution (psd) which were coated with a porous layer of a few micrometre thickness. These particles were packed into a column of 1 mm inner diameter (i.d.) [1]. In 1973, packing technologies were developed that made it possible for the first time to reproducibly prepare high-efficiency columns from 10 µm particles. Also during that year, the modification of the silica surface via silanization became commercially feasible. These breakthroughs in the technology led to the marketing of the first 10 µm reversed-phase columns. HPLC had now become competitive with GC because it was able to deal with a broader range of samples and had the advantage of simplified sample preparation, *e.g.*, it can run underivatized mixtures. Consequently, the number of application areas of HPLC expanded rapidly [5].

HPLC has developed into the most widely practiced analytical method today. While there are various alternatives, including spectroscopic and other techniques for the analysis of small molecules and materials, LC is playing an increasingly important role in unravelling the analytical problems of the modern life sciences [3]. HPLC is used extensively in the pharmaceutical industry in applications ranging from content uniformity assays to pharmacokinetic studies. The chemical industry relies on HPLC in the quality control of raw materials, intermediates, and finished products. In environmental laboratories, HPLC is used for the analysis of pesticides and other contaminants in soil and water. Applications of HPLC in food industry include the analysis of pesticide residues or the content of nutrients or additives. In clinical analysis, therapeutic drug monitoring is performed by HPLC [5].

A milestone in this advancement of HPLC was its coupling to a mass spectrometer, which acted as a detector beginning in 1973/74 [6]. As starting point in the history of MS one can consider publications by J. J. THOMSON and W. WIEN close to the end of the 19th century [7]. Since then, the technique has been rapidly improved. In 1955, a time-of-flight mass spectrometer was developed that measured spectra at a 10 kHz rate for oscilloscopic display. The instrument provided the required scan speed for successful online-coupling to a gas chromatograph and first experiments were done by McLAFFERTY and GOHLKE in 1955/56 [8]. Interfacing the GC and MS instruments posed a significant challenge because the effluent (carrier gas) could overwhelm the vacuum system. The jet separator soon solved this problem

[9], but only two decades later did LC combined with MS become important. The basic incompatibility between LC and MS stems primarily from two factors. First, the mass spectrometer requires ions in the gas phase at rather low background gas pressures (~ 1.3 x 10^{-9} bar) while LC employs liquid solutions often containing non-volatile solutes and buffers at atmospheric pressure and high flow rates (~ 1 mL/min). This mass flow corresponds typically to about 100 times the amount that can be accommodated by the mass spectrometer vacuum system. Thus, it is necessary to vaporize the LC effluent and to modify either the LC or the MS. The second major problem is that in LC, unlike GC, sample volatility is not an issue; therefore, to be generally useful the mass spectrometer must utilise an ionisation technique which produces the required gas phase ions without necessarily requiring thermal vaporisation of the sample [6]. Early methods included thermospray, plasma spray, the moving belt and moving wire interfaces, membrane separators, the pneumatic nebuliser interface, direct liquid introduction, the particle beam interface, and dynamic fast atom bombardment [10-12]. These interfaces were not user friendly and the development of improved liquid based ionisation techniques was required. The introduction of atmospheric pressure liquid ionisation techniques such as atmospheric pressure chemical ionisation (APCI) and electrospray ionisation (ESI) has led to the development of easy to use interfaces that have improved ionisation efficiencies and are now the method of choice for many LC-MS applications [11]. One of the main advantages of ESI is that it can be used with a flowing liquid, thus facilitating online coupling of chromatographic separations to the mass spectrometer. For example, ESI is an obvious approach for online interfacing of microchips to mass spectrometry. In particular, the nanoliter to microliter per minute flow rate used in microfluidic separations is a good match to that used in nanoflow ESI sources [13]. The application of ESI methods enables large, non-volatile molecules to be analysed directly from the liquid phase with little molecule fragmentation, making it ideal for the analysis of non-volatile, thermally instable biomolecules [11].

After early discoveries and experiments on electrospraying of various liquids [14], electrospray was further studied by ZELENY, who visualized the process [15,16] at the beginning of the 20th century. The sprays characterised in ZELENY's work are structurally similar to those employed nowadays in mass spectrometry in which a liquid is drawn into a conical shape before breaking up into a fine mist of droplets. This seminal work was followed by detailed studies of WILSON and TAYLOR. Based on a theoretical work published by TAYLOR in 1964, the conical shape has finally been termed TAYLOR cone [17,18]. Electrospray as an ionisation source for MS was introduced as a scientific tool in 1968. DOLE

and co-workers used the technique to transfer high molecular weight polystyrene ions into gas phase from a benzene/acetone solution [19,20]. During their extensive studies, they defined many of the experimental parameters important for the ESI process. However, they used only ion retardation and ion mobility measurements for mass analysis. In 1984, FENN and his co-workers first successfully combined electrospray and mass instrument to do mass detection [21-23].

As people began to grasp the concept and advantages of working at lower flow rates, the conventional ESI systems gave way to the development of various microelectrospray systems, which were soon followed by nanoelectrospray systems. Microelectrospray is the term coined by CAPRIOLI and co-workers to describe their online miniaturised electrospray device fitted with a sprayer tip of 10 – 20 μm i.d. that operated at 300 – 800 nL/min flow rates and produced small micron-sized droplets [24]. The term nanoelectrospray was later coined by WILM and MANN to describe the spray observed from the use of static needles filled with solution with no external pumping. Their primary interest was an electrospray source for which much smaller quantities of analyte are required. Such a device would be particularly important for applications in biochemistry and where in general very small samples are available. With conventional ESI, most of the analyte is wasted. With nanospray, the spray tip of the needle has a much smaller diameter resulting in a more efficient generation of gas phase ions. The flow from these needles is induced by the electrospray process itself, giving flows of terms of nanoliters per minute. However, the definition of the term nanospray has recently been refined to ES regimes with flow rates of less than 50 nL/min [11].

1.2 Separation modes

Chromatography is a separation method based on differences in equilibrium constants for the components of a mixture placed in a diphasic system. A chromatographic system is one in which a fluid mobile phase percolates through a stationary phase. These phases need excellent contact so that concentrations in the stationary phase are always very near their equilibrium values and rapid mass transfer takes place. In all cases the mobile phase is responsible for transporting the sample components through the stationary phase to the detector. The velocity of each component depends on both the mobile phase velocity and the distribution equilibrium constant for that component [25].

The mobile phase is a fluid. The main criteria for its selection are good solubility for the analytes and low viscosity. All types of fluids have been used, but the chief types of chromatography are gas, dense-gas (supercritical-fluid), and liquid chromatography. With increasing viscosity of the mobile phase (gas < supercritical-fluid < liquid), the mass transfer rate, characterised by the diffusion coefficient, decreases. Small diffusion coefficients and mass transfer rates limit the speed of the chromatographic separation and its efficiency. To compensate for this drawback finer particles are used as the mobile phase becomes denser which results in smaller mass transfer distances. The practical lack of compressibility of liquids supports this trade-off, since the use of small particles results in higher system pressures [25].

The stationary phase may be a solid – *i.e.*, an adsorbent with a relatively large specific surface area and very accessible pore channels to enhance column efficiency and ensure sufficient retention – or a liquid coated on a solid support to avoid stripping of the stationary phase by the streaming action of the mobile phase. Intermediate systems include immobilized polymers or surface-bonded shorter chemical species (*e.g.*, $C_{18}H_{37}$) of widely varying chain length and molecular mass. However, the stationary phase must be compatible with the mobile phase. Lack of solubility of the stationary phase in the mobile phase is required. The employed materials include polymeric, inorganic, hybrid, and liquid species [25,26]. At present, inorganic materials, which include silica, hydroxyapatite, graphite, and metal oxides are widely used in research and applications [26]. Among these materials silica has developed as the most widely used HPLC packing as it provides favourable characteristics, *e.g.,* good mechanical strength, high chemical and thermal stability, controllable pore structure and surface area [26]. Silica comes in two broad types: Pure or underivatized silicas (bare-silica) and the chemically bonded silicas [25]. A great variety of chemical groups – from alkyl derivatives to sugars and peptides – have been bonded to silica, leading to a large number of phases, each with its specific properties and applications.

The nature of the stationary and the mobile phases, together with the mode of the transport through the column are the basis for the classification of chromatographic methods. Gas-solid, gas-liquid, and liquid-solid chromatography are the most popular methods. Another useful distinction involves the mechanism by which the mobile phase is transported through the stationary phase. The most popular approach is forced convection by pressurisation. In thin layer chromatography capillary forces suffice to draw a liquid stream through a dry, porous bed in the form of a paper sheet or a thin layer of adsorbent coated on a sheet. In the

case of capillary electrochromatography electroosmosis is used to transport a liquid stream through a column.

The main types of HPLC techniques are normal-phase (NP), reversed-phase (RP), hydrophilic interaction chromatography (HILIC), ion-exchange (IEX), ion-pair, and ion chromatography (IC), size-exclusion chromatography (SEC), and affinity chromatography [5,27,28]. The principal characteristic defining the identity of each technique is the dominant type of molecular interactions employed. There are three basic types of molecular forces: ionic forces, polar forces, and dispersive forces.

Normal-phase chromatography

Normal-phase HPLC explores the differences in the strength of the polar interactions of the analytes in the mixture with the stationary phase. A relatively polar material with a high specific surface area is used as the stationary phase, silica being the most popular, but alumina and magnesium oxide are also often used. The mobile phase is relatively non-polar and non-aqueous. A non-polar solvent elutes more slowly than a medium-polar solvent. The retention mechanism is viewed as the competition of analyte molecules with mobile phase molecules that cover the surface. The interaction of solvent molecules with the surface obeys the same rules as the interaction of the analyte molecules.

Reversed-phase chromatography

As opposed to normal-phase HPLC, RP HPLC employs mainly dispersive forces (hydrophobic or van-der-Waals interactions). The polarities of mobile and stationary phases are reversed, such that the surface of the stationary phase in RP HPLC is hydrophobic and the mobile phase is polar, where mainly water-based solutions are employed. Reversed-phase HPLC is by far the most popular mode of chromatography. One of the main drivers for its enormous popularity is the ability to discriminate very closely related compounds and the ease of variation of retention and selectivity. The origin of these advantages could be explained from an energetic point of view: Dispersive forces employed in this separation mode are the weakest intermolecular forces, it allows for distinguishing very small differences in molecular interactions of closely related analytes. Adsorbents employed in this mode of chromatography are porous rigid materials with hydrophobic surfaces. In all modes of HPLC with positive analyte surface interactions a high adsorbent surface area is preferable because of the possibility of longer analyte retention. Strong retention yields in most cases in better

separation. The majority of packing materials used in RP HPLC are chemically modified porous silicas.

Hydrophilic interaction chromatography

In recent years, HILIC has emerged as a viable alternative technique to RP HPLC for the separation and analysis of hydrophilic solutes [29]. In HILIC mode a polar (often bare-silica) stationary phase common in non-aqueous NP HPLC and a mobile phase of water and a high fraction of organic solvent (usually aceotnitrile) are employed. The acknowledged advantages of HILIC are the alternative selectivity to RP HPLC, low back pressures due to low viscosity of the typically used mobile phases, higher MS sensitivity based on efficient spraying and desolvation of these liquids, and good mass transfer characteristics as a result of a higher solute diffusivity in organic-rich solvent mixtures [30]. However, the retention mechanism in HILIC is less well understood than that of RP HPLC and involves partitioning, adsorption, ion exchange, and even hydrophobic interactions.

Ion-exchange chromatography

IEX is based on the different affinities of the analyte ions for the oppositely charged ionic centres in the resin or adsorbed counterions in the hydrophobic stationary phase. Thus, it retains analyte molecules based on COULOMB (ionic) interactions. Depending on the charge of the exchange centres on the surface, the resin could be either anion-exchanger (positive ionic centres on the surface) or cation-exchanger (negative centres on the surface). Cross-linked styrene-divinylbenzene is the typical base material for ion-exchange resin. Exchange groups are attached to the phenyl rings in the structure. Analyte retention and selectivity are strongly dependent on the pH and ionic strength of the mobile phase.

Ion-pair chromatography

Ion-pair chromatography may also be used for the separation of ionic compounds and overcomes certain problems inherent in the IEX method. Ionic sample molecules are masked by a suitable counterion. The main advantages are that the widely available reversed-phase system can be used and, acids, bases, and neutral products can be analysed simultaneously.

Ion chromatography

IC was developed as a means of separation the ions of strong acids and bases (*e.g.*, chloride, nitrate, sodium, potassium). IC is a special case of IEX chromatography. The basic idea is to use an eluent of low ionic concentration for the separation and to convert this eluent to a neutral form after the separation. Detection is then easily carried out with a conductivity detector that now operates against a virtually blank background. Therefore, high sensitivity can be achieved.

Size-exclusion chromatography

SEC is the method for dynamic separation of molecules according to their size. As indicated by its name, the separation is based on the exclusion of the molecules from the porous space of packing material due to their steric hindrance. Hydrodynamic radius of the analyte molecule is the main factor determining its retention. It is dependent on molecular weight and molecular weight distribution of the analyte molecules and on the analyte interaction with the solvent. Historically, two different names are used for this method; it is called gel-filtration chromatography and gel-permeation chromatography. This is the only chromatography separation method where any positive interaction of the analyte with the stationary phase should be avoided, which brings specific requirements to the selection of the column packing material – in particular its pore size and pore size distribution – and the mobile phase. The eluent must be a good solvent for the sample mixture and should stronger interact with the surface of the stationary phase than the analytes. Under these conditions, the smaller the size of the molecule, the more it is able to penetrate inside the pore space of the packing material and the movement through the column is retarded. The molecules are separated in order of decreasing molecular weight, with the largest molecule eluting from the column first and smaller molecules eluting last. Molecules larger than the pore size do not enter the pore space and elute together as the first peak in the chromatogram. This is called total exclusion volume which defines the exclusion limit for a particular column. Molecules that can enter the pores diffuse into the internal pore structure of the gel to an extent depending on their hydrodynamic radius and the pore size distribution of the stationary phase. Molecules that are smaller than the pore size have the longest residence time on the column and will elute together as the last peak in the chromatogram. This last peak determines the total permeation limit for a particular column. The effective volume in which separation can occur – the intermediate volume ranging from total exclusion to total permeation – is called the selective permeation region.

The inverse application of the SEC concept, inverse size-exclusion chromatography (ISEC), utilises a set of molecular probes with defined sizes to determine pore size dimensions of stationary phase materials. ISEC provides an alternative to mercury porosimetry or nitrogen adsorption. The nondestructive nature of ISEC is of advantage in structural characterisation of a variety of chromatographic materials.

Affinity chromatography

In this case, highly specific biochemical interactions provide the means of separation. The stationary phase contains specific groups of molecules which can adsorb only the sample if certain steric and charge-related conditions are satisfied. Affinity chromatography can be used to isolate a molecule of interest (*e.g.*, protein, lipid, carbohydrate) from complex mixtures without involving any great expenditure.

1.3 Miniaturization and Instrumentation

The growing number of applications in chemical and biochemical analysis – especially in the identification and quantification of proteins and peptides – led to an enormous technological progress of LC-MS methods and instrumentations. In the early 1970s, the investigation of mass-transport processes and the distribution equilibria of analytes in a LC column as well as consideration of the hydrodynamics led to equations that gave clear directions of how to substantially improve classical liquid chromatography from gravity-operated separations at slow linear velocities (~ 0.01 mm/s) into a more efficient version: Reduce the particle size of the adsorbents to about 10 µm, pack these particles into pressure-stable columns, and operate the separation at high and constant linear velocities of about 1 mm/s [3]. Continuing the trend to improve separation speed and efficiency resulted in further reduction of the particle size, development of new stationary phase materials (*e.g.*, monolithic beds, core-shell particles), reducing the column diameter, and miniaturisation and integration of the whole analysis system [5,26,31-33].

As a first approximation, the column efficiency is inversely proportional to the average partice size of the packing media. In the last years, manufacturers began to commercialize columns packed with 3, then 2, and now with sub-2 µm particles, which have average sizes between 1.5 and 1.7 µm. To avoid the high system pressures and the resulting disadvantages of friction forces of very small particles, the concept of shell particles was revived. The core-

shell particles consist of a solid, nonporous core and a layer of porous material surrounding it. The increased separation efficiency of columns packed with core-shell particles compared to columns packed with fully porous particles is due to a lower longitudinal diffusion term, a reduced transcolumn eddy dispersion, and a reduced trans-particle mass transfer resistance [32].

However, the necessity to deal with high-throughput applications and small sample volumes required new equipment for instrumental analysis. Separation science has been one of the first operations taking benefits from lab-on-a-chip conceptualization. When downsizing conventional separation systems to the micron scale, many improvements are observed in terms of separation performances, instrument versatility, and effective costs [33]. The most important advantages of micro- and nanocolumn LC are the ability to work with minute sample sizes, small volumetric flow rates, reduced analysis times, improved efficiencies, and the enhanced detection performance with the use of concentration sensitive detection devices due to reduced chromatographic dilution [31]. The integration of injectors minimizes the injected volumes to picoliter, which reduces both sample consumption and band broadening. The zero dead-volume interconnections to the detection systems contribute as well to this gain in efficiency. Moreover, microfabrication techniques allow the integration of multiple operations and the creation of multiple or parallel analytical devices – highly-integrated portable devices are referred to as micro total analysis systems (μ-TAS) – reducing the cost of the whole analytical chain. Mass production of these miniaturized devices and the extended use of thermoplastics participate in the reduction of costs and therefore encourage the development of disposable analytical microsystems [34].

Microchip LC offers the ability to integrate all fluidic components such as pumps, sample injectors, separation column, and detection onto one credit card-sized device [35-37]. Open tubulars, ordered pillary arrays, monoliths as well as particulate packed beds are used as separation media. While monoliths offer the advantage of *in situ* preparation particulate stationary phases are desirable because of all the knowledge on silica particles that have traditionally been employed in LC columns as stationary phases could be utilised. The catalog of available surface chemistry is wide and the expected chromatographic performances are well known [34]. The introduction of stationary phase materials into microfabricated channels is a nontrivial process. Frits must be fabricated within the channel structure to retain the packing, and a high pressure interface between the microchip and an external pump must be made [38]. In addition, due to the reduced channel dimensions and the complexities of the manifold pattern, the packing process is difficult. The microchip separation channels are often

filled manually with a syringe or with the help of pumps at low to moderate pressure. Microchip separation channels, fittings, and packaging can usually not tolerate the high packing pressures used in conventional column packing, and the application of ultrasound that is often crucial to achieve good packing structure can be detrimental to the microchip devices. Carefully optimized packing conditions that provide most densely packed beds without microchip damage are essential for obtaining separation efficiencies comparable to – or even better than – those in nano HPLC [39].

The format of an HPLC column is usually referred to as a cylinder (or a tube) with defined length and diameter. On the one hand, a cylindrical geometry simplifies models and calculations, while on the other hand cylindrical tubing from different materials and with a range of internal diameters (i.d.) is easily available. While typical dimensions in analytical LC include column diameters from 4 to 5 mm at flow rates of 1 – 10 mL/min, the internal diameters of the separation columns in nano LC range from 25 – 100 µm with applied flow rates of 25 – 4000 nL/min [40]. However, geometry of the separation channels in microchip LC is inherently noncylindrical due to the employed fabrication processes. In contrast to nano LC where the separation column consists of a coated fused-silica capillary, the separation medium in microchip LC is contained in a microfluidic channel. Such channels have been realised in several different materials: silicon, glass, quartz, diamond, and a variety of polymers [41,42]. The format of the separation channels – depending on the material and the fabrication process – includes semicircular, quadratic, rectangular, trapezoidal, and elliptical geometries, often with irregularly angled corners and curved sides [35,36,43,44]. Particle-packed microchip channels and nano LC columns usually have a low channel-to-particle size ratio (particle-aspect ratio), as the reduction of channel and column dimensions with respect to conventional HPLC is not accompanied by a corresponding reduction in mean particle size. The influence of the conduit geometry on flow and dispersion in open microchannels has been extensively studied, mostly by numerical analysis methods [45-51]. In packed beds, where the packing microstructure determines time and lengths scales governing flow and dispersion [52-56], the effect of noncylindrical conduits has rarely been addressed [43]. The presence of corners in noncylindrical cross-sectional geometries impacts axial dispersion in particulate beds. Regions of advanced fluid flow exist in the corners of microchip packings, leading to larger axial dispersion coefficients compared to cylindrical packings with equal cross-sectional area [57,58]. The dimensions of the corner channels are determined by the specific conduit geometry and average bed porosity of the packing: In densely packed beds – *i.e.*, at low bed porosity – these regions are smaller than at higher bed porosity and hydrodynamic

dispersion comes close to that observed for cylindrical packings [57]. It was also found that the reduced symmetry of noncylindrical conduits translates to increased characteristic lengths for lateral equilibration of solute molecules between different velocities. Axial dispersion increased from the circular, *via* quadratic and rectangular, to semicircular packed-bed geometry [57].

This is further complicated by the small particle-aspect ratios in microchip LC. For example, packing spheres against a hard wall results in systematic fluctuations of the interparticle porosity in the immediate vicinity to the wall, starting with a maximum value of unity, followed by a damped oscillation – being influenced by the particle size distribution – with a period close to a sphere diameter over a distance of 4 – 5 monodisperse particles towards the centre of the packing [53,59]. This purely geometrical wall effect originates in a decrease of packing order as the distance from the wall increases and is inherently present in packed beds. However, while it becomes unimportant for the relatively high aspect ratios in analytical LC, it gains strong impact on macroscopic flow heterogeneity and axial dispersion at low aspect ratios when this wall fraction occupies a substantial volumetric fraction of the packing.

1.4 Nanoelectrospray

Despite from the challenges that have to be faced when bringing the chromatographic separation into microchip format, the development of a stable and effective interface with minimal dead volume for the coupling of chip-based HPLC to ESI-MS is required to improve separation efficiencies, reproducibility, and robustness of the method. The combination of HPLC with ESI-MS has emerged as the standard analytical tool for many applications, from screening of small molecule libraries to peptide and protein identification and structural characterization [13]. The flow rates employed in microchip LC are well suited to nanoelectrospray emitters. The nanospray ion source employs capillaries with spraying orifices of 1 – 2 µm i.d., and is able to produce a stable electrospray signal with flow rates in the low nL/min range. From a practical point of view, nanoelectrospray operation is often prone to difficulties associated with clogging of the fine conduits and apertures required for the small flow rates. However, nanospray results in higher ion signal intensities and it offers a better tolerance towards salt contamination, *e.g.*, from buffers, than normal electrospray. This is because smaller droplets are formed through the nanospray process, so that fewer

generations of offspring droplets are required before ions are formed. The larger droplets formed by ES require solvent evaporation to occur before sufficient charge density for droplet fission can build up, concentrating salts to levels higher than those found in the small droplets formed by nanospray [11]. On the other hand, mass spectrometers are mass flow-dependent detectors. Therefore, if ions are continuously introduced into a mass spectrometer, the signal will decrease as the flow rate decreases. The extension of the flow rate effect on the MS response is very dependent on the interface characteristics. For example, it has been shown that ionisation and ion sampling efficiency increase inversely with flow rate, counteracting the direct dependence of detector signal on absolute mass. As a result, ESI mass spectrometers can behave as if they were concentration-sensitive detectors or even show an enhanced response at lower flow rates. The latter effect is generally observed with micro- and nano ESI interfaces [60].

The quality of ion sampling from the atmospheric pressure plume strongly affects the total number of ions reaching the MS inlet. Several parameters of the ESI emitter, *e.g.* the inner and outer diameter of the spray tip and its position relative to the sampling orifice, can be optimized to improve ionisation efficiency and ion sampling. Low flow ESI emitters, *i.e.,* with reduced diameters, can be placed very close to the inlet of the MS and thus a larger part of the ESI plume is focused into the analyser. Furthermore, nanoelectrospray allows the use of lower electric fields to achieve stable spray so that the needle tip can be positioned closer to the gas vortex entering the skimmer inlet of the MS. In this way, much higher sampling rates can be obtained [24]. Another way to increase the number of ions sampled to the MS is by using larger i.d. entrance skimmers or capillaries. This implies also a higher gas flow entering the MS and therefore additional pumping capacity has to be provided [60].

The adjustment of flow rate and spray tip diameters determines the size of the droplets from which ions will be desorbed. At lower flow rates, the radius of the emission region at the tip of the TAYLOR cone is much smaller. This translates into a higher droplet surface area to volume ratio, enhancing desorption of ions into the gas phase. In other words, ions are closer to the surface in smaller volume drops – which are built in nanospray emitters – and can be more easily desorbed by the high electrical field with the consequent increase in ionisation efficiency [24]. The combination of improved ion sampling efficiency and spray performance has a dramatic effect on the performance of the ESI source. In a conventional interface, a small amount of analyte molecules in the solvent is detected by the MS detector. The nano ESI tip improved this ratio, being about 500-fold better [60].

In the design and manufacturing of a microchip HPLC/ESI-MS interface it has to be considered that the approach ensures high electrospray ionisation efficiency from the microfabricated device to obtain high sensitivities and that the contribution of the interface to band broadening must be minimized. In 1997, KARGER and co-workers [61] and RAMSEY and RAMSEY [62] were the first to hyphenate microchips in ESI-MS. KARGER's group developed a glass chip with nine microfluidic channels for direct infusion of samples. The spray was formed from the blunt edge of the glasschip. RAMSEY and RAMSEY built a similar microstructure in glass where the pumping was induced by electroosmotic flow, high enough to obtain a constant spray current. The electrospray was generated from the flat edge of the glass channel. Both designs eliminated complexity by using the open-end exit of the microchannel as the emitter. Although the ability to generate electrospray directly from the chip surface was clearly demonstrated, the flat edge is not suitable for direct coupling with on-chip separations. The eluent is spreading at the interface, which is due to the hydrophilic properties of the glass. This ultimately causes difficulty in controlling the spray direction. Moreover, polar liquids wet a large area at the edge of the hydrophilic glass chip, which limits the resolution of separations due to band broadening in the relatively large extra-column volume of the electrospray. To improve the situation the surface was made hydrophobic by coating or derivatizing [21]. Although these methods reduced the wetting of the chip edge, there was still the potential for chemical stability being affected by electrical discharge.

As with column separations, a sharp electrospray tip is required to minimize dead volumes – especially the volume of the TAYLOR cone – and to improve ionisation efficiency. An alternative approach to spraying directly from the chip is to attach an electrospray capillary to the chip channel. This kind of design was first introduced by AEBERSOLD's group [63]. Although capillary nanospray emitters are more stable, dead volumes in the coupling between chip and capillary can compromise separation performance. Also, attachment of the emitters is labor intensive and potentially a high-cost process for commercial devices. In addition, the glue used to attach the emitter can be dissolved by certain organic solvents and thus produce interference peaks or render the device inoperable [13].

Electrospray emitter tips from microfluidic chips can be constructed in the microfluidic chip itself. Microfabrication procedures allow for microfluidic channels and emitters to be constructed during chip fabrication. However, the microfabrication of fine electrospray tips as an integral part of a microdevice is not a trivial task, and suitable microfabrication procedures are still under development. In 2005, a commercial device has been developed by Agilent Technologies [44]. It consists of a microchip made by laser

ablation of polyimide foils in which an HPLC system, consisting of a sample enrichment column, a separation channel, and a nanoelectrospray tip are integrated. A face-seal rotary valve provides the switching with minimal dead and delay volumes while allowing operation pressures up to 150 bar. This HPLC-chip has found applications in proteomics, phosphoproteomics, and glycomics [64-66].

Apart from the design and manufacturing of microchips for HPLC/ESI-MS applications, the operating conditions are also important to their performance. The physical processes involved in the electrospray are complex, and many parameters have been established by trial and error. Electrospray is the dispersion of a liquid into electrically charged droplets and, as such, combines two processes: droplet fromation and droplet charging. The sample solution is fed through a capillary tube – the ESI emitter – and a high electric field is applied between the outlet of the ESI emitter and a counter electrode positioned in the outside air facing the ESI emitter. As samples are electrolyte solutions in general, the basic charging mechanism is electromechanical in nature. In the case of positive charging, the emitter acts as the anode, *i.e.,* anions are discharged at the inner capillary wall and thus negative charge is removed from the solution. The excess cations then accumulate in a liquid cone extending out of the emitter and are transported to the cathode – the counterelectrode – by the electrospray process, where they are discharged as well and thus close the current circuit if there is an interconnection at ground potential between the parts of the apparatus [67]. The conical shape of the liquid emerging from the emitter outlet under the influence of the electric field is referred to as the TAYLOR cone [17,18] although this term implies a number of conditions which are usually not fulfilled. The apex of this cone is drawn out into a liquid jet which subsequently disintegrates into an aerosol of charged droplets when electric repulsion has become larger than the cohesive force that keeps the liquid together [68]. During its flight through the ambient air the droplet undergoes size reduction by evaporation of solvent, so that charge density at the droplet surface increases. The droplet approaches the point where the forces of surface tension and the COULOMB repulsion counterbalance each other – generally called the RAYLEIGH limit [69] – then it will suffer what is called a COULOMB explosion or RAYLEIGH fission. The offspring droplets undergo further fissions, which finally results in ion emission.

Early investigations by ZELENY [15,16] demonstrated that the fluid and subsequent spray emitting from the nozzle may evolve a wide variety of morphologies. The resulting spray modes are highly dependent on a number of parameters related to instrumental design (geometry and wettability of the emitter, distance between emitter and counter electrode,

strenght and shape of the electrial field) as well as to flow rate and physicochemical properties of the fluid (surface tension, dielectric constant, viscosity, density, electrical conductivity) [70-75]. Spray modes vary in size and geometry of the liquid at the emitter outlet, the duty cycle of liquid ejection, size and charge distribution of the generated droplets, and may exhibit pulsating behavior in which droplet characteristics vary periodically. CLOUPEAU and PRUNET-FOCH [76] and JAWOREK and KRUPA [77] differentiated between electrospray modes using optical criteria. They analysed the geometrical form of the fluid meniscus – and/or jet – and the behaviour of fluid disintegration. Using the AC component of the electrospray current JURASCHEK and RÖLLGEN [78] characterized three axisymmetric spray modes which they observed at increasing voltage difference: two pulsating modes – axial mode I and II – and a continuous mode – axial mode III. Their cone imaging data identified axial modes I and II as pulsating cone-jet modes and axial mode III as a stable cone-jet mode. Axial modes I and II involve cone pulsation, ejection of a liquid jet, and its break-up into charged droplets. Instability between surface tension, which tends to minimize the surface area, and electrostatic repulsion creates this oscillating behaviour. Using FOURIER analysis of the spray current and fast imaging, evidence for a direct relationship between mechanical pulsations of the cone and spray current oscillations was reported [79]. The sequence of regimes observed by JURASCHEK and RÖLLGEN [78] did not include the dripping regime prevalent at low voltages.

The different spray modes ultimately impact measurement sensitivity and precision. An electrospray operating in the cone-jet regime provides a relatively large and stable spray current as well as smaller initial droplets, both prerequisites for higher sensitivity and quality of mass spectrometric analyses [70,80]. It would be advantageous to keep the spray mode in the desirable stable cone-jet regime throughout an entire experiment. However, the dynamic conditions encountered, for example, in gradient elution HPLC create difficulties for continuous operation in this regime. Thus, one set of ESI tuning conditions is unlikely to yield a stable cone-jet spray mode throughout the whole HPLC gradient, but results in electrospray mode changes, which sensitively affect the outcome of qualitative and quantitative HPLC/ESI-MS analyses.

1.4 Aim of this work

This work will provide an experimental investigation on the chromatographic performance of typical particulate packings of HPLC microchips and on spray stability and MS response of the microchip-ESI interface. In particular, the impact of conduit geometry on packing structure and separation efficiency is investigated. For this purpose HPLC/UV microchips with separation channels of quadratic, trapezoidal, and Gaussian cross-section are slurry-packed with either 3 or 5 µm spherical C8-silica particles under optimized packing conditions. Experimentally determined plate height curves for the empty microchannels are compared with dispersion coefficients from theoretical calculations. Packing densities and plate height curves for the microchip packings are presented and conclusively explained. The study shows that the conduit geometry influences the performance of the microchips, but the effects cannot be isolated from the particle-aspect ratio of the packings. When packing density is not influenced by the conduit geometry, the dispersion behaviour reflects dispersion in the empty microchannels, *i.e.*, is governed by geometry and dimensions of the conduit cross section. On the other hand, the symmetry advantages disappear when the particles are difficult to pack densely into the separation channel.

Two methods for the determination of packing densities or interparticle porosities are presented using the example of packed capillaries and commercially available, analytical, reversed-phase HPLC columns. The operational domain of DONNAN exclusion – for the determination of packing densities on the one hand – is characterized for bare-silica, reversed-phase, and strong cation-exchange materials with different constructions, particle sizes, and intraparticle pore sizes. The data agree well with those obtained by the independent and well-established method of inverse size-exclusion chromatography. The results confirm that intraparticle DONNAN exclusion presents a most simple, fast, and reliable approach for the analysis of packing densities.

The third part deals with the electrospray characteristics of a microchip-HPLC/ESI-MS configuration. A commercial system is modified to enable *in situ* electrospray diagnostics by frequency analysis of the microchip emitter current and spray imaging. This approach facilitates the detection of different electrospray modes together with their onset potentials. The established spray modes are described and the differences in onset potentials and stability regions explained by the physicochemical properties of the electrosprayed liquid. A microchip equipped with an enrichment column, a separation column, and a make-up flow (MUF) channel is used to investigate the impact of eluent composition on spray stability and MS response by infusion and injection experiments with a small tetrapeptide in water–acetonitrile

mixtures with and without post-column MUF compensation. Spray conditions and signal response vary significantly during a routine HPLC gradient run. The application of a post-column MUF just before the ESI tip with exactly inverted mobile phase composition reduces these variations and results in smaller errors in quantification without influencing separation performance.

References

[1] L.S. Ettre, Chromatographia 51 (2000) 7-17.

[2] M. Tswett, Ber. dtsch. Botan. Ges. 24 (1906) 316-326.

[3] K.K. Unger, R. Ditz, E. Machtejevas, R. Skudas, Agew. Chem. Int. Ed. 49 (2010) 2300-2312.

[4] A.J.P Martin, R.L.M. Synge, Biochem. J. 35 (1941) 1358-1368.

[5] U.D. Neue, HPLC Columns: Therory, Technology, and Practice, Wiley-VCH, New York, 1997.

[6] M.L. Vestal, Science 226 (1984) 275-281.

[7] H. Budzikiewicz, R.D. Grigsby, Mass Spectrom. Rev. 25 (2006) 146-157.

[8] F.W. McLafferty, Annuv. Rev. Anal. Chem. 4 (2011) 1-22.

[9] R. Ryhage, Anal. Chem. 36 (1964) 759-764

[10] J. Abian, J. Mass Spectrom. 34 (1999) 157-168.

[11] E. Edwards, J. Thomas-Oates, Analyst 130 (2005) 13-17.

[12] W.M.A. Niessen, J. Chromatogr. A 794 (1998) 407-435.

[13] J. Lee, S.A. Soper, K.K. Murray, J. Mass Spectrom. 44 (2009) 579-593.

[14] M. Prudent, H.H. Girault, Analyst 134 (2009) 2189-2203.

[15] J. Zeleny, Phys. Rev. 3 (1914) 69-91.

[16] J. Zeleny, Phys. Rev. 10 (1917) 1-6.

[17] G. Taylor, Proc. R. Soc. London, Ser. A. 280 (1964) 383-397.

[18] G. Taylor, Proc. R. Soc. London, Ser. A. 291 (1966) 159.

[19] M. Dole, L.L. Mack, R.L. Hines, R.C. Mobley, L.D.Ferguson, J. Chem. Phys. 49 (1968) 2240-2249.

[20] L.L. Mack, P. Kralik, A. Rheude, M. Dole, J. Chem. Phys. 52 (1970) 4977-4986.

[21] W.-C. Sung, H. Makamba, S.-H. Chen, Electrophoresis 26 (2005) 1783-1791.

[22] J.B. Fenn, M. Mann, C.K. Meng, S.F. Wong, C.M. Whitehouse, Science 246 (1989) 64-71.

[23] M. Yamashita, J.B. Fenn, J. Phys. Chem. 88 (1984) 4451-4459.

[24] E. Gelpí, J. Mass Spectrom. 37 (2002) 241-253.

[25] H. Günzler, A. Williams, Handbook of Analytical Techniques, Wiley-VCH, Weinheim, 2001.

[26] H. Qiu, X. Liang, M. Sun, S. Jiang, Anal. Bioanal. Chem. 399 (2011) 3307-3322.

[27] Y. Kazakevich, R. LoBrutto, HPLC for pharmaceutical scientists, Wiley-VCH, New Jersey, 2007.

[28] V.R. Meyer, Practical High-Performance Liquid Chromatography, Fourth edition, John Wiley & Sons, Ltd., 2004.

[29] P. Jandera, Anal. Chim. Acta 692 (2011) 1-25.

[30] D.V. McCalley, J. Chromatogr. A 1217 (2010) 3408-3417.

[31] J.P.C. Vissers, J. Chromatogr. A 856 (1999) 117-143.

[32] G. Guiochon, F. Gritti, J. Chromatogr. A 1218 (2011) 1915-1938.

[33] A. Rios, A. Escarpa, B. Simonet, Miniaturization of Analytical Systems: Principles, Designs and Applications, John Wiley & Sons, Ltd., 2009.

[34] K. Faure, Electrophoresis 31 (2010) 2499-2511.

[35] J. Xie, Y. Miao, J. Shih, Y.-C. Tai, T.D. Lee, Anal. Chem. 77 (2005) 6947-6953.

[36] I.M. Lazar, P. Trisiripisal, H.A. Sarvaiya, Anal. Chem. 78 (2006) 5513-5524.

[37] J.F. Borowsky, B.C. Giordano, Q. Lu, A. Terray, G.E. Collins, Anal. Chem. 80 (2008) 8287-8292.

[38] A. deMello, Lab Chip 2 (2002) 48N-54N.

[39] S. Ehlert, K. Kraiczek, J.-A. Mora, M. Dittmann, G.P. Rozing, U. Tallarek, Anal. Chem. 80 (2008) 5945-5950.

[40] G. Rozing, LC-GC Europe 16 (2003) 14-19.

[41] S. Coster, E. Verpoorte, Lab Chip 7 (2007) 1394-1412.

[42] J.P. Kutter, J. Chromatogr. A 1221 (2012) 72-82.

[43] G. Rozing, T. van de Goor, H. Yin, K. Killeen, B. Glatz, K. Kraiczek, H.H. Lauer, J. Sep. Sci. 27 (2004) 1391-1401.

[44] H. Yin, K. Killeen, R. Brennen, D. Sobek, M. Werlich, T. van de Goor, Anal. Chem. 77 (2005) 527-533.

[45] H. Poppe, J. Chromatogr. A 948 (2002) 3-17.

[46] D. Dutta, A. Ramachandran, D.T. Leighton, Microfluid. Nanofluid. 2 (2006) 275-290.

[47] A. Ajdari, N. Bontoux, H.A. Stone, Anal. Chem. 78 (2006) 387-392.

[48] N. Bontoux, A. Pépin, Y. Chen, A. Ajdari, H.A. Stone, Lab Chip 6 (2006) 930-935.

[49] E.K. Zholkovskij, J.H. Masliyah, Chem. Eng. Sci. 61 (2006) 4155-4164.

[50] H. Eghbali, G. Desmet, J. Sep. Sci. 30 (2007) 1377-1397.

[51] M. Bahrami, M.M. Yovanovich, J.R. Culham, Int. J. Heat Mass Transfer 50 (2007) 2492-2502.

[52] J.C. Giddings, Dynamics of Chromatography, Part 1: Principles and Theory, Marcel Dekker, New York, 1965.

[53] A. de Klerk, AIChE J. 49 (2003) 2022-2029.

[54] R.S. Maier, D.M. Kroll, H.T. Davis, AIChE J. 53 (2007) 527-530.

[55] U. Tallarek, E. Bayer, G. Guiochon, J. Am. Chem. Soc. 120 (1998) 1494-1505.

[56] R.S. Maier, D.M. Kroll, R.S. Bernard, S.E. Howington, J.F. Peters, H.T. Davis, Phys. Fluids 15 (2003) 3795-3815.

[57] S. Khirevich, A. Höltzel, D. Hlushkou, U. Tallarek, Anal. Chem. 79 (2007) 9340-9349.

[58] S. Khirevich, A. Höltzel, D. Hlushkou, A. Seidel-Morgenstern, U. Tallarek, Lab Chip 8 (2008) 1801-1808.

[59] S. Ehlert, T. Rösler, U. Tallarek, J. Sep. Sci. 31 (2008) 1719-1728.

[60] J. Abian, A.J. Osterkamp, E. Gelpí, J. Mass Spectrom. 34 (1999) 244-254.

[61] Q. Xue, F. Foret, Y.M. Dunayevskiy, P.M. Zavracky, N.E. McGruer, B.L. Karger, Anal. Chem. 69 (1997) 426-430.

[62] R.S. Ramsey, J.M. Ramsey, Anal. Chem. 69 (1997) 1174-1178.

[63] D. Figeys, Y. Ning, R. Aebersold, Anal. Chem. 69 (1997) 3153-3160.

[64] M. Fortier, E. Bonneil, P. Goodley, P. Thibault, Anal. Chem. 77 (2005) 1631-1641.

[65] M. Ghitun, E. Bonneil, M. Fortier, H. Yin, *et al.*, J. Sep. Sci. 29 (2006) 1539-1549.

[66] P.E. Groleau, P. Desharnais, L. Coté, C. Ayotte, J. Mass Spectrom. 43 (2008) 924-935.

[67] Th. Dülcks, R. Juraschek, J. Aerosol. Sci. 30 (1999) 927-943.

[68] A.P. Bruins, J. Chromatogr. A 794 (1998) 345-357.

[69] F.R.Strutt Lord Rayleigh, Philos. Mag. Ser. 5 14 (1882) 184-186.

[70] R.T. Kelly, K. Tang, D. Irimia, M. Toner, R.D. Smith Anal. Chem. 80 (2008) 3824-3831.

[71] R. Kostiainen, T.J. Kauppila, J. Chromatogr. A 1216 (2009) 685-699.

[72] I. Marginean, R.T. Kelly, D.C. Prior, B.L. LaMarche, K. Tang, R.D. Smith, Anal. Chem. 80 (2008) 6573-6579.

[73] I. Marginean, R.T. Kelly, R.J. Moore, D.C. Prior, B.L. LaMarche, K. Tang, R.D. Smith, J. Am. Soc. Mass Spectrom. 20 (2009) 682-688.

[74] T. Sikanen, S. Franssila, T.J. Kauppila, R. Kostiainen, T. Kotiaho, R.A. Ketola, Mass Spectrom. Rev. 29 (2010) 351-391.

[75] G.A. Valaskovic, J.P. Murphy, M.S. Lee, J. Am. Soc. Mass Spectrom. 15 (2004) 1201-1215.

[76] M. Cloupeau, B. Prunet-Foch, J. Aerosol. Sci. 25 (1994) 1021-1036.

[77] A. Jaworek, A. Krupa, J. Aerosol. Sci. 30 (1999) 873-893.

[78] R. Juraschek, F.W. Röllgen, Int. J. Mass Spectrom. 177 (1998) 1-15.

[79] I. Marginean, L. Parvin, L. Heffernan, A. Vertes, Anal. Chem. 76 (2004) 4202-4207.

[80] P. Kebarle, U.H. Verkerk, Mass Spectrom. Rev. 28 (2009) 898-917.

Theory

2.1 Important chromatographic parameters

HPLC theory could be subdivided in two distinct aspects: kinetic and thermodynamic. Kinetic aspect of chromatographic zone migration is responsible for the band broadening, and the thermodynamic aspect is responsible for the analyte retention in the column. From the analytic point of view, kinetic factors determine the width of chromatographic peaks whereas the thermodynamic factors determine the peak position on the chromatogram [1]. The following parameters are commonly used to report characteristics of the chromatographic system and separation.

NERNST partition coefficient K_C

Chromatography is based on phase-equilibrium phenomena. The components of the analyte sample are caused to equilibrate between two phases, a mobile phase and a stationary phase. A dynamic equilibrium for a two-phase system appears if substances cross over the phase boundary reversibly.

$$A_m \rightleftharpoons \tag{2.1}$$

A_m is the analyte present in the mobile phase, whereas A_s depicts the analyte in the stationary phase. A_m and A_s are in direct dependence on the concentration of the analytes in the related phases. The ratio of the analyte concentration in these phases in state of equilibrium is described by the partition coefficient K_C. The NERNST distribution law states that any species will distribute between two immiscible solvents so that the ratio of the concentrations remains constant.

$$K_C = \frac{[A_s]}{[A_m]} \tag{2.2}$$

where K_C, the fraction of the analyte's concentration in different immiscible phases, is termed the partition coefficient and was defined by NERNST, $[A_s]$ is the concentration of the analyte in the stationary phase, and $[A_m]$ is the concentration of the analyte in the mobile phase [2]. Separation can be obtained whenever the partition coefficients of the analytes differ significantly.

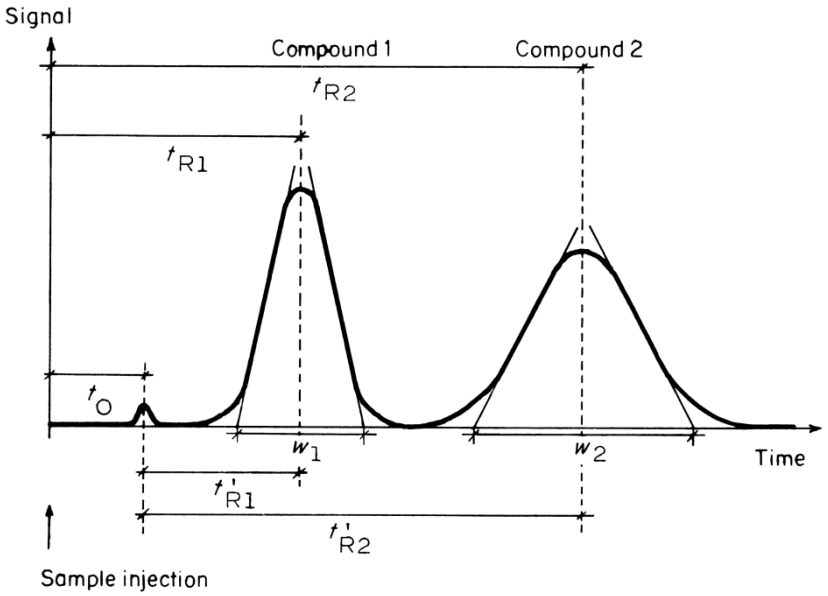

Figure 2.1: Chromatogram of two compounds and its characteristic features [3]. Reprinted with permission from ref. [3] © John Wiley & Sons, Ltd., 2004.

Column dead time t_0 and retention time t_R

The retention time of the analyte t_R can be defined as distance divided by speed (or band velocity), where the distance is the column length L and the band velocity is u_A:

$$t_R = \frac{L}{u_A} \tag{2.3}$$

Similarly the retention time of the solvent peak or an unretained analyte – often referred to as the column dead time – t_0 is

$$t_0 = \frac{L}{u_0} \tag{2.4}$$

where u_0 is the linear velocity of the solvent peak or the unretained analyte.

Equations (2.3) and (2.4) can also be expressed in terms of retention volume:

$$V_R = t_R F_v \tag{2.5}$$

where F_v is the mobile phase flow rate (mL/min).

Linear velocity u, superficial velocity u_{sf}, and volumetric flow rate F_v

In chromatography the linear velocity of an unretained tracer u_0 is defined as:

$$u_0 = \frac{L}{t_0} = \frac{F_v}{\varepsilon_{total} A} \tag{2.6}$$

with total porosity of the packed bed ε_{total} and cross section of the conduit A.

The superficial velocity u_{sf} is defined as the ratio of volumetric flow rate and conduit cross section

$$u_{sf} = \frac{F_v}{A} = \varepsilon_{total} u_0 \tag{2.7}$$

Retention factor k

Retention factor k is the dimensionless measure of the retention of a particular compound on a particular chromatographic system at given conditions defined as

$$k = \frac{V_R - V_0}{V_0} = \frac{t_R - t_0}{t_0} \tag{2.8}$$

The retention factor is independent on the column dimensions and the mobile phase flow rate.

Selectivity α

Selectivity α is the ability of the chromatographic system to discriminate two different analytes. It is defined as the ratio of the corresponding retention factors ($k_2 > k_1$):

$$\alpha = \frac{k_2}{k_1} \tag{2.9}$$

Resolution R

Resolution R is the ability of the column to resolve two analytes in two separate peaks (or chromatographic zones). In a more general form, the resolution can be defined as the half of the distance between the centres of gravity of two chromatographic zones (X_2 and X_1, respectively) related to the sum of their standard deviations σ:

$$R = \frac{X_2 - X_1}{2(\sigma_2 + \sigma_1)} \tag{2.10}$$

In case of symmetrical peaks, centres of peak gravity X could be substituted with the peak maxima; and using the relationship of the peak width w with its standard deviation σ (shown in Figure 2.2, $w = 4\sigma$), a common expression for the resolution is obtained:

$$R = 2\frac{t_{R2} - t_{R1}}{w_2 + w_1} \tag{2.11}$$

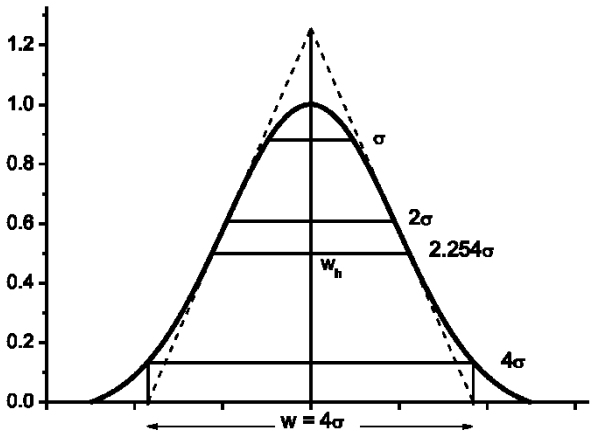

Figure 2.2: A GAUSS peak and its characteristics.

Peak shape

Under ideal conditions, chromatographic peaks should have Gaussian peak shapes. In reality, most peaks are not perfectly symmetrical and can be either fronting or tailing. The asymmetry factor A_S is used to measure the degree of peak symmetry. It is defined as the peak width of the tail ($B_{0.1}$) to the width of the front of the peak ($A_{0.1}$) at 10% peak height.

$$A_S = \frac{B_{0.1}}{A_{0.1}} \tag{2.12}$$

Usually, peaks in a chromatogram will typically show more or less tailing behaviour ($A_S > 1$). Peak tailing can be characterised in either two ways: by the asymmetry factor A_S or by the tailing factor T_f. The tailing factor is similar to the asymmetry factor but calculated using the peak width at 5% peak height:

$$T_f = \frac{w_{0.05}}{2A_{0.05}} \tag{2.13}$$

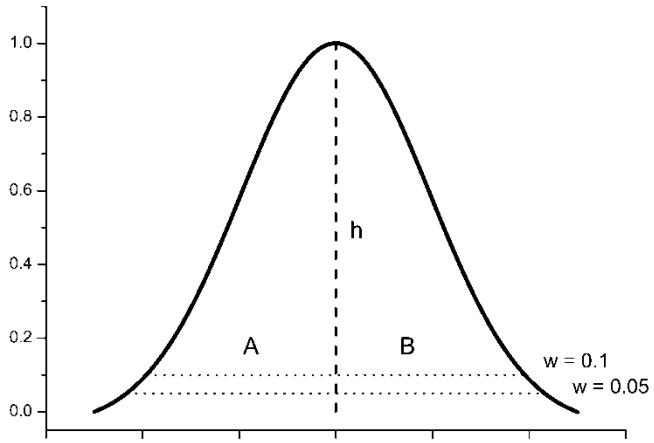

Figure 2.3: Calculation of the asymmetry factor A_S and the tailing factor T_f. In case of peak tailing A_S and T_f are > 1; in case of peak fronting A_S and T_f are < 1.

Efficiency

Just like resolution, the efficiency or plate count is a measure of the quality of the separation. While resolution is based on both the distance between two peaks and their dispersion, plate count takes into account only peak dispersion.

An analyte is injected into the column in the form of a very narrow zone with even distribution of the analyte within this zone. While this zone is moving through the column, it gets broadened. The degree of this band broadening is called the efficiency.

If column properties could be considered isotropic, then symmetrical peaks of Gaussian shape are expected, and the variance of this peak is – in accordance to the EINSTEIN diffusion equation – proportional to the axial or effective dispersion coefficient D_{ax}

$$\sigma^2 = 2D_{ax}t \tag{2.14}$$

At given linear velocity u the component moves through the column with length L during the time t

$$L = ut \tag{2.15}$$

Substituting t from equation (2.15) in (2.14) results in

$$\sigma^2 = \left(\frac{2D_{ax}}{u}\right)L \tag{2.16}$$

A plot of the variance against length is a straight line. The slope has units of length and is essentially the measure of band spreading at a given velocity on the distance L of the column. This parameter is the height equivalent to a theoretical plate (HETP or H) and could be denoted as

$$H \equiv \frac{\sigma^2}{L} \tag{2.17}$$

In the form of equation (2.17) the definition of H is exactly identical to the plate height as it evolved from the distillation theory and was brought to chromatography by MARTIN and SYNGE [5]. In this concept, a certain length of the chromatographic column was occupied by a theoretical plate. This length was the height equivalent to the theoretical plate. If H is the theoretical plate height the total number of the theoretical plates – or plate counts – in the column is

$$N \equiv \frac{L}{H} = \left(\frac{L}{\sigma}\right)^2 \tag{2.18}$$

The time necessary to move the analyte zone in the column on the distance of one σ can be defined as τ

$$\tau = \frac{\sigma}{u_c} \tag{2.19}$$

provided the migration velocity u_c is constant. In this case, the plate count can be expressed as

$$N = \left(\frac{t_R}{\tau} \right)^2 \tag{2.20}$$

Considering symmetrical band broadening of Gaussian shape, efficiency is

$$N = 16\left(\frac{t_R}{w_b} \right)^2 = 5.545\left(\frac{t_R}{w_{0.5}} \right)^2 \tag{2.21}$$

Reduced parameters

To illustrate column performance the plate height H is usually plotted *versus* the average mobile phase velocity u. However, a comparison of chromatographic systems to one another is not possible by their corresponding H-u plot. The plate height expresses the combined results of flow pattern effects which cannot simply be transferred from one column or chromatographic system to another. Thus, the concepts of reduced velocity ν and reduced plate height h were introduced with

$$\nu = \frac{d_P u}{D_m} \tag{2.22}$$

and

$$h = \frac{H}{d_P} \tag{2.23}$$

where d_P denotes the particle diameter of the column packing and D_m is the molecular diffusion coefficient of the solute component in the bulk mobile phase [6]. The dimensionless parameters are used to compare the separation efficiencies of different column packings. The reduced velocity ν describes the relative role of diffusion and flow on the movement of a solute molecule. The reason for introducing the reduced plate height is that the minimum possible value of H is limited by the particle diameter d_P.

2.2 Diffusion and kinetics in chromatography

2.2.1 Open channel dispersion

Dispersion resulting solely from physical mass transport is depending on concentration gradients and velocity profiles of the considered system. In a pressure-driven flow system at

REYNOLDS numbers < 300 ($Re = u_{sf}\ h\ \nu^{-1}$, calculated with the superficial velocity u_{sf}, tube height h, and kinematic viscosity ν) the flow profile is generally considered to be of laminar type [7]. When a zone of solute component is injected into a purely laminar flow of a Newtonian fluid moving in z-direction of a linear tube with constant cross-section area distinct diffusion and convection processes give rise to a distortion of the zone and to a broadening of concentration distribution with increasing time t. The fundamental transport function regarding both diffusion and convection is given by the differential equation

$$\frac{\partial c}{\partial t} = D_m \frac{\partial^2 c}{\partial x^2} + D_m \frac{\partial^2 c}{\partial z^2} - u(x)\frac{\partial c}{\partial z} \tag{2.24}$$

where c is the concentration, D_m the molecular diffusion coefficient of the solute component in the fluid, and u the local linear fluid velocity depending on the lateral coordinate x. It is assumed that D_m can be treated as flow-independent and that solute particles are small compared to the tube height [8]. Applying the boundary conditions of

(i) no-slip condition at the retentionless tube walls,

(ii) $c(x,y,0) = c_0(x,y)$, and

(iii) that no material is lost,

the solution for $t \rightarrow \infty$ is given by the well-known TAYLOR-ARIS equation [9,10]:

$$D_{ax} = D_m + \frac{u^2 h^2}{192 D_m} \tag{2.25}$$

with the axial or effective dispersion coefficient D_{ax} and the tube height or cylinder diameter h. The second term is often referred to in literature as dynamic dispersion. Equation (2.25) can be transformed into the dimensionless form

$$\frac{D_{ax}}{D_m} = 1 + \frac{1}{192}\left(\frac{uh}{D_m}\right)^2 = 1 + \frac{1}{192}Pe^2 \tag{2.26}$$

with the square of the PECLET number Pe, which estimates the relative magnitude of convective to diffusive transport rates in the system.

The residence time τ necessary for radial equilibration, which is only affected by diffusion, inside the tube is:

$$\tau = \frac{h^2}{8 D_m} \tag{2.27}$$

If at any time the dispersing component spread over a length of tube of order Δz fulfills the constraint

$$\frac{\Delta z}{u} > \frac{h^2}{4D_m} \tag{2.28}$$

the resulting concentration profile is nearly of Gaussian shape [9,11] and can be described by variance σ^2 of the GAUSS error distribution curve (*cf.* Equation (2.16) and (2.17)).

In case of a noncylindrical cross-section the equation that governs the concentration profile c(x,y,z,t) is given by

$$\frac{\partial c}{\partial t} = D_m \frac{\partial^2 c}{\partial x^2} + D_m \frac{\partial^2 c}{\partial y^2} + D_m \frac{\partial^2 c}{\partial z^2} - u(x,y)\frac{\partial c}{\partial z} \tag{2.29}$$

where x is the coordinate in direction of channel height and y the coordinate in direction of channel width. The TAYLOR-ARIS dispersion for two parallel plates – hypothetical infinite channel width – is described by

$$\frac{D_{ax}}{D_m} = 1 + \frac{1}{210}\left(\frac{uh}{D_m}\right)^2 = 1 + \frac{1}{210}Pe^2 \tag{2.30}$$

To describe dispersion in noncylindrical channels the exact cross section geometry has to be known. A general expression was introduced by DUTTA et al. [12]:

$$\frac{D_{ax}}{D_m} = 1 + \frac{1}{210}\left(\frac{uh}{D_m}\right)^2 f \tag{2.31}$$

where h is the characteristic narrower transverse dimension of the channel and f the dispersion coefficient, which quantifies dispersion due to the actual velocity profile. For a flat rectangular cross section with $x/y \rightarrow 0$, a factor of 7.95 was first obtained by DOSHI et al. [13] and confirmed by several authors [12] (and references therein), which is significantly higher than the parallel plate limit. In the opposite limit for a quadratic cross section ($x/y = 1$) the dispersion coefficient is $f \approx 1.76$. The discrepancy between the dispersion coefficients reflects differences in the actual velocity profiles caused by the presence of channel walls. They introduce additional regions where the fluid velocity is slowed down by friction forces.

The axial dispersion coefficient D_{ax} can be substituted with the chromatographic axial plate height H through the relation $D_{ax} = Hu/2$ (*cf.* Equations (2.16) and (2.17)) to give the normalized plate height equations H/h *versus* $Pe = uh/D_m$ in open cylindrical channels (h is the tube height or cylinder diameter)

$$\frac{H}{h} = \frac{2}{Pe} + \frac{1}{96}Pe \tag{2.32}$$

or in open noncylindrical channels (h is the characteristic narrower transverse dimension of the channel)

$$\frac{H}{h} = \frac{2}{Pe} + \frac{1}{105} f \cdot Pe \tag{2.33}$$

The first term in Equations (2.32) and (2.33) refers to the contribution of axial molecular diffusion to band broadening, and the second term describes the contribution from mass transfer resistance.

2.2.2 Dispersion in packed beds

In packed beds physical mass transport is influenced by molecular diffusion processes, adsorption-desorption kinetics, and flow pattern effects. Additionally to open channels, where dispersion depends on fluid properties – or mobile phase properties – only, in packed beds zone spreading is governed by stationary and mobile phase properties – especially the packing microstructure – leading to a much more complicated transport function. Axial dispersion is no longer determined by the geometry of the cross-section, but by the pore network of the packing microstructure, which is influenced by many different factors, *e.g.,* physical properties of the packing material and packing conditions [14]. In the literature a number of different equations for calculating plate heights have been published for either open-tubular [15] or particle-packed columns [6,16-19], all of them including functions that describe dispersion due to longitudinal diffusion and dispersion resulting from the resistance to mass transfer in the stationary and the mobile phase.

The VAN DEEMTER equation was developed in 1956 to explain band broadening in chromatography by correlating plate height H with linear velocity u. It is conceptually the simplest among the plate height equations and assumes that H is composed of three different, random, noninteracting, and, therefore, independent contributions. Thus, the variances of these contributions add up to form the observed relationship:

$$H = A + \frac{B}{u} + Cu \tag{2.34}$$

The three terms of the equation represent three different processes that contribute to the overall chromatographic band broadening. The A term represents the multipath effect of column packing, called eddy diffusion, the B term represents the molecular diffusion in the mobile phase, and the C term accounts for the mass transfer in the stationary and mobile phase. A, B, and C terms represent constants for a particular solute, column, and set of experimental conditions.

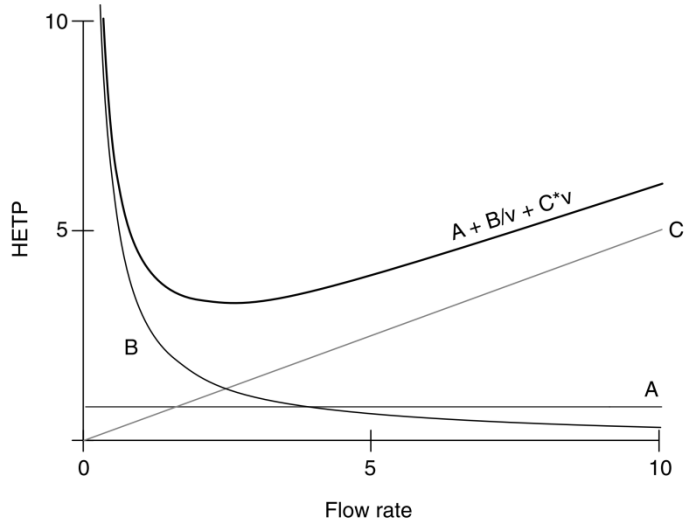

Figure 2.4: VAN DEEMTER curve showing the relationship of HETP (H) *vs.* the flow rate v. The VAN DEEMTER curve is a composite plot of A, B/v, Cv terms [1]. Reprinted with permission from ref. [1]. © Wiley-VCH, 2007.

A term – Eddy diffusion

In a packed bed the solute molecules will describe a tortuous path through the interstices between the particles and obviously some will travel shorter paths than the average and some will travel longer paths. Consequently, some molecules will move ahead of the average and some will lag behind. The inhomogeneity of the packing depends on the pattern in which the particles are arranged relative to each other. Thus, the A term of the VAN DEEMTER equation is proportional to the particle size and the shape of the particles, which can expressed in

$$A = \lambda_i d_P \tag{2.35}$$

The coefficient λ_i depends on shape and size distribution of the particles and their arrangement. The narrower the particle size distribution and the more regular (spherical) the particles, the smaller is λ.

B term – longitudinal diffusion

Longitudinal diffusion is the spreading due to molecular diffusion in the direction of the concentration gradient. Molecular diffusion is proportional to the molecular diffusion coefficient of the solute and inversely proportional to the flow rate. Therefore band broadening by molecular diffusion will increase with decreasing mobile phase velocity.

$$B = 2\gamma \frac{D_m}{u} \tag{2.36}$$

The factor γ is called the obstruction factor and depends on the amount and the nature of the obstruction that is in the way of free movement of the molecules inside the packed bed.

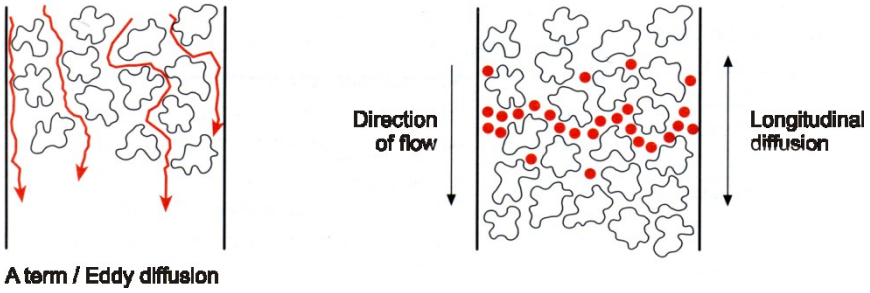

Figure 2.5: Schematic presentation of the A term or eddy diffusion and the B term or longitudinal diffusion of analytes in a particle-packed column.

C term – mass transfer phenomena

This term includes the mass transfer from the centre of the mobile phase to the surface of the particle, through the stagnant mobile phase in the pores to the stationary phase on the internal surface of the packing, the interactions with the stationary phase (*e.g.*, adsorption and desorption kinetics), and the way back into the moving mobile phase (Figure 2.6).

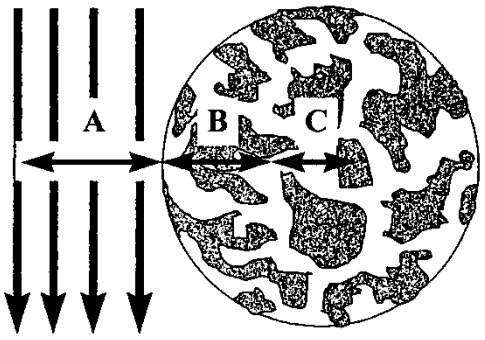

Figure 2.6: Mass transfer phenomena: the analyte needs to be transported from the moving mobile phase to the surface of the particle (A), through the stagnant mobile phase in the pores to the stationary phase on the internal surface of the packing (B), followed by the interactions with the stationary phase (C) and its transport back into the moving mobile phase [20]. Reprinted with permission from ref. [20] © Wiley-VCH, 1997.

In principle, two major contributions to the resistance to mass transfer can be distinguished: Mass transfer in the mobile phase and mass transfer in the stationary phase. Both contributions increase with linear velocity. Solute molecules are continually transferring from the mobile phase into the stationary phase and back when a solute band progresses along a column. This transfer process is not instantaneous, because a finite time is required for the molecules to traverse through the mobile phase in order to reach the stationary phase.

Movement of solute molecules is due to diffusion in the mobile phase. The contribution to the C term of the mobile phase is a function of the molecular diffusion coefficient D_m, the width of the channel through which the mobile phase is flowing, the retention factor k, and the actual velocity profile of the mobile phase. The dispersion resulting from the resistance to mass transfer in the stationary phase can be described in a similar way. Molecules closer to the surface of the stationary phase will leave and enter the mobile phase earlier than those who have diffused farther into the stationary phase. The term is a function of the diffusivity of the solute in the stationary phase, the thickness of the stationary phase, and the retention factor k.

Because of the complexity of the phenomena it is difficult to derive generally valid mass transfer terms for the packed bed. A rough estimation of the C term in a packed bed with porous particles in the practical range of retention factors of $2 \leq k \leq 10$ is

$$C = \omega \frac{d_P^2}{D_m} u \tag{2.37}$$

The coefficient ω is found to be between 1/10 and 1/5 in most experiments [20].

The VAN DEEMTER equation provides a simple and useful description of the basic hydrodynamic phenomena in a packed bed, but is incorrect in concept inasmuch that it predicts a finite contribution to dispersion, independent of solute diffusivity, in the limit of zero mobile phase velocity. However, due to the complexity of the three contributions to the overall dispersion inside chromatographic columns packed with porous silica particles a correct analytical solution for the dispersion problem is not available. Regarding separation systems packed with the same packing material and characterized under equal conditions no differences in retention behaviour and/or diffusion within the stationary phase are expected. Thus, variations of H-u curves between the considered packed beds can be ascribed to the respective flow profile resulting from the packing microstructure. GIDDINGS [6] proposed five different contributions to eddy dispersion in the mobile phase percolating through a packed bed:

(i) transchannel effect, a term derived from the radial velocity profile in each interstitial flow channel between the particles. It resembles the HAGEN-POISEUILLE flow profile in a cylinder, though channels in a packed bed deviate from cylindrical geometry;

(ii) short-range interchannel effect, resulting from small tightly packed regions surrounded by a rather loosely filled space, leading to flow heterogeneities;

(iii) long-range interchannel effect, due to repeating units of the short-range interchannels;

(iv) transcolumn effect, arising from variations in flow profile and velocity between the wall regions and the centre of the packed bed;

(v) transparticle effect, occurring through the stagnant part of the mobile phase within the porous particles.

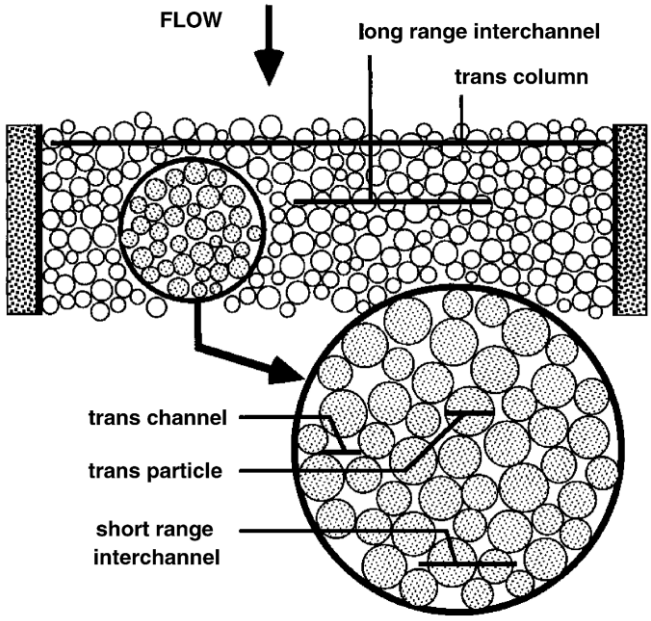

Figure 2.7: Definitions, locations, and scales of the different classes of velocity heterogeneities contributing to eddy dispersion [21]. Reprinted with permission from ref. [21]. © American Chemical Society, 1998.

Since only flow and diffusion effects couple, while longitudinal diffusion and stationary phase mass transfer do not, the complete equation for the dependence of the plate height on the linear velocity can be written as [6]

$$H = \frac{B}{u} + C_s u + \sum \frac{1}{\frac{1}{A} + \frac{1}{C_m u}} \tag{2.38}$$

2.3 Thermodynamics

The retention of a solute in a chromatographic system is determined firstly by the magnitude of the distribution coefficient of the solute between the two phases, and secondly by the amount of stationary phase available to the solute for interaction. The distribution coefficient

is an equilibrium constant and, consequently, it can be treated rationally by conventional thermodynamics [20].

The retention factor k is measured as the retention time of an analyte minus the retention time of an unretained tracer divided by the retention time of the unretained tracer (*cf.* Equation (2.8)). An unretained tracer spends all its time in the mobile phase. Thus, the difference between the total time that an analyte spends in the column and the time that an unretained tracer spends in the column has to be spent in the stationary phase. Therefore, the retention factor can be expressed as the ratio of the time t_s that an analyte spends in the stationary phase and the time t_m that it spends in the mobile phase

$$k = \frac{t_s}{t_m} \tag{2.39}$$

Under isocratic conditions it is also the ratio of the number of molecules N_s that are at any time in – or on – the stationary phase to the number of molecules N_m that are in the mobile phase. In partition chromatography, the number of molecules in the stationary phase and in the mobile phase can be related to their respective concentrations c_s and c_m, respectively,

$$k = \frac{N_s}{N_m} = \frac{c_s V_s}{c_m V_m} \tag{2.40}$$

where V_s and V_m are the volumes of the stationary and the mobile phases, respectively. Their ratio is called the phase ratio β:

$$\beta = \frac{V_s}{V_m} \tag{2.41}$$

The ratio of the concentrations c_s and c_m is the NERNST partition coefficient K_C, which is identical to the equilibrium constant K :

$$K_C = \frac{c_s}{c_m} = K \tag{2.42}$$

The retention factor can be expressed as the product of the phase ratio and the partition coefficient:

$$k = \beta K_C \tag{2.43}$$

The relationship between the equilibrium constant and the standard GIBBS free-energy difference associated with this chemical equilibrium is:

$$\Delta G° = -RT \ln K \tag{2.44}$$

with the temperature T and the gas constant R.

Therefore, the logarithm of the retention factor is a function of the free energy:

$$\ln k = \ln \beta - \frac{\Delta G^\circ}{RT} \tag{2.45}$$

2.4 Physical properties of HPLC packings

2.4.1 Packing materials

A wide variety of stationary phases are employed in chromatographic separations [22,23]. Four distinct characteristics can be used for column classification:

(i) Type (monolithic, porous, nonporous)

(ii) Geometry (surface area, pore volume, particle size and shape, pore diameter)

(iii) Surface chemistry (type of bonded ligands, bonding density)

(iv) Type of base material (silica, polymer, zirconia)

Silica is the most often used base material. The hydrophilic surface contains several types of silanols (isolated, vicinal, and geminal) and siloxanes. There are three types of bare-silica materials, silica type A, silica type B, and silica type C.

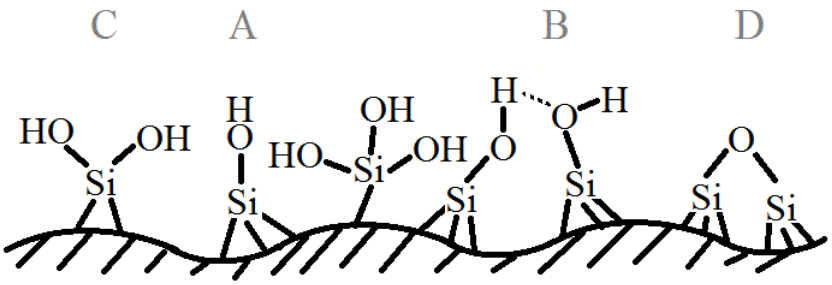

Figure 2.8: Schematic of the bare-silica surface. The different arrangement of silicium and oxygen leads to the formation of isolated (A), vicinal (B), and geminal (C) silanols as well as siloxanes (D).

Type A silica is the original all-purpose chromatographic material, produced by precipitation from alkali silicate solutions. It is usually contaminated with metals. Spherical particles of the type B silica are formed by the aggregation of silica sols in the air, contain very low amounts of metal impurities and are relatively stable at intermediate and higher pH to at least pH 9. Type C, the hydride silica, has large part of the Si-OH silanol surface groups replaced by Si-H groups during the hydrosilation process.

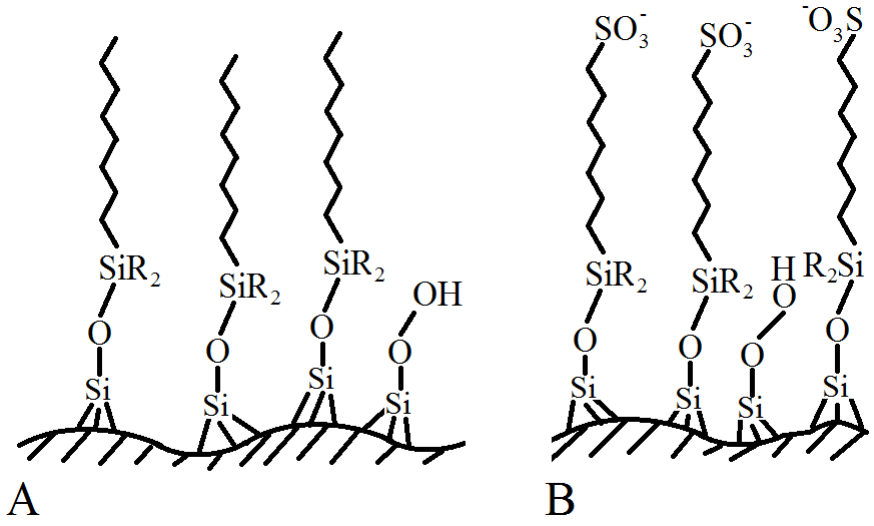

Figure 2.9: Schematic of a silica surface modified with octyl groups (A) and strong cation-exchange groups (B).

In reversed-phase HPLC chemically modified silica is used. Surface silanols could react with many different functional groups to form the so-called bonded phase. The majority of the bonding agents used are chlorosilanes. The chemical nature of the ligands bonded on the surface defines the main type of chemical interactions of the surface with the mobile phase and analyte molecules. The employed stationary phases in RP HPLC are strictly of hydrophobic nature. The most popular types of bonded phases are octadecyl (C18), octyl (C8), phenyl, and cyanopropyl bonded phases. The functional group of strong cation exchangers is the sulfonic acid group $-SO_3^-$. It could be either an aromatic sulfonic acid or an aliphatic sulfonic acid.

2.4.2 Particle size and size distribution

The particle size of a packing is of utmost importance as it determines the permeability of a column and the column efficiency. The size of a particle is easy to define if the particle is spherical: it is its diameter. It is undefined for irregular particles, which makes it difficult to quantitatively compare the performance of columns packed with materials made of spherical and of irregular materials. Three common definitions of the average particle size are used:

$$\overline{d_P} = \frac{\sum d_{P,i} d_{P,i}^k n_i}{\sum d_{P,i}^k n_i} \tag{2.46}$$

With k = 0 the number-averaged $d_{P,\#}$, with k = 2 the surface-averaged $d_{P,s}$, and with k = 3 the volume-averaged $d_{P,v}$ particle diameter is obtained [24]. For symmetrical distributions all mean diameters are coinciding. For nonsymmetrical distributions the determined values for

the different mean diameters increase with k. The surface-averaged particle diameter $d_{P,s}$ is called SAUTER mean diameter.

Specific surface area – or surface-to-volume ratio – S_V of a collection of spherical particles with a variable size can be calculated by

$$S_V = \frac{A_P}{V_P} = \frac{4\pi\left(\frac{d_{P,s}}{2}\right)^2}{\frac{4}{3}\pi\left(\frac{d_{P,v}}{2}\right)^3} = \frac{3\left(\frac{d_{P,s}}{2}\right)^2}{\left(\frac{d_{P,v}}{2}\right)^3} = \frac{6}{d_{P,s}} \tag{2.47}$$

where A_P is the actual surface area of the particle and V_P its volume.

Most packings used in HPLC have a distribution of particle sizes. This is inherent in the manufacturing process. A particle size distribution (PSD) can be displayed in several different ways. The simplest view is a plot of the number of the particles in a narrow particle diameter window *versus* the average particle diameter in this window. Form this distribution, called the population distribution, the number-averaged particle size $d_{P,\#}$ can be calculated [20].

2.4.3 Column porosity

The total column volume V_C can be calculated from its geometrical dimensions:

$$V_C = \pi r_C^2 L_{bed} \tag{2.48}$$

where r_C is the column radius in case of cylindrical cross-section and L_{bed} is the length of the packed bed. The interparticle column volume V_{inter} together with the intraparticle volume V_{intra} and the volume of the stationary phase V_{par} add up to the total column volume V_C.

$$V_C = V_{inter} + V_{intra} + V_{par} \tag{2.49}$$

V_{inter} is the interparticle or interstitial volume of the packed bed which is accessible to an analyte that is excluded from the intraparticle or pore volume V_{intra} of the packing. The interparticle and total bed porosity (ε_{inter} and ε_{total}, respectively) are directly related to V_C:

$$\varepsilon_{inter} = \frac{V_{inter}}{V_C} \tag{2.50}$$

$$\varepsilon_{total} = \frac{V_{total}}{V_C} \tag{2.51}$$

V_{total} denotes the total pore volume of the packing that is accessible to a small unretained analyte. Interparticle and total porosity are related by the intraparticle porosity (ε_{intra}):

$$\varepsilon_{total} = \varepsilon_{inter} + (1 - \varepsilon_{inter})\varepsilon_{intra} \tag{2.52}$$

Intraparticle porosities are related to V_C by the following equation:

$$\varepsilon_{intra} = \frac{V_{intra}}{V_C(1-\varepsilon_{inter})} \tag{2.53}$$

The random-close-packing limit for packings of monodisperse particles is $\varepsilon_{inter} = 0.354$ [25]. Experimental realised packing densities are on the order of $0.36 \leq \varepsilon_{inter} \leq 0.4$. These slightly elevated values compared to the random-close-packing limit are caused by the presence of friction forces between the column walls and the particles on the one hand [26,27], and the geometrical wall effect which originates from the inability of hard spheres to form a close packing against the flat surface of the column wall and from the friction forces between the particles.

2.4.4 Permeability

To sustain the percolation at a constant velocity of a stream of mobile phase along a column, a certain pressure must be maintained at the column inlet. This pressure is the major obstacle that prevents maximizing resolution and minimizing analysis time simultaneously. It depends on flow rate, column length, column diameter, particle size, and fluid viscosity.

The flow situation in the porous medium comprising the particle-packed bed is a complex one. It can be assumed that the fluid is Newtonian and that the flow is laminar. The general physical law governing the resistance to flow of a Newtonian fluid with viscosity η through a packed bed is DARCY's law which is a linear relationship between the superficial velocity u_{sf} and pressure drop over the length of the packed bed $\Delta p/L_{bed}$ multiplied with the specific DARCY permeability κ_D and inversely proportional to the dynamic viscosity η [28]:

$$u_{sf} = \frac{\kappa_D \Delta p}{\eta L_{bed}} \tag{2.54}$$

DARCY's law is valid for the case of creeping flow – linear-laminar flow regime – and that both Newtonian fluid and porous medium remain incompressible. Starting deviations from this law for packed beds at Reynolds numbers – $Re = (u_{sf}/\varepsilon_{inter}) \cdot (d_P/\nu)$, calculated with the kinematic viscosity ν – larger than 1 are attributed to inertial forces (nonlinear-laminar or viscous-inertial flow regime) [7]. As can be seen from Equation (2.54) the specific permeability κ_D is simply defined as proportionality constant which can be accurately observed experimentally, but it does not provide any insight into the physics of flow through the actual material.

One approach to model flow through porous media has been to consider the medium as made up of bundles of straight capillaries or assemblages of randomly oriented straight pores or capillaries in which the flow is laminar. The starting point in this model is HAGEN-POISEUILLE's law governing the steady flow through a single, straight circular capillary tube of diameter d [29]:

$$u_{sf} = -\frac{d^2}{32} \cdot \frac{\Delta p}{\eta L_{bed}} = -\frac{d^2}{16 k_0} \cdot \frac{\Delta p}{\eta L_{bed}} \tag{2.55}$$

The analogy between Equation (2.55) and DARCY's law is obvious. In Equation (2.55) the factor $d^2/32$ is analogous to the specific permeability κ_D for a cylindrical tube. In case of a noncylindrical cross-section geometry, the shape factor k_0 has to be considered [30]. The diameter of the tubes is identified by a hydraulic diameter d_h which is conventionally defined as four times the cross-sectional area divided by the wetted perimeter, and measures the ratio of volume to surface of the pore space. In terms of the porous medium characteristics,

$$d_h = \frac{4V_{inter}}{A} = \frac{4\varepsilon_{inter} V_C}{A} \tag{2.56}$$

where A is the total surface area. It is common to express the total surface area in terms of an inverse length, termed the specific surface area S_V. In case of the porous medium, S_V is the ratio of the surface area to the volume of the solid's fraction of the porous medium:

$$S_V = \frac{A}{(1-\varepsilon_{inter}) V_C} \tag{2.57}$$

Substituting Equation (2.57) into Equation (2.56), the following expression for the hydraulic diameter is obtained:

$$d_h = \frac{4\varepsilon_{inter}}{S_V (1-\varepsilon_{inter})} = \frac{4\varepsilon_{inter}}{\left(\frac{6}{d_{P,s}}\right)(1-\varepsilon_{inter})} \tag{2.58}$$

Regarding the interstitial velocity $u_{inter} = u_{sf}/\varepsilon_{inter}$ – which is greater than the superficial velocity due to the volume occupied by the solid – the specific permeability in the KOZENY-CARMAN approach can be formulated analogue to DARCY's law

$$u_{sf} = -\frac{\varepsilon^3}{k_0 \mu (1-\varepsilon_{inter})^2} \left(\frac{d_{P,s}}{6}\right)^2 \cdot \frac{\Delta p}{\eta L_{bed}} \tag{2.59}$$

where μ is the hydraulic tortuosity factor. According to CARMAN [31], the best value of the combined factor $k_0\mu$ to fit most experimental data on packed beds is equal to 5. Usually, the factors 6^2 and $k_0\mu = 5$ are combined to yield the KOZENY-CARMAN factor $f_{KC} = 180$. Thus, the specific permeability of a particle-packed bed in the KOZENY-CARMAN approach is [28]:

$$\kappa_{KC} = \frac{d_{P,s}\varepsilon_{inter}^3}{(1-\varepsilon_{inter})^2 f_{KC}} \tag{2.60}$$

2.5. Reversed-phase HPLC

In reversed-phase HPLC the stationary phase is nonpolar (hydrophobic) and the mobile phase is polar. A typical stationary phase consists of a long-chain hydrocarbon attached to a support, while a typical mobile phase comprises mixtures of water or buffer with polar solvents such as methanol, acetonitrile, or tetrahydrofuran. Retention is a function of the hydrophobicity of the analyte, which, in turn, is largely a function of the size of the hydrophobic area of a molecule. Therefore, RP HPLC is ideal for the separation of members of a homologous series. In many cases, it is also possible to assign the elution order of the analytes based on their structures. Retention increases with an increase in the water content of the mobile phase in a predictable manner. One will find that the larger the hydrophobic part of the analyte, the longer is the retention. Polar functional groups of the analyte molecule reduce retention also in a rather predictable way, but their incremental contribution depends on their position, on the molecule, and on the solvent [20].

2.5.1 Isocratic and gradient elution

Most HPLC separations are performed under isocratic conditions in which the same mobile phase composition – or in a more general definition the same separation conditions – are applied throughout the elution of the entire sample. Although isocratic analysis works well for simple mixtures, gradient analysis, in which the strength of the mobile phase is increased with time during sample elution, is preferred for more complex samples containing analytes of diverse polarities. Retention of later peaks is reduced within the separation process resulting in reduced run times. Advantages of gradient analysis are better detection of early and late eluting peaks and better sensitivity of late eluting peaks as well as a higher peak capacity. The disadvantages are that method development, implementation, and transfer are more complicated and typically longer assay times are required since the column must be equilibrated with the initial mobile phase. Considering the detection, a gradient analysis may alter the signal-to-noise ratio during analysis due to the changing physicochemical properties of the mobile phase.

2.6. Inverse size-exclusion chromatography (ISEC)

The structure of the pore space of chromatographic adsorbents is of principal significance in determining the functional properties. Most natural and synthetic porous media contain pores with irregular geometry and heterogeneous sizes. To describe the complicated pore structure, a number of structural parameters are relevant, among which the pore size distribution represents the distribution density of pores within a certain range of dimensions and serves as a statistical descriptor of the diverse size features.

The commonly used techniques can be categorized into four main classes: gas sorption, mercury intrusion, microscopy, and solute exclusion, among which solute exclusion is the most suitable for the investigation of structures under similar conditions to those in chromatographic applications. Solute exclusion is routinely applied in size-exclusion chromatography to determine solute size based on known pore dimensions of the adsorbents or empirical retention information relative to that of standards. The inverse application of the SEC concept utilizes a set of molecular probes with defined sizes to determine pore dimensions. The ISEC principle was introduced by HALÁSZ and MARTIN for characterization of chromatographic stationary phases [32]. The pore size distribution of an unknown stationary phase can be determined from the distribution of retention volumes of a series of polymer standards if their molecular weight is known. The polymers were then assigned "rotation coil diameters" as a function of their molecular weight. Assuming that all polymeric chains form a random coil of invariant size and shape during chromatographic analysis, the average molecular weights of the polymer standards are correlated with the average diameter of the pores from which they are size-excluded:

$$M_W = a \cdot d_{pore}^b \tag{2.61}$$

with the constants a and b depending on the polymer material and the solvent properties.
For each packing material, there are two thresholds, a low and a high one, which can be expressed by the elution volumes of the polymers V_A according to

$$V_A = V_{inter} + V_{pore} K_A \tag{2.62}$$

where V_{pore} denotes the total pore volume of the packing material and K_A is the permeation extent that represents the fraction of pore space ($0 \leq K_A \leq 1$) accessible to a certain probe A. Ideally an infinitesimally small solute that does not interact with either other solutes or the stationary phase is used to access the complete pore space ($V_{inter} + V_{pore}$), and the interstitial space V_{inter} is measured by a large probe that is excluded from all pores but explores the total interparticle void [33].

Plots of the logarithm of the molecular weight of polymers *versus* their elution time reveal a bimodal pore size distribution representing the intraparticle and interparticle porosity of the packed bed. Plots of the polymers' elution volume *versus* the cubic root of their molecular weight yield a pore size distribution that denotes the maximal interparticle void volume V_{inter}. Employing the elution volumes of only size-excluded polymers, the elution volume of a fictitious point mass analyte can be determined *via* linear regression. The so-derived values of V_{inter} are not falsified by the actual molecular size of the excluded polymer standards [34].

ISEC has a number of advantages over alternative methods. Column experiments with intact samples packed in a bed can conserve sample integrity and are easy to carry out, as opposed to the special sample preparation procedures in electron microscopy. No additional equipment other than a chromatography system is necessary for ISEC, so it is relatively inexpensive and convenient. Operation conditions such as high pressure, low temperature, and drying conditions, which are involved in gas sorption or mercury intrusion, are not imposed in ISEC. Experimental conditions similar to those in normal operations result in less significant morphological changes, which is especially important for swellable gels [33].

Based on a simplified pore model, ISEC is capable of providing comparative descriptions for pore statistics, which can be used for understanding macromolecular retention and transport behaviour. However, no information on the pore geometry can be deduced from ISEC. Similarly, the connectivity of the pore space in the stationary phase, an important parameter governing solute transport, cannot be probed directly by ISEC.

Drawbacks of this method are the assumption about formation and hydrodynamic stability of the polymeric coils, the necessity of using rather aggressive organic solvents such as dichloromethane or tetrahydrofurane for chromatographic analysis, and the fact that V_{inter} and ε_{inter} are determined by linear regression executed on a limited data set.

2.7. DONNAN exclusion

An alternative method to ISEC for determination of ε_{inter} is the DONNAN exclusion method. Like ISEC, the analysis of V_{inter} and ε_{inter} is executed on-column, based on the interparticle elution of organic or inorganic ions which are completely electrostatically excluded from the intraparticle pore space due to the DONNAN potential [35-37]. This approach originates as a

limiting variant of the much explored use of organic and inorganic ions as dead time marker in RP HPLC. Compared to ISEC, it offers the advantage to use aqueous mobile phases.

In contact with water or aqueous solvent mixtures the silanol groups present on the surface of silica-based stationary phases may be deprotonated resulting in a negative surface charge. The extent of this deprotonation and the corresponding electric field depend on the solvents pH and the ionic strength as well as on the structure and the size of the (porous) solid medium. The surface potentials can be described by two different models, the electric double layer and the DONNAN model.

2.7.1 The electric double layer (EDL)

Generally, most substances will acquire a surface electric charge when brought into contact with an aqueous medium. The effect of any charged surface in an electrolyte solution will be to influence the distribution of nearby ions in the solution. Cations, which possess opposite charge (counterions) to the negative charge of the silica surface are attracted toward the surface while ions of like charge (co-ions) are repelled from the surface (Figure 2.10).

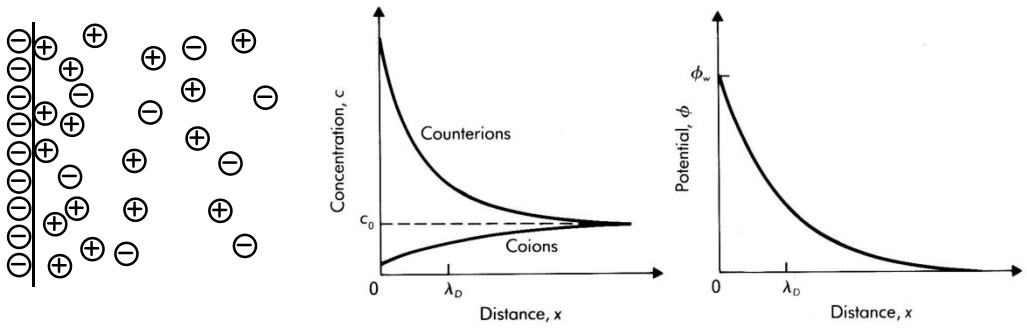

Figure 2.10: Schematic presentation of the diffuse electric double layer establishing on a silica surface and the dependency of ion concentration and the corresponding potential on the distance [38]. Reprinted with permission from ref. [38] © Wiley, 1994.

This attraction and repulsion, when combined with the mixing tendency resulting from the random thermal motion of the ions, leads to the formation of an electric double layer. In the simplest model of an electric double layer, the counterions bind directly to the surface and neutralise the surface charges much like in a plate capacitor, which is called the HELMHOLTZ layer. The electric field generated by the surface charges is accordingly limited to the thickness of a molecular layer. But the model failed to explain the capacitance of an electric double layer. GOUY and CHAPMAN took into account a thermal motion of the ions. This leads

to the formation of a diffuse layer, which is more extended than a molecular layer (Figure 2.10).

For the simple case of a planar, infinitely extended surface, the potential cannot change in the y- and z-direction because of the symmetry. The surface is taken to be negatively charged and the co-ions of the electrolyte are assumed to be absent. Then, the electrical potential Φ from the POISSON equation is defined by

$$\frac{d^2\Phi}{dx^2} = -\frac{Fz_i c_i}{\varepsilon_0 \varepsilon_r} \tag{2.63}$$

where x is the coordinate parallel to the plane charged surface, F is the FARADAY constant, z_i is the valency of ionic species, c_i its concentration in the electroneutral bulk solution, and ε_0 and ε_r are the permittivity of vacuum and relative permittivity of bulk solution, respectively. The electrical potential energy W per mole of positive ion is

$$W = -Fz_i\Phi \tag{2.64}$$

The change in W across a plane layer of width x is obtained by integrating Equation (2.63):

$$\Delta W = -\frac{F^2 z_i^2 c_i x^2}{2\varepsilon_0 \varepsilon_r} \tag{2.65}$$

This result assumes that the electric field vanishes on one side of the plane layer. Assuming only planar translational motion, the value of x for which the absolute value of ΔW equals RT is

$$x \equiv \lambda_D = \left(\frac{\varepsilon_0 \varepsilon_r RT}{F^2 \sum z_i^2 c_i} \right)^{\frac{1}{2}} \tag{2.66}$$

The quantity λ_D is termed the DEBYE length which depends on the ionic strength and characterizes the electric double layer thickness.

The treatment given above is based on the assumption that the ions in the electrolyte are treated as point charges. Considering the finite size limits the inner boundary of the diffuse part of the double layer, since the centre of an ion can only approach the surface to within its hydrated radius without becoming specifically adsorbed (Figure 2.11). To take this effect into account, an inner part of the double layer is introduced next to the surface, the STERN layer. The plane separating the inner layer and the outer diffuse layer is called the STERN plane. The potential at this plane is close to the zeta (ζ) potential, which is defined as the potential at the shear surface between the charged surface and the electrolyte solution.

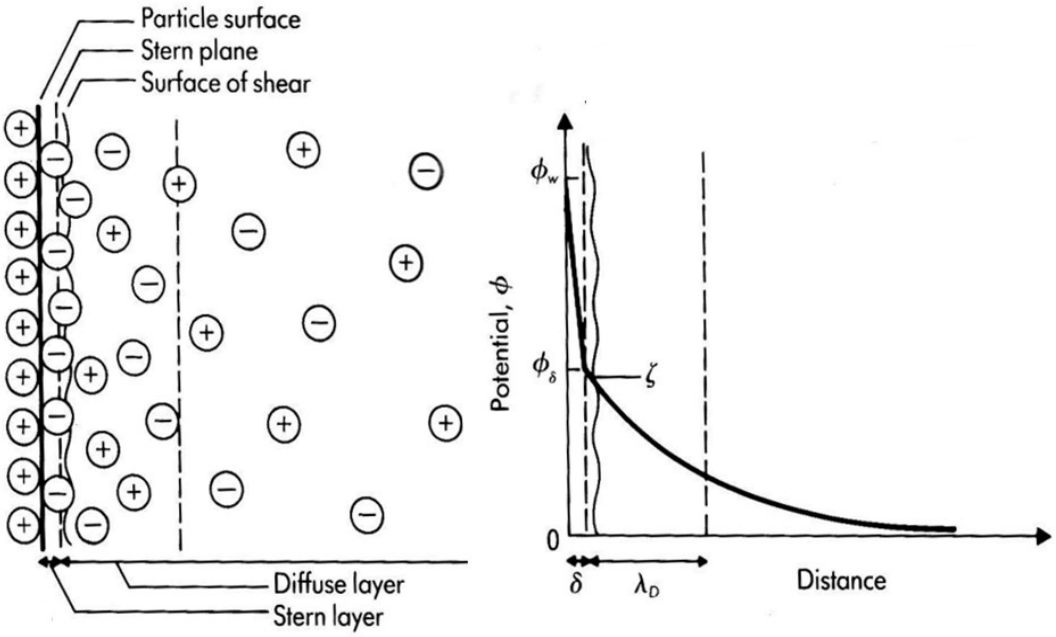

Figure 2.11: Structure of electric double layer with inner STERN layer [38]. In this example the surface is positively charged. Reprinted with permission from ref. [38]. © Wiley, 1994.

If the dimensions of the system L are much larger than λ_D, then whenever local charge concentrations arise or external potentials are introduced into the solution they are shielded out in a distance short compared with L, leaving the bulk of the solution free of large electric potentials of fields. However, in the case of very small charged microscopic capillaries or particles the electric double layer is central to the calculation of the solute and ion fluxes. For the limiting case of small DEBYE length ratio, shown schematically in Figure 2.12, $\Phi = 0$ at the centre and the solution is electrically neutral there. For the limiting case of large λ_D, the entire pore is within the double layer [37].

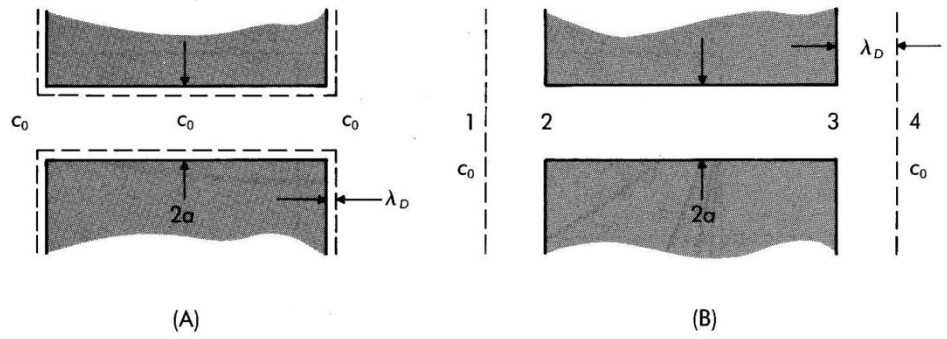

Figure 2.12: DEBYE layer location in a cylindrical pore for (A) small DEBYE length and (B) large DEBYE length. The positions 1 and 4 are outside of the electric double layer, the positions 2 and 3 are located within the electric double layer. C_0 denotes the concentration of the bulk solution [38]. Reprinted with permission from ref. [38]. © Wiley, 1994.

Figure 2.13 shows a potential distribution across a cylindrical pore for various values of the DEBYE length ratio. It can be seen that for large pore diameters d_{pore} compared to the electric double layer thickness $\delta_{EDL} \approx 5–10\ \lambda_D$ ($d_{pore} >> \delta_{EDL}$) the potential is zero over most of the pore cross-section, whereas for $d_{pore} << \delta_{EDL}$ the potential is nearly constant over the cross-section. The overlap of the electric double layers results in counterion enrichment and co-ion exclusion with respect to the concentrations in bulk solution.

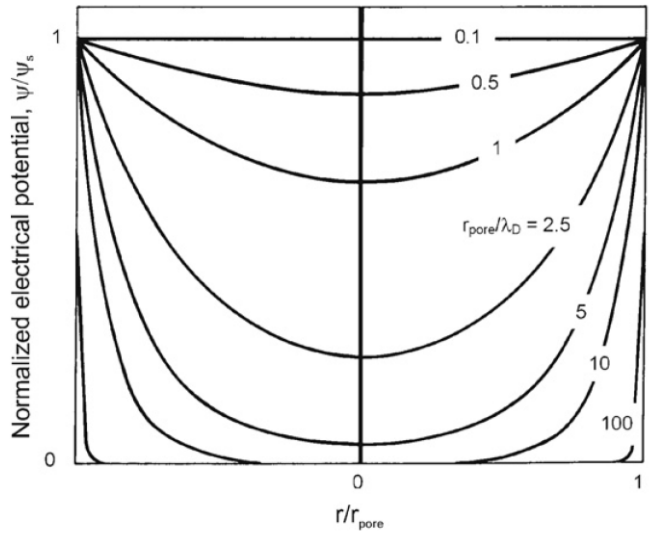

Figure 2.13: Dimensionless potential distribution across a cylindrical pore for different values of the DEBYE length reflecting EDL overlap and co-ion exclusion. Adapted from [38] and reprinted with permission from ref. [38]. © Wiley, 1994.

By adjusting the ionic strength of a mobile phase the elution volume of a small co-ionic analyte with respect to the silica surface can be switched from complete permeation over a broad intermediate range to complete exclusion of the intraparticle pore space of a packed bed.

2.7.2 DONNAN model

The main problem in describing the electrostatic interaction in charged systems is to find an exact description of the magnitude of the electrostatic potential at different points in the system. In chromatographic systems the simplest possible approach is to consider the charges constituting the stationary phase as a separate phase and assuming that the electrostatic potential has a constant value in this phase, the DONNAN potential. In this model the concentration change of counter and co-ions between the two phases is considered to take place at a sharp boundary, and it does not give rise to the above described diffuse double layer.

Assuming that a distinct boundary exists between the electrolyte solution (mobile phase) and the stationary phase and that the total ionic concentration in the stationary phase – including the charged surface groups, which may be silanols or sulfonic acid groups for example – is higher than in the electrolyte solution. This is depicted in Figure 2.14 where the electrolyte solution is denoted E and the stationary phase R.

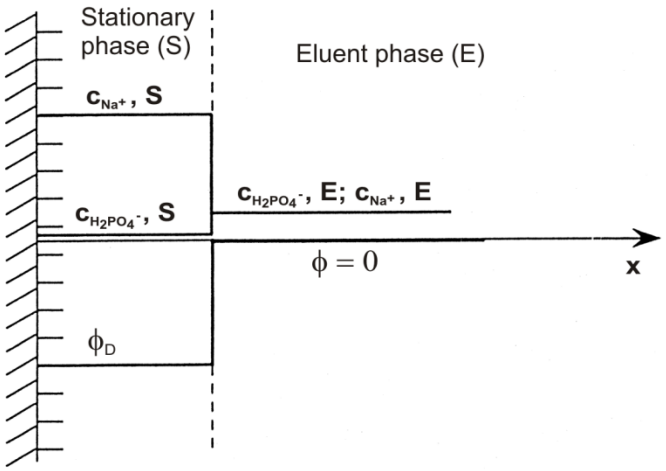

Figure 2.14: Schematic description of the concentration profiles for a counterion, a co-ion, and the electrostatic potential profile in the vicinity of a negatively charged surface according to the DONNAN model. In the example, the resin phase is a cation exchanger with Na^+ as counterions placed in a dilute water solution of NaH_2PO_4 (the eluent phase) [39]. Adapted and reprinted from ref. [39] © 1999, with permission from Elsevier.

Due to thermal motion the ionic species of the mobile phase and the counterions of the charged surface, a redistribution of these ions will occur between the two phases. Depending on the surface potential and the physicochemical properties of the electrolyte solution, the result can be regarded as an accumulation of positive charge in the solution and negative charge at the solid's surface which creates a difference in electrostatic potential between the two phases, the DONNAN potential ϕ_D. In the final ionic distribution, an equilibrium is established in which the tendency of the ions to level out the existing concentration differences between the two phases is balanced by the DONNAN potential ϕ_D.

A quantitative treatment of the distribution of the ions between the two phases is obtained from thermodynamics which states that at equilibrium the electrochemical potential μ of an ionic species is the same in the two phases. For the involved cationic species the thermodynamic condition for equilibrium between the stationary phase and the electrolyte phase is written as

$$\mu_C^0 + RT \ln \gamma_{C,S} \cdot c_{C,S} + z_C F \phi_D = \mu_C^0 + RT \ln \gamma_{C,E} \cdot c_{C,E} \qquad (2.67)$$

where μ_C^0 is the standard chemical potential of the cation – in case of aqueous solutions and bare-silica particles hydronium H_3O^+ – its value is assumed to be equal in the two phases; $c_{C,S}$ and $c_{C,E}$ are the cation concentrations in the stationary and the mobile phase, respectively; and $\gamma_{C,S}$ and $\gamma_{C,E}$ are the corresponding activity coefficients [35]. Rearrangement of Equation (2.67) gives

$$\phi_D = \frac{RT}{z_C F} \cdot \ln \frac{\gamma_{C,E} c_{C,E}}{\gamma_{C,S} c_{C,S}} \tag{2.68}$$

If there are several types of cations in the system the above thermodynamic analysis is applicable to each of them as well as for anionic species. In ideal solutions, the ion concentration equals the activity. A general expression for the DONNAN potential of porous particles in a packed bed including all involved ionic species can be expressed as [35]

$$\phi_D \equiv \phi_{intra} - \phi_{inter} = -\frac{RT}{z_i F} \cdot \ln \frac{c_{i,intra}}{c_{i,inter}} \tag{2.69}$$

The distribution coefficient $c_{i,intra}/c_{i,inter}$ represents the ion-permselectivity of the particles and depends on the mobile phase ionic strength, the surface charge density in the intraparticle pore space, and the valencies of the co-ionic and counterionic species, similar to the electric double layer model.

2.8 Electrospray ionisation – mass spectrometry (ESI-MS)

Mass spectrometry is widely recognized as a powerful analytical tool which can provide both qualitative and quantitative data that may not be readily available by other techniques. In particular, it can provide molecular weight, empirical formula through precise mass measurement, isotope ratios, detection of functional groups and other substituents, and elucidation of structure, including in some cases stereochemical features [40]. MS is an analytical method by which gaseous ions of a sample material are selected by their mass-to-charge (m/z) ratio. Hence, the crucial point in every mass spectrometric technique is the generation of gas-phase ions from the given sample material. This usually requires three steps: vaporisation, ionisation, and transportation of ions, which can occur consecutively or simultaneously. Electrospray ionisation has become one of the most important ionisation techniques for the online coupling of liquid phase separation methods with mass spectrometry. It is a simple and elegant method that handles small and big molecules, operates

at atmospheric pressure and at a moderate temperature, and is probably the most gentle ionisation technique available for MS [41].

2.8.1 Application areas

There are currently three principal application areas. The first main area is compound discovery and identity confirmation in pharmaceutical manufacturing or drug discovery. The second application area, called proteomics, is protein structure determination by LC-ESI/MS, since ESI enables the formation of multiply charged ions. The multiply charged ions will appear in the mass spectrum at m/z values that are fractions of the mass of the ions. This allows the detection of high molecular weights of proteins and peptides using standard quadrupole mass analyser. In addition, the detection of multiply charged ions provides precise measurements of molecular mass of proteins and peptides *via* the deconvolution method. A mass accuracy of better than 0.01% can be achieved for proteins with masses up to 100 kDa [42]. A growing subset of the proteome analysis is in the field of DNA/RNA structure studies; which could be termed nucleomics. The third area of application is in metabolite and trace contaminates studies [43].

But ESI is not only a versatile tool for any aspect of peptide and protein characterisation or metabolomics; it also offers numerous other fields of application. In general, ESI can be well applied to ionic metal complexes and related compounds if these are soluble to at least 10^{-6} M in solvents suitable for the method. Another application field of ESI is the analysis of surfactants which belong to a group of where a low price is crucial. Therefore, they are usually synthesized from coarsely defined mineral oil fractions or vegetable oils both of which represent (sometimes complex) mixtures. As demonstrated by a large number of applications, ESI permits molecular weight determination and structure elucidation for oligosaccharides as well as closely related compounds such as glycoproteins, gangliosides, and liposaccharides. These substances require polar solvents and very soft ionisation, in particular when the molecules are branched [44]. An application of ESI/MS that has gained growing interest is the study of molecular interactions. Those interactions can be found in case of noncovalently bound complexes like, *e.g.*, antibody-antigen, receptor-ligand, and enzyme-substrate pairings [45].

2.8.2 General characteristics

Generally, polar liquids are employed in ESI since unpolar liquids cannot be electrosprayed. For the establishment of a stable TAYLOR cone the surface tension of the electrosprayed solution is of major importance because it influences the onset field strength of the electrospray. In air, the usable field strength is limited by the onset of a corona discharge. For this reason the use of pure water is difficult in ESI-MS and organic solvents such as methanol, acetone, or acetonitrile are added to the electrosprayed solution to reduce the required field strength for the onset of a stable electrospray [45].

The ionisation in an ESI interface is considered primarily a liquid-phase ionisation technique: preformed ions in solution are desorbed or evaporated to the gas phase and can subsequently be mass analysed. Because all the processes leading to ion formation occur at atmospheric pressure ESI is a soft ionisation technique where no or only little fragmentation occurs, and where radical ions are usually not observed. In positive mode the observed ions are typically proton- or cation-attached sample molecules, depending on the nature of the predominant charge carrier in solution. When the ESI source is set up for the detection of negative ions, all power supplies are at reversed polarity and current flows in the opposite direction. Removal of positive ions inside the capillary tip provides droplets that are depleted of positive charge. The supply of negative charge to the solution may also take place; electrons released from the spray capillary can be captured by sample molecules having a high electron affinity [41].

A feature unique to ESI/MS is the fact that molecules with higher masses often appear as multiply charged ions. For biomolecules such as proteins, the number of charges roughly correlates with the molecular mass. The appearance of these high charge states offers two advantages: (i) the charge state distribution allows the accurate determination of the molecular mass; (ii) since most analyte ion signals fall into the mass range below m/z = 2000, inexpensive mass analysers can be used, *i.e.*, the mass analyser can be chosen according to the analytical requirements. Since fragment ions in ESI are often absent or exhibit very low intensity, MS/MS capability of the mass analyser is beneficial [44].

Sample consumption is chiefly determined by the concentration of the analyte solution and the liquid flow. Typically, samples at concentrations of about 10^{-6} – 10^{-4} mol/L are injected [44,45]. In conventional ESI this concentration range corresponds to a few picomol of the sample molecule (at a flow rate of ~ 4 µL/min) whereas in nano ESI this reduces to a few femtomol (F ~ 40 nL/min) for the same solution [44]. Therefore, ESI responses are directly related to the concentration of the analyte entering the ion source. The mass

sensitivity can be substantially increased with a lower flow rate if the same concentration sensitivity is maintained. Thus, ESI can be considered a concentration-dependent ionisation process, a fact that pushed the development of nano ESI sources and its coupling to nano LC.

2.8.3 Ion sources

The effective coupling of LC-based techniques to mass spectrometry *via* an ESI source was originally introduced by FENN and co-workers [46-48]. The dilute sample solution is forced by a syringe pump through a hypodermic needle. The needle is maintained at a few kilovolts relative to the surrounding cylindrical electrode that helps shape the distribution of potential and directs the flow of the gas (Figure 2.15). The electrosprayed aerosol expands into a countercurrent stream of dry nitrogen gas that serves as a heat supply for vaporisation of the solvent. A small portion of the sprayed material enter the aperture of a short capillary (0.2 mm i.d., 60 mm length) that interfaces the atmospheric pressure spray to the first pumping stage (*ca*. 10^2 Pa). Most of the gas expanding from the desolvating aerosol is pumped off by a rotary vane pump as it exits from the capillary. A minor portion passes through the orifice of a skimmer into the high vacuum behind (*ca.* 10^{-3} Pa). At this stage, desolvation of the ions is completed, while the ions are focused into a mass analyser [44].

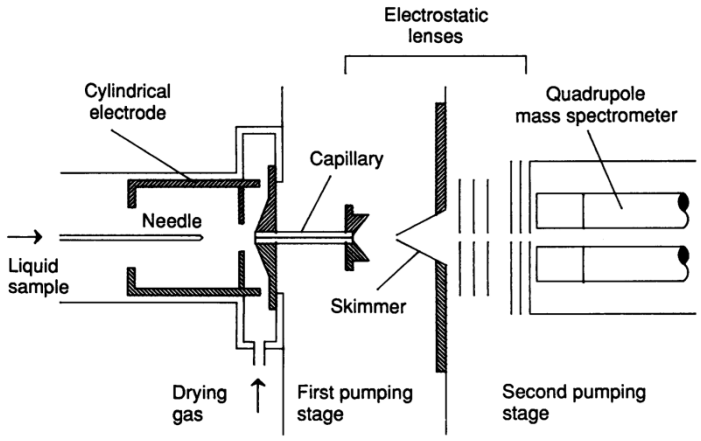

Figure 2.15: Schematic of the early electrospray ion source [48]. Reprinted with permission from ref. [48]. © American Chemical Society, 1985.

Modern ESI sources are constructed in many variations of this basic design [49-53]. ESI emitters have been extensively studied because the characteristics of the emitter, such as the emitter i.d., the surface area of the emitter orifice, and the hydrophobicity, have a great impact on the observed ESI signal in addition to influencing working parameters of the system, such as flow rate or ESI voltage [51]. Whatever the details, they are all derived from a nozzle-

skimmer system proposed by KANTROWITZ and GREY [54] that delivers an intense cool molecular jet into the high vacuum environment. The adiabatic expansion of the gas on the first pumping stage reduces random motion of the particles due to extensive cooling. Furthermore, a portion of the thermal motion is converted into directed flow by the nozzle-skimmer arrangement. In summary, this causes the heavier, analyte ion-containing clusters to travel close to the centre of the flight path through the interface, whereas light solvent molecules escape from the jet [55].

Conventional LC can be coupled with ESI interfaces by using post-column splitting or optimised ESI interfaces capable of attaining flows of up to 2 mL/min. However, the first choice results in significant sample losses and the latter has not entailed noticeable sensitivity gains. Practical work has shown that miniaturisation of the detector geometry yields lower absolute concentration detection limits [56,57]. This entails the appropriate down-scaling of the LC injection and column parameters, to accommodate for the reduced flow rates, as well as the down-scaling of the associated LC/MS coupling devices. From the point of view of the interfaces, microseparation techniques, such as micro-, nano-, and chip-LC, and capillary electrophoresis, have been coupled to nanospray by any of three different approaches or variations [53]. All of them deal with the requirement for the application of the high voltage needed to achieve ionisation. These approaches are basically the following:

(A) application of the high voltage *via* a conductive sheath flow,

(B) application of the high voltage *via* a metal-coated tapered spraying tip, or

(C) a stainless-steel or other conductive junction in contact with a liquid junction gap joining the spraying tip and the column (Figure 2.16).

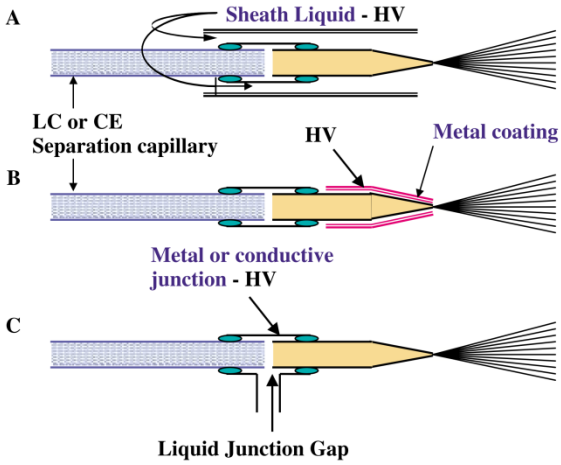

Figure 2.16: Schematics of the possible arrangements for an ESI liquid junction interface. (A) Application of the high voltage (HV) *via* a conductive sheath flow over the spraying tip, (B) application of HV *via* a metal coated tapered spraying tip, (C) application of HV *via* e metal sleeve in contact with a liquid junction gap [53]. Reprinted with permission from ref. [53]. © John Wiley & Sons, Inc., 2002.

System A implies a considerable dilution of the sample in the sheath flow and thus loss of response, while system B is hampered by the limited lifetime of the metal coatings. In contrast, the most popular and versatile interfaces are those based on the liquid junction arrangement.

Unprocessed commercially available stainless-steel and fused-silica capillaries of adequate i.d.s have been used for micro and nano ESI. To optimize spray formation at the low flow rates, some changes are usually made to the capillary tip. Fused-silica capillaries with small i.d.s are commonly etched with hydrogen fluoride or the tip is rubbed using sandpaper, resulting in very sharp ESI tips. Electropolishing has also been used with metal capillaries to produce similarly sharp tips. The so-obtained ESI tips have i.d.s of down to 10 µm. By using a micropipette puller, spray tips as small as a few µm with tapered inner and outer dimensions can be prepared from fused-silica capillaries [51,56].

For the measurement, the nano ESI capillary is adjusted at about 1 mm distance to the entrance of the counter electrode by means of a micromanipulator. Thus, precise optical control is needed during positioning to prevent crashing of the tip or electrical discharges during operation. Commercial nano ESI sources are therefore equipped with a built-in microscope or camera.

2.8.4 Microchip ESI devices

There are two approaches to obtain mass spectral data from continuously flowing samples on chips: (i) the direct spray from an exposed channel or (ii) the spray from a transfer capillary attached to the microchip. The formation of a stable electrospray directly from the channel opening at the flat surface of a microchip results in a relatively large droplet size with corresponding increase in band broadening and sample dilution. In this case no electrospray tip is needed because the electric field strength at the exposed liquid surface is sufficient to form the electrospray cone, provided a high enough voltage is applied to overcome the fluid surface tension to initiate an electrospray. Here, the liquid droplet serves as the ESI tip and upon application of the required voltage this droplet is shaped into a cone and forms the electrospray tip. Nevertheless, this arrangement involves difficult coupling of on-chip separation to ESI-MS owing to the tendency of the liquid droplet from which the TAYLOR cone is formed to spread out over the surface of the chip depending on the hydrophobicity of the ejected liquid and the chip surface material [52,53,58].

A variety of approaches have been taken to generate electrospray by inserting capillary emitters in the microchip device, resulting generally in performances comparable to those found for microcolumn separations. One of the problems of using transfer capillaries for joining to microfluidic devices is that any such connection must be of sufficiently small dead volume.

Batch generation of microchips with integrated electrospray emitters/tips can result in improved emitter reproducibility and the potential of simple, disposable devices. However, the microfabrication of fine electrospray tips as an integral part of a microdevice is not a trivial task, and suitable microfabrication procedures are still under development. The microfabrication of disposable plastic devices is attractive from the commercial perspective and a number of fabrication procedures can be found in the literature [49,53,59,60] (and references therein).

The most integrated system in the HPLC/ESI-MS chip technology was introduced by Agilent Technologies in 2005 [61]. The microchip was made up of laminated polyimide foils integrating sample injection, sample enrichment column, separation column, and ESI tip (Figure 2.17). The fabrication process consists of, in order: laser ablation of polyimide film to form the microfluidic channels, ports, chambers, and columns; cleaning to remove the laser-ablation residues; deposition of electrical contacts for the electrospray; lamination of polyimide film layers; using laser ablation to trim the chip to its final shape and to form the electrospray tip; and packing the sample enrichment column and LC column with retention

media. Three layers of film – top, middle, and bottom – were used to fabricate each chip. Holes of 200 µm diameter were ablated through the top and bottom layers of the device to provide access to the channels and chambers inside the finished device. After laser ablation the films were cleaned and laminated in a vacuum at 340 °C and a pressure of 200 psi. Laser ablation was also used to trim the structure to its final shape and to cut the electrospray tip using a circular path around the desired laminated chip channel. The final tip shape was conical with a circular end with dimensions from 35 to 100 µm o.d. and up to 2 mm in length. The inner shape is Gaussian like with a base length of ~ 10 µm. Electrical contacts for the electrospray tip voltage bias were applied by vacuum evaporation or sputtering of a thin platinum layer that was deposited on one of the polyimide layer surfaces and directly laminated into the final structure such that the metal was inside the device [61].

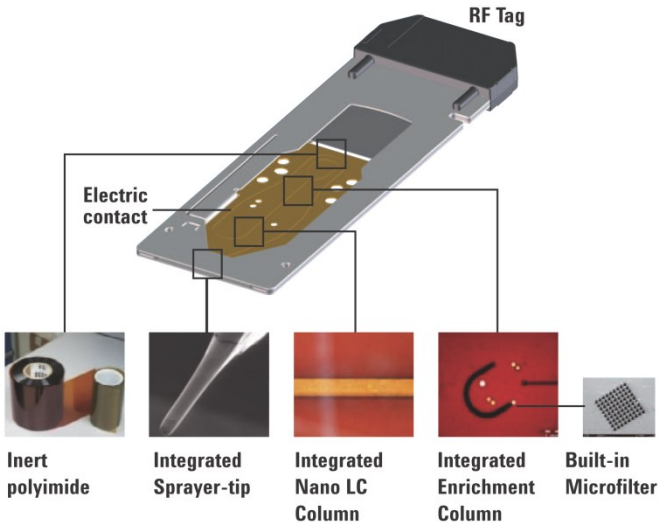

Figure 2.17: Fully-integrated Agilent HPLC/ESI-MS microchip with sample injection, sample enrichment column, separation column, and nano ESI tip [62].

2.8.4 Ion formation

The production of gas-phase ions from electrolyte ions in solution can be divided into three steps:

(i) production of charged droplets at the electrospray capillary tip,

(ii) shrinkage of the charged droplets due to solvent evaporation and repeated charge-induced droplet disintegrations leading ultimately to very small highly charged droplets capable of producing gas-phase ions,

(iii) the actual mechanism by which gas-phase ions are produced from these droplets.

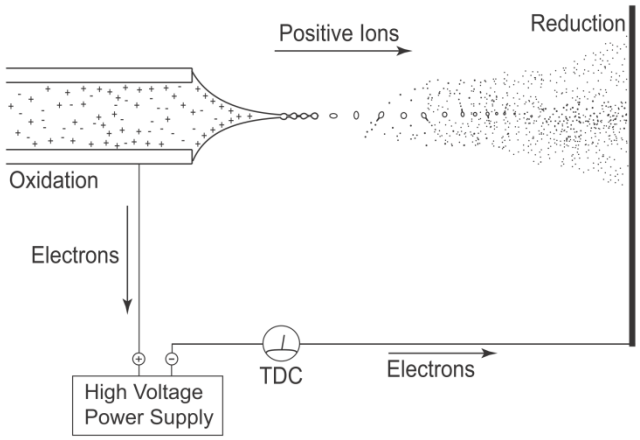

Figure 2.18: Illustration of an electrospray ion source run in the positive ion mode. Penetration of the imposed electric field into the liquid leads to an enrichment of positive ions at the capillary tip. This causes the formation of an electrified drop or cone. A liquid jet is emitted from the apex of the cone which splits into droplets charged with an excess of positive ions. The droplets evaporate as they move towards the MS entrance to produce charged analyte molecules [63]. Reprinted with permission from ref. [63]. © John Wiley & Sons, Inc., 2009.

The most simplistic view of an electrospray source contains a capillary with a few kilovolts applied to it and a counter electrode. The capillary – emitter electrode – is in contact with the electrolyte solution and is placed at or upstream of the point at which the charged ES droplet plume is generated. The solution that is within the capillary will experience the applied electric field, causing the ions to propagate in accordance to the field lines established between the capillary and the counter electrode. The value of the field at the capillary tip opposite to a large and planar counter electrode can be estimated with the approximate relationship [63]:

$$E_c = \frac{2V_c}{r_c \ln\left(\frac{4d}{r_c}\right)} \tag{2.70}$$

where V_c is the applied potential difference, r_c the capillary outer radius, and d the distance from capillary tip to the counter electrode. The most important parameter is r_c, the electric field is essentially inversely proportional to r_c, but decreases very slowly with the electrode separation due to the logarithmic dependence on d. Of course the field lines change significantly when the geometrical arrangement of the electrodes is varied.

The electric field causes the polarisation of the solvent near the meniscus of the fluid. In the case of positive ion mode with the capillary acting as the anode, electromigration leads to an enrichment of positive ions near the liquid-gas interface formed at the capillary outlet. The electrical shear stress causes a distortion of the meniscus into an electrified drop or cone

pointing towards the counter electrode. The acceleration of the ions and the solvent and the actual shape of the liquid cone are a result of the force balance of surface tension, gravity, electric stresses in the liquid surface, inertia and viscous stresses (Figure 2.19). The surface tension retracts the liquid to minimize the surface area and the retracting force is determined by the curvature of the surface [64]. If the applied field is sufficiently high, the tip becomes unstable and liquid is ejected as a droplet or a fine jet. In the latter case, varicose wave instabilities developing along the surface, lateral kink instabilities, or numerous ramifications cause the jet to break up into charged droplets (Figure 2.19).

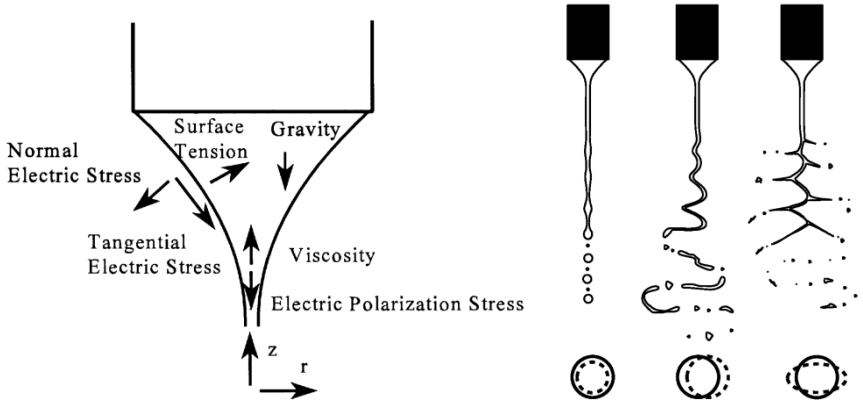

Figure 2.19: Forces acting on the liquid meniscus/cone (left) [65]; and three jet break-up modes: the axisymmetric varicose break-up, the lateral kink break-up, and the ramified jet break-up (right) [66]. Reprinted from refs. [65] © 1999 and [66] © 2000, with permission from Elsevier.

Axisymmetric instabilities along the jet's surface are also called varicose wave instabilities. If the jet is slowed down by external forces like the drag force of the surrounding air, or when the jet is charged, lateral instabilities or kink instabilities occur which become noticeable by a whipping motion of the jet. In case of a highly charged jet or high potential difference, the jet is no longer circular. The permanent part of the jet disappears and the aspect of the spraying changes constantly [67].

The charged droplets released from the fluid within the capillary are accelerated towards the counter electrode carrying an excess of positive ions. Solvent evaporation at constant charge leads to droplet shrinkage and an increase of the electric field normal to the surface of the droplets. At a given radius the increasing repulsion between the charges overcomes the surface tension at the droplet surface. The upper limit to charge on a droplet is called the RAYLEIGH limit:

$$q_{Ray} = 8\pi\sqrt{\varepsilon_0 \gamma r^3} \tag{2.71}$$

Where q_{Ray} is the charge at which point the radius of the droplet creates a repulsion force of the surface charges equal to the surface tension of the droplet, ε_0 is the vacuum permittivity, γ is the surface tension, and r the droplet radius. Exceeding the RAYLEIGH limit causes a COULOMB fission of the droplet. During the fission process a jet of small, charged progeny droplets is released. Repeated droplet fissions will ultimately lead to very small charged droplets that are the precursors of the gas-phase ions. The average number of required droplet fission events depends on the initial droplet size. Ions are formed more rapidly from smaller droplets and with less need for heating [68]. Therefore the nanoelectrospray ion source is beneficial to conventional ES ion sources since fewer droplet fissions are required to efficiently produce very small, charged droplets and the distance between the emitter capillary and the counter electrode can be reduced as illustrated in Figure 2.20.

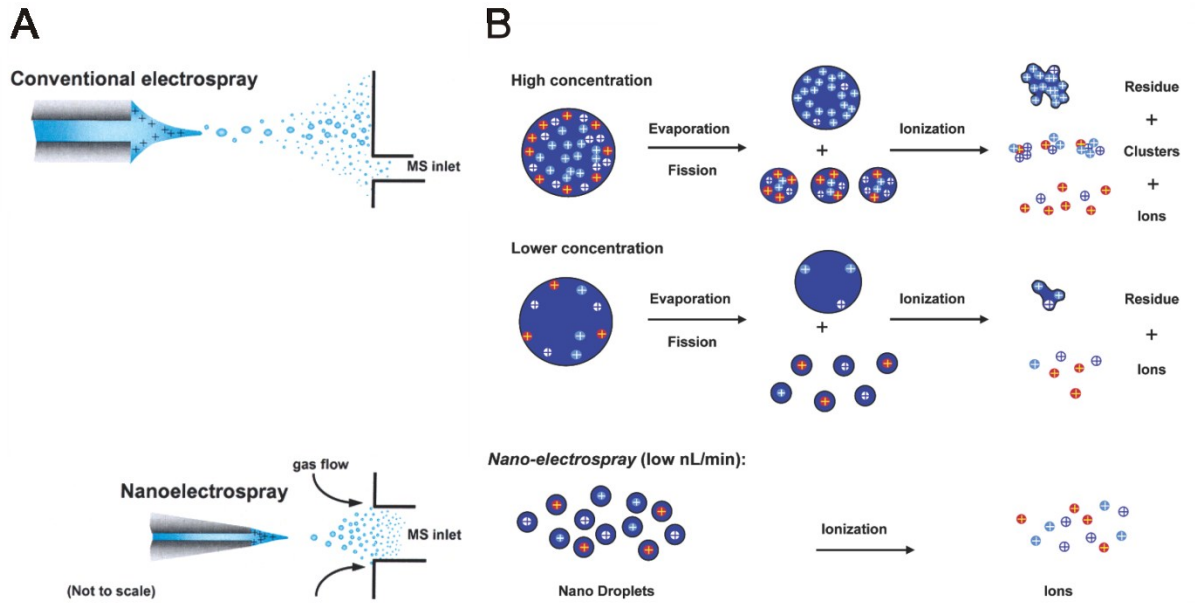

Figure 2.20: (A) By allowing closer proximity to the MS inlet, the nanoelectrospray affords more efficient ion introduction; (B) for larger flow rates, analyte surface activity, concentration, and competition from other species can affect overall ionisation efficiency. At sufficiently low flow rates these suppression and matrix effects are eliminated, each droplet contains on average one molecule [68]. Reprinted and adapted with permission from ref. [68]. © American Chemical Society, 2004.

When progeny droplets have shrunk to a radius of ~ 10 nm, further disintegration to yet smaller droplets is not supposed to take place in order to remove excess charge at the RAYLEIGH limit [41]. Instead, droplet charge is reduced by the release of ions from the droplet surface. Two different mechanisms are discussed in literature for the formation of gas-phase

ions from the very small and highly charged droplets: (i) the charged residue model (CRM) and (ii) the ion evaporation model (IEM).

The first mechanism was proposed by DOLE who was interested in analytes of high molecular mass [69]. For such macromolecules he assumed that, when very small droplets are formed by droplet evaporation through a cascade of COULOMB fissions, some of these droplets would contain one analyte molecule as well as the ionic charges on the surface of the droplet. The charges of these ultimate droplets are then transferred onto the molecule. This would allow that even large protein molecules can form singly charged ions.

The IEM predicts that direct ion emission from the droplets will occur after the radii of the droplets shrink to less than 10 nm. The ion evaporation process replaces COULOMB fission [70,71]. Ionic solvation energies are in the range of 3–6 eV, but thermal energy can only contribute about 0.03 eV at 300 K to their escape from solution. Thus, the electric force has to provide the energy needed. It has been calculated that a field of 10^9 V/m is required for ion evaporation which corresponds to a final droplet diameter of 10 nm [71]. The IEM corresponds well to the observation that the number of charges is related to the fraction of the microdroplet's surface that a molecule can cover. As the radius diminishes, molecule size and number of droplet charges remain constant; however, the spacing of the surface charges decreases, and thus the increasing charge density brings more charges within the reach of an analyte molecule. Flat and planar molecules therefore exhibit higher average charge states than spherical ones [44].

In summary, the IEM is experimentally well-supported for small (in)organic ions. However, the theoretical derivation of the model does not apply for very large ions such as proteins. For these macromolecular species, the CRM is much more plausible.

2.8.5 Electrospray modes

Depending on the actual geometrical form taken by the liquid at the capillary outlet (drop, cone), the duty cycle of a liquid ejection, the number, structure (axial, non-axial), and disintegration behaviour of the emitted jets, the resulting shapes, sizes, and size distributions of the generated droplets, and the relation between the applied potential difference between capillary outlet and counter electrode and resulting spray current, different electrospray modes and regimes can be classified. Electrospray is an electrohydrodynamic process which can be regarded as a branch of fluid mechanics concerned with electric force effects. In the 1960s G.I. TAYLOR introduced the leaky dielectric model to explain the behaviour of droplets deformed by a steady field, and J.R. MELCHER [72] used it extensively to develop

electrohydrodynamics. The involved physics in the electrospray modes are complex governing mass and momentum conservation equations in which electrical and mechanical forces are involved, coupled with MAXWELL's equations [72]. Since mathematically description of electrospray modes – especially of the ones exhibiting pulsating properties – is difficult, several researchers have reported scaling laws to describe the operational range [73,74].

In 1914, ZELENY's research indicated that an electrospray could be operated in several regimes [75]. These regimes are determined by the electrohydrodynamic disintegration mechanism of the liquid meniscus and result in profoundly different droplet characteristics, such as size and velocity distributions in the spray plume. Electrospray modes can be classified by visual criteria [67,76] and/or by measuring the AC and DC components of the spray current [77-79]. Initial classifications included four regimes – dripping, pulsating, stable jet, and multijet – that were readily apparent at increasing applied voltages [80]. Newer classifications [67,76,77,81] have grown more complex and confusing, partly due to a lack of consensus on nomenclature, and partly due to the scattered experimental conditions. Detailed descriptions of the spray modes can be found in refs. [66,75,76,78,80].

Four electrospray modes were observed in this work described below on the basis of the work by JURASCHEK and RÖLLGEN [77] and NEMES *et al*. [79]. Both observed three axial spray modes with increasing potential difference between capillary tip and counter electrode and a nonaxial regime for high potential differences. The employed experimental conditions were similar to the solvents and instrumental setups commonly used in HPLC-ESI/MS: Methanol/water mixtures were electrosprayed through stainless steel capillaries of i.d.s in the range from 100 – 260 µm, the solvents were delivered by syringe pumps working at flow rates of a few µL/min.

Axial spray mode 1

The axial spray mode 1 is observed at lower capillary potentials and is characterised by the regular appearance of peak groups in the capillary current *versus* time oscillogram (Figure 2.21, green curve observed by NEMES *et al.* [79]). JURASCHEK and RÖLLGEN [77] found by monitoring the spray current on the counter electrode occasional rise and oscillation of the current followed by a period of inactivity. Flash microphotographs taken at different stages of a single pulse showed that a single current pulse is correlated with the emission of an axial liquid jet emerging from the apex of the cone, whereas a "relaxed" cone is observed between two current pulses. Single current pulses indicate a transient emission of liquid *via* a jet that

accordingly appears and disappears at a high frequency. In the time interval between two pulse sequences the overall cone volume is small and no emission of liquid can be observed, which corresponds to the nearly vanishing capillary current. This observation corresponds to the spray current measurements of the burst mode or axial mode 1 by NEMES *et al.,* displayed by the green curve in Figure 2.21 [79]. The overall cone volume decreases by the emission of liquid *via* the formation of jets and increases again between the emission pulse sequences because of the continuous supply of liquid from the capillary. Increasing the capillary potential leads to a decrease of the time interval between the peak sequences, *i.e.,* the signal frequency increases.

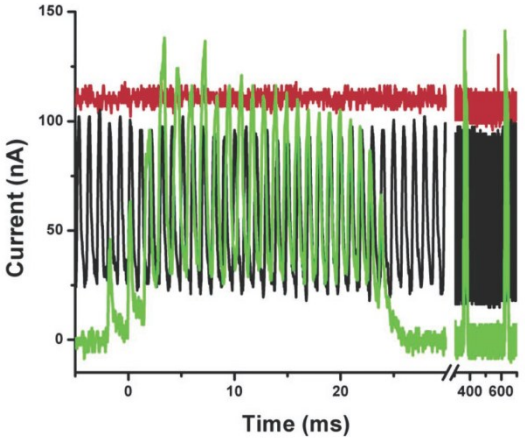

Figure 2.21: Oscillograms of spray current measurement of 3-methoxybenzylpyridinium in methanol/water solutions. The spraying modes axial mode 1 (green), axial mode 2 (black), and axial mode 3 (red) are displayed at emitter potentials of 2750, 2950, and 4050 V, respectively. The flow rate was 1 µL/min [79]. Reprinted with permission from ref. [79]. © American Chemical Society, 2007.

Fast imaging of the meniscus region enabled NEMES *et al.* [79] to reproducibly follow the production and initial fission of primary droplets in the different spray modes. Figure 2.22 shows the different phases of liquid ejection in a single current spike observed by NEMES *et al.* [79]. Initially the liquid filament ejected from the capillary tip exhibits kink instabilities and produces relatively small droplets. The majority of the ejected liquid, however, is carried away by a few very large droplets that vary in shape between a spindle and a bottle. These shapes relax into oscillating large droplets that undergo division. This process is driven by the fluid dynamics of the oscillation and results in approximately equally sized offspring. Such equal division is in sharp contrast to the fission of droplets with those to critical charge, which exhibit the ejection of much smaller droplets. The overall size distribution of the droplets is broad with respect to the size distributions found in axial mode 2 and 3. Compared to the smaller droplets emitted initially, the large droplets carry a smaller amount of charge per

volume and require additional generations of fission to become sufficiently small for ion production. This results in marginal ion production and, therefore, axial mode 1 is not favourable for analytical applications.

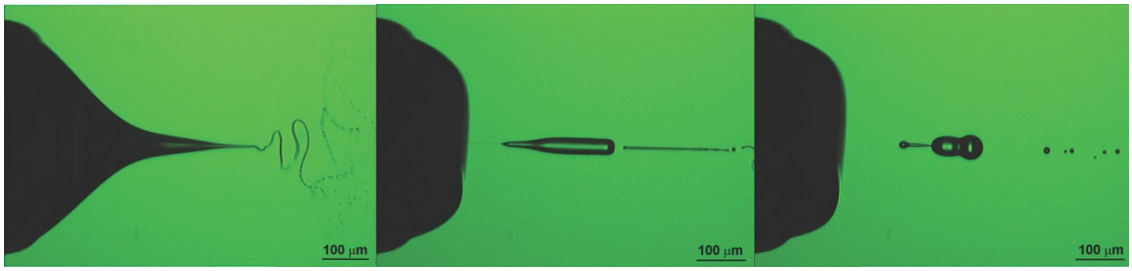

Figure 2.22: Typical meniscus shapes and disintegration in a single current spike of the axial mode I. Initially the liquid filament exhibits kink instabilities and produces relatively small droplets. The majority of the liquid is carried away by a few very large droplets that vary in initial shape between a spindle and a bottle [79]. Reprinted with permission from ref. [79]. © American Chemical Society, 2007.

The pulsation phenomena (low and high frequencies) observed in axial spray mode 1 arise from an imbalance between the loss of liquid *via* emission and its supply into different regions of the liquid cone [77]. After an emission pulse sequence the cone volume is small and the radius of curvature at the apex large. The cone volume is continuously built up by the liquid supply maintained by the syringe pump until the radius of curvature of the liquid surface at the cone apex decreases below a critical value at which the MAXWELL stress, *i.e.*, the outward electrostatic pressure, exceeds the surface tension forces, *i.e.*, capillary pressure, for the breakup of the surface and the formation of a liquid jet. During the following pulse sequence the liquid is intermittently emitted at an average emission rate exceeding the liquid supply rate. As a consequence of the liquid emission the cone volume decreases. Because of the continuous liquid supply from the capillary the cone volume increases again and the cycle illustrated in Figure 2.22 repeats.

After the loss of a critical amount of liquid the jet tears off and the liquid surface relaxes to its equilibrium shape in the external field. With increasing capillary potential the MAXWELL stress increases and accordingly the cone volume subjected to the pulse emission decreases, which cause the increase of the pulsation frequency [77].

The pulsation phenomena can be expressed by the leaky dielectric model using the hydrodynamic time t_h and the electrical relaxation time t_e. The hydrodynamic time of a system is defined as the time required for the fluid particles with characteristic velocity u to move across a zone of characteristic size L

$$t_h \sim \frac{L}{u} \tag{2.72}$$

and the electrical relaxation time t_e can be calculated by

$$t_e = \frac{\varepsilon_r}{\kappa} \tag{2.73}$$

with the relative permittivity ε_r and the conductivity κ of the electrosprayed solution.
If t_h/t_e is on the order of unity, the charge layer at the surface of the meniscus is no longer relaxed giving rise to electrohydrodynamic perturbations during the jet break-up process. These perturbations result in a low duty cycle with pulsed jet emission processes.

Due to a lack of consensus in nomenclature in the field of electrospraying, which partly is the result of the associated observation procedures and instruments, the terms used by individual researchers for ES modes vary. CLOUPEAU and PRUNET-FOCH [67] and JAWOREK and KRUPA [76] reviewed the different modes existing in electrohydrodynamic spraying and classified them. The axial spray mode 1 (or burst mode) described by JURASCHEK and RÖLLGEN [77] and NEMES *et al.* [79] can be compared to the dripping and spindle mode described by CLOUPEAU and PRUNET-FOCH [67] and JAWOREK and KRUPA [76]. The dripping mode occurs at low capillary voltages and the emitted drops are large with low emission frequency. In the spindle mode the droplet formation cycle includes the stretching of a rounded meniscus at the capillary tip, emerging of a fine jet from the apex which finally breaks up into droplets. At the tapered part of the elongated meniscus a spindle-shaped liquid volume detaches and contracts to form a main drop, while the remaining jet continues to break up into fine droplets [67,76].

Since the transition from dripping mode to spindle mode can be gradual, it was not possible to distinguish these modes with the setup used in this work. It can be assumed that at small potential differences the dripping mode occurred for mobile phases of low conductivity, *i.e.*, high fraction of organic modifier.

Axial spray mode 2 or pulsating cone-jet mode

With increasing capillary potential axial spray mode 2 or the pulsating cone-jet mode emerges from axial spray mode 1. This spray mode is characterised by a constant (one principal) frequency of the current pulsations in the lower kilohertz range and by a constant amplitude and peak shape of the pulses (*cf.* black curve in Figure 2.21). The DC current remains constant with increasing capillary potential within axial spray mode 2 in contrast to axial spray mode I, where the DC current shows Ohmic behaviour [77]. In axial spray mode 2 a spindle-like large droplet is accompanied by a significant amount of smaller ones produced by lateral kink instabilities at the end of the jet during liquid ejection (Figure 2.23). The droplet

diameter distribution becomes nearly monodisperse. Compared to axial spray mode 1, both the larger quantity of small – and monosized – droplets and the higher duty cycle contribute to the increased ion production rate [79].

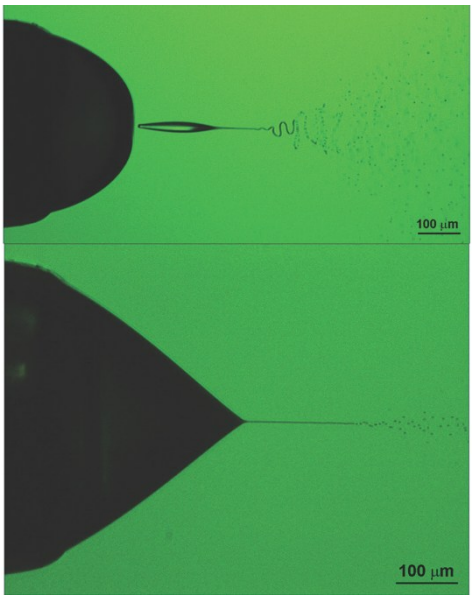

Figure 2.23: Liquid ejection in axial spray mode 2. A spindle-like large droplet is accompanied by a significant amount of smaller ones produced by lateral kink instabilities [79]. Reprinted with permission from ref. [79]. © American Chemical Society, 2007.

Axial spray mode 2 is mentioned as pulsed cone-jet by CLOUPEAU and PRUNET-FOCH [67]. It occurs at slightly lower voltages than that for which a single permanent jet is obtained. The jet is emitted only intermittently, the apex of the meniscus alternately taking on a pointed or rounded form, producing a multitude of fine droplets. The emission phases occur at perfectly regular time intervals.

Axial spray mode 3 or steady cone-jet mode

Axial spray mode 3 is by far the most intensively investigated electrospray mode. It is the most stable electrospray mode and therefore the most well understood, in which the balance between electrostatic stresses and surface tension forces results in a stable conical formation from the apex of which a liquid jet is emitted. From the first pioneering experimental studies by ZELENY [75] until the work by VONNEGUT and NEUBAUER [82], noticing the monodispersity of the droplets, very little knowledge on this subject was gained. Thereafter, TAYLOR [83] gave, for perfectly conducting liquids, a first explanation of the conical shape – which was named TAYLOR cone – as a hydrostatic balance between electrical and surface tension forces at any point on the surface of the cone. Experimental investigations on the

stability limits of the cone-jet mode as well as those on the dependence on the liquid properties, liquid flow rate, and electrostatic conditions of the current and droplet size emitted from an electrified conical point have been done by a variety of researchers [65,67,74,76,77,79,80,84-88] (and references therein). Scaling laws of the spray current emitted from an electrified meniscus in the cone-jet mode were found by DE LA MORA and LOSCERTALES [73] and GAÑÁN-CALVO *et al*. [74]. In general, if the electrical relaxation time t_e is small compared to the hydrodynamic time t_h, the liquid bulk is quasi-neutral and the free charges are confined to a very thin layer underneath the liquid-gas interface. The thickness of the surface layer is always small as compared to any other characteristic length of the liquid. In the stable cone-jet mode, charges must be relaxed at the cone-jet surface since the motion of charges inside the liquid bulk would be incompatible with the steadiness of the TAYLOR cone. Consequently, the inequality

$$\frac{\varepsilon_r}{K} \ll \frac{L R^2}{1} \tag{2.74}$$

must be satisfied; L and R are the axial and radial characteristic lengths of the jet [74]. Therefore, for liquids of a given conductivity, the cone-jet mode occurs within a certain range of flow rates. Considering the ideal case of a cone with a straight axisymmetric generatrix, in which the hydrostatic pressure is zero, TAYLOR showed that this equilibrium is obtained only for a single value of the applied potential, when the half-angle at the apex of the cone is equal to 49.3° [83]. Experience shows, however, that there are stable conical menisci for a certain range of variations in hydrostatic pressure and potential. The value of the angle at the apex is variable and the generatrix of the cone may be straight, concave, or convex. For liquids with relatively high conductivities (> 10^{-4} S/m), the jet formation zone is limited to the apex of the meniscus [67,89]. The remaining surface is practically equipotential and an almost static equilibrium of forces exists at each point. The cone may then have a straight generatrix (Figure 2.24a) or a rather convex one (Figure 2.24b). For decreasing conductivities, the acceleration zone extends further toward the base of the cone. In the limit, it begins at the outlet of the capillary (Figure 2.24c and d) [67].

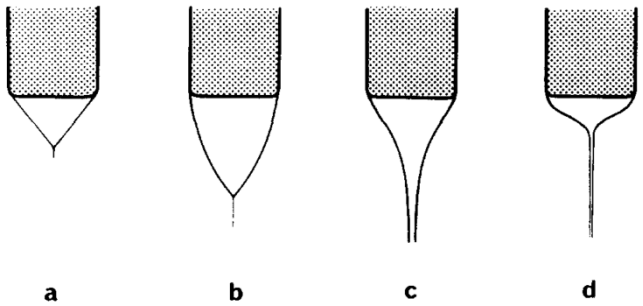

Figure 2.24: Different forms of meniscus in the cone-jet mode: At relatively high conductivities, the cone may have a straight (a) or convex (b) generatrix. With decreasing conductivities, the cone shape is rather concave (c and d) [67]. Reprinted from ref. [67], © 1994, with permission from Elsevier.

The space charge in the steady cone-jet mode is much more stable than in other spray modes because the produced droplets are smaller and of lower mobility. The space charge reduces the electric field near the end part of the jet. The length of the jet increases with the viscosity, the resistivity, and the flow rate of the liquid. The end part of the jet undergoes instabilities of either varicose wave or lateral kink form. In case of varicose wave instabilities, the waves are generated on the surface of the jet, but the jet does not change its linear position. The wave contracts in the nodes, and the jet disintegrates into equal droplets. In case of lateral kink instabilities the jet moves irregularly off the axis of the capillary, and breaks up into fine droplets [67,76].

In the axial spray mode 3, which appears at further increased emitter potential, a continuous emission of liquid *via* a stable cone-jet is observed. In contrast to the pulsating cone-jet mode, in the steady cone-jet mode the whole liquid cone appears uniform and stationary [77]. JURASCHEK and RÖLLGEN and NEMES *et al.* measured a constant capillary current in the cone-jet mode (*cf.* red curve in Figure 2.21) [79], which was increased about a factor of two compared to the DC current of the pulsating cone-jet mode [77]. This corresponds to an increase of the duty cycle of the liquid emission process. The continuous supply rate of the liquid equals the loss rate of the liquid *via* the jet in the steady cone-jet mode. The charge carried off with the jet depends more strongly on the duty cycle of its appearance than on the emitted liquid volume, which remains constant on average. Thus, a stable cone-jet may be regarded as a constant-current generator [73]. The jet diameter is significantly decreased compared to the pulsating cone-jet mode which in turn results in smaller droplet size and narrow – even monodisperse – size distribution [67,76,79]. Due to the large and stable spray current and the formation of smaller initial droplets of narrower size

distributions the stable cone-jet mode is the targeted spray condition for mass spectrometric analysis.

Nonaxial spray mode or multi-jet mode

When the emitter potential is gradually increased the transition to a nonaxial spray mode takes place. Usually, first the TAYLOR cone becomes skewed, leading to a single jet at the rim. This situation is, however, unstable and two jets at opposite sides relative to the axis are formed. The number of jets increases with the applied voltage [67,76]. The meniscus becomes perfectly flat with only short cones at the emission points. The jets disintegrate due to lateral kink instabilities into small droplets, forming a fine mist around the capillary axis. The stable cone-jet mode probably changes to the multi-jet mode because of the limited velocity of the jet formation as compared to the liquid velocity at the outlet of the capillary resulting from the flow rate.

Current pulsations with a corresponding number of different frequencies in the lower kilohertz range can be detected in the multi-jet mode [77]. It is reasonable to assume that each jet emerges from a liquid cone with a specific pulsation frequency.

References

[1] Y. Kazakevich, R. LoBrutto, HPLC for pharmaceutical scientists, Wiley-VCH, New Jersey, 2007.

[2] L.R. Snyder, J.J. Kirkland, J.W. Dolan, Introduction to modern liquid chromatography, Wiley-VCH, New Jersey, 2010.

[3] V.R. Meyer, Practical High-Performance Liquid Chromatography, Fourth edition, John Wiley & Sons, Ltd., 2004.

[4] M.W. Dong, Modern HPLC for practicing scientists, John Wiley & Sons, Inc., New Jersey, 2006.

[5] A.J.P Martin, R.L.M. Synge, Biochem. J. 35 (1941) 1358-1368.

[6] J.C. Giddings, Dynamics of Chromatography, Part 1: Principles and Theory, Marcel Dekker, New York, 1965.

[7] D. Hlushkou, U. Tallarek, J. Chromatogr. A 1126 (2006) 70-85.

[8] W.E. Morf, P.D. van der Wal, N.F. de Rooij, Anal. Chim. Acta 622 (2008) 175-181.

[9] G. Taylor, Proc. R. Soc. Lond. A 219 (1953) 186-203.

[10] R. Aris, Proc. R. Soc. Lond. A 235 (1956) 67-77.

[11] E. Wicke, Ber. Bunsenges. Phys. Chem. 77 (1973) 160-171.

[12] D. Dutta, A. Ramachandran, D.T. Leighton, Microfluid. Nanofluid. 2 (2006) 275-290.

[13] M.R. Doshi, P.M. Daiya, W.N. Gill, Chem. Eng. Sci. 33 (1978) 795-804.

[14] J.P.C. Vissers, J. Chromatogr. A 856 (1999) 117-143.

[15] M.J.E. Golay in D.H. Desty (Editor), Gas Chromatography, Butterworths, London, 1958, pp. 36-55.

[16] J.N. Done, J.H. Knox, J. Chromatogr. Sci. 10 (1972) 606-612.

[17] J.F.K Huber, J.A.R.J. Hulsman, Anal. Chim. Acta 38 (1967) 305-313.

[18] C. Horvath, H.-J. Lin, J. Chromatogr. A 126 (1976) 401-420.

[19] J.J. van Deemter, F.J. Zuiderweg, A. Klinkenberg, Chem. Eng. Sci. 5 (1956) 271-289.

[20] U.D. Neue, HPLC Columns: Therory, Technology, and Practice, Wiley-VCH, New York, 1997.

[21] U. Tallarek, E. Bayer, G. Guiochon, J. Am. Chem. Soc. 120 (1998) 1494-1505.

[22] P. Jandera, Anal. Chim. Acta 692 (2011) 1-25.

[23] H. Qiu, X. Liang, M. Sun, S. Jiang, Anal. Bioanal. Chem. 399 (2011) 3307-3322.

[24] G. Guiochon, J. Chromatogr. A 1126 (2006) 6-49.

[25] A.V. Anikeenko, N.N. Medvedev, Phys. Rev. E 77 (2008) 031101-1-9.

[26] R.A. Shalliker, B.S. Broyles, G. Guiochon, J. Chromatogr. A 888 (2000) 1-12.

[27] G. Guiochon, E. Drumm, D. Cherrak, J. Chromatogr. A 835 (1999) 41-58.

[28] F.A.L. Dullien, Porous Media – Fluid Transport and Pore Structure, Academic Press, San Diego, CA, 1991.

[29] J. Bear, Dynamics of Fluids in Porous Media, Dover Publications, Inc., New York, 1988.

[30] G. Rozing, T. van de Goor, H. Yin, K. Killeen, B. Glatz, K. Kraiczek, H.H. Lauer, J. Sep. Sci. 27 (2004) 1391-1401.

[31] P.C. Carman, Flow of Gases Through Porous Media, Academic Press, New York, 1956.

[32] I. Halász, K. Martin, Angew. Chem. Int. Ed. Engl. 17 (1978) 901-908.

[33] Y. Yao, A.M. Lenhoff, J. Chromatogr. A 1037 (2004) 273-282.

[34] F. Gritti, A. Cavazzini, N. Marchetti, G. Guiochon, J. Chromatogr. A 1157 (2007) 289-303.

[35] F. Helfferich, Ion Exchange, McGraw-Hill, New York, 1962.

[36] I. Nischang, G. Chen, U. Tallarek, J. Chromatogr. A 1109 (2006) 32-50.

[37] A. Höltzel, U. Tallarek, J. Sep. Sci. 30 (2007) 1398-1419.

[38] R.F. Probstein, Physicochemical Hydrodynamics, Wiley, New York, 1994.

[39] J. Ståhlberg, J. Chromatogr. A 855 (1999) 3-55.

[40] M.L. Vestal, Science 226 (1984) 275-281.

[41] A.P. Bruins, J. Chromatogr. A 794 (1998) 345-357.

[42] R.D. Smith, J.A. Loo, C.G. Edmonds, C.J. Barinaga, H.R. Udseth, Anal. Chem. 62 (1990) 882-899.

[43] M.C. McMaster, LC/MS A Practical User's Guide, John Wiley & Sons, New Jersey, 2005

[44] J.H. Gross, Mass Spectrometry, Springer, Berlin Heidelberg, 2004.

[45] Th. Dülcks, R. Juraschek, J. Aerosol. Sci. 30 (1999) 927-943.

[46] J.B. Fenn, M. Mann, C.K. Meng, S.F. Wong, C.M. Whitehouse, Science 246 (1989) 64-71.

[47] M. Yamashita, J.B. Fenn, J. Phys. Chem. 88 (1984) 4451-4459.

[48] C.M. Whitehouse, R.N. Dreyer, M. Yamashita, J.B. Fenn, Anal. Chem. 57 (1985) 675-679.

[49] M. Prudent, H.H. Girault, Analyst 134 (2009) 2189-2203.

[50] W.-C. Sung, H. Makamba, S.-H. Chen, Electrophoresis 26 (2005) 1783-1791.

[51] B.R. Reschke, A.T. Timperman, J. Am. Soc. Mass Spectrom. 22 (2011) 2215-2124.

[52] I.M. Lazar, J. Grym, F. Foret, Mass Spectrom. Rev. 25 (2006) 573-594.

[53] E. Gelpí, J. Mass Spectrom. 37 (2002) 241-253.

[54] A. Kantrowitz, J. Grey, Rev. Sci. Inst. 22, (1951) 328-332.

[55] M. Dole, R.L. Hines, L.L. Mack, R.C. Mobley, L.D. Ferguson, M.B. Alice, Macromolecules 1 (1968) 96-97.

[56] J. Abian, A.J. Osterkamp, E. Gelpí, J. Mass Spectrom. 34 (1999) 244-254.

[57] E. Edwards, J. Thomas-Oates, Analyst 130 (2005) 13-17.

[58] R.S. Ramsey, J.M. Ramsey, Anal. Chem. 69 (1997) 1174-1178.

[59] S. Coster, E. Verpoorte, Lab Chip 7 (2007) 1394-1412.

[60] J. Lee, S.A. Soper, K.K. Murray, J. Mass Spectrom. 44 (2009) 579-593.

[61] H. Yin, K. Killeen, R. Brennen, D. Sobek, M. Werlich, T. van de Goor, Anal. Chem. 77 (2005) 527-533.

[62] Agilent Technologies, Infinitely better for microfluidic nanospray LC/MS, Brochure 5990-62221EN, Agilent Technologies, 2010.

[63] P. Kebarle, U.H. Verkerk, Mass Spectrom. Rev. 28 (2009) 898-917.

[64] M.S. Wilm, M. Mann, Int. J. Mass Spectrom. Ion Processes 136 (1994) 167-180.

[65] R.P.A. Hartman, D.J. Brunner, D.M.A. Camelot, J.C.M. Marijnissen, B. Scarlett, J. Aerosol Sci. 30 (1999) 823-849.

[66] R.P.A. Hartman, D.J. Brunner, D.M.A. Camelot, J.C.M. Marijnissen, B. Scarlett, J. Aerosol Sci. 31 (2000) 65-95.

[67] M. Cloupeau, B. Prunet-Foch, J. Aerosol. Sci. 25 (1994) 1021-1036.

[68] R.D. Smith, Y. Shen, K. Tang, Acc. Chem. Res. 37 (2004) 269-278.

[69] M. Dole, L.L. Mack, R.L. Hines, R.C. Mobley, L.D.Ferguson, J. Chem. Phys. 49 (1968) 2240-2249.

[70] J.V. Iribarne, B.A. Thomson, J. Chem. Phys. 64 (1976) 2287-2294.

[71] B.A. Thomson, J.V. Iribarne, J. Chem. Phys. 71 (1979) 4451-4463.

[72] J.R. Melcher, G.I. Taylor, Annu. Rev. Fluid Mech. 1 (1969) 111-146.

[73] J.F. de la Mora, I.G. Loscertales, J. Fluid Mech. 260 (1994) 155-184.

[74] A.M. Gañán-Calvo, J. Dávila, A. Barrero, J. Aerosol Sci. 28 (1997) 249-275.

[75] J. Zeleny, Phys. Rev. 3 (1914) 69-91.

[76] A. Jaworek, A. Krupa, J. Aerosol. Sci. 30 (1999) 873-893.

[77] R. Juraschek, F.W. Röllgen, Int. J. Mass Spectrom. 177 (1998) 1-15.

[78] I. Marginean, R.T. Kelly, J.S. Page, K. Tang, R.D. Smith, Anal. Chem. 79 (2007) 8030-8036.

[79] P. Nemes, I. Marginean, A. Vertes, Anal. Chem. 79 (2007) 3105-3116.

[80] I. Hayati, A.I. Bailey, Th.F. Tadros, J. Colloid Interface Sci. 117 (1987) 205-221.

[81] J.M. Grace, J.C.M. Marijnissen, J. Aerosol Sci. 25 (1994) 1005-1019.

[82] B. Vonnegut, R.L. Neubauer, J. Colloid. Sci. 7 (1952) 616-623.

[83] G.I. Taylor, Proc. R. Soc. Lon. A 280 (1964) 383-397.

[84] G.A. Valaskovic, J.P. Murphy, M.S. Lee, J. Am. Soc. Mass Spectrom. 15 (2004) 1201-1215.

[85] I. Marginean, L. Parvin, L. Heffernan, A. Vertes, Anal. Chem. 76 (2004) 4202-4207.

[86] I. Marginean, R.T. Kelly, D.C. Prior, B.L. LaMarche, K. Tang, R.D. Smith, Anal. Chem. 80 (2008) 6573-6579.

[87] I. Marginean, R.T. Kelly, R.J. Moore, D.C. Prior, B.L. LaMarche, K. Tang, R.D. Smith, J. Am. Soc. Mass Spectrom. 20 (2009) 682-688.

[88] K.L. Smith, M.S. Alexander, J.P.W. Stark, J. Appl. Phys. 100 (2006) 014905-1-6.

[89] K.-G. Reinsberg, U. Effelsberg, U. Tallarek, Lap Chip 9 (2009) 2914-2923.

Chapter I – Part A

Determination of the interparticle void volume in packed beds *via* intraparticle DONNAN exclusion

3.1 Introduction

The measurement and meaning of void volumes in reversed-phase liquid chromatography (RPLC) has been the subject of a considerable number of publications, as reviewed a few years ago by RIMMER *et al.* [1] and, consequently, has been studied extensively from theoretical and experimental point of views [2]. The total volume of a particle-packed RPLC column can be written as the sum of three contributions: (i) the interparticle, interstitial, or external pore volume; (ii) the intraparticle or internal pore volume; and (iii) the inaccessible volume which can be split into the stationary-phase solid volume, the closed-pore volume, and the volume of the bonded chains [3]. The different void volumes of a packed column are important in both kinetic and thermodynamic measurements, particularly when attempts are made to correlate solute retention with solvent composition [4,5].

In this work we are concerned with the interparticle void volume (V_{inter}) and porosity (ε_{inter}). Its accurate determination and the corresponding analysis of packing densities provides essential feedback, *e.g.*, during the optimisation of column packing conditions and dynamic bed consolidation [6-9], or in the discussion of hydraulic permeabilities *via* phenomenological models and so-derived correlations [10]. This is reflected in the strong dependence on ε_{inter} of different porosity functions that have been used to characterise the resistance to low REYNOLDS number flow of liquid through packed beds, including the most popular one $(1 - \varepsilon_{inter})^2/\varepsilon_{inter}^3$ after BLAKE, KOZENY, and CARMAN, or $4(1 - \varepsilon_{inter})\varepsilon_{inter}^{-4.55}$ after RUMPF and GUPTE which appears to be more accurate [11].

Traditionally, V_{inter} (and ε_{inter}) in packed beds are analysed by inverse size-exclusion chromatography (ISEC) [12]. While classical SEC uses the known pore structure of an adsorbent to determine the molecular weight distribution of a polymer mixture [13], the pore-size distribution of an unknown stationary phase can be determined from the distribution of retention volumes of a series of polymer standards if their molecular weight is known. Provided that standard samples are available for calibration, experiments show that there

exists a correlation between the average molecular weight of the polymers and average diameter of the pores from which they are excluded, assuming that all polymeric chains remain in the same conformation of a random coil [13]. For each packing material, there are two thresholds, a low and a high one. Molecules larger than the high threshold have no access to any significant fraction of the intraparticle porosity. Molecules smaller than the low threshold have access to the entire pore volume. In ISEC solutions of known polymeric samples are injected into a column packed with an unknown adsorbent, and the retention behaviour of these solutes can be correlated with the pore size distribution of the packing material [3,12]. Plots of the logarithm of the molecular weight of the polystyrenes *versus* their retention time reveal a bimodal pore-size distribution representing the internal (intraparticle) and external (interparticle) porosity of the packed bed.

To overcome drawbacks of ISEC for the analysis of V_{inter} (and ε_{inter}) in packed beds [14] CABOOTER *et al.* [15] recently presented a method that relies on measuring the elution time of an unretained small tracer after having filled the intraparticle pores of the particles with a hydrophobic solvent that is completely immiscible with the mobile phase employed during the elution time measurements. Thus, based on the total blocking of the intraparticle pores in a packed bed it allows to perform interparticle void volume measurements with a single, small tracer rather than a large polymer standard. While the total pore blocking method requires careful, time-consuming pre-treatment of the materials, it does not need the regression analysis underlying ISEC.

Another and at least as accurate, but far simpler method than total pore blocking and ISEC for the analysis of V_{inter} (and ε_{inter}) in packed beds is based on the interparticle elution of organic or inorganic ions which are completely, but in this case electrostatically excluded from the intraparticle pore space due to the DONNAN potential [16-18]. This approach originates as a limiting variant of the much explored use of organic or inorganic ions as dead time markers in RPLC (see Chapter 4.3 in [1] and references therein). In this context, it has been noted that mobile phases and/or samples with sufficient ionic strength are required to effectively screen the surface charges of the intraparticle pores and prevent DONNAN exclusion of the charged dead time markers (which behave co-ionic with respect to the surface charge). As, towards the opposite electrostatic extreme, mobile phase composition is tuned for complete intraparticle DONNAN exclusion a small, unretained, co-ionic tracer permeates through the interparticle void space only. It allows the fast, non-invasive analysis of V_{inter} (and ε_{inter}) using water-soluble, UV-detectable ions such as nitrate.

The use of simple organic or inorganic ions as selective markers for V_{inter} (and ε_{inter}) in packed beds based on the intraparticle DONNAN exclusion has been observed and explored before [4,14,17,19-23]. In this work, we present further insight into the operational domain of this simple as elegant approach by addressing, together with a variation of the mobile phase ionic strength, the influence of the intraparticle mean pore size and surface charge density, as well as the onset of DONNAN exclusion already on the interparticle pore level in dependence of the mean particle size. Values of ε_{inter} are compared with those obtained by the traditional ISEC method.

3.2 Background

In porous adsorbents like membranes, sphere packings, and monoliths which contain charged solid-liquid interfaces and through which ionic species (simple ions, analytes, or colloidal particles) are transported, several electrical fields may be superimposed. This includes local fields near the wall of charged pores, or around devised spacer groups and bonded chains which extend from the surface, the DONNAN potentials between different compartments in hierarchically structured materials, the quasi-equilibrium electrical double layer (EDL) at the phase boundaries, as well as externally applied fields [18,24].

Ion-permselectivity (charge-selectivity) is a unique and often tailored characteristic of porous media which they can show either as a whole (*e.g.*, membranes separating completely adjacent solutions) or by means of local, discrete ion-permselective regions (meso- and/or microporous domains) in materials which are macroscopically charge-nonselective (packed beds, monoliths). While charge-selectivity traditionally plays a central role in membrane science [25,26], ion-permselective transport also prevails in the intraparticle or intraskeleton mesopores of particulate and monolithic columns typically used in HPLC (Figure 3.1) [17,18]. It is therefore also relevant to reversed-phase silica particles, even those with a conventional endcapping, due to the persistence of residual silanol groups which, in turn, contribute a pH-dependent surface charge [27].

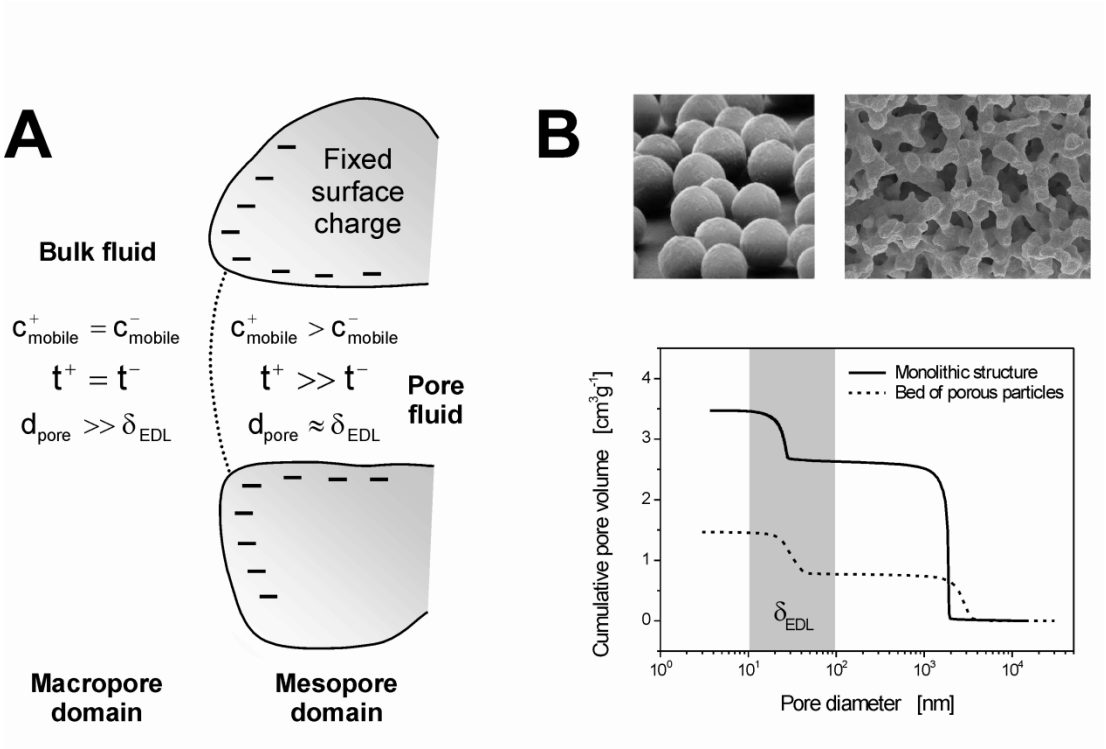

Figure 3.1. **(A) Schematic representation of equilibrium ion concentrations (for a strong, symmetrical background electrolyte), transport numbers, and the ratio of the local pore diameter (d_{pore}) to the EDL thickness (δ_{EDL}) in the interconnected macropore and mesopore spatial domains of hierarchically structured materials. The concentration of mobile counterions (c^+_{mobile}) and their transport number (z^+t^+; t^+ is the transference number [16]) in the pore fluid of the mesopore domain exceed those of the co-ions.**
(B) SEM (scanning electron microscopy) images and pore size distributions characterizing many sphere packings and monolithic structures. These fixed beds reveal bimodal pore size distributions due to the intraparticle (intraskeleton) mesopores and the interparticle (interskeleton) macropores [24].

The characteristic pore sizes d_{pore} of the interparticle (interskeleton) macropore space of a packed bed (monolith) usually substantially exceed the typical EDL thickness δ_{EDL} at the particles external surface (along the monolith skeleton), as illustrated in Figure 3.1A (d_{pore} » δ_{EDL}). Thus, liquid in the macropore space is quasi-electroneutral (thin-EDL-limit) and transport numbers of the co-ions and counterions in the background electrolyte are well balanced. By contrast, intraparticle or intraskeleton mesopore sizes are comparable with the EDL thickness (Figure 3.1A, $d_{pore} \approx \delta_{EDL}$), as shown in Figure 3.1B for a representative silica-based monolith and a packed bed [24]. The mesopore-scale EDL interaction (also referred to as EDL overlap) results in counterion enrichment and co-ion exclusion with respect to the bulk solution. As illustrated in Figure 3.2 it is governed by the surface electrical potential

inside the mesopores (ψ_S) and r_{pore}/λ_D, the ratio of the intraparticle or intraskeleton mesopore radius r_{pore} (if we assume cylindrical pores for simplicity) and the DEBYE screening length λ_D which characterizes the EDL thickness and which depends on the mobile phase ionic strength according to [28]

$$\lambda_D = \left(\frac{\varepsilon_0 \varepsilon_r RT}{F^2 \sum z_i^2 c_{i,\infty}} \right)^{\frac{1}{2}} \tag{3.1}$$

where ε_0 and ε_r are the permittivity of vacuum and relative permittivity of the bulk solution, respectively. R is the gas constant, T is the absolute temperature, and F is the FARADAY constant; z_i is the valency of ionic species i and $c_{i,\infty}$ its concentration in the electroneutral, bulk solution (that is, beyond the EDL).

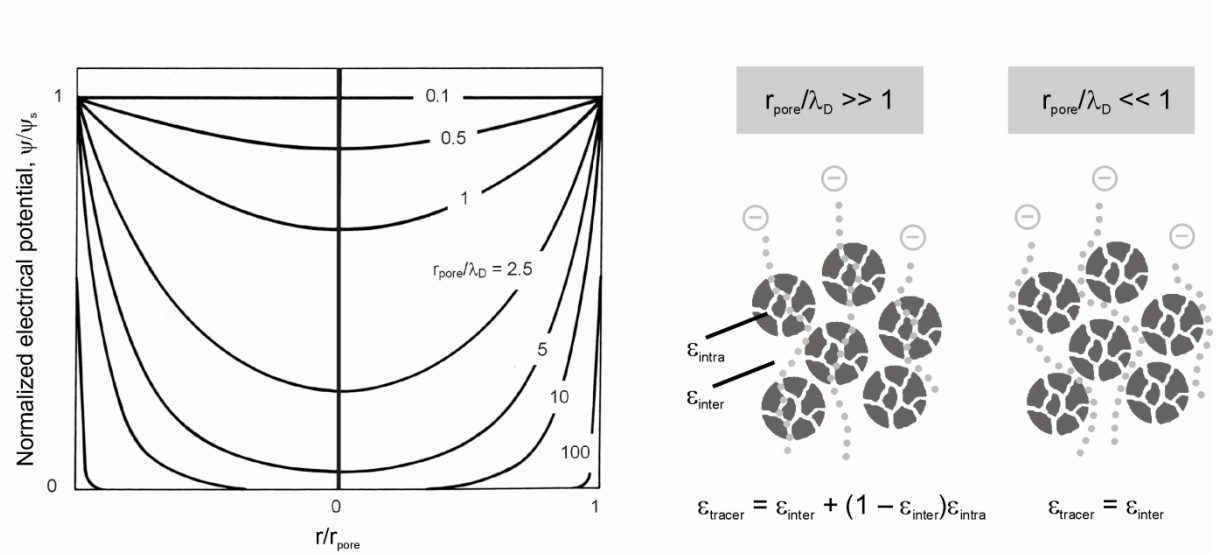

Figure 3.2. Pore-scale distribution of electrical potential normalized by the surface potential ψ_S for different values of r_{pore}/λ_D reflecting EDL overlap and co-ion exclusion (adapted from [28]). For $r_{pore}/\lambda_D >> 1$ a co-ionic (here negatively charged) tracer has access to the total porosity of the packed bed, while for $r_{pore}/\lambda_D << 1$ it samples only the interparticle porosity. Plots of the elution volumes of a co-ionic tracer versus r_{pore}/λ_D reveal a bimodal pore-size distribution with a plateau region at low ionic strength representing the interparticle porosity and another plateau region at high ionic strength where the charge-selectivity of the particles has disappeared and the co-ionic tracer experiences the entire pore space.

Depending on the actual intensity of EDL overlap, *e.g.*, inside mesoporous particles of a packed bed represented by r_{pore}/λ_D, we expect the complete permeation ($\varepsilon_{tracer} = \varepsilon_{total}$) and exclusion ($\varepsilon_{tracer} = \varepsilon_{inter}$ only) of an unretained, co-ionic tracer as the extreme scenarios (Figure 3.2) [17,19,20,23]. For $r_{pore}/\lambda_D \approx 1$, the EDL extends over the whole pore fluid, the pore is

ion-permselective and excludes co-ions. Their transport numbers decrease at increasing EDL overlap, while those of the counterions increase. For $r_{pore} \gg \lambda_D$, the EDL is confined to a thin layer at the pore walls only, meaning that the whole pore fluid is quasi-electroneutral and its charge-selectivity disappears. The transport numbers of co-ions and counterions become balanced. These extremes ($r_{pore}/\lambda_D < 1$ and $r_{pore}/\lambda_D \gg 1$) and the broad intermediate regime can be easily tuned in chromatographic practice by the mobile phase ionic strength ($\rightarrow \lambda_D$) and the intraparticle pore dimensions ($\rightarrow d_{pore}$). Apart from the ion-exclusion chromatography, this adjustable electrostatic on-off behaviour [18,29-34] of the intraparticle permeation in chromatographic media (Figure 3.2) is relevant also for the design of preparative separations and purification processes [35-38], because the actual electrolyte concentration determines the availability of chromatographic sites and "effective porosity" for co-ionic analytes, as well as the pore-level concentrations of charged analytes (co-ion exclusion, counterion enrichment), in general.

Alternatively, the situation illustrated by Figures 3.1 and 3.2 can be analysed in terms of DONNAN exclusion [16]. At electrochemical equilibrium between electrolyte solutions in both compartments (Figure 3.1A) counterion concentration in the intraparticle (intraskeleton) mesopore space is higher and co-ion concentration lower than in the interparticle (interskeleton) macropore space. An electrical phase boundary potential between interconnected bulk and ion-permselective domains balances the tendency of ions to level out these concentration (chemical potential) differences. This potential is also known as the DONNAN potential (Φ_{Don}) [39,40]. It pulls cations back into the negatively charged intraparticle (intraskeleton) pore space and anions back into the positively charged interparticle (interskeleton) compartment [41]. For ideal solutions we have

$$\Phi_{Don} \equiv \phi_{intra} - \phi_{inter} = -\frac{RT}{z_i F} \ln \frac{c_{i,intra}}{c_{i,inter}} , \qquad (3.2)$$

where i applies to $TrisH^+$, H_3O^+, and K^+ ($z_i = +1$) as well as to Cl^-, OH^-, and NO_3^- ($z_i = -1$) for the buffer (Tris-HCl) and tracer salt (KNO_3) used in the present work. The distribution coefficient $c_{i,intra}/c_{i,inter}$ (which represents the ion-permselectivity of the particles or the monolith skeleton) depends on the mobile phase ionic strength, the surface charge density in the intraparticle or intraskeleton pore space, and on valencies of the co-ionic and counterionic species. Actually, these parameters similarly influence EDL overlap and resulting co-ion exclusion in a double-layer model.

The considerations on relevant parameters (Figures 3.1 and 3.2) which define the operational domain of co-ion exclusion and inorganic ions as selective markers for V_{inter} (and ε_{inter}) in packed beds have motivated us to conduct the following capillary HPLC experiments. For an extended range of mobile phase ionic strengths (Tris-HCl buffer) and with KNO_3 as the tracer salt particles with similar intraparticle mean pore sizes, but different surface charge densities (reversed-phase, bare-silica, strong cation-exchange); particles with different intraparticle pore sizes (100 and 1000 Å); as well as different mean particle sizes (3, 5, and 10 µm) were compared to retrieve DONNAN exclusion not only inside, but already between the particles.

3.3 Experimental section

3.3.1 Chemicals and materials

Organic solvents of HPLC grade (acetonitrile, methylene chloride, methanol, ethanol, and acetone) were purchased from Sigma-Aldrich (Taufkirchen, Germany). Benzene and KNO_3 were obtained from Carl Roth (Karlsruhe, Germany). Hydrochloric acid was bought from VWR International (Briare, France). Polystyrene standards with a molecular weight of 2500, 5000, 9000, 30000 and 50000 g/mol were purchased from Supelco (Bellefonte, PA). Polystyrene standards with 20000, 100000, 500000, 1000000, 2000000, and 4000000 g/mol as well as Tris(hydroxymethyl)aminomethane came from Fluka Chemie (Buchs, Switzerland). HPLC-grade water was prepared with a Milli-Q gradient water purification system (Millipore, Bedford, MA).

In our capillary HPLC studies we employed the following support particles: 3 and 10 µm-sized 120 Å Hypersil MOS (monomeric octyl silica, C8) (Thermo Fisher Scientific, Waltham, MA); 3 µm-sized 80 Å Spherisorb SCX (propanesulfonic acid-modified silica) (Waters, Milford, MA); and 5 µm-sized 100 Å and 1000 Å Nucleosil 100-5 and Nucleosil 1000-5 (bare-silica) (Macherey-Nagel, Düren, Germany). These particles were slurry-packed into 75 µm i.d., 360 µm o.d. cylindrical fused-silica capillaries (Polymicro Technologies, Phoenix, AZ).

3.3.2 Apparatus

All data were acquired with an Agilent 1100 liquid chromatograph (Agilent Technologies, Waldbronn, Germany) consisting of a degasser and a nanopump, equipped with a variable

wavelength UV detector (VWD) and a high-sensitivity cell (SunChrom, Friedrichsdorf, Germany) working at 254 nm for the ISEC experiments with the polystyrene standards and at 210 nm for the DONNAN exclusion experiments with KNO_3. Manual sample injection was performed *via* a two-position injection valve with a 4 nL internal loop volume (Model CN4 from Vici AG Valco Europe, Schenkon, Switzerland). The loop was continuously flushed by use of a syringe installed on a syringe pump (Harvard Apparatus, Holliston, MA). Fused-silica restriction capillaries having a length of either 900 mm (15 µm i.d.) or 500 mm (10 µm i.d.) were used as pre-columns to ensure a sufficient working pressure. Volumetric flow rates were continuously monitored by an external flow sensor (Model SLG-1430-150, Sensirion, Stäfa, Switzerland) connected to the outlet of the detection cell. To avoid daily fluctuations of the nanopump the actual flow rates recorded by the external flow sensor were used to calculate elution volumes of the analytes. All experiments were carried out at 298 ± 1 K under isocratic elution conditions. Injections were thrice-repeated for a given capillary and the results averaged to account for the error from manual injection.

3.3.3 Capillary packing

Capillaries were slurry-packed using a WellChrom K-1900 pneumatic pump (Knauer, Berlin, Germany) with a 500 µm i.d. glass-lined metal tubing as the slurry reservoir [8,42]. A micro-union with a 1 µm mesh stainless-steel frit (Upchurch Scientific, Oak Harbor, WA) was connected to each capillary to provide a temporary outlet frit during packing. Slurries were prepared by suspending the dry particles in 1 mL of the appropriate solvent while applying ultrasound for 10 min (Table 3.1).

The degassed pushing (packing) solvents were also used for rinsing and conditioning of the fused-silica capillaries prior to the packing process. 70 µL of the slurries were injected into the reservoir and a pressure of 300 bar was applied for at least 5 min. After a short optical inspection to verify whether the packing of the capillary had started or blockage occurred, the pressure was raised (Table 3.1) and the capillaries were inserted into an ultrasonic bath (Bandelin Electronic, Berlin, Germany) for 40 min during packing and consolidation. As demonstrated earlier the application of ultrasound appeared to be critical for obtaining densely packed capillaries [8].

After consolidation of the packing, the system was depressurized slowly and the capillary removed from the packing device. The pushing solvent was replaced by bidistilled, filtered, and degassed water containing NaCl which was needed for preparing mechanically stable frits (Table 3.1). Afterwards, the capillary was reassembled within the packing device

and flushed for 90 min with the aqueous electrolyte solution for a complete exchange of the packing solvent. The bed was fixed by a sintered inlet and outlet frit to obtain a total bed length of about 120 mm. Packing procedures were not evaluated for separation efficiencies; the conditions in Table 3.1 proved to be adequate for obtaining stable packed beds without gaps and further tendency for settling during the measurements.

Table 3.1.

Packing conditions for the adsorbents.

Packing material	Slurry solvent	Slurry concentration	Packing solvent	Max. applied pressure	Fritting electrolyte
Hypersil MOS; 3 µm, 120 Å	Acetone	20 mg/mL	Methanol	550 bar	1 g/L NaCl
Hypersil MOS; 10 µm, 120 Å	Acetone	20 mg/mL	Methanol	550 bar	1 g/L NaCl
Spherisorb SCX; 3 µm, 80 Å	1 M NaCl	10 mg/mL	2 M NaCl	550 bar	30 g/L NaCl
Nucleosil; 5 µm, 100 Å	Ethanol	35 mg/mL	Water	400 bar	1 g/L NaCl
Nucleosil; 5 µm, 1000 Å	Ethanol	15 mg/mL	Water	300 bar	1 g/L NaCl

3.3.4 Porosity measurements

Interparticle void volumes and porosities (V_{inter} and ε_{inter}) of the packed capillaries were analysed by ISEC (size-exclusion) and DONNAN (electrostatic) exclusion. In the former case benzene (1 mmol/L) and a total of eleven polystyrene standards ranging from 2500 to 4000000 g/mol (0.6 mg/mL each) were dissolved in methylene chloride. Analytes were injected and chromatographed at a flow rate of 200 nl/min and detection at 254 nm. For the determination of V_{inter} and ε_{inter} *via* DONNAN exclusion in capillaries packed with the Hypersil MOS phases KNO_3 in 70/30 acetonitrile/water (v/v) was injected and detected at 210 nm. For the bare-silica and SCX materials KNO_3 was used in 30/70 acetonitrile/water (v/v). The concentration of Tris-HCl buffer (pH 8.1) in the mobile phases was varied from 0.01 to 40 mM and is, where useful, also presented as λ_D (the DEBYE screening length, Equation (3.1)) to express the DONNAN exclusion of nitrate also *via* r_{pore}/λ_D (*cf.* Figure 3.2). The relative

permittivity (ε_r) in Equation (3.1) for the mobile phases was taken from MOREAU and DOUHÉRET [43].

For low buffer concentrations in the running mobile phase (from 0.01 to 0.1 mM) KNO_3 solutions in the respective, but unbuffered mobile phase were injected. In this case, the KNO_3 concentration was adjusted to the ionic strength of the running mobile phase which resulted in negligible disturbances of the intraparticle DONNAN exclusion during elution of the nitrate due to the mismatch between injected sample and running mobile phase. At higher buffer concentrations (> 0.1 mM) a fixed KNO_3 concentration of 0.04 mM was added to the respective and now buffered mobile phase for sample injection.

3.4 Results and Discussion

Interparticle void volumes and porosities (V_{inter} and ε_{inter}) have been determined by ISEC and Donnan exclusion for all packings. In ISEC eleven polystyrene standards with molecular weights (M_W) from 2500 to 4000000 g/mol and benzene dissolved in dichloromethane were injected onto the packed capillaries for each packing material. Interparticle porosities ($\varepsilon_{inter} = V_{PS}/V_{column}$) were calculated from the elution volumes of the most suitable standard (V_{PS}), which is just size-excluded from the intraparticle pore space, and the column volume (V_{column}). The latter has been determined by measuring nitrate elution volumes for the empty capillaries that were subsequently used for packing.

It should be mentioned that the elution volume of even the smallest (yet completely size-excluded) polystyrene standard is expected to differ from the real morphological interstitial column volume. Depending on its finite size an analyte like the polystyrene standard intrinsically has a reduced access to the interparticle pore space compared with a fictitious "point mass analyte" [44]. To ensure that the so-derived values of ε_{inter} are not falsified by the actual molecular size of the identified polystyrene standard the elution volumes of all polystyrene standards were complementary plotted against the cubic root of their molecular weight (Figure 3.3) [45]. Employing the elution volumes of only the size-excluded polystyrene standards the intersection with the ordinate for "zero molecular weight" ($M_W^{1/3} = 0$) reflects the morphological interparticle void volume experienced by a fictitious "point mass analyte" and can be calculated *via* linear regression (see Figure 3.3). ε_{inter} is then recalculated from this maximal V_{inter} (intersection with the ordinate) and V_{Column}. Under the conditions of the present study differences in V_{inter} were only on the order of 1–3% .

According corrections to the values of ε_{inter} based on the elution volumes of the most suitable polystyrene standard thus remained insignificant. This result can be rationalized by considering the large interparticle pore dimensions of the packings made of 3 or 10 µm particles [46] with respect to the size of the smallest polystyrene standard that is completely size-excluded from their mesopores and used for the determination of V_{inter} (Figure 3.3).

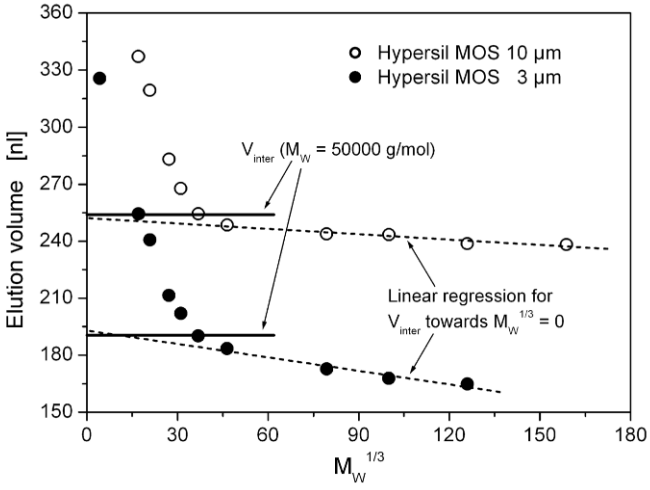

Figure 3.3: Elution volumes of polystyrene standards *vs.* the cubic root of their molecular weight. Linear regression for size-excluded polystyrene standards towards $M_W^{1/3} = 0$ (dotted lines) determines the maximal interparticle void volume V_{inter} of capillaries packed with the 3 and 10-µm sized Hypersil MOS particles (120 Å nominal pore size) which would be experienced by a size-excluded, fictitious "point mass analyte". The solid lines denote the real elution volumes of the smallest size-excluded polystyrene standard (M_W = 50,000 g/mol).

Plots of log(M_W) of the polystyrene standards *vs.* their elution volume revealed a bimodal pore size distribution for all packings (only for capillaries packed with macroporous Nucleosil 1000-5 material the determination of the high threshold was not unambiguous, as discussed later). The intersection of the calibration curves providing the smallest polystyrene coil which is completely excluded from the intraparticle pore space was determined graphically by linear regression. The associated pore diameter of each stationary phase was calculated by [12]

$$d_{pore}\left[\text{Å}\right] = 0.62\left(M_W\right)^{0.59} \tag{3.3}$$

and values are summarized in Table 3.2. HALÁSZ and MARTIN [12] found that the pore diameter of a solid assigned by Equation (3.3) to a polystyrene of molecular weight M_W dissolved in methylene chloride is 2.5 times larger than the rotational coil diameter of the same polystyrene molecule. They introduced the factor of 2.5 to fit their SEC data to the mean pore diameter found by classical methods. Thus, HALÁSZ and MARTIN [12] shifted the SEC

Table 3.2.

Characteristics of the packed capillaries.

Material	d_{pore} [Å]	DONNAN exclusion ε_{inter} (NO_3^-)	ISEC approach ε_{inter} (PS)
Hypersil MOS; 3 µm, 120 Å	110	n.a.	0.36
Hypersil MOS; 10 µm, 120 Å	119	0.42	0.41
Spherisorb SCX; 3 µm, 80 Å	95	0.42	0.43
Nucleosil; 5 µm, 100 Å	162	0.43	0.44
Nucleosil; 5 µm, 1000 Å	1295	< 0.49	n.a.

curves to mean pore diameters 2.5 times larger than the rotational coil diameter. The so-obtained "new" pore size distribution bears little relation to the pore size distribution derived by mercury porosimetry or computational approaches [47], but it provides a reasonable value for the mean pore diameter [47]. Although the pore diameters calculated with Equation (3.3) (Table 3.2) should be taken with caution, they enable a comparison with manufacturers' data and the other silica-based materials used in this work.

When comparing the results in Table 3.2 with manufacturers' data only slight differences are resolved for Hypersil MOS and Spherisorb SCX particles. For Nucleosil 100-5 particles, however, the calculated pore diameter turned out to be significantly higher (162 Å instead of the nominal 100 Å); similarly, the 2000000 g/mol polystyrene standard denotes d_{pore} = 1295 Å for the Nucleosil 1000-5 particles (nominal d_{pore}: 1000 Å). Although the determined pore diameters of the Nucleosil particles deviate from the manufacturers' data the resulting ratio of ~ 8 (Nucleosil 1000-5 to Nucleosil 100-5) is at least comparable to the nominal ratio of 10.

Interparticle porosities determined by DONNAN exclusion were calculated from the nitrate elution volumes at a buffer concentration of 0.02 mM, where elution volumes (V_{tracer}) for most packings reached the plateau region (see below) indicating complete intraparticle

DONNAN exclusion, and the geometrical column volume (V_{column}). To realise maximum surface charge of all packing materials the aqueous part of all mobile phases was buffered with Tris-HCl (pH 8.1). This caused a complete dissociation of silanol groups on the surface of the bare-silica, reversed-phase silica, and SCX particles.

Interparticle porosities are summarized in Table 3.2 and show good agreement between the two methods (ISEC and DONNAN exclusion). Packing densities for the Hypersil MOS phases with $\varepsilon_{inter} = 0.36$ for the 3 µm and $\varepsilon_{inter} = 0.41 – 0.42$ for the 10 µm particles at a particle-aspect ratio (column-to-particle diameter ratio) of $d_c/d_p = 25$ and 7.5, respectively, agree with the trend in earlier investigations where the packing density of confined cylindrical sphere packings was found to decrease exponentially at low particle-aspect ratios due to the increasing contribution of the geometrical wall effect [8,48]. The value of $\varepsilon_{inter} = 0.36$ realisrealiseed with the 3 µm Hypersil MOS particles closely reflects the maximum density of disordered (random) hard sphere packings [49,50]. Nucleosil bare-silica particles were packed at lower pressures to avoid damage of the highly porous particle structure (Table 3.1). The application of high packing pressures turned out to be essential for generation of densely packed beds, thus the lower packing pressures limited by the stability of the Nucleosil material explain the slightly higher porosities of Nucleosil 100-5 ($\varepsilon_{inter} = 0.43 – 0.44$) and Nucleosil 1000-5 ($\varepsilon_{inter} < 0.49$) packings. Additionally, the Nucleosil particles show a stronger deviation from spherical shape and higher surface roughness than the other materials which also contributes to lower packing densities [8,51].

Despite these obvious differences in packing densities all packings were consolidated, rigid, and therefore met the requirements for a reliable data acquisition by chromatographic measurements of the interparticle void volumes. Careful microscopic inspection revealed that all packings remained densely packed; no voids were observed in the axial direction before and after the chromatographic analysis.

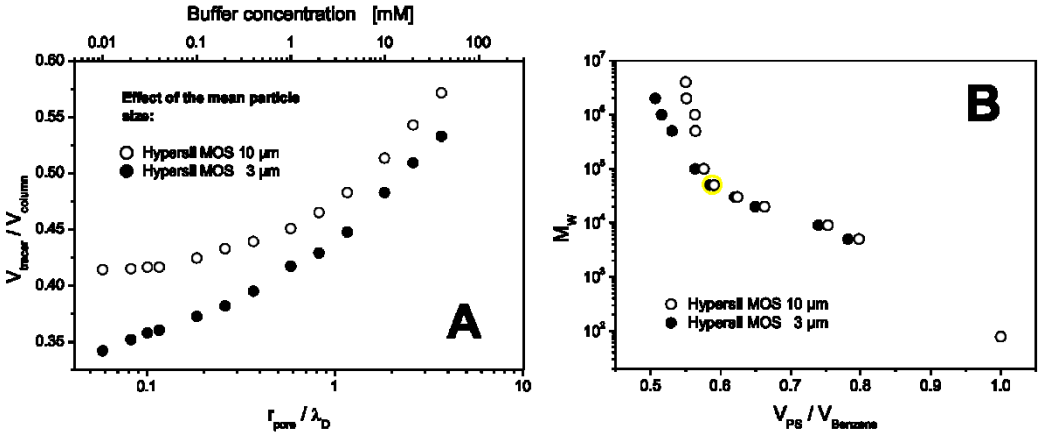

Figure 3.4: (A) Electrostatic exclusion curves of nitrate *vs.* r_{pore}/λ_D and (B) inverse size-exclusion curves of polystyrene standards with known molecular weight (M_W) for capillaries packed with the 3 and 10 µm-sized Hypersil MOS particles (120 Å nominal pore size). The elution volumes of nitrate (V_{tracer}) were normalised by the empty capillary volume (V_{column}), while polystyrene elution volumes (V_{PS}) were normalised by that of benzene.

3.4.1 Effect of the mean particle size

Figure 3.4 shows the calibration curves for electrostatic exclusion (Figure 3.4A) and size-exclusion (Figure 3.4B) acquired with the Hypersil MOS particles (120 Å nominal pore size). Comparing the calibration curves for the two differently sized materials (d_p = 3 and 10 µm nominal particle size) it is first noticed that both size-exclusion and DONNAN exclusion with the 10 µm particles develop relatively discretely. Complete DONNAN exclusion in Figure 3.4A (open circles) is characterized by the plateau region at low buffer concentrations where the normalized elution volumes V_{tracer}/V_{column} are plotted versus the dimensionless ratio r_{pore}/λ_D characterizing intraparticle EDL overlap (or DONNAN exclusion). In this plateau region nitrate is completely excluded from the negatively charged intraparticle pore space (thus, $V_{tracer} \equiv V_{inter}$). This exclusion persists up to r_{pore}/λ_D = 0.12 (which translates to a Tris buffer concentration of 0.04 mM) and these "plateau" elution volumes can be used for calculating the interparticle porosity according to $\varepsilon_{inter} = V_{inter}/V_{column}$. At higher ionic strength nitrate ions begin to penetrate the intraparticle pore space (and $V_{tracer} > V_{inter}$). The hyperbolic shape of the graph in Figure 3.4A (open circles) results from the inverse dependence of λ_D on the square root of the counterion concentration (Equation (3.1)), so that the electrostatic (DONNAN) exclusion is only slowly developing (or disappearing) over a wide range of mobile phase ionic strengths. At the highest buffer concentration (40 mM) the nitrate ions are still not able to penetrate the complete pore space; otherwise, the elution volumes would reach a second

plateau (where $V_{tracer} \equiv V_{total}$). This illustrates that relatively high ionic strengths need to be realised in order to use the nitrate ions as a tracer for the column dead volume [1,17]. The size-exclusion curve for the 10 µm Hypersil MOS particles (Figure 3.4B, open circles) reveals a bimodal distribution. Benzene has access to the entire pore space and it therefore denotes the overall void volume of the packing. Complete size-exclusion is reached with the polystyrene standard of 50000 g/mol (*cf.* Figure 3.3). With further increasing molecular weight of the polystyrene standards a sharp increase in slope is observed leading to a nearly vertical calibration curve.

Calibration curves for electrostatic and size-exclusion in the case of capillaries packed with the smaller (3 µm-sized) Hypersil MOS particles reveal a different trend. The DONNAN exclusion curve in Figure 3.4A at high ionic strengths (and, correspondingly, high values of r_{pore}/λ_D) is similar to the calibration data for the 10 µm particles with a nearly identical surface chemistry and pore size distribution; however, at decreasing ionic strength (and decreasing r_{pore}/λ_D) V_{tracer}/V_{column} does not enter into a plateau region. Instead, the nitrate elution volumes continue to decrease. To explain this behaviour, another aspect of packing morphology needs to be considered. Compared with the d_p = 3 µm packings the 10 µm packings not only consist of larger particles (translating to a larger d_p/λ_D ratio), but they are also more loosely packed (*cf.* Table 3.2). The mean nearest-neighbour distance in random sphere packings depends on the packing density [46]. As a result (concerning absolute particle size and packing density), significant EDL overlap does not develop between the loosely packed 10 µm particles, even as the EDL thickness continues to increase at decreasing buffer concentration. By contrast, EDL overlap in the interparticle pore space becomes important for the densely packed 3 µm packings and explains the continued decrease in nitrate elution volumes at decreasing r_{pore}/λ_D (without entering a plateau). In other words, while still increasingly excluded from the intraparticle pore space the nitrate ions already become partly excluded from the interparticle pore space as well.

The relevance of the interparticle pore space dimensions is also reflected in the ISEC graphs (Figure 3.4B), but now in view of size-exclusion, not electrostatic exclusion. For the densely packed 3 µm packings the high-molecular-weight polystyrenes indicate a stronger exclusion from parts of the interparticle void space than in the loosely packed 10 µm packings. The smaller slope in Figure 3.4B for the size-excluded polystyrenes in case of the 3 µm packings can be explained by the onset of size-exclusion from the interparticle pore space already where these polystyrenes are unable to fully penetrate the cusp regions between the small (and densely packed) 3 µm particles. However, as we have shown in Figure 3.3 this

effect remains negligible for the smallest size-excluded polystyrene (M_W = 50,000 g/mol) which is used in the determination of V_{inter} and ε_{inter} by ISEC.

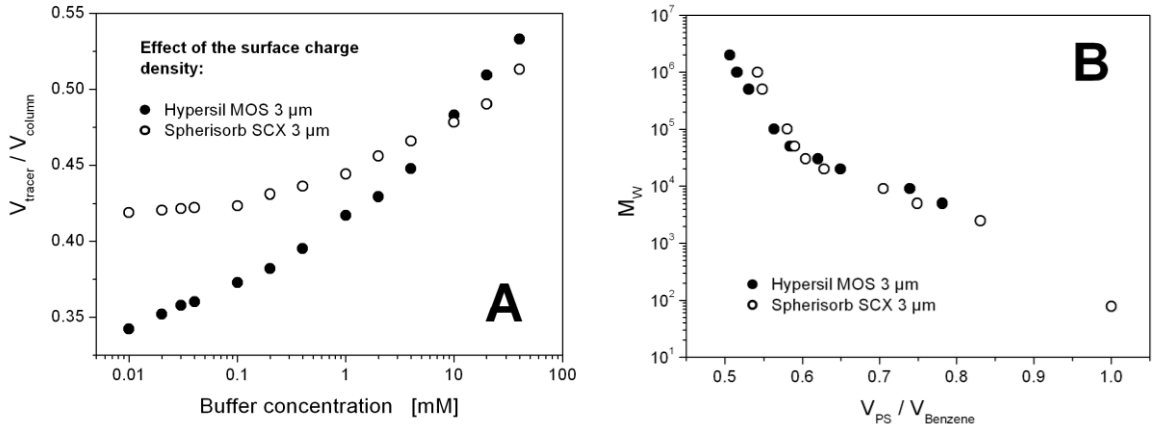

Figure 3.5: (A) Electrostatic exclusion curves of nitrate *vs.* the concentration of Tris-HCl buffer in the mobile phase and (B) inverse size-exclusion curves of polystyrene standards with known molecular weight (M_W) for capillaries packed with 3 µm Hypersil MOS (monomeric octyl silica, non-endcapped) and 3 µm Spherisorb SCX (propanesulfonic acid-modified silica) particles.

3.4.2 Effect of the surface charge density

To study the influence of the intraparticle surface charge density on DONNAN exclusion nitrate elution curves for the 3 µm Hypersil MOS particles and 3 µm Spherisorb SCX particles are compared in Figure 3.5A. Both particles have similar intraparticle pore sizes (110 and 95 Å, Table 3.2), but their surface modification is very different. Hypersil MOS is a dimethyloctylsilane non-endcapped silica, whereas the Spherisorb SCX is a propanesulfonic acid-modified silica. By comparing calibration curves in Figure 3.5A, where normalized elution volumes of nitrate ions are plotted *versus* the Tris buffer concentration, we notice that V_{tracer}/V_{column} for the Hypersil MOS particles decreases monotonically with decreasing ionic strength, while elution volumes on the Spherisorb SCX material run into a plateau below a buffer concentration of 0.1 mM. The discrete DONNAN exclusion regime with a fully developed pleateau can be explained by the significantly higher surface charge density of the Spherisorb SCX particles. This property leads to a much stronger DONNAN exclusion of the nitrate ions, in turn enabling the observation of a discrete plateau region (Figure 3.5A).

Figure 3.5B shows the results of the ISEC calibration. Both curve shapes in this case are similar, in contrast to Figure 3.5A, because size-exclusion of the larger polystyrene standards from parts of the interparticle pore space is independent of the surface charge

density of the particles and is therefore similar for packing materials with a similar mean particle size and size distribution.

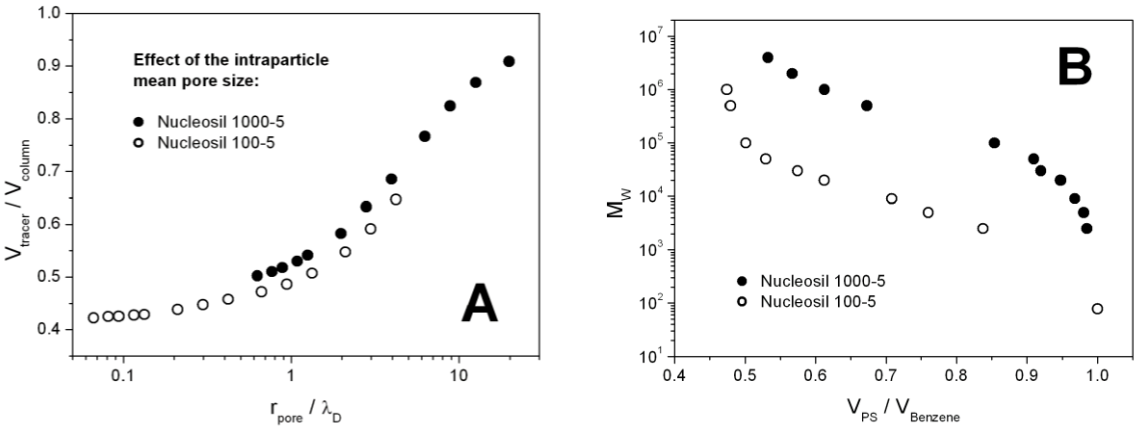

Figure 3.6: (A) Electrostatic exclusion curves of nitrate *vs.* r_{pore}/λ_D and (B) inverse size-exclusion curves of polystyrene standards with known molecular weight (M_W) for capillaries packed with 5 µm Nucleosil 100-5 (100 Å nominal pore size) and Nucleosil 1000-5 bare-silica particles (1000 Å).

3.4.3 Effect of the mean intraparticle pore size

Intraparticle co-ion exclusion for a packing material is expected to depend sensitively on the mean pore size, *i.e.*, the actual pore-scale EDL overlap expressed in r_{pore}/λ_D (Figure 3.2), assuming that the particle size (*cf.* Figure 3.4) and the surface potential (*cf.* Figure 3.5) of the stationary phases are identical. To demonstrate the influence of r_{pore} in r_{pore}/λ_D, the calibration curves for packed capillaries obtained with Nucleosil 100-5 (5 µm-sized particles, nominal 100 Å pores) and Nucleosil 1000-5 (nominal 1000 Å pores) are shown in Figure 3.6A. The surface charge density of these Nucleosil bare-silica particles is higher than that of the Hypersil MOS reversed-phase particles, which leads to predict a more pronounced plateau region in the DONNAN exclusion data for the Nucleosil 100-5 particles (open circles, Figure 3.6A) compared to the 10 µm Hypersil MOS particles (open circles, Figure 3.4A). This is indeed confirmed by the experimental data when comparing the slopes of both curves at low buffer concentrations. The asymptotic limit of intraparticle exclusion is almost reached at $r_{pore}/\lambda_D = 0.21$ for Nucleosil 100-5 (Figure 3.6A), whereas for 3 µm Hypersil MOS (Figure 3.4A) the nitrate ions at this ratio still are not completely excluded. The higher surface electrical potential in the even slightly larger pores of the bare-silica (162 Å) compared to the C8-silica material (119 Å) results in a stronger DONNAN exclusion.

In a comparison of columns packed with the Nucleosil 100-5 (162 Å pores, Table 3.2) and Nucleosil 1000-5 (1295 Å pores) particles, the differences in DONNAN exclusion are

nearly independent of the surface electrical potential, but should reflect exclusively the dependence on the mean pore diameter. The much smaller EDL overlap for the Nucleosil 1000-5 particles results in an immediately sharp increase in the V_{tracer}/V_{column} data of the DONNAN exclusion curve at $r_{pore}/\lambda_D = 0.63$ (already with the low buffer concentrations), whereas the calibration curve of the Nucleosil 100-5 particles starts much earlier, at $r_{pore}/\lambda_D = 0.07$ (Figure 3.6A). An accurate determination of the point of complete exclusion from the intraparticle pore space cannot be made for the macroporous Nucleosil 1000-5 particles, because the nitrate elution volumes do not reach, but just approach the asymptotic limit (plateau region at still lower values of r_{pore}/λ_D indicating complete DONNAN exclusion). Although the slope of the V_{tracer}/V_{column} data at buffer concentrations below 0.03 mM ($r_{pore}/\lambda_D = 1.09$) starts to decrease, the deviation of the calculated $\varepsilon_{inter} = 0.49$ (using the nitrate elution volume with 0.01 mM Tris) from the real packing density is difficult to estimate by extrapolation. Thus, the smallest nitrate elution volume for the macroporous particles at $r_{pore}/\lambda_D = 0.63$ (lowest Tris buffer concentration used) provides only an upper limit and $\varepsilon_{inter} < 0.49$ (Figure 3.6A).

Regarding the analysis of ISEC data for the small-pore and wide-pore silicas (Figure 3.6B) a discrete point of complete size-exclusion can be recognized only for the Nucleosil 100-5 particles (open circles) at a molecular weight of 100,000 g/mol translating to the pore diameter of 162 Å in Table 3.2. For the Nucleosil 1000-5 particles, however, the opposite extreme can be observed: here, the pores are so large to become almost fully penetrated not only by benzene, but also the polystyrene standards with 2500 and 5000 g/mol. A significant size-exclusion from the pores starts with 9000 g/mol, *i.e.*, for a pore diameter of 54 Å, and reaches the upper limit in this work at 4,000,000 g/mol (translating to a pore diameter of d_{pore} = 1948 Å). Although the point of complete size-exclusion cannot be identified exactly, elution volumes of the 2,000,000 g/mol and 4,000,000 g/mol polystyrene standards are already slightly higher than expected from the linear fit to the data of intermediate-sized polystyrenes indicating the onset of size-exclusion from the interparticle pore space. Thus, the coil diameter of the 2,000,000 g/mol polystyrene standard (d_{pore} = 1295 Å) represents a more reliable pore diameter of the Nucleosil 1000-5 material.

3.5 Conclusions

Interparticle void volumes (V_{inter}) and porosities (ε_{inter}) of particle-packed, 75 µm i.d. fused-silica capillaries have been determined by careful adjustment for complete intraparticle DONNAN exclusion of a small, unretained, co-ionic tracer (nitrate ions). Electrostatic exclusion provides a theoretically clear, physically sharp definition of the boundary between (charge-selective) mesopore space and (charge-nonselective) macropore space in typical hierarchically structured porous media like packed beds and monoliths (Figure 3.1).

The operational domain of this approach has been studied for bare-silica, reversed-phase, and strong cation-exchange materials with different particle sizes and intraparticle pore sizes. This allowed realizing a wide range of conditions under which this simple approach could be tested by analysing – in combination with the mobile phase ionic strength (Tris-HCl buffer) – the intraparticle EDL overlap and co-ion exclusion (Figure 3.2) in dependence of the intraparticle pore size (Figure 3.6) and the surface charge density of the particles (Figure 3.5). For all investigated surface chemistries the intraparticle DONNAN exclusion approach resulted in values of ε_{inter} that agreed well with those obtained independently by ISEC. Limitations to the use of DONNAN exclusion (electrostatic exclusion) and ISEC (mechanical exclusion) arise as either type of exclusion becomes noticeable also in the cusp regions between the particles (Figure 3.4), or as the intraparticle pores are so large that complete electrostatic and size-exclusion are difficult to realise (Figure 3.6).

Because mesoporous packing materials are common in HPLC and a sufficient surface charge density even exists on typical reversed-phase particles (Figure 3.4) DONNAN exlusion for the determination of ε_{inter} presents a most simple, fast, and reliable approach, with convenient mobile phases and detection. It thereby offers advantages compared to ISEC and it also shows that the total pore blocking of reversed-phase packings using a hydrophobic solvent [15] is redundant in most cases, particularly because CABOOTER *et al.* [15] recommended the use of an inorganic salt like $NaNO_3$ or KI anyway as tracer for the determination of ε_{inter} after pore blocking. The results of this study confirm that the long-known “electrostatic pore blocking” [1] (using just the inorganic salt) is far easier, faster, and not limited by the surface chemistry.

References

[1] C.A. Rimmer, C.R. Simmons, J.G. Dorsey, J. Chromatogr. A 965 (2002) 219-232.

[2] F. Gritti, Y. Kazakevich, G. Guiochon, J. Chromatogr. A 1161 (2007) 157-169.

[3] H. Guan, G. Guiochon, J. Chromatogr. A 731 (1996) 27-40.

[4] A. Alhedai, D.E. Martire, R.P.W. Scott, Analyst 114 (1989) 869.

[5] A. Felinger, M. Kele, G. Guiochon, J. Chromatogr. A 913 (2001) 23-48.

[6] G. Guiochon, M. Sarker, J. Chromatogr. A 704 (1995) 247-268.

[7] J.-H. Koh, B.S. Broyles, H. Guan-Sajonz, M. Z.-C. Hu, G. Guiochon, J. Chromatogr. A 813 (1998) 223-238.

[8] S. Ehlert, T. Rösler, U. Tallarek, J. Sep. Sci. 31 (2008) 1719-1728.

[9] S. Ehlert, K. Kraiczek, J.-A. Mora, M. Dittmann, G.P. Rozing, U. Tallarek, Anal. Chem. 80 (2008) 5945-5950.

[10] F.A.L. Dullien, Porous Media – Fluid Transport and Pore Structure, Academic Press, San Diego, CA, 1991.

[11] H. Rumpf, A.R. Gupte, Chem.-Ing.-Tech. 43 (1971) 367-375.

[12] I. Halász, K. Martin, Angew. Chem. Int. Ed. 17 (1978) 901-908.

[13] W.W. Yau, J.J. Kirkland, D.D. Bly, Modern Size-Exclusion Liquid Chromatography, John Wiley & Sons, New York, 1979.

[14] F. Gritti, G. Guiochon, J. Chromatogr. A 1136 (2006) 192-201.

[15] D. Cabooter, F. Lynen, P. Sandra, G. Desmet, J. Chromatogr. A 1157 (2007) 131-141.

[16] F. Helfferich, Ion Exchange, McGraw-Hill, New York, 1962.

[17] I. Nischang, G. Chen, U. Tallarek, J. Chromatogr. A 1109 (2006) 32-50.

[18] A. Höltzel, U. Tallarek, J. Sep. Sci. 30 (2007) 1398-1419.

[19] G.E. Berendsen, P.J. Schoenmakers, L. de Galan, G. Vigh, Z. Varga-Puchony, J. Inczédy, J. Liq. Chromatogr. Rel. Technol. 3 (1980) 1669-1686.

[20] M.J.M. Wells, C.R. Clark, Anal. Chem. 53 (1981) 1341-1345.

[21] H. Engelhardt, H. Müller, B. Dreyer, Chromatographia 19 (1984) 240-245.

[22] M. Shibukawa, N. Ohta, Chromatographia 25 (1988) 288-294.

[23] L.G. Daignault, D.C. Jackman, D.P. Rillema, J. Chromatogr. 462 (1989) 71-84.

[24] F.C. Leinweber, M. Pfafferodt, A. Seidel-Morgenstern, U. Tallarek, Anal. Chem. 77 (2005) 5839-5850.

[25] T.S. Sørensen (Ed.), Surface Chemistry and Electrochemistry of Membranes, Marcel Dekker, New York, 1999.

[26] H. Strathmann, Ion Exchange Membrane Separation Processes, Elsevier, Amsterdam, The Netherlands, 2004.

[27] S.M. Melnikov, A. Höltzel, A. Seidel-Morgenstern, U. Tallarek, J. Phys. Chem. C 113 (2009) 9230-9238.

[28] R.F. Probstein, Physicochemical Hydrodynamics, Wiley, New York, 1994.

[29] P.J. Kemery, J.K. Steehler, P.W. Bohn, Langmuir 14 (1998) 2884-2889.

[30] T.C. Kuo, L.A. Sloan, J.V. Sweedler, P.W. Bohn, Langmuir 17 (2001) 6298-6303.

[31] J.R. Ku, P. Stroeve, Langmuir 20 (2004) 2030-2032.

[32] D. Stein, M. Kruithof, C. Dekker, Phys. Rev. Lett. 93 (2004) 035901.

[33] R. Schmuhl, K. Keizer, A. van den Berg, J.E. ten Elshof, D.H.A. Blank, J. Colloid Interface Sci. 273 (2004) 331-338.

[34] A. Plecis, R.B. Schoch, P. Renaud, Nano Lett. 5 (2005) 1147-1155.

[35] G. Guiochon, S. Golshan-Shirazi, A.M. Katti, Fundamentals of Preparative and Nonlinear Chromatography, Academic Press, Boston, MA, 1994.

[36] N.S. Pujar, A.L. Zydney, J. Chromatogr. A 796 (1998) 229-238.

[37] D.B. Burns, A.L. Zydney, AIChE J. 47 (2001) 1101-1114.

[38] D. Getáz, G. Ströhlein, M. Morbidelli, J. Chromatogr. A 1216 (2009) 933-940.

[39] F.G. Donnan, Z. Elektrochem. 17 (1911) 572-581.

[40] F.G. Donnan, E.A. Guggenheim, Z. Phys. Chem. 162 (1932) 346-360.

[41] J. Ståhlberg, J. Chromatogr. A 855 (1999) 3-55.

[42] G. Chen, M. Pačes, M. Marek, Y. Zhang, A. Seidel-Morgenstern, U. Tallarek, Chem. Eng. Technol. 27 (2004) 417-428.

[43] C. Moreau, G. Douhéret, J. Chem. Thermodyn. 8 (1976) 403-410.

[44] E.F. Casassa, J. Phys. Chem. 75 (1971) 3929-3939.

[45] F. Gritti, A. Cavazzini, N. Marchetti, G. Guiochon, J. Chromatogr. A 1157 (2007) 289-303.

[46] S. Torquato, Phys. Rev. Lett. 74 (1995) 2156-2159.

[47] J.H. Knox, H.J. Ritchie, J. Chromotagr. A 387 (1987) 65-84.

[48] A. de Klerk, AIChE J. 49 (2003) 2022-2029.

[49] C. Song, P. Wang, H.A. Makse, Nature 453 (2008) 629-632.

[50] A.V. Anikeenko, N.N. Medvedev, Phys. Rev. E 77 (2008) 031101.

[51] F. Gritti, G. Guiochon, J. Chromatogr. A 1166 (2007) 30-46.

Chapter I – Part B

Fast, accurate, and convenient analysis of bed densities for columns packed with fine reversed-phase particles

3.6 Introduction

For particulate fixed beds the accurate determination of the interparticle void volume (or interstitial volume, V_{inter}) and the interparticle (or external) porosity $\varepsilon_{inter} = V_{inter}/V_{column}$, which relates the interparticle void to the total column volume, is of great importance. ε_{inter} is directly related to the bed density (column volume fraction occupied by the particles) $\rho_{bed} = 1 - \varepsilon_{inter}$, and as such an indispensable parameter for the optimisation of packing conditions and dynamic bed consolidation [1-3]. But ε_{inter} is also an important indicator for the quality and performance of a packed-bed separation column: the contribution to band broadening from hydrodynamic dispersion is correlated to ε_{inter} [4,5], and the column's hydraulic permeability also depends strongly on ε_{inter} [6]. The hydraulic permeability of separation columns is one of the discussed points in the on-going debate over the relative merits of fully porous sub-2 µm particles and the slightly larger core-shell particles [7-9]. Core-shell columns can provide speed and efficiency similar to columns packed with sub-2 µm particles but with smaller backpressure [7].

An established method for determination of ε_{inter} is based on inverse size-exclusion chromatography using as samples a series of polymer standards with increasing molecular weight [10]. Assuming that all polymeric chains form a random coil of invariant size and shape during chromatographic analysis, the average molecular weights of the polymers are correlated with the average diameter of the pores from which they are size-excluded. Plots of the polymers' elution volumes *versus* the cubic root of their molecular weight yield a pore size distribution that denotes the maximal interparticle void volume [11]. Employing the elution volumes of only size-excluded polymers the elution volume of a fictitious point mass analyte can be determined *via* linear regression. The so-derived values for the interparticle void volume are not falsified by the actual molecular size of the excluded polymer standards. The drawbacks of this method are the assumption about the formation and hydrodynamic stability of the polymeric coils, the necessity of using aggressive organic solvents like dichloromethane or tetrahydrofurane for chromatographic analysis, and the fact that ε_{inter} is

determined by linear regression executed on a limited data set [10] (and references therein). As an alternative, CABOOTER *et al.* [12] and later LIEKENS *et al.* [13] proposed measuring the elution volume of a small, unretained tracer after filling the intraparticle pores with a hydrophobic solvent. This method requires careful and time-consuming pretreatment of the separation column including the equilibration of the silica-based packing material with a highly apolar organic solvent. This procedure limits the applicability of the method to stationary phase materials with sufficiently hydrophobic character, *i.e.*, to reversed-phase HPLC columns due to wetting problems of polar phases with highly apolar solvents.

We recently developed a method based on DONNAN (electrostatic) exclusion of a small, unretained inorganic ion from the intraparticle pore space to determine V_{inter} and ε_{inter} of particle-packed HPLC columns [14]. Our approach is faster, far simpler, and at least as accurate than the established methods. Silica-based particles contain residual silanol groups, whose pH-dependent dissociation may be the cause for a surface charge. Some silanol groups remain on the particles' surfaces after hydrophobic modification and endcapping. As a consequence, even reversed-phase particles possess enough residual silanol groups to develop a surface charge and resulting electrical double layer (EDL) when in contact with a suitable electrolyte solution. Although hierarchically structured porous media like packed beds (interparticle macropore space, intraparticle mesopore space) are macroscopically charge-nonselective, ion-permselectivity exists in the discrete mesoporous domains (*i.e.*, inside the particles), when the EDL thickness is comparable with the mesopore size [15]. EDL overlap inside the mesopores of the packed bed results in counterion enrichment and co-ion exclusion with respect to the bulk solution [16]. The ionic concentration difference at electrochemical equilibrium between the intraparticle pores and the interparticle void space is alternatively expressed in terms of the DONNAN potential, an electrical phase-boundary potential, which balances the tendency of ions to level out the concentration (chemical potential) difference between interconnected bulk and ion-permselective domains [17].

The actual intensity of intraparticle EDL overlap is governed by the surface charge density inside the mesopores and by r_{meso}/λ_D, the ratio of the intraparticle mesopore radius and the DEBYE screening length λ_D that characterizes the EDL thickness. Surface charge density and r_{meso} are properties of the packing material, whereas λ_D depends on the mobile phase, namely its solvent composition and ionic strength. Variation of the mobile phase ionic strength manipulates the ratio r_{meso}/λ_D and thus, the accessible void volume for a small, nonretained, co-ionic tracer: from complete permeation of the packing's void volume ($\varepsilon_{tracer} = \varepsilon_{total}$) for $r_{meso} >> \lambda_D$ to complete exclusion of the tracer from the intraparticle pores ($\varepsilon_{tracer} =$

ε_{inter}) at $r_{pore} \approx \lambda_D$, over a broad intermediate range, where the tracer has partial access to the intraparticle pore space [14].

In our previous study [14] we used in-house packed capillary columns and determined ε_{inter} for a variety of packing materials, analyzing the influence of r_{meso} and the surface charge density on the onset of DONNAN exclusion. In this work we extend the DONNAN exclusion method to determine the interparticle porosity ε_{inter} of commercially available analytical HPLC columns packed with fine reversed-phase particles of different nominal sizes (1.8, 2.7, 3.5, and 5 µm) and construction (fully porous and core-shell).

3.7 Experimental section

3.7.1 Chemicals and materials

HPLC grade solvents acetonitrile and methanol and Tris(hydroxymethyl)aminomethane (Tris) were purchased from Sigma-Aldrich (Taufkirchen, Germany). Potassium nitrate and sodium chloride were obtained from Carl Roth (Karlsruhe, Germany) and hydrochloric acid and HPLC grade dichloromethane from VWR International (Briare, France). HPLC grade water was prepared with a Milli-Q gradient water purification system (Millipore, Bedford, MA). Analytical HPLC columns ZORBAX Eclipse Plus C_{18} (4.6 mm i.d. × 100 mm length) packed with 1.8 µm, 3.5 µm, and 5 µm particles with 95 Å nominal pore diameter and ZORBAX Poroshell EC-C_{18} (3.0 mm i.d. × 50 mm length) packed with 2.7 µm particles with 120 Å nominal pore diameter came from Agilent Technologies (Waldbronn, Germany). The Poroshell particles have a solid core of 1.7 µm diameter and a porous shell of 0.5 µm thickness.

3.7.2 Hardware configuration

All data were acquired with an Agilent 1100 liquid chromatograph (Agilent Technologies, Waldbronn, Germany) consisting of a degasser, a standard autosampler, a binary pump, and a variable-wavelength UV-detector with a standard flow cell (14 µL, 10 mm path length). An interfacing capillary (0.17 mm i.d. × 400 mm length) connects the binary pump with the injection valve, a standard needle-seat capillary tube (0.17 mm i.d., 2.3 µL), and an injection loop (100 µL). The separation column was connected to the injection valve and the inlet of the flow cell with stainless-steel tubing (0.12 mm i.d. × 105 mm length). The system is controlled by the Agilent ChemStation software. All experiments were carried out at 298 ± 1

K under isocratic elution conditions at a volumetric flow rate of 0.5 mL/min and detection at 210 nm. Ten successive injections were made and the results averaged.

3.7.3 Porosity measurements

Interparticle void volumes and porosities (V_{inter} and ε_{inter}) of the analytical columns were determined by DONNAN exclusion of nitrate ions, using a mobile phase of Tris-HCl (pH 8.1) in acetonitrile/water 80/20 (v/v). The buffer concentration in the mobile phase was varied from 0.01 to 60 mM. The injection volume was 1 µL for all experiments. At low buffer concentrations (0.01 – 0.1 mM), samples of KNO_3 dissolved in the unbuffered mobile phase were injected, for which the KNO_3 concentration was matched to the buffer concentration of the mobile phase to prevent disturbances of the intraparticle DONNAN exclusion due to a concentration mismatch of the injected sample and the running eluent. For buffer concentrations > 0.1 mM in the mobile phase, samples consisted of 0.04 mM KNO_3 dissolved in the buffered mobile phase. The elution times of the analyte were multiplied by the flow rate and corrected for the overall dead volume to obtain accurate elution volumes. The dead volume (54.6 µL) of the chromatographic system was determined by removing the column and connecting the stainless-steel tubings with a stainless-steel zero-volume union. The elution volumes at low buffer concentrations (*cf.* plateau regions in Figures 3.7 and 3.8) were divided by the geometrical empty-column volume to yield ε_{inter}.

Total bed porosities ε_{total} were determined by the minor-disturbance method, where a sample of the mobile phase is injected to produce a minor-disturbance peak in the chromatogram. The resulting elution volumes were divided by the geometrical empty-column volume to yield ε_{total}. Experiments were carried out with three different mobile phases: acetonitrile/water 80/20 (v/v), acetonitrile, and dichloromethane. The reproducibility for ten successive measurements was very good with a standard deviation range of σ = 0.001–0.004 for the elution times of all experiments. Porosities are listed in Table 3.3. The maximal deviation for ε_{inter} determined from the plateau region at acetonitrile/water 80/20 (v/v) is $\Delta\varepsilon_{inter,max}$ = 0.003. Variations of total porosities are equal ($\Delta\varepsilon_{total,max}$ = 0.003) for acetonitrile-containing eluents and slightly higher ($\Delta\varepsilon_{total,max}$ = 0.006) for dichloromethane-containing mobile phases. The latter is explained by the high sensitivity of dichloromethane towards temperature variations.

Table 3.3.

Experimental porosities determined for analytical HPLC columns.

Mobile phase	Porosity	Column type			
		Poroshell EC-C_{18} (2.7 µm)	Eclipse Plus C_{18} (1.8 µm)	Eclipse Plus C_{18} (3.5 µm)	Eclipse Plus C_{18} (5 µm)
Acetonitrile/water 80/20 (v/v)	ε_{total} [a]	0.489 ± 0.0011	0.494 ± 0.0005	0.484 ± 0.0011	0.491 ± 0.0012
	$\varepsilon_{inter,nitrate}$	0.373 ± 0.0014	0.377 ± 0.0017	0.373 ± 0.0012	0.378 ± 0.0009
	ε_{intra} [b]	–	0.188	0.177	0.182
	$\varepsilon_{intra,shell}$ [c]	0.247		–	
Dichloromethane	ε_{total} [a]	0.563 ± 0.0014	0.544 ± 0.0012	0.553 ± 0.0010	0.546 ± 0.0013
	ε_{intra} [b]	–	0.269	0.287	0.271
	$\varepsilon_{intra,shell}$ [c]	0.399		–	
Acetonitrile	ε_{total} [a]	0.549 ± 0.0007	0.539 ± 0.0006	0.527 ± 0.0002	0.539 ± 0.0005
	ε_{intra} [b]	–	0.260	0.246	0.259
	$\varepsilon_{intra,shell}$ [c]	0.374		–	

[a] Experimentally determined by the minor-disturbance method (eluent injection).

[b] Values of ε_{intra} were calculated from the experimentally determined values for ε_{total} (eluent injection) and ε_{inter} (Donnan exclusion of nitrate ions) according to $\varepsilon_{total} = \varepsilon_{inter} + (1 - \varepsilon_{inter})\varepsilon_{intra}$.

[c] Calculated with Equation (3.7).

3.8 Results and discussion

Figure 3.7 shows the curve for electrostatic exclusion of nitrate ions in a mobile phase of Tris-HCl (pH 8.1) in acetonitrile/water 80/20 (v/v) acquired for a 1.8 µm ZORBAX Eclipse Plus C_{18} column. Complete DONNAN exclusion of nitrate ions is indicated by the plateau region at low buffer concentrations (≤ 0.04 mM). The plateau elution volume is assumed to equal the interparticle void volume V_{inter}, from which the interparticle porosity of the column is then calculated as $\varepsilon_{inter} = V_{inter}/V_{column}$. At buffer concentrations > 0.04 mM, the nitrate ions begin to penetrate the intraparticle pore space. The shape of the elution curve mimics the functional dependence of the DEBYE screening length λ_D from the mobile phase ionic strength:

$$\lambda_D = \left(\frac{\varepsilon_0 \varepsilon_r RT}{F^2 \sum z_i^2 c_{i,\infty}} \right)^{\frac{1}{2}}, \qquad (3.4)$$

where ε_0 and ε_r are the vacuum permittivity and the relative permittivity of the bulk solution, respectively, R is the gas constant, T the absolute temperature, and F the FARADAY constant, z_i is the valency of ionic species i and $c_{i,\infty}$ its concentration in the electroneutral bulk solution [18]. The relative permittivity of the mobile phase was taken from MOREAU and DOUHÉRET as $\varepsilon_r = 41.42$ [19]. λ_D decreases with the buffer concentration: from 700 Å at 0.01 mM *via* 222 Å at 0.1 mM, where tracer ions begin to penetrate the intraparticle pore volume, to 22 Å at 10 mM. Between 0.1 mM and 10 mM, the elution volumes are increasing functions of the buffer concentration, before the curve flattens out at buffer concentrations ≥ 20 mM. At high buffer concentrations λ_D decreases only slowly with the mobile phase ionic strength (*cf.* Equation (3.4)), which results in the flattening of the electrostatic exclusion curve.

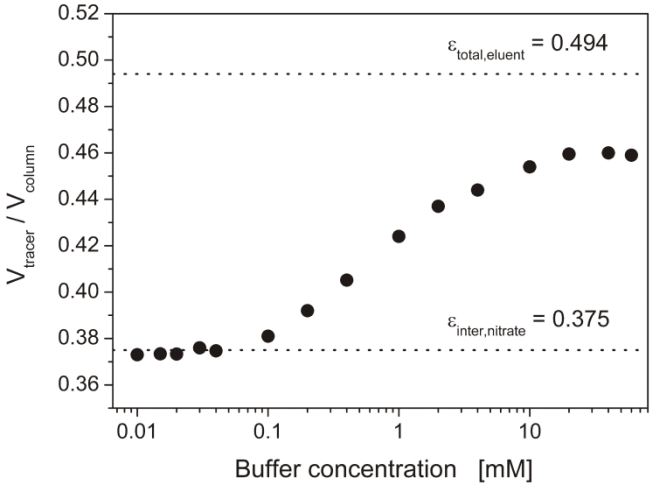

Figure 3.7: Electrostatic exclusion of nitrate ions *vs.* buffer concentration in the mobile phase. Tris-HCl (pH 8.1) in acetonitrile/water 80/20 (v/v). Column: 1.8 µm ZORBAX Eclipse Plus C_{18}. Error bars are of similar size as symbols.

Contrary to the previous experience in Figure 3.4 with packings of fine (3 µm) particles, for which a continuous decrease of nitrate elution volumes even at low buffer concentrations were observed due to interparticle EDL overlap, the electrostatic exclusion curve for the 1.8 µm ZORBAX Eclipse Plus C_{18} column displays a clearly defined plateau region at low buffer concentrations, from which the column's interparticle porosity is easily determined as $\varepsilon_{inter} = 0.375$ (Figure 3.7). The explanation for this diverging behaviour lies in the surface chemistry of the particles. The previously used non-endcapped C_8-modified Hypersil MOS particles possess a larger density of residual silanol groups at the silica surface

and therefore higher surface potential [14]. The doubly-endcapped C_{18}-modified Eclipse Plus material is highly hydrophobic, with a low amount of residual silanol groups. The associated surface potential is lower compared to non-endcapped reversed-phase, bare-silica, or ion-exchange particles. The lower surface charge density decreases the electrostatic field affecting the ions in the bulk solution. Due to the resulting weaker interaction between EDL's from neighboured surfaces significant EDL overlap occurs only in the intraparticle, but not in the interparticle pore space. Thus, the DONNAN exclusion method for determination of V_{inter} and ε_{inter} is applicable to modern fine-particle packings (sub-2 µm particles), if the particles' surface potential is sufficiently reduced through modification to prevent interparticle EDL overlap. The total porosity of the column was determined by eluent injection with a mobile phase of acetonitrile/water 80/20 (v/v) as $\varepsilon_{total} = 0.494$. This value is higher than the porosity-value indicated by the flattened DONNAN exclusion curve at buffer concentrations of 20 – 60 mM (Figure 3.7). Eluent injection is known as a reliable method for determination of ε_{total} and yields values that deviate only slightly from those determined with other established procedures [20-23]. This points to the conclusion that buffer concentrations of 20 – 60 mM are not sufficient to reduce λ_D enough to permit the tracer full access to the intraparticle pore space. At a buffer concentration of 60 mM, the DEBYE screening length ($\lambda_D \approx 9$ Å) is about one fifth of the particles' nominal pore radius ($r_{meso} = 47.5$ Å), so nitrate ions still experience noticeable exclusion from the intraparticle pore space. Complete permeation of the pore space by the nitrate ions (resulting in a negligible exclusion volume) would require a DEBYE screening length of $\lambda_D \approx 2$ Å, which corresponds to a buffer concentration of ~ 1 M. This is impractical, due to the limited solubility of Tris-HCl buffer and/or inorganic (indifferent) salts in acetonitrile/water mixtures with a high organic modifier content.

To estimate the remaining exclusion volume for nitrate ions at a buffer concentration of 60 mM, the intraparticle volume V_{intra} was calculated from $V_{intra} = \varepsilon_{intra} V_{column}(1 - \varepsilon_{inter,nitrate})$. Assuming that an individual pore is represented by a cylinder of height h and diameter d_{pore}, the intraparticle void volume V_{intra} is given by the sum of all cylinder volumes:

$$V_{intra} = \sum_{pores} \pi(0.5 d_{pore})^2 h \quad . \tag{3.5}$$

Reduction of the pore diameter d_{pore} by $2\lambda_D$ accounts for the inaccessible part of a cylindrical pore. The exclusion volume $V_{exclusion}$ of the packing is then the difference between V_{intra} and the sum of the volumes of cylindrical pores with a diameter of $d_{pore} - 2\lambda_D$:

$$V_{exclusion} = V_{intra} - \sum_{pores} \pi 0.25(d_{pore} - 2\lambda_{D,60mM})^2 h \quad . \tag{3.6}$$

Although we do not know the number of pores nor the height, we can calculate a fictitious height h by inserting V_{intra} (calculated with the determined ε_{intra} and ε_{inter}), any value for the number of pores (*e.g.*, 1), and d_{pore} given by the manufacturer in Equation (3.5). The same values for the number of pores and h have to be used to solve Equation (3.6). The resulting exclusion volume $V_{exclusion}$ is added to the experimental elution volume of the nitrate ions at 60 mM buffer concentration, the result should equal V_{total} as determined by eluent injection. Indeed, the calculated value of $\varepsilon_{total,nitrate,60mM} = 0.497$ approaches closely the determined value of $\varepsilon_{total} = 0.494$ (Table 3.4).

Table 3.4.

Comparison of experimental and calculated total porosities.

Porosity	**Column type**			
	Poroshell EC-C_{18} (2.7 µm)	Eclipse Plus C_{18} (1.8 µm)	Eclipse Plus C_{18} (3.5 µm)	Eclipse Plus C_{18} (5 µm)
$\varepsilon_{exp,nitrate,60mM}$ [(a)]	0.475 ± 0.0010	0.457 ± 0.0004	0.453 ± 0.0005	0.459 ± 0.0003
$\varepsilon_{total,nitrate,60mM}$ [(b)]	0.505	0.497	0.491	0.498
$\varepsilon_{total,eluent}$ [(c)]	0.489 ± 0.0011	0.494 ± 0.0005	0.484 ± 0.0011	0.491 ± 0.0012

[(a)] Experimentally determined from the exclusion volumes of nitrate ions at 60 mM buffer concentration.

[(b)] The sum of $\varepsilon_{exp,nitrate,60mM}$ and the exclusion volume $V_{exclusion}$ calculated with Equation (3.6).

[(c)] Experimental determined by the minor-disturbance method in acetonitrile/water 80/20 (v/v), *cf.* Table 3.3.

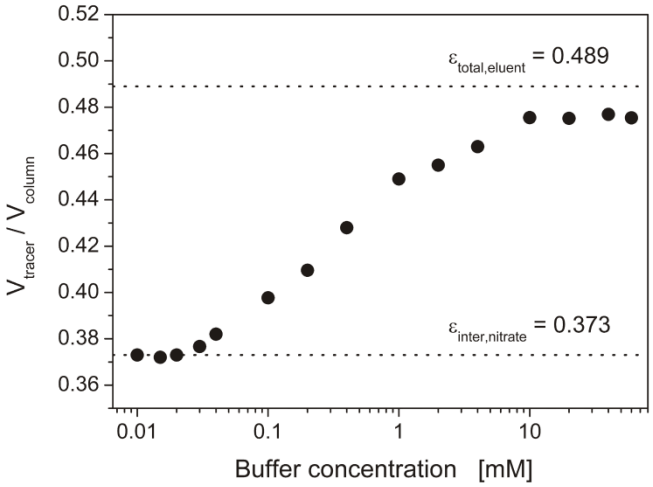

Figure 3.8: Electrostatic exclusion of nitrate ions *vs.* buffer concentration in the mobile phase. Tris-HCl (pH 8.1) in acetonitrile/water 80/20 (v/v). Column: 2.7 µm ZORBAX Poroshell EC-C_{18}. Error bars are of similar size as symbols.

Figure 3.8 shows the DONNAN exclusion curve for the 2.7 µm ZORBAX Poroshell EC-C_{18} column. The curve progression is very similar to that observed for the 1.8 µm Eclipse Plus C_{18} column (Figure 3.7). The plateau region for the nitrate elution volumes is at slightly lower buffer concentrations (≤ 0.02 mM) compared with the 1.8 µm particles, which could result from a smaller EDL overlap inside the intraparticle pores of the Poroshell particles due to the larger mean intraparticle pore radius (r_{meso} = 60 Å compared with r_{meso} = 47.5 Å for the 1.8 µm particles). The curve-flattening limit is approached at a buffer concentration of 10 mM and indicates a porosity below the total porosity of ε_{total} = 0.489 determined by eluent injection (Figure 3.8). The total porosity value calculated from the elution volume at 60 mM buffer concentration and the estimated exclusion volume is $\varepsilon_{total,nitrate,60mM}$ = 0.505 (Table 3.4). Although not as close to the eluent-injection determined value as was the case for the 1.8 µm fully porous particles, the agreement is acceptable (relative error: 3.7%). This deviation might be due to differing pore size distributions between the fully porous and core-shell particles, or originate from deviations of the true mean pore size from the nominal value.

The DONNAN exclusion curves for the 3.5 µm and 5 µm Eclipse Plus C_{18} columns are very similar to Figures 3.7 and 3.8 and therefore not shown. Table 3.3 lists the experimentally determined porosities ε_{inter} and ε_{total} for all investigated columns as well as values for the intraparticle porosities ε_{intra} and shell porosities $\varepsilon_{intra,shell}$ calculated from ε_{inter} and ε_{total} according to $\varepsilon_{total} = \varepsilon_{inter} + (1 - \varepsilon_{inter})\varepsilon_{intra}$ and

$$\varepsilon_{intra,shell} = \frac{\varepsilon_{total} - \varepsilon_{inter}}{(1-\varepsilon_{inter})(1-\rho^3)}\,, \qquad (3.7)$$

where ρ is the ratio of the solid core's to the particle's radius and $(1 - \rho^3)$ gives the volume fraction of the total particle volume occupied by the porous shell (75% for the Poroshell particles) [11].

All columns are densely packed with interparticle porosities around $\varepsilon_{inter} \approx 0.375$. Similar values were found by CABOOTER *et al*. [24] for commercial sub-2 µm columns. Lower packing densities have been reported for columns packed with core-shell particles ($\varepsilon_{inter} = 0.40 - 0.43$), but these columns came from different manufacturers [25,26]. The total porosity of the columns is around $\varepsilon_{total} \approx 0.490$ (Table 3.4), which appears quite low compared to a range of $\varepsilon_{total} = 0.5 - 0.65$ [24-26]. Consequently, the calculated intraparticle porosities are also low ($\varepsilon_{intra} \approx 0.182$). The mobile phase composition influences the determined value of ε_{total} [20, 23] (and references therein), because the accessible column void volume depends on the wetting behaviour of the packing material towards the chosen mobile phase. The bonded alkyl chains of reversed-phase materials may experience different solvation in mixed aqueous-organic than in neat organic-solvent mobile phases [27,28], or the components of a solvent mixture may be differently excluded from part of the column void volume [20]. Therefore we additionally determined ε_{total} in neat acetonitrile and dichloromethane mobile phases (Table 3.3). The obtained values of ε_{total} are larger ($\varepsilon_{total} \approx 0.539$ for acetonitrile and $\varepsilon_{total} \approx 0.552$ for dichloromethane) than those determined in acetonitrile/water 80/20 (v/v) and agree with published data [24,25,27]. Under these circumstances, delineation of ε_{intra} from ε_{inter} and ε_{total} is questionable. ε_{inter} is insensitive towards the chosen mobile phase as the part of the surface on the particles' outer sphere is small compared to the overall surface area. Thus, the interparticle void volumes determined in different solvent compositions using DONNAN exclusion and ISEC agree very well, revealing the accuracy of the DONNAN exclusion method in the determination of bed densities for a variety of packing materials (with different surface chemistry and mean particle as well as mean intraparticle pore size) [14]. On the contrary, the determined values for ε_{total} and ε_{intra} differ from each other depending on chromatographic conditions and wetting behaviour and should rather be linked to a specific mobile phase.

3.9 Conclusions

We determined the interparticle porosities (ε_{inter}) of commercially available analytical columns packed with particles of different sizes (from 5 to 1.8 µm) and construction (fully porous and core-shell) by intraparticle DONNAN exclusion of nitrate ions. The experimental data demonstrate that the method is highly reproducible with a commercial chromatograph, and the small nitrate concentrations inherent to the method were easily detected with a standard detection cell. The DONNAN exclusion method provides a theoretically clear and physically sharp definition of the boundary between charge-selective mesopore space and charge-nonselective macropore space in hierarchically structured porous media like packed beds. A distinct plateau region in the elution curve at low buffer concentrations indicates EDL overlap in the intraparticle mesopores, so that a small, co-ionic tracer is completely excluded from the intraparticle pore space and the elution volume of the tracer equals the interparticle void volume of the fixed bed. The method worked for all investigated stationary phase materials, including the 2.7 µm core-shell and the fully porous sub-2 µm particles. Together with the results in Chapter I – Part A the DONNAN exclusion method has been shown to be a fast, accurate, and convenient procedure for the determination of interparticle porosity for packings, encompassing a variety of stationary-phase chemistries (reversed-phase, bare-silica, and ion-exchange particles), particle constructions (fully porous and core-shell particles), and particle sizes.

At high buffer concentrations in the mobile phase, the elution volumes approach an asymptotic limit that is expected to denote the total column void volume V_{total}. But due to the slow decrease of the EDL thickness over a wide range of ionic strengths a noticeable exclusion from parts of the mesopore volume persists even at high buffer concentrations. Adding the calculated exclusion volume at high buffer concentration (assuming that all pores have cylindrical shape and equal diameter) to the experimental elution volumes demonstrates good agreement between the such-obtained and the total porosities ε_{total} determined by the minor-disturbance method. These results confirm the statement that small ions are not suited for an accurate determination of the column void volume without exact knowledge of the extent of possible electrostatic exclusion from the intraparticle pore space [23] (and references therein).

References

[1] A. Alhedai, D.E. Martire, R.P.W. Scott, Analyst 114 (1989) 869-875.

[2] A. Felinger, M. Kele, G. Guiochon, J. Chromatogr. A 913 (2001) 23-48.

[3] S. Ehlert, T. Rösler, U. Tallarek, J. Sep. Sci. 31 (2008) 1719-1728.

[4] S. Jung, A. Höltzel, S. Ehlert, J.-A. Mora, K. Kraizcek, M. Dittmann, G.P. Rozing, U. Tallarek, Anal. Chem. 81 (2009) 10193-10200.

[5] S. Khirevich, A. Höltzel, D. Hlushkou, U. Tallarek, Anal. Chem. 79 (2007) 9340-9349.

[6] F.A.L. Dullien, Porous Media – Fluid Transport and Pore Structure, Academic Press, San Diego, 1991.

[7] D. Guillarme, J. Ruta, S. Rudaz, J.-L. Veuthey, Anal. Bioanal. Chem. 397 (2010) 1069-1082.

[8] I. Kiss, I. Bacskay, F. Kilár, A. Felinger, Anal. Bioanal. Chem. 397 (2010) 1307-1314.

[9] M.M. Fallas, U.D. Neue, M.R. Hadley, D.V. McCalley, J. Chromatogr. A 1217 (2010) 276-284.

[10] W.W. Yau, J.J. Kirkland, D.D. Bly, Modern Size-Exclusion Liquid Chromatography, John Wiley & Sons, New York, 1979.

[11] F. Gritti, A. Cavazzini, N. Marchetti, G. Guiochon, G., J. Chromatogr. A 1157 (2007) 289-303.

[12] D. Cabooter, F. Lynen, P. Sandra, G. Desmet, J. Chromatogr. A 1157 (2007) 131-141.

[13] A. Liekens, D. Cabooter, J. Denayer, G. Desmet, J. Chromatogr. A 1217 (2010) 6754-6761.

[14] S. Jung, S. Ehlert, M. Pattky, U. Tallarek, J. Chromatogr. A 1217 (2010) 696-704.

[15] I. Nischang, G. Chen, U. Tallarek, J. Chromatogr. A 1109 (2006) 32-50.

[16] I. Nischang, U. Reichl, A. Seidel-Morgenstern, U. Tallarek, Langmuir 23 (2007) 9271-9281.

[17] J. Ståhlberg, J. Chromatogr. A 855 (1999) 3-55.

[18] R.F. Probstein, Physicochemical Hydrodynamics, Wiley, New York, 1994.

[19] C. Moreau, G. Douhéret, J. Chem. Thermodyn. 8 (1976) 403-410.

[20] F. Gritti, Y. Kazakevich, G. Guiochon, J. Chromatogr. A 1161 (2007) 157-169.

[21] Y. Kazakevich, H.M. McNair, J. Chromatogr. Sci. 31 (1993) 317-322.

[22] I. Rustamov, T. Farcas, F. Ahmed, F. Chan, R. LoBrutto, H.M. McNair, Y.V. Kazakevich, J. Chromatogr. A 913 (2001) 49-63.

[23] C.A. Rimmer, C.R. Simmons, J.G. Dorsey, J. Chromatogr. A 965 (2002) 219-232.

[24] D. Cabooter, J. Billen, H. Terryn, F. Lynen, P. Sandra, G. Desmet, J. Chromatogr. A 1178 (2008) 108-117.

[25] F. Gritti, I. Leonardis, J. Abia, G. Guiochon, J. Chromatogr. A 1217 (2010) 3819-3843.

[26] J.S. Baker, J.C. Vinci, A.D. Moore, L.A. Colón, J. Sep. Sci. 33 (2010) 2547-2557.

[27] J. Urban, P. Jandera, Z. Kučerová, M.A. van Straten, H.A. Claessens, J. Chromatogr. A 1167 (2007) 63-75.

[28] B. Buszewski, S. Bocian, R. Zera, Adsorption 16 (2010) 437-445.

Chapter II

Impact of conduit geometry on the performance of typical particulate microchip packings

4.1 Introduction

Recent advances in on-chip liquid chromatography include the development of fully integrated systems, which contain all fluidic components such as pumps, sample injectors, and separation columns on-chip [1-3], as well as the fabrication of high-pressure rating microfluidic devices [4,5]. Open tubulars [6-8] ordered pillar arrays [9,10] polymer and silica monoliths [11-18] as well as slurry-packed particulate beds [19-22] have all been used for chromatographic separation on microchips, but up to now rarely with a focus on separation efficiency. The use of particulate packings offers the advantage over microfabricated support structures that all issues regarding the wide variety of desired surface chemistries for tailoring separations can be addressed externally (off-chip) on bulk stationary phase material, as done in HPLC practice. However, slurry-packing of microchips is often carried out manually with a syringe or with pumps at low to moderate pressure, as most microchip channels, fittings, and packaging are sensitive against high pressure. But if particulate microchip packings are to achieve separation efficiencies comparable with (or even better than) those in nano-HPLC, optimised packing conditions including high packing pressures and the application of ultrasound are essential [23].

Microchip packings also deviate from the packed fused-silica capillaries of nano-HPLC by their noncylindrical conduit geometry, whose influence on hydrodynamic dispersion and thus separation efficiency has to be considered. The exact cross-sectional geometry of a microchannel depends on the methods and materials used for its fabrication. Separation channels on LC-microchips have featured semicircular, quadratic, rectangular, trapezoidal, and elliptical cross-sections, often with deviations from regular geometry. A systematic numerical simulations study of random sphere packings in conduits with circular, quadratic, rectangular, and semicircular cross-section revealed increased axial dispersion with increasing deviation from cylindrical conduit symmetry [24]. Additionally, the corner regions of noncylindrical conduits are more difficult to pack densely. In trapezoidal conduits, a large

ratio between the two base lengths and the deviation from orthogonality of the base corners increase dispersion [25]. The effects that lead to increased dispersion depend strongly on the packing density. In densely packed beds the effects of the specific conduit geometry become small and band broadening approaches that of comparable cylindrical packings [24].

A third aspect that influences packing structure and thus separation efficiency is the low particle-aspect (conduit-to-particle size) ratio of particulate microchip packings [26]. This aspect is also relevant in nano-HPLC as the reduction of channel or capillary dimensions with respect to conventional HPLC columns is not accompanied by a corresponding reduction in mean particle size [27-30]. The geometrical wall effect results from the inability of the particles to form a close packing against the conduit walls. The particle layer closest to the conduit wall is highly ordered and differs significantly from subsequent layers, because the interstitial space between wall and first particle layer cannot be partially occupied by other particles. In subsequent layers towards the centre the order decreases until the arrangement of the particles becomes random [31]. At low particle-aspect ratios, the highly ordered wall region – which can cover a distance of 4-5 particle diameters for spherical monodisperse particles – constitutes a large fraction of the conduit volume, and the mean interparticle porosity of the packing increases [26,30,31].

While the merits of numerical simulation methods are unquestionably the systematic study of isolated parameters like conduit geometry, conduit dimensions, particle-aspect ratio, or packing density, with high precision and detail, experimental studies of microchip packings are a necessary complement as they represent real-life conditions and applications [32]. For example, the decision to use a certain separation channel geometry on a microchip is not only a design option informed by considerations about hydrodynamic dispersion, but also a fabrication issue as certain geometries are more or less elaborate or even impossible to realise with a chosen method.

The current work is an experimental study of axial dispersion in particulate microchip packings contained in channels of different cross-sectional geometry. Polyimide HPLC/UV-microchips were used that integrate sample injection, separation, and UV detection (Figure 4.1). Microchips containing separation channels with trapezoidal, quadratic, or Gaussian cross-section were fabricated by direct laser ablation and lamination of multiple polyimide layers (Figure 4.2). Due to the Gaussian-shaped energy profile of the laser, Gaussian cross-sections are straightforward to realize with this fabrication method, while quadratic cross-sections require the most effort. The investigated microchips represent typical real-life examples where deviations from regular cross-sectional geometry and small variations in

channel dimensions are the inevitable result of the fabrication process. Microchips were slurry-packed with spherical porous C8-modified silica particles of either 3 or 5 µm nominal particle size. Both packing materials have the same surface chemistry as well as very similar particle size distributions, mean intraparticle pore sizes and porosities [26], enabling us to study the influence of the particle-aspect ratio on the performance of the microchip packings.

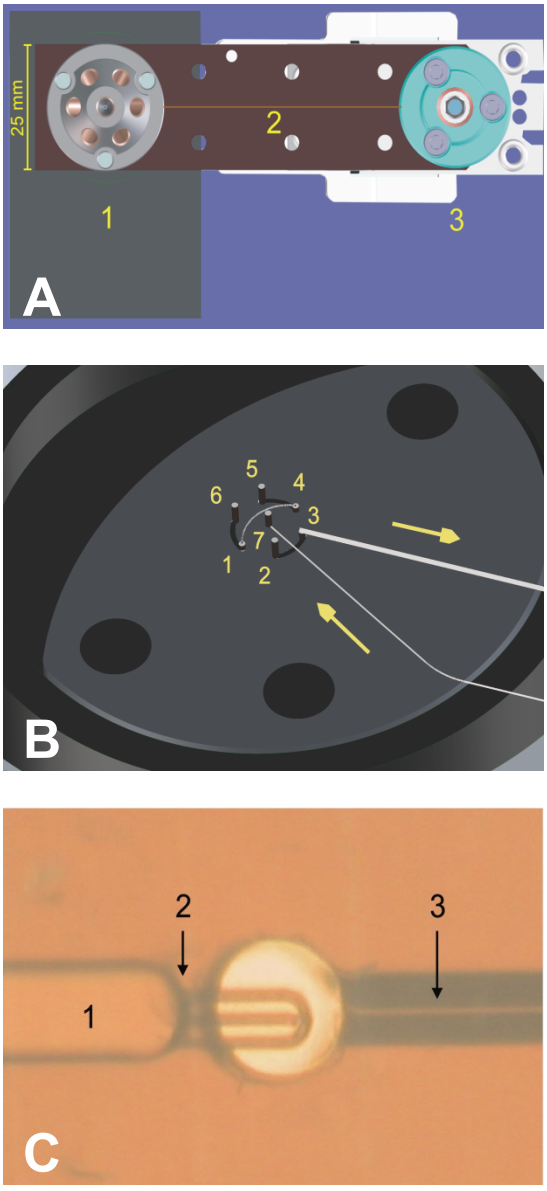

Figure 4.1. **(A) Microchip sandwiched between the stator and rotor of a Rheodyne injection valve (1), providing dead-volume-free injection onto the separation channel (2) and on-chip UV detection with a special holder (3). (B) The injection unit of the microchips consists of seven ports with an internal sample loop between ports 1 and 4. The sample is injected onto the separation channel at port 3 and redirected after passing the detection cell *via* port 7 to an external flow sensor. (C) A micromachined outlet frit (2) is used to retain the packing material at the end of the separation channel (1). A narrow channel (3) provides the connection between outlet frit and detection cell.**

4.2 Experimental section

4.2.1 Chemicals and materials

HPLC grade organic solvents (acetonitrile, methylene chloride, methanol, and acetone) and analytes (uracil, benzene, ethylbenzene, n-propylbenzene, n-butylbenzene, and n-pentylbenzene) were purchased from Sigma-Aldrich Chemie GmbH (Taufkirchen, Germany). HPLC grade water was prepared using a Milli-Q gradient water purification system (Millipore, Bedford, MA, USA). Polystyrene standard (100,000 g/mol) was purchased from Fluka Chemie GmbH (Buchs, Switzerland). Chromatographic packing materials Hypersil MOS (monomeric octyl silica, C8) of 3 and 5 μm nominal particle diameter were bought from Thermo Fisher Scientific Inc. (Waltham, MA, USA). Both packing materials have a mean intraparticle pore diameter of 126-142 Å, a surface area of 165-180 m^2/g, and an intraparticle porosity of $\varepsilon_{intra} \sim 0.4$ [26].

4.2.2 Microchip fabrication

The fabrication process consists of UV laser ablation of polyimide foils to form microfluidic channels and ports, followed by a cleaning step to remove residues from laser ablation; the polyimide films are then precisely aligned before vacuum lamination under heat and pressure [19]. Two types of polyimide foils are used in the fabrication: (i) 50 μm thick bonding foils, which have a co-extruded thermoplastic polyimide adhesive layer on each side that bonds to polyimide when heat and pressure are applied, and (ii) 75 or 125 μm thick foils without adhesive layer (non-adhesive foils), which confine the microchips at the exterior. Different cross-sectional symmetries for the separation channels were realised by varying the thickness and number of the polyimide layers and the parameters of direct laser ablation. Microchips with trapezoidal separation channel consist of three polyimide layers: a central bonding layer (50 μm) out of which the channel features were laser-cut, and non-adhesive top and bottom layers of 125 μm thickness each. Microchips with quadratic and Gaussian channel cross-sections are based on a five-layer design, in which a central (non-adhesive) foil is enveloped by two bonding inner foils (50 μm each) and two non-adhesive outer foils (125 μm each) that prevent the microchips from sticking to the lamination device. Microchips with a quadratic separation channel have a central layer of 75 μm thickness out of which the channel features were laser-cut. For microchips with a Gaussian separation channel, the spatial energy distribution of the laser was used to cut a Gaussian profile into the central layer of 125 μm thickness. The separation channels on each microchip have a total length of 73 mm and a

micromachined outlet frit at the end to retain the packing. Microchips showing signs of channel deformation, polyimide damage, or other aberrations (*e.g.*, large channel volumes indicating leakage) were discarded.

For sample injection the microchips were attached to a face-seal rotary valve (Figure 4.1A) with a 0.7 nL internal loop between ports 1 and 4 (Figure 4.1B). Each port contributes another 2.2 nL to the sample volume. The sample is injected dead-volume free onto the packed bed inside the separation channel (port 3, Figure 4.1B). A prototype UV detection cell of 50 µm i.d. was installed behind the outlet frit. The path length of the cell equals the overall thickness of the respective microchips (*i.e.*, 300 µm for trapezoidal, 425 µm for quadratic, and 475 µm for Gaussian cross-sections). The detection cell was connected to a diode-array UV detector with a special holder. The resulting dead volume between outlet frit and detection cell for the microchips (Figure 4.1C) varied between 2.5 and 3 nL, depending on number and thickness of the polyimide layers. Compared with the volume of the empty separation channels (Table 4.1), the dead volume from sample injection and detection is negligibly small.

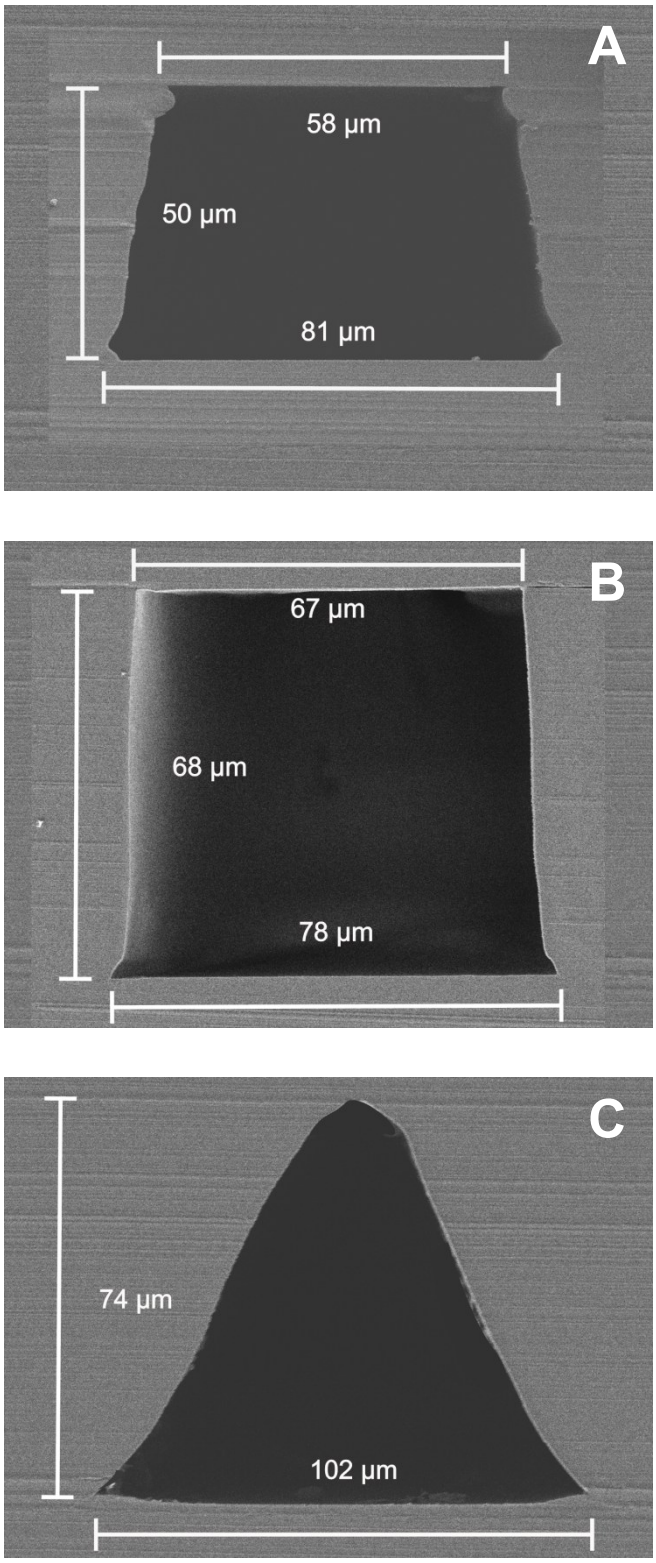

Figure 4.2: **SEM images (equal scaling) of empty microchip separation channels with trapezoidal (A), pseudo-quadratic (B), and Gaussian (C) cross-sections. Unpacked microchips were cut vertically through their separation channels. The gap visible in the upper right corner of the pseudo-quadratic channel (B) is an artefact from the cutting process.**

4.2.3 Microchip packing

Slurry liquids were prepared by suspending 50 mg of dry particles in 1 mL acetone. Methanol was used as pushing solvent in the packing process [33]. The microchips were tightly fixed into a custom-built stainless-steel holder to avoid damage to the polyimide foils during the application of high packing pressures and ultrasonication and connected to the packing station *via* port 3 (Figure 4.1B). The packing station consists of a WellChrom K-1900 pneumatic pump (Knauer GmbH, Berlin, Germany) connected by a SSI three-way valve (ERC, Riemerling, Germany) to a 500 µm i.d. glass-lined metal tubing used as slurry reservoir. After filling the slurry reservoir the microchips were inserted into an ultrasonic bath and the packing procedure started by applying 300 bar pressure and ultrasound for 15 min. Then, the ultrasonic bath was switched off and the system slowly depressurised for at least 20 min. Afterwards, microchips were inspected microscopically for damages along the separation channel and gaps inside the packing. For quadratic and Gaussian channels, two microchips of each geometry were packed with 3 µm particles and two with 5 µm particles. Three microchips with trapezoidal channels were packed with 3 µm particles and three with 5 µm particles.

4.2.4 Chromatographic measurements

All data were acquired with an Agilent 1100 liquid chromatograph consisting of a degasser, a nanopump, and a diode-array UV detector. Volumetric flow rates were continuously monitored by an external flow sensor (Model SLG-1430-150, Sensirion, Stäfa, Switzerland) connected to the analytical system *via* port 7 (Figure 4.1B) to which the mobile phase was redirected after passing the detection cell to determine actual pump errors and identify possible leakage immediately. The chromatograph was operated with Agilent ChemStation software (Rev. B.02.01-SR1). All experiments were carried out at 298 ± 1 K under isocratic elution conditions. Injections were repeated three times for a given microchip and flow rate and the results averaged to account for the error from manual injection.

Channel volumes V_{ch} and plate height curves of the empty microchips were determined by injection of 0.66 mM n-pentylbenzene dissolved in the mobile phase of acetonitrile/water 70/30 (v/v) and detection at 210 nm. Ten individual microchips of each channel geometry were investigated and the results were averaged to account for slight variations in channel dimensions (Table 4.1).

Table 4.1.

Dispersion in the empty microchannels.

Cross-sectional geometry	Channel volume V_{ch}[(a)]	Narrower transverse length h in Eq (4.2)[(b)] [35]	Shape function f in Eq (4.2)[(c)] [35]	
			range[c]	mean[c]
Trapezoidal	265 ± 8.8 nL	50 µm (height)	2.2 - 2.7	2.4
Quadratic	424 ± 8.1 nL	68 µm (height)	1.9 - 2.3	2.2
Gaussian	291 ± 2.4 nL	54 µm (FWHM)	2.6 - 3.2	2.8
		74 µm (height)	1.4 - 1.7	1.5
		51 µm (half the bottom length)	2.8 - 3.5	3.1

(a) Channel volumes were experimentally determined and represent the average of ten individual microchips with the indicated channel geometry.

(b) Values were taken from the SEM cuts of individual microchips (Figure 4.2).

(c) Values were calculated from the normalised plate height curves of ten individual microchips with the indicated channel geometry.

Porosities of the packed microchips were analysed by inverse size-exclusion chromatography [26,30]. A sample of 1 mM benzene (a small, non-retained analyte with access to the total pore volume of the packing, V_{total}) and 0.66 mM polystyrene standard (100,000 g/mol, completely size-excluded from the intraparticle pore space) dissolved in the mobile phase of methylene chloride was injected and chromatographed at a flow rate of 300 nL/min and detection at 230 nm. Total bed porosities (ε_{total}) were derived from $\varepsilon_{total} = V_{total}/V_{ch}$, and interparticle porosities (ε_{inter}) from $\varepsilon_{inter} = V_{inter}/V_{ch}$ where V_{inter} is the interparticle void volume of the microchip packings determined from the elution volume of the polystyrene standard. Finally, intraparticle porosities (ε_{intra}) were calculated from the relation $\varepsilon_{total} = \varepsilon_{inter} + (1 - \varepsilon_{inter})\varepsilon_{intra}$.

Plate height curves of the packed microchips were determined with acetonitrile/water 70/30 (v/v) as mobile phase and detection at 210 nm. The sample consisted of 0.33 mM uracil, 0.66 mM benzene, and 0.66 mM of each alkylbenzene dissolved in the mobile phase. Plate heights were calculated using the Agilent ChemStation software based on a pseudo-method of moments.

4.3 Results and discussion

In Figure 4.2 scanning electron microscopy (SEM) images of vertical cuts through the unpacked microchip separation channels visualise each of the investigated cross-sectional geometries. Trapezoidal and quadratic channels were fabricated by cutting a hole of the required width and length (73 mm) into a polyimide foil of the necessary thickness and then laminating the cut-out foil to the enveloping polyimide layers. Accordingly, the side walls of trapezoidal and quadratic channels originate from the central polyimide foil, while top and bottom walls are formed by the enveloping polyimide layers. The trapezoidal cross-section (Figure 4.2A) has a height of 50 µm, a top base of 58 µm, a bottom base of 81 µm, and a base angle of *ca.* 80°. The four corners are irregular and each of a different shape, a result of the spatial energy profile of the laser, laser defocusing effects, and the lamination process. The cross-section of the quadratic channel (Figure 4.2B) is in fact trapezoidal. The top corners are nearly rectangular, but the bottom corners are peaked, and the base lengths are unequal with 67 µm at the top and 78 µm at the bottom. A truly quadratic channel turned out too difficult to fabricate, as particularly the effects of the lamination process on the final cross-sectional shape cannot be directed precisely. For example, the height of the quadratic channel that was expected to equal the thickness of the central polyimide foil (75 µm) is only 68 µm. For fabrication of the Gaussian channel, the Gaussian spatial energy profile of the laser was used to carve the channel profile into a polyimide layer of sufficient thickness. The side walls and the top originate from the central layer, while the bottom wall is formed by one of the enveloping layers. The Gaussian cross-section (Figure 4.2C) has a bottom length (from corner to corner) of 102 µm, a height of 74 µm, and a FWHM (full-width-at-half-maximum) of 54 µm. The channel base is bordered by two corners with a *ca.* 45° opening.

4.3.1 Dispersion in the empty separation channels

The influence of the conduit geometry on flow and dispersion in open microchannels has been extensively studied, mostly by numerical analysis methods [34-40]. Axial dispersion of a tracer pulse injected into a fluid in laminar flow through a conduit is caused by the interaction of lateral diffusion and the nonuniform flow profile. TAYLOR [41] and ARIS [42] have shown that axial dispersion of the solute leads to a Gaussian area-average concentration profile sufficiently far downstream (long-time limit). Dispersion in cylindrical conduits can then be described by [43]

$$\frac{D_{ax}}{D_m} = 1 + \frac{1}{192}\left(\frac{ud}{D_m}\right)^2 = 1 + \frac{1}{192}Pe^2 \tag{4.1}$$

where D_{ax} is the axial dispersion coefficient, D_m the molecular diffusion coefficient, u the flow velocity averaged over the cross-section, d the cylinder diameter, and $Pe = ud/D_m$ the PÉCLET number, which gives the ratio of convective to diffusive transport rates.

A general expression to describe dispersion in noncylindrical channels was introduced by DUTTA *et al*. [35] based on pressure-driven laminar flow between two parallel plates

$$\frac{D_{ax}}{D_m} = 1 + \frac{1}{210} f\left(\frac{uh}{D_m}\right)^2 = 1 + \frac{1}{210} f\, Pe^2 \tag{4.2}$$

where h is the characteristic narrower transverse dimension of the channel (*e.g.*, the distance between two parallel plates) and f is a shape function that quantifies dispersion based on the actual velocity profile in the channel and depends on its exact cross-sectional geometry and dimensions (f = 1 for the parallel-plate geometry). f values have been calculated for various microchannel cross-sections, including rectangular and trapezoidal geometries, but not Gaussian profiles.

The axial dispersion coefficient D_{ax} (usually discussed in the engineering literature) in eqs 1 and 2 can be substituted with the chromatographic axial plate height H through the relation $D_{ax} = Hu/2$ to give the normalised plate height equations H/d or H/h *vs*. $Pe = ud/D_m$ or $Pe = uh/D_m$, respectively, for dispersion of an unretained solute in open cylindrical channels

$$\frac{H}{d} = \frac{2}{Pe} + \frac{1}{96}Pe \tag{4.3}$$

or in open noncylindrical channels

$$\frac{H}{h} = \frac{2}{Pe} + \frac{1}{105} f\, Pe \tag{4.4}$$

The first term in Equations 4.3 and 4.4 refers to the contribution of axial molecular diffusion to band broadening and the second term describes the contribution from mass transfer resistance. In the investigated range of velocities the first term is negligible.

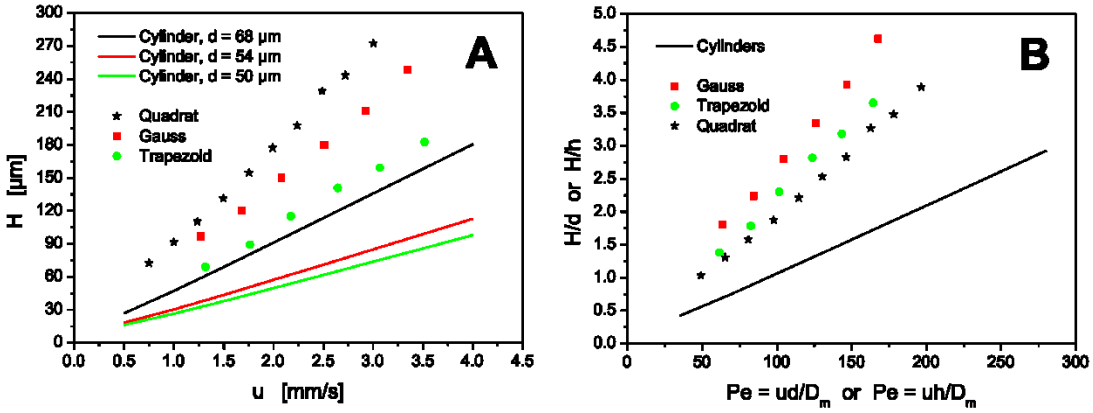

Figure 4.3: **(A) Plate height curves for empty separation channels with trapezoidal (green circles), quadratic (black stars), Gaussian (red squares), and circular (solid lines) cross-sections. Experimental plate height data represent the average of ten individual microchips of a given channel geometry. Values for cylindrical channels whose diameters d correspond to the narrower transverse length h of the noncylindrical channels were calculated from Equation 4.3. (B) Experimental and calculated plate height data H normalised by the respective narrower transverse length h of the channels or the cylinder diameter d, respectively, *vs.* the PÉCLET number.**

Experimental plate height data were acquired for ten individual microchips of each channel geometry with the unretained analyte n-pentylbenzene and acetonitrile/water 70/30 (v/v) as mobile phase. Figure 4.3A shows the resulting plate height data for the three channel geometries, averaged over the results from the individual microchips, as well as data calculated with Equation 4.3 for cylindrical conduits. Good reproducibility of experimental data was observed with a *ca.* 5% variation in plate heights at 1% variation in average flow velocity. The respective regression lines have correlation coefficients of $R^2 > 0.996$, which is fairly good for manual injection onto a short separation column. The diameters of the cylindrical conduits were chosen to match the respective narrower transverse length of the microchip channels, *i.e.*, the height of the trapezoidal (50 µm) and quadratic (68 µm) channels. For the Gaussian channel the FWHM (54 µm) was taken as a first approximation. The general trend visible in the plate height curves of Figure 4.3A is expected: Dispersion increases with increasing channel diameter d (Equation 4.1) or respective narrower transverse length h (Equation 4.2), and dispersion in the empty noncylindrical microchannels is always larger than in the cylindrical conduits due to the influence of the confining walls on the flow profile.

For better comparison plate height data were normalised by the cylinder diameter (d) or the respective narrower transverse length (h) of the microchannels. The molecular diffusion

coefficient of n-pentylbenzene in the mobile phase was taken from LI and CARR [44] as D_m = 1.07 x 10^{-9} m^2/s. The normalised data H/d or H/h *vs*. Pe = ud/D_m or Pe = uh/D_m in Figure 4.3B show a change in the relative order of the dispersion curves for the noncylindrical channels. The quadratic channel has the lowest normalized plate height curve (H/h) followed by the trapezoidal and the Gaussian channels. This finding is explicable from the symmetry of the respective channel cross-sections [24]. The quadratic cross-section has the highest symmetry, resulting in a more symmetrical flow profile and a smaller flow maldistribution term. Flow maldistribution increases with decreasing symmetry due to the growing distance between different velocities over which exchange of solute molecules needs to occur by lateral diffusion to approach asymptotic dispersion in the long-time limit. Thus, the velocity inequality of the flow pattern intrinsic to a particular conduit geometry increases with decreasing symmetry of the conduit [24]. Although the quadratic channel has a trapezoidal rather than quadratic cross-section as shown in Figure 4.2B, the differences in side lengths are small enough to provide a more homogeneous flow profile and smaller axial dispersion than in the trapezoidal channel. The Gaussian cross-section has one symmetry axis, but the continuous decrease in lateral diffusion length from bottom to top translates to larger friction forces in the upper part of the channel and more pronounced velocity differences between top and bottom part.

Experimental f values for the empty separation channels were derived by setting the slopes of the normalised plate height curves (determined by linear regression) equal to the mass transfer coefficient f /105 of Equation 4.4. Results are summarised in Table 4.1. The narrow range of the experimental f values reflects the good reproducibility of the cross-sectional geometry in microchip fabrication, as deviations in geometry would strongly affect empty channel dispersion. In a rectangular channel the velocity slow-down in the vertical side regions causes a substantial increase in the magnitude of f that grows with the ratio of channel width (w) to channel height (h), from f = 1.76 for a quadratic cross-section (w/h = 1) to a limiting value of f = 7.95 for rectangular cross-section where w/h → 0 [35]. For microchips with quadratic channels the mean experimental value of f = 2.2 is higher than the theoretical value of f = 1.76 [35] reflecting the deviations of the channel cross-section from regular quadratic geometry, *i.e.*, unequal base lengths, a ratio of the mean width (w = 72.5 μm) to height (68 μm) of w/h = 0.87, and the deviation from orthogonality of the bottom corners. Microchips with trapezoidal channels show a similar upward deviation from theoretical values. In trapezoidal channels the scaling of additional dispersivity quantified by f increases with the ratio of smaller base length (w_s) to height (h) of the channel and with

increasing deviation of the base angle from orthogonality. According to DUTTA *et al*. [35] a conduit with an isosceles trapezoidal cross-section, a base angle of 80°, and a ratio of w_s/h = 1.0 would give a value of f ≈ 2 (*cf*. Figure 6 in ref. [35]). The SEM image of the trapezoidal channel cross-section in Figure 4.2A reveals a ratio of w_s/h = 1.2, but this would increase f only slightly. The main reason for the increased experimental value of f = 2.4 are the four different irregularly angled corners in the trapezoidal channel that reduce the symmetry of the cross-section and cause additional velocity slow-down in the corner regions [32]

In the Gaussian channel the narrower transverse length is not straightforward to define, therefore the channel height (74 µm) and half the bottom length (51 µm) were evaluated besides the FWHM (54 µm) for calculation of f. Choosing the channel height underestimates dispersion, because the resulting f values are smaller than those of the quadratic channel (Table 4.1). The choice of FWHM and half the bottom length as narrower transverse dimension give reasonable results. While the so-calculated f values approach those of the trapezoidal channel, they are still larger, reflecting the velocity slow-down caused by the Gaussian channel's tapering profile. Considering that the exact channel dimensions vary between individual microchips due to the fabrication process (Table 4.1), both parameters are suitable for a first approximation of dispersion behaviour in the Gaussian channel.

4.3.2 Microchip packing densities

Interparticle porosities of the microchip packings were determined by inverse size-exclusion chromatography using a polystyrene standard with a molecular weight of 100,000 g/mol. This standard had been identified in previous experiments for both packing materials as a suitable probe for the interparticle void space [26]. Total and interparticle porosities (ε_{total} and ε_{inter}) were calculated from the elution volumes of benzene and the polystyrene standard, respectively, measured in one chromatographic run. Results are summarized in Table 4.2 and demonstrate that the achieved packing densities depend essentially on the particle size of the packing material. All 3 µm packings display the low interparticle porosities ($\varepsilon_{inter} \approx 0.38$) characteristic of random-close packings, which proves that optimized packing conditions enable dense packings even in a difficult conduit geometry. The interparticle porosities of the 5 µm packings are only moderate ($\varepsilon_{inter} \approx 0.41$), reflecting looser packings. As the intraparticle porosities are practically identical for both packing materials ($\varepsilon_{intra} \approx 0.40$), the total porosities of the 3 µm packings are also lower (Table 4.2).

Table 4.2.

Porosities of the microchip packings.

Nominal particle size	Conduit Geometry	Particle-aspect ratio[(a)]	ε_{total} [(b)]	ε_{inter} [(b)]	ε_{intra}
3 µm	Trapezoidal	17	0.633 ± 0.001	0.383 ± 0.002	0.405 ± 0.002
	Quadratic	23	0.630 ± 0.005	0.383 ± 0.003	0.399 ± 0.006
	Gaussian	18	0.633 ± 0.002	0.379 ± 0.004	0.409 ± 0.005
5 µm	Trapezoidal	10	0.643 ± 0.001	0.405 ± 0.004	0.400 ± 0.004
	Quadratic	14	0.654 ± 0.002	0.423 ± 0.012	0.400 ± 0.012
	Gaussian	11	0.641 ± 0.006	0.397 ± 0.004	0.405 ± 0.007

[(a)] Particle-aspect ratios were calculated from the nominal particle size and the narrower transverse dimension of the channel cross-sections (Table 4.1). For Gaussian channels, the FWHM was used.

[(b)] Interparticle and total porosities were determined for two (quadratic, Gaussian) or three (trapezoidal) individual packings of a given type (conduit geometry, particle size). No statistical variance was found between individual packings of a given type. RMSD values refer to thrice-repeated experiments with an individual microchip and reflect the error from manual injection.

The particle-aspect (conduit-to-particle size) ratio of confined packings is often the cause for systematic differences in packing density: At low particle-aspect ratios, a combination of the geometrical wall effect and particle characteristics like surface roughness, size distribution, and shape, leads to a decreased packing density [31]. For example, for cylindrical fused-silica capillaries with inner diameters between 30 and 250 µm that were slurry-packed with 5 µm porous C18-silica particles (d_p = 5.5 µm), densely packed beds with ε_{inter} = 0.36-0.37 could be achieved at large particle-aspect ratios ($d/d_p > 35$), while at decreasing particle-aspect ratio an exponential increase in the interparticle porosity was observed up to ε_{inter} = 0.46 at $d/d_p \approx 5.5$ [30]. Considering that the particle size distributions of the packing materials used are very similar to each other [26] and also to the packing material used in the related study with fused-silica capillaries [30], the observed increase of interparticle porosities from ε_{inter} = 0.38

for the 3 µm packings to $\varepsilon_{inter} \approx 0.41$ for the 5 µm packings can be explained accordingly by the concomitant decrease of the particle-aspect ratios (Table 4.2). It is not straightforward to decide which dimension should be used to calculate the particle-aspect ratio for a noncylindrical conduit whose cross-sectional geometry is defined by more than one parameter. We calculated particle-aspect ratios based on the identified narrower transverse dimensions of the microchannels (Table 4.1), but the so-derived particle-aspect ratios are tentative rather than strict values for the Gaussian and trapezoidal channels.

For the 5 µm packings a slight increase in interparticle porosity from $\varepsilon_{inter} = 0.397$ for the Gaussian *via* $\varepsilon_{inter} = 0.405$ for the trapezoidal to $\varepsilon_{inter} = 0.423$ for the quadratic channels can be perceived. This is most likely related to the quantity and shape of the corners in the different channels. The Gaussian cross-section has only two bottom corners with angles ≤ 45°, while the top of the channel is curved with a plateau width of ~ 10 µm. Thus, there is little steric hindrance for the particles to access the top part of the channel, only the two base corners are expected to be partially unoccupied. The smaller bottom corners of the trapezoidal cross-section are expected to be more difficult to pack than the top corners with angles > 90°. The SEM image of the empty channel cross-section (Figure 4.2A) reveals that the trapezoidal channel corners are "softened", probably from a creeping of glue inside the corners during the lamination step. These corners are better accessible to particles, so that ε_{inter} of the microchip packings in the trapezoidal channels is lower than in the quadratic channels, which contain four sharp corners.

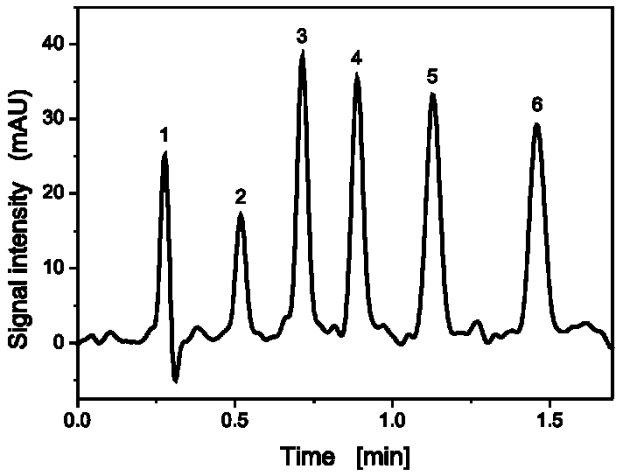

Figure 4.4: Isocratic separation of an alkylbenzene sample (1: uracil, 2: benzene, 3: ethylbenzene, 4: n-propylbenzene, 5: n-butylbenzene, and 6: n-pentylbenzene) on a microchip with quadratic separation channel packed with 3 µm porous C8-silica particles. Mobile phase: acetonitrile/water 70/30 (v/v) at an average flow velocity of u = 4.4 mm/s.

4.3.3 Separation efficiencies

Analysis of axial dispersion in the microchip packings was based on the isocratic separation of benzene and four alkylbenzenes, with uracil as dead-time marker and acetonitrile/water 70/30 (v/v) as mobile phase. Figure 4.4 shows a chromatogram from a microchip with a quadratic 3 µm packing (ε_{inter} = 0.383), acquired at an average flow velocity of u = 4.4 mm/s, which resulted in a back-pressure of 150 bar. The highly symmetrical peak shapes of the chromatogram in Figure 4.4 were also observed with the other investigated microchip packings. Axial plate heights (H) were determined from the n-pentylbenzene peak characterized by a retention factor of $k = (t_r - t_0)/t_0 = 3.9$ (t_r is the retention time of n-pentylbenzene and t_0 is the dead-time of uracil). Figure 4.5 shows the resulting plate height curves for all investigated microchip packings. Axial plate heights were averaged over two or three individual microchip packings of a given type (conduit geometry, particle size) and thrice-repeated experiments with individual microchips. Good reproducibility was achieved, with *ca.* 3% variation in plate heights at 1% variation in average flow velocity at the curve minimum. For chromatographic beds of the same packing material and operated with the same mobile phase no differences in the adsorption-desorption kinetics and/or diffusion within the stationary phase are expected. Thus, the observed differences in plate height curves can be ascribed to the respective cross-sectional flow profiles resulting from the actual packing microstructure.

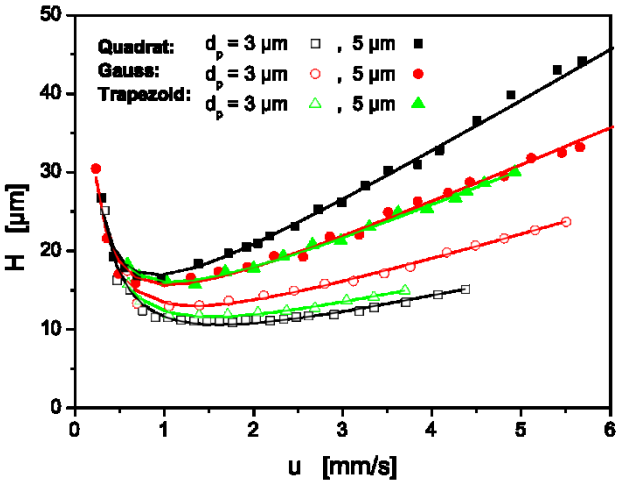

Figure 4.5: Experimental plate height curves for microchips with trapezoidal, quadratic, or Gaussian separation channels packed with 3 or 5 µm porous C8-silica particles. Mobile phase: acetonitrile/water 70/30 (v/v), analyte: n-pentylbenzene (k = 3.9). For each data point the result of three individual chromatographic experiments with a particular microchip packing as well as the results for individual packings of a given type (conduit geometry, particle size) were averaged.

Among the 3 µm packings those with quadratic cross-section show the best performance, followed by the trapezoidal packings whose plate height curve is only slightly elevated. Plate height data for quadratic and trapezoidal packings are identical up to an average flow velocity of u = 1 mm/s, but quadratic packings have the advantage of a relatively small slope at higher velocities. This implies that the analysis time in quadratic packings can be reduced without a significant loss of performance. Gaussian packings display the highest band broadening, with a higher plate height minimum and steeper slope at higher velocities than the other 3 µm packings. This emphasizes the fact that the conduit geometry significantly influences dispersion even if it does not influence the packing density (ε_{inter} = 0.38 for all 3 µm packings). For the 3 µm packings, the influence of the conduit geometry on dispersion is comparable with that observed for the empty channels (Figure 4.3B), *i.e.*, governed by the flow profile as it depends on the conduit cross-sectional geometry and dimensions.

The performance characteristics of the 5 µm packings differ from the corresponding 3 µm packings. Here, the plate height curves of the trapezoidal and Gaussian packings are very similar. While the Gaussian packings perform slightly better around the minimum, trapezoidal packings gain a small advantage at higher flow velocities. Quadratic packings differ not too much from the other 5 µm packings around the plate height minimum, but suffer from a significantly steeper slope at higher velocities. For an explanation of the plate height curves, the different packing densities of the 5 µm packings have to be considered. The higher packing density of the Gaussian 5 µm packings (ε_{inter} = 0.40, compared with ε_{inter} = 0.41 of the trapezoidal 5 µm packings) partially compensates for the negative influence of the Gaussian profile on dispersion. The sparsely occupied corners of the quadratic channel, which are reflected in the lower density (ε_{inter} = 0.42) of the 5 µm packing, increase the velocity inequality of the macroscopic flow pattern and thus hydrodynamic dispersion [24]. The impact of the lower packing density on band broadening is sufficiently high to overcome the geometrical advantage, so that quadratic 5 µm packings demonstrate the worst performance among the investigated microchip packings.

4.4 Conclusions

Our study has shown that the conduit geometry influences the performance of typical particulate microchip packings in various ways, but the effects cannot be isolated from the particle-aspect ratio of the packings. While the packing density of the 3 µm packings is not influenced by the conduit geometry, the dispersion behaviour reflects dispersion in the empty channels, *i.e.*, is governed by the geometry and dimensions of the conduit cross-section. Gaussian 3 µm packings are disadvantaged, while the good performance of quadratic 3 µm packings at higher velocities provides an important gain in analysis time.

The dispersion behaviour of the 5 µm packings reflects their respective packing densities, which are limited by the number and shape of corners in a channel that determine the inaccessible volume fraction for packing particles. The performance of the Gaussian 5 µm packing is comparable to that of the trapezoidal 5 µm packing, because the higher packing density balances the dispersion disadvantage from the Gaussian conduit shape. On the other hand, quadratic conduits, whose fabrication requires the most effort with the chosen method, loose their symmetry advantage when the particles are difficult to pack densely into the channel.

References

[1] J. Xie, Y. Miao, J. Shih, Y.-C. Tai, T.D. Lee, Anal. Chem. 77 (2005) 6947-6953.

[2] I.M. Lazar, P. Trisiripisal, H.A. Sarvaiya, Anal. Chem. 78 (2006) 5513-5524.

[3] J.F. Borowsky, B.C. Giordano, Q. Lu, A. Terray, G.E. Collins, Anal. Chem. 80 (2008) 8287-8292.

[4] J. Liu, C.-F. Chen, C.-W. Tsao, C.-C. Chang, C.-C. Chu, D.L. DeVoe, Anal. Chem. 81 (2009) 2545-2554.

[5] M.T. Koesdjojo,C.R. Koch, V.T. Remcho, Anal. Chem. 81 (2009) 1652-1659.

[6] A. Manz, Y. Miyahara, J. Miura, Y. Watanabe, H. Miyagi, K. Sato, Sens. Actuators B 1 (1990) 249-255.

[7] P.G. Vahey, S.A. Smith, C.D. Costin, Y.N. Xia, A. Brodsky, L.W. Burgess, R.E. Synovec, Anal. Chem. 74 (2002) 177-184.

[8] M. Schlund, S. Gilbert, S. Schnydrig, P. Renaud, Sens. Actuators B 123 (2007) 1133-1141.

[9] W. De Malsche, H. Eghbali, D. Clicq, J. Vangelooven, H. Gardeniers, G. Desmet, Anal. Chem. 79 (2007) 5915-5926.

[10] X. Illa, W. De Malsche, J. Bomer, H. Gardeniers, J. Eijkel, J.R. Morante, A. Romano-Rodriguez, G. Desmet, Lab Chip 9 (2009) 1511-1516.

[11] D.S. Reichmuth, T.J. Shepodd, B.J. Kirby, Anal. Chem. 77 (2005) 2997-3000.

[12] K.W. Ro, J. Liu, D.R. Knapp, J. Chromatogr. A 1111 (2006) 40-47.

[13] J. Carlier, S. Arscott, V. Thomy, J.C. Camart, C. Cren-Olivé, S. Le Gac, J. Chromatogr. A 1071 (2005) 213-222.

[14] Y. Yang, C. Li, J. Kameoka, K.H. Lee, H.G. Craighead, Lab Chip 5 (2005) 869-876.

[15] D.A. Mair, E. Geiger, A.P. Pisano, J.M.J. Fréchet, F. Svec, Lab Chip 6 (2006) 1346-1354.

[16] A. Ishida, T. Yoshikawa, M. Natsume, T. Kamidate, J. Chromatogr. A 1132 (2006) 90-98.

[17] J. Liu, K.W. Ro, R. Nayak, D.R. Knapp, Int. J. Mass Spectrom. 259 (2007) 65-72.

[18] P.A. Levkin, S. Eeltink, T.R. Stratton, R. Brennen, K. Robotti, H. Yin, K. Killeen, F. Svec, J.M.J. Fréchet, J. Chromatogr. A 1200 (2008) 55-61.

[19] H. Yin, K. Killeen, R. Brennen, D. Sobek, M. Werlich, T. van de Goor, Anal. Chem. 77 (2005) 527-533.

[20] C.-Y. Shih, Y. Chen, J. Xie, Q. He, Y.-C. Tai, J. Chromatogr. A 1111 (2006) 272-278.

[21] A. Gaspar, M.E. Piyasena, F.A. Gomez, Anal. Chem. 79 (2007) 7906-7909.

[22] Y. Yang, J. Chae, Appl. Phys. Lett. 94 (2009) 173902.

[23] S. Ehlert, K. Kraiczek, J.-A. Mora, M. Dittmann, G.P. Rozing, U. Tallarek, Anal. Chem. 80 (2008) 5945-5950.

[24] S. Khirevich, A. Höltzel, D. Hlushkou, U. Tallarek, Anal. Chem. 79 (2007) 9340-9349.

[25] S. Khirevich, A. Höltzel, D. Hlushkou, A. Seidel-Morgenstern, U. Tallarek, Lab Chip 8 (2008) 1801-1808.

[26] S. Jung, S. Ehlert, J.-A. Mora, K. Kraiczek, M. Dittmann, G.P. Rozing, U. Tallarek, J. Chromatogr. A 1216 (2009) 264-273.

[27] R.T. Kennedy, J.W. Jorgenson, Anal. Chem. 61 (1989) 1128-1135.

[28] S. Hsieh, J.W. Jorgenson, Anal. Chem. 68 (1996) 1212-1217.

[29] K.D. Patel, A.D. Jerkovich, J.C. Link, J.W. Jorgenson, Anal. Chem. 76 (2004) 5777-5786.

[30] S. Ehlert, T. Rösler, U. Tallarek, J. Sep. Sci. 31 (2008) 1719-1728.

[31] A. de Klerk, AIChE J. 49 (2003) 2022-2029.

[32] S. Khirevich, A. Höltzel, S. Ehlert, A. Seidel-Morgenstern, U. Tallarek, Anal. Chem. 81 (2009) 4937-4945.

[33] J.P.C. Vissers, H.A. Claessens, J. Laven, C.A. Cramers, Anal. Chem. 67 (1995) 2103-2109.

[34] H. Poppe, J. Chromatogr. A 948 (2002) 3-17.

[35] D. Dutta, A. Ramachandran, D.T. Leighton, Microfluid. Nanofluid. 2 (2006) 275-290.

[36] A. Ajdari, N. Bontoux, H.A. Stone, Anal. Chem. 78 (2006) 387-392.

[37] N. Bontoux, A. Pépin, Y. Chen, A. Ajdari, H.A. Stone, Lab Chip 6 (2006) 930-935.

[38] E.K. Zholkovskij, J.H. Masliyah, Chem. Eng. Sci. 61 (2006) 4155-4164.

[39] H. Eghbali, G. Desmet, J. Sep. Sci. 30 (2007) 1377-1397.

[40] M. Bahrami, M.M. Yovanovich, J.R. Culham, Int. J. Heat Mass Transfer 50 (2007) 2492-2502.

[41] G. Taylor, Proc. R. Soc. Lond. A 219 (1953) 186-203.

[42] R. Aris, Proc. R. Soc. Lond. A 235 (1956) 67-77.

[43] W.M. Deen, Analysis of Transport Phenomena, Oxford University Press, New York, 1998.

[44] J. Li, P.W. Carr, Anal. Chem. 69 (1997) 2530-2536.

Chapter III – Part A

Microchip electrospray: Cone-jet stability analysis for water-acetonitrile and water-methanol mobile phases

5.1 Introduction

Microfluidic devices have become increasingly important in analytical and bioanalytical chemistry [1-6]. They offer the ability to save time, sample amount, and costs by miniaturizing and integrating sample pre-treatment and analysis steps on a microfluidic chip. Micro total analysis systems (μ-TAS) [7] also offer parallelisation and automation, ideal for high-throughput screening and proteomic workflows. Among a variety of separation and detection methods [8,9], the combination of high performance liquid chromatography (HPLC) with electrospray ionization (ESI) mass spectrometry (MS) has emerged as the standard analytical method for many applications, from screening of small molecule libraries to peptide and protein identification and structural characterization [10]. Anticipating the trend towards chip-based technologies, efforts to couple microfluidic devices to mass spectrometers started a decade ago [11-13]. ESI – a soft, atmospheric-pressure ionization method for small and large molecules alike, provided they possess polar functionalities that can be protonated or deprotonated – is well suited to microfluidic flow rates and to the aqueous methanol or aqueous acetonitrile-based mobile phases used in reversed-phase (RP) HPLC. There has also been strong interest to bring the chromatographic separation into microchip format, but the difficulties related to generating and maintaining high-pressure liquid flow on the (usually pressure-sensitive) chips and to preparing homogeneous packed beds in the noncylindrical microfluidic channels had to be overcome first [14]. Another challenge for the coupling of chip-based HPLC to ESI-MS was the development of a stable and effective interface with minimal dead volume [15].

Apart from the design and manufacturing of microchips for HPLC/ESI-MS, the operating conditions are also important to their performance. The physical processes involved in the electrospray are complex, and many parameters have been established by trial and error. Today, we have arrived at a better understanding of the ESI mechanism [16], which enables rational choices for the proper conditions in ESI-MS. Electrostatic spraying exhibits a

variety of spray morphologies and dynamics [17], depending on a number of parameters related to instrumental design (geometry and wettability of the emitter, distance between emitter and counter electrode, strength and shape of the electrical field) as well as to flow rate and physicochemical properties of the electrosprayed liquid (surface tension, permittivity, viscosity, density, electrical conductivity) [11,18-22]. Although spray morphologies and dynamics depend on the actual experimental conditions, the involved physical and electrohydrodynamic phenomena are transferable between individual systems allowing a comparison between the observed electrospray modes and their related instrument settings. In general, microchip emitters demonstrate similar or even better chromatographic performance and comparable ESI-MS sensitivities with respect to nanoelectrospray needles with similar emitter diameters [19,23-25].

Electrospray modes are classified by visual criteria [17,26] and/or by measuring the AC and DC components of the spray current [27-31]. The different spray modes impact sensitivity and precision of the measurement. The targeted spray condition for mass spectrometric analysis is the cone-jet mode, which provides a relatively large and stable current as well as smaller initial droplets, both prerequisites for high sensitivity and precision [16,19]. Choosing the experimental parameters so as to operate in the cone-jet mode throughout the detection duty cycle is desirable, but in conflict with the reality of typical screening applications, where RP HPLC separation is carried out with steep mobile phase gradients to cover a broad range of analytes in a short analysis time. A gradually changing mobile phase composition implies a dynamic change of the physicochemical properties of the electrosprayed liquid (the eluate from the chip's separation channel), which could result in transitions between different spray modes and alterations in the detected signal. There have been a few attempts to automatically maintain the electrospray in the cone-jet mode by adjusting the voltage based on feedback from spray imaging [22] or spray current measurements [20,32]. Alternatively, the effects of a changing mobile phase composition could be counterbalanced by post-column combination with an inverted mobile phase gradient to provide constant physicochemical properties of the electrosprayed liquid during MS analysis [33,34].

In this work we analyse the electrospray characteristics of a microchip-HPLC/ESI-MS configuration for formic acid-containing mobile phases of aqueous acetonitrile and aqueous methanol. We study the flow-rate dependence, the influence of water fraction and formic acid content in the mobile phase, and the effect of a gradually changing bulk conductivity of the electrosprayed liquid. The electrospray is monitored with an oscilloscope for frequency

analysis of the emitter current's DC and AC components and with a video camera for spray imaging. This approach enables identification of different spray modes as well as the determination of their stability islands depending on the applied voltage and actual mobile phase conditions. The results are discussed in terms of the physicochemical properties of the electrosprayed liquid, particularly its conductivity, and focus on the effects that accompany the gradual variation of solvent volumetric ratios in gradient elution RP HPLC. As the electrospray characteristics strongly depend on a number of parameters, the direct transfer of our results to other microchip-HPLC/ESI-MS configurations is difficult, but the general trends reported in this work will assist in better understanding of the instabilities observed during HPLC/ESI-MS analysis.

5.2 Experimental section

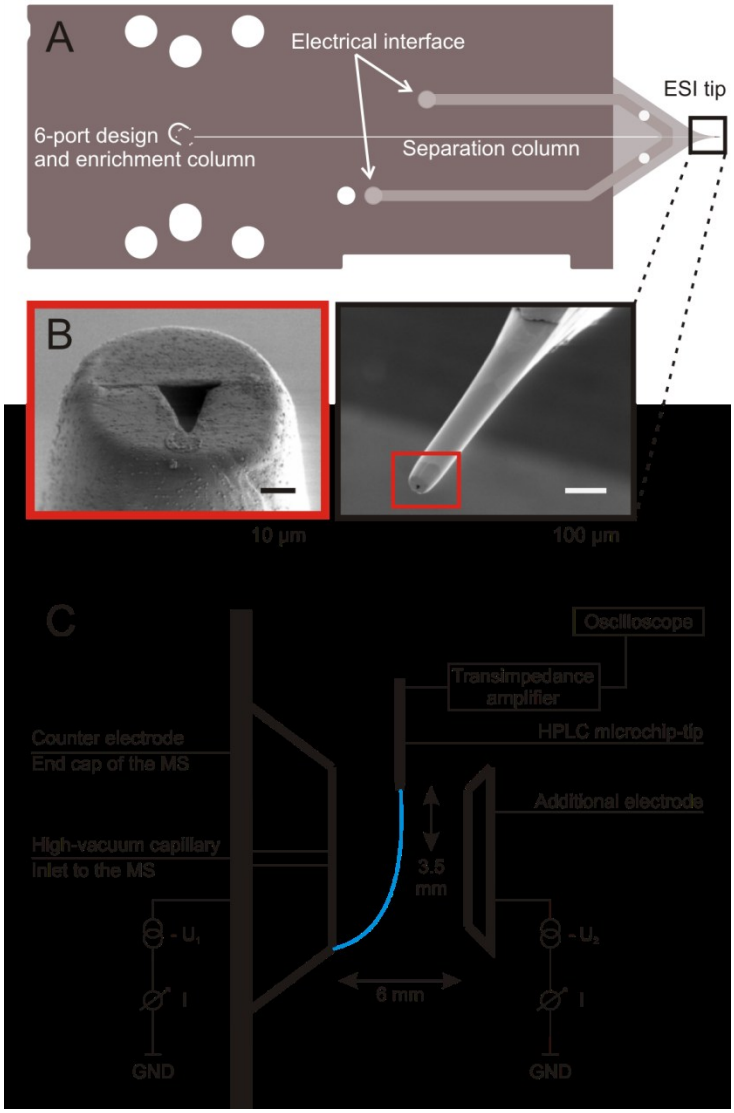

Figure 5.1: Layout of the microchip-HPLC/ESI-MS configuration. (A) Polyimide-based microchip with U-shaped sample enrichment column, straight separation column (43 mm long), ESI tip and electrical interface. (B) Magnification of the ESI tip and its outlet. (C) Positioning of the microchip within the ESI-MS interface.

5.2.1 Microchip electrospray configuration and analysis

We used an Agilent HPLC-ChipCube MS interface with a HPLC-MS microchip coupled to a 1200 LC/MSD XCT Ultra ion trap mass spectrometer (Agilent Technologies, Waldbronn, Germany). The polyimide-based microchip [35,36] contains a 6-port valve for mobile phase and sample injection, two particle-packed microchannels that serve as sample enrichment (U-shaped) and separation column (straight), and a nanoelectrospray tip; an integrated interface provides the electrical contact to the liquid at *ca*. 6 mm distance from the chip outlet, within a narrow transfer channel between separation column and nanoelectrospray tip (Figure 5.1A).

The tip has an outer diameter of *ca*. 45 µm and a Gaussian-shaped opening of *ca*. 15 µm height (Figure 5.1B).

The HPLC-MS microchip was positioned inside the ChipCube spray chamber between a counter electrode (end cap of the MS) and an additional electrode, 90° off-axis with respect to the MS inlet cone such that the ESI tip was *ca*. 3 mm away from the cone and *ca*. 3.5 mm above its axis (Figure 5.1C). For operation in the positive ion mode, ground potential was applied to the liquid and negative potential to end cap and additional electrode. A constant potential difference of 500 V between end cap (U_1) and additional electrode (U_2) made the end cap the part with the most negative potential in the system. Following the settings of the standard Agilent calibration procedure, a drying gas flow rate of 4 L/min and a drying temperature of 300 °C were used.

The potential difference between emitter tip and end cap of the MS was varied *via* the TrapControl software, which allows changes in minimal steps of 50 V. A camera installed in the spray chamber was used to observe the spray performance visually. The electrospray current was measured through the electrical interface on the microchip using a custom-built transimpedance amplifier that converted the incoming current into an outgoing potential difference at 100 nA/V. The transimpedance amplifier was connected (Figure 5.1C) to a 10 MHz digital pc-oscilloscope (PicoScope 2204, Pico Technology, St Neots, UK). The oscillosope's FOURIER transformation software was used for frequency analysis.

2.2 Mobile phase composition and conductivity measurements

Mobile phases consisted of water and acetonitrile (W/MeCN) or water and methanol (W/MeOH) and contained 0 – 100 vol% water (Table 1) and 0.001 – 0.1 vol% formic acid (FA). Acetonitrile and methanol (HPLC grade) were purchased from Sigma-Aldrich Chemie GmbH (Taufkirchen, Germany) and formic acid (*p.a.*) from Fluka-Chemie GmbH (Buchs, Switzerland). HPLC grade water (5.5×10^{-6} S/m) was obtained from a Milli-Q gradient water purification system (Millipore, Bedford, MA, USA).Conductivity measurements were carried out at room temperature using the Lab 970 conductometer with LF 913T measurement cell from SI Analytics (Mainz, Germany).

5.3 Results and discussion

5.3.1 Electrospray mode definitions

There are three major steps in the production of gas-phase ions from the electrolyte ions in solution: (i) production of charged droplets at the electrospray capillary tip; (ii) shrinkage of the charged droplets due to solvent evaporation and repeated charge-induced droplet disintegrations leading ultimately to very small highly charged droplets; (iii) the actual mechanism by which gas-phase ions are produced from these droplets [16] (and references therein). The electric field, which is highest near the spray capillary tip, causes the polarisation of the solvent near the meniscus of the fluid. In the presence of even traces of an electrolyte the solution will be sufficiently conducting and positive and negative ions will move under the influence of the electric field. The electromigration leads to an enrichment of positive ions near the liquid-gas interface formed at the capillary outlet in the positive ion mode. The electrical shear stress causes a distortion of the meniscus into an electrified drop growing at the tip or a cone pointing towards the counter electrode. The increase of the liquid's surface is resisted by its surface tension. If the applied field is sufficiently high, the tip becomes unstable and liquid is ejected as a droplet or a fine jet. In the latter case, varicose wave instabilities developing along the surface, lateral kink instabilities, or numerous ramifications cause the jet to break up into charged droplets [17]. The charged droplets are accelerated towards the counter electrode. Solvent evaporation at constant charge leads to droplet shrinkage and an increase of the electric field normal to the surface of the droplets. If the RAYLEIGH limit is exceeded COULOMB explosion occurs generating smaller droplets which finally results in ion emission.

Depending on the actual geometrical form taken by the liquid at the capillary outlet (drop, cone), the duty cycle of a liquid ejection, the number, structure (axial, non-axial), and disintegration behaviour of the emitted jets, the resulting shapes, sizes, and size distributions of the generated droplets, and the relation between applied potential difference between capillary outlet and counter electrode and resulting spray current, different electrospray modes and regimes can be classified. Confronted with a lack of consensus for the nomenclature of spray modes we chose to follow the classification by JURASCHEK and RÖLLGEN [27], because they differentiate four distinct spray modes by criteria that could be precisely determined with our instrumental setup. Axial spray mode 1 occurs at lower capillary potentials and features a regular appearance of peak groups in the oscillogram. Axial spray mode 2 is identified by a constant frequency, amplitude, and peak shape of the current pulses (pulsating cone-jet mode). Axial spray mode 3 is characterised by a constant current in the oscillogram and a

uniform appearance of the whole liquid cone (steady cone-jet mode). Beyond a critical value of the capillary potential, the nonaxial regime (spray mode 4) with ejection of multiple jets sets in.

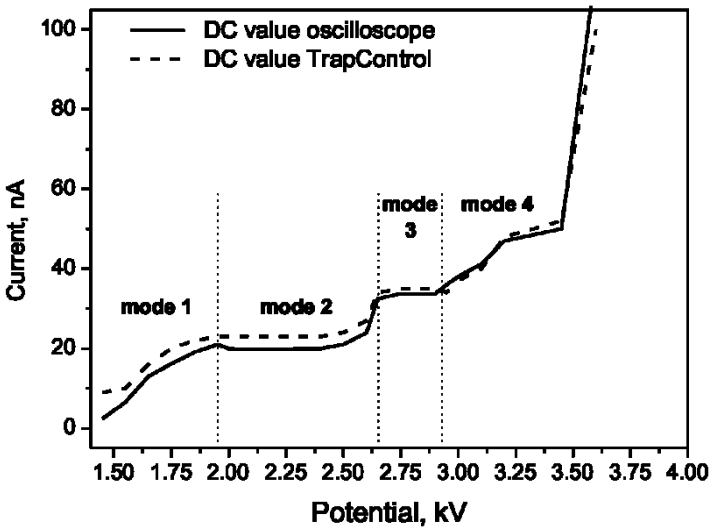

Figure 5.2: Microchip emitter current *vs.* applied electrical potential at the end cap of the mass spectrometer's inlet. Mobile phase: 60/40 (v/v) W/MeCN with 0.001% FA, flow rate: 0.3 µL/min. The solid line denotes the DC values detected with the oscilloscope, the dashed line the DC values recorded by the TrapControl software. Changes in slope indicate transitions between individual electrospray modes.

5.3.2 Experimental analysis of electrospray modes

Figures 5.2 and 5.3 document the four electrospray modes observed for a mobile phase of 60/40 (v/v) W/MeCN with 0.001% FA at a flow rate of 0.3 µL/min, while the potential difference between microchip emitter tip and end cap of the MS was increased from 1.45 to 3.6 kV. Figure 5.2 records the capillary current – the values recorded by the TrapControl software as well as those calculated from the DC component measured by the oscilloscope – as a function of the applied potential. The differences between TrapControl and oscilloscope-based curves are due to rounding errors: the TrapControl software considers only two decimal places, whereas the oscilloscope rounds to the third decimal place. Figure 5.3 provides images from the camera in the spray chamber alongside the corresponding oscillograms. At 1.45 kV (Figure 5.2 and Figure 5.3A) a stream of fluid from the emitter tip is accelerated towards the end cap. Several separated signals at frequencies in the lower kHz range (1.8 – 5.7 kHz) appear in the associated oscillogram, reflecting polydisperse droplets (mode 1).

Between 1.45 and 1.95 kV the DC current shows Ohmic behaviour (Figure 5.2), as has also been observed by others [21,27]; the number of observed frequencies decreases and the

frequencies are shifted towards higher values. At 2.0 kV, as the pulsating cone-jet mode sets in, the slope changes abruptly (Figure 5.2) and the current remains constant over the next range of potential differences [21]. Current oscillations are regular with a well-defined, principal frequency of 10.1 kHz. The camera captures a less pronounced stream line surrounded by a distinct plume (Figure 5.3B). At 2.55 kV (Figure 5.3C), the frequency of the current oscillations increases to 21.1 kHz, which indicates shrinking droplets and ejection at a higher duty cycle [22,29]. While the camera monitors a plume without a visible stream line, the stable DC current as well as the presence of one principal frequency put the region between 2.0 and 2.55 kV firmly into the pulsating cone-jet mode. This example shows that visual inspection of the spray using a camera of a low exposure time and magnification is not adequate to determine the spray mode.

Further increase of the applied voltage leads to a sudden jump in the capillary current (Figure 5.2) and a distinct change in oscillogram and spray appearance (Figure 5.3D): The oscillogram becomes indistinguishable from the background noise pattern and liquid is ejected as a jet from the apex of a steady cone at the exit of the ESI tip (cone-jet mode, mode 3). The jet subsequently breaks up into smaller droplets due to varicose wave instabilities developing along its surface [17]. To establish the TAYLOR cone the electrical relaxation time must be shorter than the characteristic time of the liquid supply (the hydrodynamic time). The electrical relaxation time can be calculated according to $t_e = \varepsilon_r/\kappa$, where ε_r is the relative permittivity and κ the conductivity of the electrosprayed solution. The hydrodynamic time is given by $t_h \sim L/U$ with the characteristic dimension L and the fluid velocity U [37]. The stable capillary current in the steady cone-jet mode is explained by the constant generation rate of monodisperse, charged droplets [38]. The current emitted from a TAYLOR cone is independent from the applied voltage and higher than the current in the pulsating cone-jet mode due to a higher duty cycle [27,39]. Modelling the morphology of a TAYLOR cone, REINSBERG *et al.* [31] observed that with increasing applied potential the cone shape transforms from initially convex *via* a straight generatrix to concave. Concomitantly, the cone volume and tip height as well as the jet diameter decrease and the jet velocity increases as the upper voltage-boundary of the cone-jet stability island is approached.

Above 2.95 kV the axial cone disappears in favour of two jets at opposite sides relative to the axis (Figure 5.3E). The capillary current becomes an increasing function of the potential difference (Figure 5.2) and oscillates irregularly, so that FOURIER analysis revealed no principal frequency. It can reasonably be assumed that each jet emerges with a different pulsation frequency, which would explain the absence of well-defined peaks in the FOURIER

spectra. At 3.45 kV the plume of each jet opens up, resulting in a steep rise of the capillary current (Figure 5.2). Operating the microchip at capillary currents > 100 nA decreases its lifetime significantly, which is why we usually stopped our experiments at this limit unless otherwise indicated.

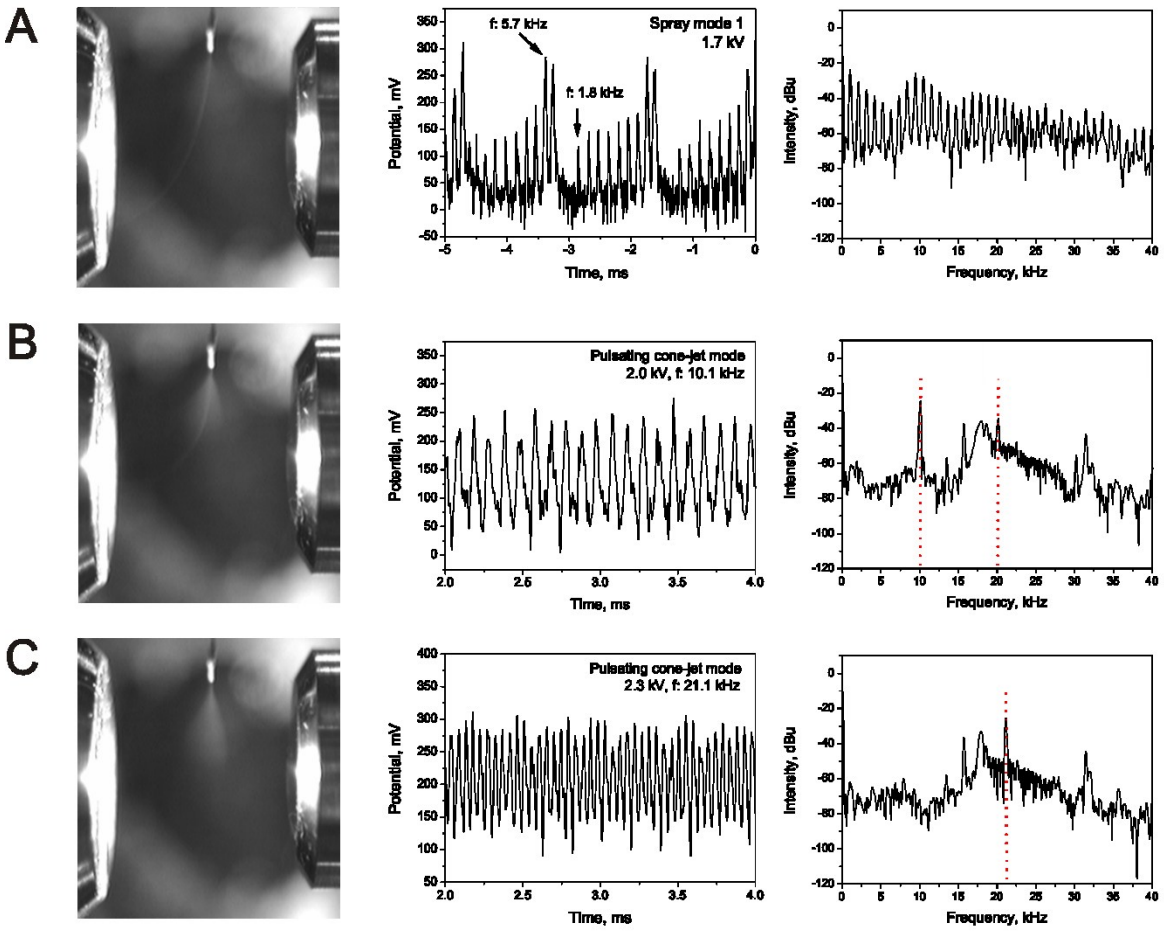

Figure 5.3: Analysis of the four observed electrospray modes at increasing potential difference between microchip emitter and end cap of the mass spectrometer by visualisation of the spray (left column) and detection of the emitter current *via* the oscilloscope (middle) and corresponding frequency (right column). Mobile phase: 60/40 (v/v) W/MeCN with 0.001% FA, flow rate: 0.3 µL/min.

(A) Spray mode 1, potential difference: 1.7 kV, oscillation frequency: 1.8 – 5.7 kHz; several separated frequencies and their harmonics reflect the polydispersity of the produced droplets.

(B) Spray mode 2 (pulsating cone-jet), 2.0 kV, one principal frequency and its second harmonic (f = 10.1 kHz, 2 x f = 20.2 kHz) are marked with red lines indicating monodisperse droplets.

(C) Spray mode 2, 2.3 kV, with increasing potential difference the principal frequency increases as well due to a higher duty cycle of the emitted droplets (f = 21.1 kHz).

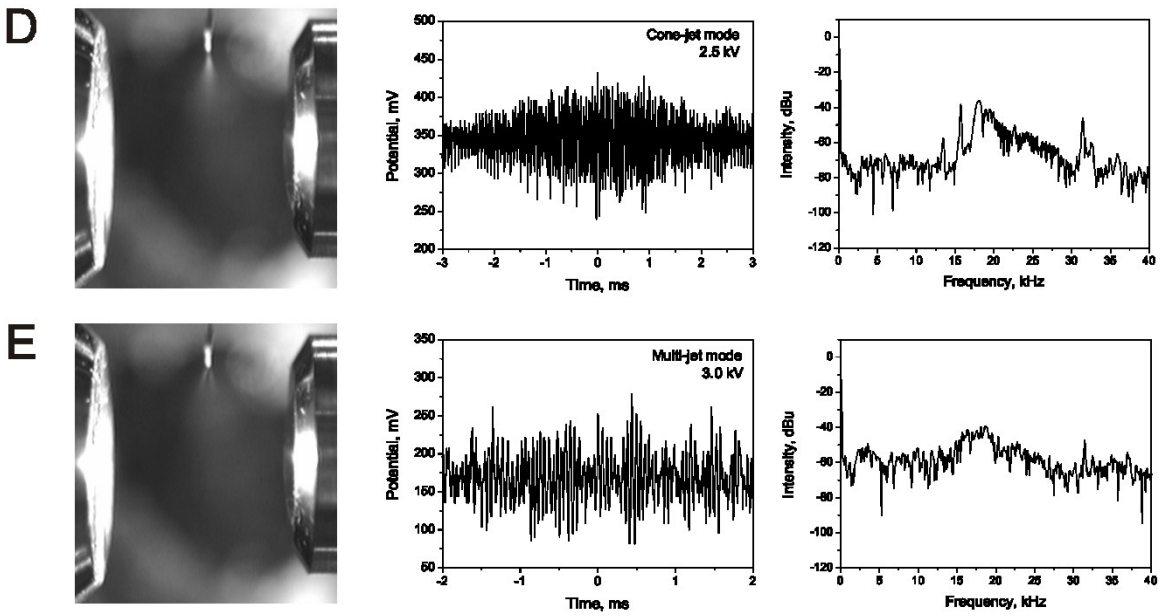

(D) **Spray mode 3 (steady cone-jet), 2.5 kV, oscillogram and corresponding FOURIER spectra become indistinguishable from the background noise pattern.**

(E) **Spray mode 4 (multi-jet), 3.0 kV; the different jets emit polydisperse droplets leading to a larger number of frequencies. The resulting FOURIER spectra show indefinable signals.**

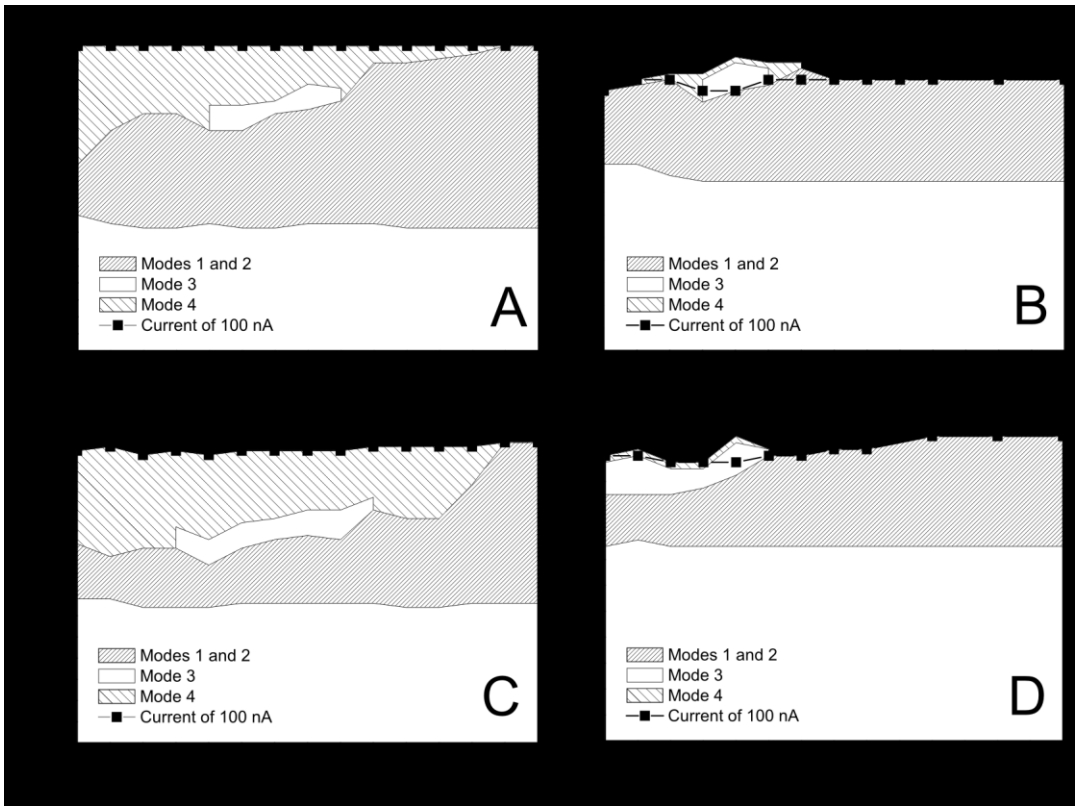

Figure 5.4: Flow-rate dependence of the cone-jet stability island for various mobile phase compositions: (A) 45/55 (v/v) W/MeCN, 0.001% FA; (B) 45/55 (v/v) W/MeCN, 0.1% FA; (C) 45/55 (v/v) W/MeOH, 0.001% FA; (D) 45/55 (v/v) W/MeOH, 0.1% FA.

5.3.3 Flow-rate dependence of the cone-jet stability island

The flow-rate dependence of the cone-jet stability island [40] has been investigated for various emitters [19,38,41]. The flow rate affects size distribution and charge of the droplets [42] and thus the electrospray mode. To quantify the impact of different flow rates on the electrospray stability in microchip HPLC/ESI-MS system, a flow-rate range of 0.1 – 0.8 µL/min was investigated for four mobile phase compositions. Figures 5.4A and 5.4B compare the effects of 0.001% and 0.1% FA, respectively, in a mobile phase of 45/55 (v/v) W/MeCN. The conductivity of the 0.1% FA-containing W/MeCN mixture is approximately ten times higher (86.6 µS/cm) than those of the 0.001% FA-containing W/MeCN mixture (8.8 µS/cm). Because we are primarily interested in the cone-jet stability island, modes 1 and 2 were condensed to simplify the figures. The onset potentials of mode 1 are very similar for both FA concentrations (2200 and 2300 V), because mode 1 depends not only on electrical forces and conductivity, but also on gravity, liquid pressure, and surface tension. A large difference exists between the two FA concentrations for the electrical potential at which the current limit of 100 nA over the microchip is reached: 3600 V for the low-FA, low-

conductivity mixture (Figure 5.4A) and *ca.* 2400 V for the high-FA, high-conductivity mixture (Figure 5.4B).

The steady cone-jet regime of the 0.1% FA-containing W/MeCN mixture is shifted to lower flow rates (0.25 – 0.35 µL/min) and smaller electrical potentials and its stability island is smaller than that of the 0.001% FA-containing W/MeCN mixture, which covers a range of 0.3–0.5 µL/min. At higher flow rates the primary emitted droplets become too large for the development of a stable cone-jet. The shift towards lower flow rates of the steady cone-jet mode for the high-conductivity mixture (Figure 5.4B) can be explained by a faster charge migration inside the solution toward the liquid-gas interface and a shorter electrical relaxation time [42]. The conical meniscus that develops when capillary, hydrostatic, and electrostatic pressures are in equilibrium at each point of the surface [40] is less perturbed and stabilizes the steady cone-jet mode at lower flow rates.

Figures 5.4C and 5.4D display the electrospray stability diagrams for 45/55 (v/v) W/MeOH with 0.001% FA (Figure 5.4C) or 0.1% FA (Figure 5.4D). The trends are the same as observed for the W/MeCN mixtures: When the conductivity of the mobile phase is increased, the cone-jet stability island shrinks and is shifted towards lower flow rates and electrical potentials. Compared with the corresponding W/MeCN mixtures, the cone-jet stability island of the W/MeOH mixtures is larger and stretched towards lower flow rates and electrical potentials. For development of a stable cone-jet, the electrical relaxation time t_e must be small compared with the hydrodynamic time t_h. If t_h approaches t_e, the charge layer on the cone surface is no longer relaxed, and the jet break-up causes large electrohydrodynamic perturbations leading to a dripping or pulsating cone-jet mode (modes 1 and 2). The conductivities of the W/MeOH mixtures are higher than those of the corresponding W/MeCN mixtures (12.1 *vs.* 8.8 µS/cm and 133.4 *vs.* 86.8 µS/cm, for 0.001% and 0.1% FA, respectively, *cf.* Figure 5.5). The higher conductivities of the W/MeOH mixtures enhance the difference between electrical relaxation and hydrodynamic time at low flow rates, which is why their cone-jet stability islands cover a broader flow-rate range. For the 0.001% FA-containing mixtures, the cone-jet stability island of the W/MeOH mixture extends that of the W/MeCN mixture by 0.05 µL/min on each side (Figures 5.4A and 5.4C). For the 0.1% FA-containing mixtures, the cone-jet regime of the W/MeOH mixture stretches down to a flow rate of 0.1 µL/min, whereas a stable cone-jet is not observed below a flow rate of 0.25 µL/ min for the W/MeCN mixture (Figures 5.4B and 5.4D).

Figure 5.3 shows that a transition between the different spray modes can be easily induced by changing the applied voltage. Conversely, at constant voltage the spray mode can

be influenced by changing the mobile phase properties and flow rates. If a high backpressure from the chromatographic column enforces a reduced system flow rate, increasing the conductivity of the mobile phase (by adding a higher amount of acid or changing the organic modifier from MeCN to MeOH) could help to achieve a stable cone-jet.

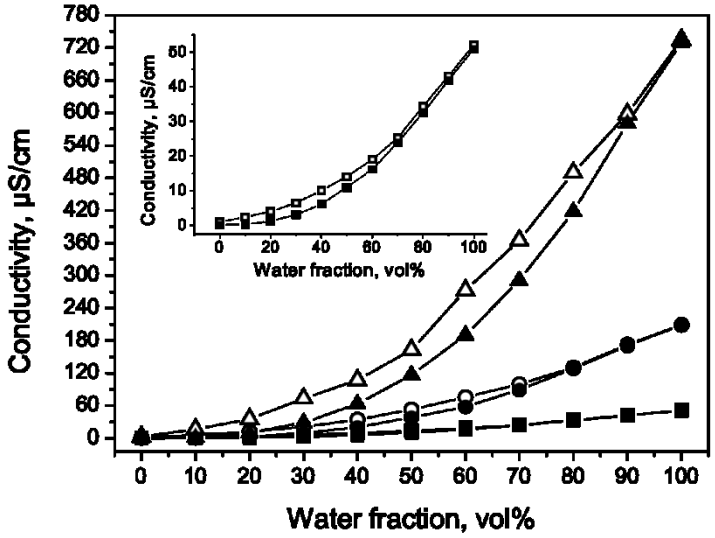

Figure 5.5: Experimentally determined electrical conductivities of W/MeCN and W/MeOH mobile phases containing varying amounts of FA. (■) W/MeCN, 0.001% FA; (●) W/MeCN, 0.01% FA; (▲) W/MeCN, 0.1% FA; (□) W/MeOH, 0.001% FA; (○) W/MeOH, 0.01% FA; (△) W/MeOH, 0.1% FA.

Table 5.1.

Physicochemical properties of the mobile phases [43-45,47-50].

	water/acetonitrile (v/v)					**water/methanol** (v/v)			
	100/0	85/15	45/55	40/60	0/100	85/15	45/55	40/60	0/100
Viscosity[47] (mPa·s)	0.89	0.99	0.77	0.72	0.35	1.29	1.58	1.54	0.56
Density (kg/m^3)	997[44]	958[44]	866[44]	855[44]	778[44]	966[50]	868[50]	851[50]	787[50]
Surface tension (10^{-3} N/m)	70.9[43]	41.5[43]	29.8[43]	29.7[43]	28.8[43]	48.5[48]	27.9[48]	26.1[48]	22.5[48]
Permittivity	78.5[49]	70.4[45]	50.8[45]	48.8[45]	35.9[45]	69.7[49]	45.5[49]	40.4[49]	31.5[49]

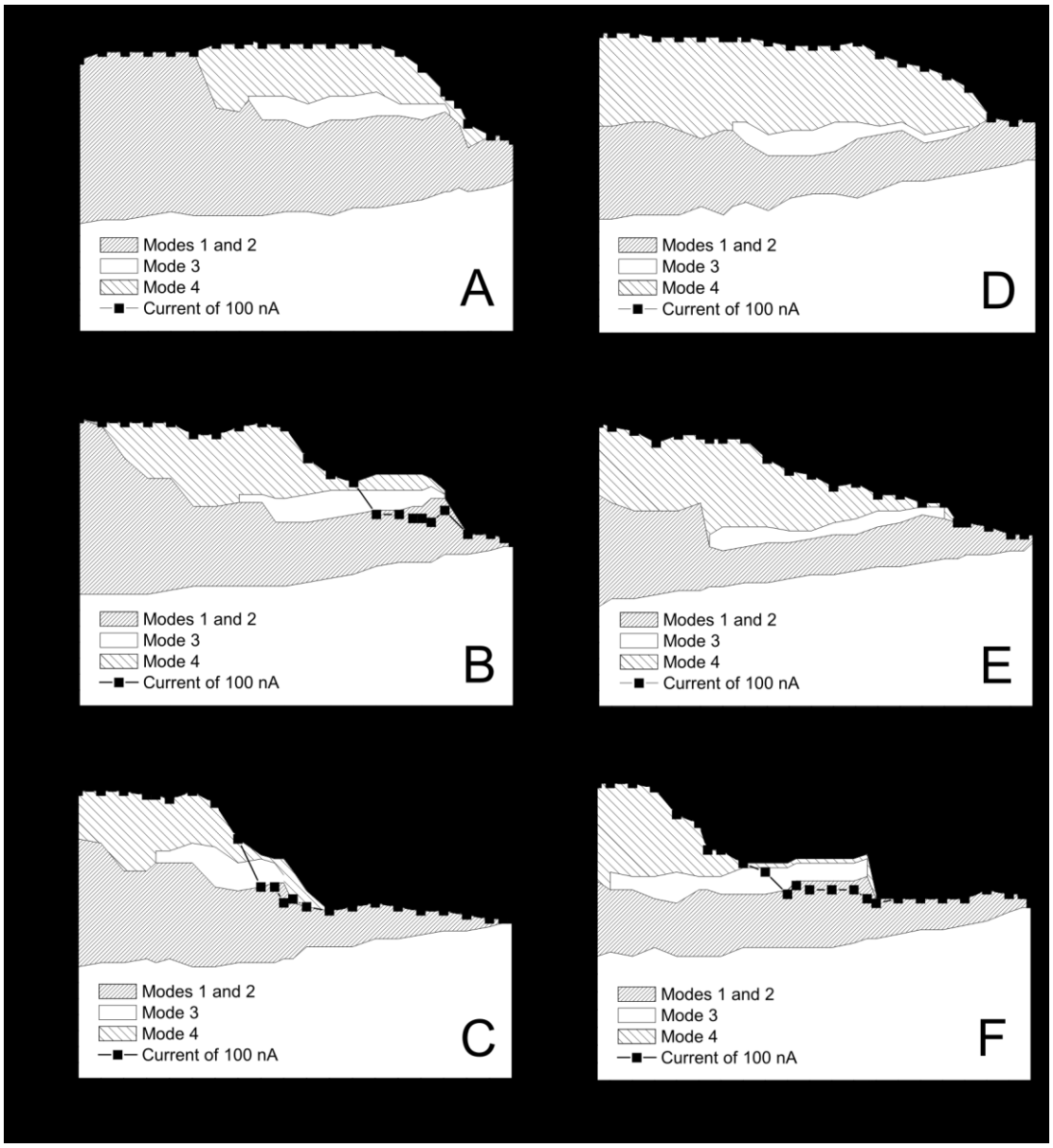

Figure 5.6: Electrospray characteristics for different mobile phase compositions at a flow rate of 0.3 µL/min. (A) W/MeCN, 0.001% FA; (B) W/MeCN, 0.01% FA; (C) W/MeCN, 0.1% FA; (D) W/MeOH, 0.001% FA; (E) W/MeOH, 0.01% FA; (F) W/MeOH, 0.1% FA.

5.3.4 Influence of water fraction and formic acid content

A decreasing water fraction in the mobile phase is generally accompanied by a decrease in bulk conductivity (Figure 5.5), surface tension, permittivity, and density (Table 5.1) of the electrosprayed solution. Figures 5.6A-C show the electrospray characteristics for W/MeCN mobile phases containing 0 – 100% water and 0.001% (Figure 5.6A), 0.01% (Figure 5.6B), or 0.1% FA (Figure 5.6C) at a flow rate of 0.3 µL/min. In all cases, the onset potentials of mode 1 increase from 0 – 100% water, because of the exponential increase of the surface tension with the water fraction in the mobile phase (*cf.* Table 1 and ref. [43]). Density and permittivity of the mobile phase (with nearly linear dependence on the water fraction [44,45]) play a

minor role, as otherwise the onset potentials would decrease with increasing water fraction. The electrical potential for the current limit of 100 nA over the microchip is a decreasing function of the conductivity and water fraction of the mobile phase (Figure 5.6A-C). W/MeCN mixtures with 0.001% FA have a stable cone-jet at 42 – 86% water (Figure 5.6A). This remains essentially unchanged for 0.01% FA (stable cone-jet for 40 – 85% water), but here the potential for the current limit is shifted towards lower values due to the higher conductivity of the solution (Figure 5.6B). The cone-jet stability island thus exceeds the current limit for water fractions > 65%. Operating in the steady cone-jet mode under these conditions would alter the nozzle and degrade the lifetime of the microchip. In Figure 5.6C the effect of the mobile phase conductivity on the electrospray characteristics is more pronounced. For a mobile phase of 85/15 (v/v) W/MeCN, for example, the conductivity changes from 37 µS/cm at 0.001% FA to 150 µS/cm at 0.01% FA (Figure 5.5), a change that the steady cone-jet mode tolerates. But a further increase to 0.1% FA raises the conductivity of the mobile phase to 495 µS/cm, a value that precludes the formation of a stable cone-jet in the instrumental setup (Figure 5.6C). Consequently, the cone-jet region for W/MeCN mixtures with 0.1% FA is shifted towards lower water fractions and confined to a range of 22 – 50% water. However, the current limit is already reached at 43% water.

If the lower limit of the cone-jet stability island is expressed in terms of the mobile phase conductivity, the values for different amounts of FA are very similar: the lower limit for W/MeCN mixtures is at bulk conductivities between 10 and 20 µS/cm (*cf.* Figure 5.5). Below this limit, at bulk conductivities < 10 µS/cm, the droplet generation rate is very slow compared with the acceleration of the charged droplets towards the counter electrode, which results in an oscillating spray current. Thus, for W/MeCN mixtures with 0.001% FA only mode 1 can be generated at water fractions < 35%.

A stable cone-jet was not observed for solutions of 0.001%, 0.01%, or 0.1% FA in neat water before the current limit was reached. The difficulty of electrospraying water without organic modifier is well known. The threshold of the critical electric field required to form a stable cone-jet increases with the surface tension of the liquid-gas atmosphere [46]. Before this value is reached for water, spontaneous corona discharges can be initiated at the capillary outlet [17].

The conductivities of W/MeOH are higher than those of W/MeCN mixtures (Figure 5.5). Yet the limiting electrical potentials (currents > 100 nA) for W/MeOH mixtures (Figures 5.6D-F) are only partly below those of W/MeCN mixtures (Figures 5.6A-C), because the higher viscosity and surface tension of W/MeOH solutions (*cf.* Table 5.1 and refs. [43], [47],

and [48]) counteract the effect of conductivity. The actual value of the emitter current depends on the distance between emitter tip and counter electrode and their vertical arrangement. Droplets from a high-viscosity liquid do not directly hit the counter electrode, but describe a longer trajectory. The additional distance covered by the charged droplets decreases the emitter current. This effect is observed for W/MeOH with 0.01% FA (Figure 5.6E), where the cone-jet regime is below the current limit, as opposed to the corresponding W/MeCN mixture (Figure 5.6B), for which the stable cone-jet region extends above the current limit at 70-85% water.

The onset potentials of mode 1 are again very similar for all investigated mobile phase compositions and conductivities, because they are mainly determined by liquid pressure, gravitational force, and surface tension. The cone-jet stability regions for W/MeOH mixtures extend over a broader range towards lower water fractions and their onset potentials are smaller than those of the W/MeCN mixtures. This is explained by the higher conductivity of W/MeOH mixtures (Figures 5.6D-F): expressed in conductivity values, the lower limits for a stable cone-jet agree well with the 10–20 µS/cm found for W/MeCN (Figure 5.5).

The upper cone-jet limit of W/MeOH mixtures is found at conductivities of 39 µS/cm (0.001% FA), 130 µS/cm (0.01% FA), and 300 µS/cm (0.1% FA). The upper cone-jet limits of the mobile phases with 0.001% and 0.01% FA are at 85% and 80% water, respectively, close to the limits of their MeCN counterparts at very similar conductivities (Figure 5.5) and slightly higher surface tension (*cf.* Table 5.1 and refs. [43] and [48]). For higher water fractions mode 2 directly transcends into mode 4 without going through a steady cone-jet phase (Figures 5.6A and 5.6D). This behaviour can be explained by the parameters that influence cone shape and height. With increasing field strength the jet formation zone extends further towards the base of the cone, yielding a rather concave shape [31], until it begins at the capillary outlet. This situation is unstable, and two jets at opposite sides relative to the axis are ejected from the rim of the capillary [26]. The meniscus is still very flat, with only short cones at the emission points. At high water fractions, surface tension and permittivity increase (*cf.* refs. [43], [45], [48], and [49]). The surface tension raises the threshold of the critical electric field required to generate a stable cone-jet. An increase in permittivity has the same effect as increasing the applied electrical field: the cone tip height decreases and the acceleration zone extends further towards the cone base. A combination of these effects destabilises the stable cone-jet and leads to the transition into a multi-jet region foregoing a stable cone-jet between the pulsating cone-jet and the multi-jet regime. A high conductivity of the mobile phase counteracts these effects. The cone morphology is elongated with a relatively large volume

and a convex shape [31]. The jet formation zone is limited to the apex of the meniscus. The remaining surface is practically equipotential, and an almost static equilibrium of forces exists at each point. From this it would be expected that the cone-jet stability island for mobile phases of higher conductivity should be extended towards higher water fractions. But W/MeOH mixtures with 0.1% FA (Figure 5.6F) develop no steady cone-jet mode for > 63% water, and the corresponding W/MeCN mixtures (Figure 5.6C) behave similarly, with an upper cone-jet limit at 50% water.

To understand why the steady cone-jet mode cannot develop for mobile phases containing a high amount of water and FA, the explanations given above must be complemented by specifying some system-dependent parameters that influence the electrospray mode, *e.g.*, the electrode arrangement inside the spray chamber (Figure 5.1) and the parameter settings. The emitted jets or droplets are attracted not only by the end cap, but also by the additional electrode. If the liquid jet or at least parts of it is side-tracked towards the additional electrode, it either oscillates between end cap and additional electrode or breaks up into several jets (mode 4). With increasing conductivity, surface tension, and permittivity of the mobile phase, the attractive forces of the additional electrode gain influence. Aside from the changes in the physicochemical properties of the mobile phase and the resulting electrical forces, the cone volume is reduced by evaporation of the liquid due to high temperature and drying gas flow in the interface. With a rather concave cone shape (resulting from an increase in permittivity and applied potential), liquid evaporation is expected to gain influence due to the increased surface-to-volume ratio of the cone. These effects are detrimental to a stable cone-jet and restrict the cone-jet stability island to comparatively low water fractions. Reducing the drying temperature and drying gas flow rate yields a higher fluid volume at the nozzle, which may build up and stabilise the cone.

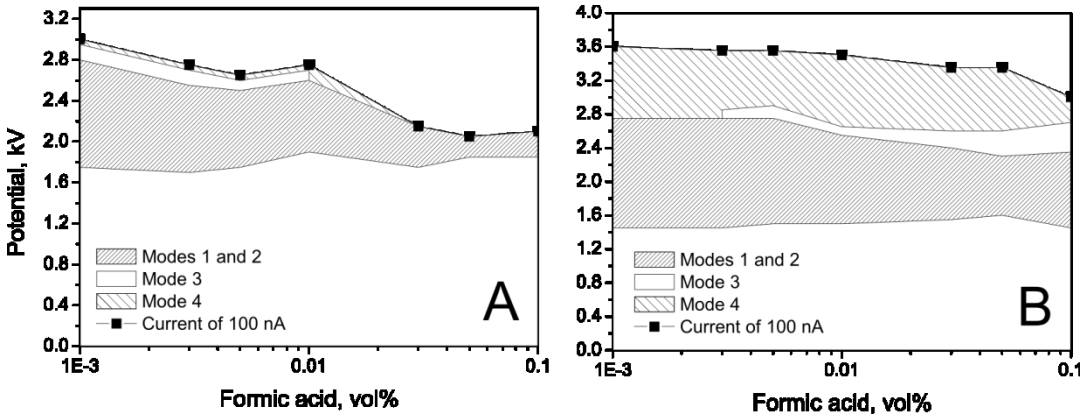

Figure 5.7: Electrospray characteristics for bulk conductivity changes of the mobile phase due to an increasing FA content (0.001 – 0.1%). Mobile phase: (A) 85/15 (v/v) W/MeCN; (B) 40/60 (v/v) W/MeCN. Flow rate: 0.3 µL/min.

5.3.5 Effect of a gradually changing mobile phase conductivity

It was studied whether a gradual change of the conductivity of the mobile phase would alter the electrospray behaviour by varying the amount of FA from 0.001% to 0.1% in mixtures of 85/15 (v/v) W/MeCN and 40/60 (v/v) W/MeCN (Figures 5.7A and 5.7B, respectively). The chosen volumetric ratios represent typical start and end mobile phase compositions in RP-HPLC gradient elution separations. A water fraction of 85% in W/MeCN mixtures is also the upper limit for the steady cone-jet mode (*cf.* Figures 5.6A and 5.6B). The flow rate was kept at 0.3 µL/min, while the potential difference was increased until the stable cone-jet disappeared or the current limit of 100 nA over the microchip was reached. With a mobile phase of 85/15 (v/v) W/MeCN a stable cone-jet can be generated at 0.001 – 0.01% FA content (Figure 5.7A). Within this range of FA concentrations, the onset potential for the steady cone-jet mode decreases and the range of electrical potentials before the current reaches 100 nA narrows with increasing mobile phase conductivity (Figure 5.7A). No stable cone-jet is observed for FA > 0.01% and for FA > 0.03% the electrospray exists only in modes 1 and 2.

With a mobile phase of 40/60 (v/v) W/MeCN (Figure 5.7B) the steady cone-jet mode is shifted to higher amounts of FA. For FA < 0.003% the conductivity is too low for a continuous droplet generation, thus, the resulting electrospray shows oscillating behaviour. With increasing conductivity the onset potentials of the steady cone-jet mode decrease and the operational range of electrical potentials widens.

A comparison of Figures 5.7A and 5.7B reveals the conditions for maintaining a stable cone-jet during a mobile phase gradient from 85/15 (v/v) to 40/60 (v/v) W/MeCN: A concentration of 0.01% FA and an electrical potential of 2.6 kV. Setting other conditions a continuous operation in the steady cone-jet mode during this mobile phase gradient is

impossible. A mobile phase gradient starting with a water fraction > 85% (98% is not uncommon) would exceed the microchip's current limit due to the high conductivity of the mobile phase (*cf.* Figure 5.6B). The conclusions from Figure 5.7 are not only relevant for gradient elution RP HPLC, where the increasing fraction of organic modifier in the mobile phase effects a gradual change of the bulk conductivity, but also for temporary increases in conductivity, which occur, *e.g.*, during analysis of biological samples that have a higher concentration of ionic species (background salts and analytes) than the running mobile phase.

If the goal is to operate continuously in the steady cone-jet mode, the experimental parameters have to be adapted during HPLC/MS analysis to the physicochemical properties of the electrosprayed solution.

5.4 Conclusions

A commercial microchip-HPLC/ESI-MS configuration was modified for electrospray diagnostics based on frequency analysis of the microchip emitter current and spray imaging. This approach enabled the detection of different spray modes, the steady cone-jet mode in particular, and their stability regimes under varied experimental conditions. Water-acetonitrile and water-methanol mixtures with formic acid were chosen as the electrosprayed solutions to represent typical mobile phases in reversed-phase HPLC.

At low water fractions in the mobile phase the stability regime is limited by the bulk conductivity: Below a critical conductivity the droplet generation rate, which depends on charge separation, is too slow for a stable cone-jet. With increasing bulk conductivity of the mobile phase the cone-jet stability island is shifted towards larger amounts of organic modifier. Due to the higher conductivity of water-methanol compared with water-acetonitrile mixtures, the cone-jet stability islands of water-methanol mobile phases are larger and tolerate higher fractions of organic modifier as well as lower flow rates.

At high water fractions and conductivities, the attractive forces of the additional electrode in the instrumental setup on the liquid jet gain influence so that the steady cone-jet mode is by-passed and the pulsating cone-jet mode transcends directly into the multi-jet mode. A water fraction > 85% in the mobile phase prevents the generation of a steady cone-jet mode even at moderate bulk conductivities (low amount of formic acid), because of the increased surface tension of the electrosprayed liquid. To counteract at least the destabilising effect of permittivity, the cone volume can be enlarged by reducing the drying temperature

and gas flow in the electrospray interface. Additionally, the current limit for operating the microchip has to be kept in mind, and this limit is shifted to lower water fractions if larger amounts of formic acid or other conductivity-enhancing solvents are present and shrinks the operational range further.

This work demonstrates that during a typical gradient elution HPLC/ESI-MS analysis the cone-jet stability island is easily crossed because of dynamic changes in bulk conductivity and surface tension of the electrosprayed liquid. With a relatively simple modification of the ESI-MS configuration by introducing a transimpedance amplifier and an oscilloscope into the electrical circuit the emitter current provides excellent feedback for electrospray diagnostics. Further investigations of the influence of electrospray instabilities on the performance of HPLC/ESI-MS analyses will assist in the development of hard- and software for online monitoring and controlling the electrospray mode which will irretrievably lead to an improvement of the sensitivity and reproducibility of HPLC-MS methods.

References

[1] X. Chen, D.-F. Cui, Microsyst. Technol. 15 (2009) 667-676.

[2] K. Ohno, K. Tachikawa, A. Manz, Electrophoresis 29 (2008) 4443-4453.

[3] I. Oita, H. Halewyck, B. Thys, B. Rombaut, Y. Vander Heyden, D. Mangelings, Anal. Bioanal. Chem. 398 (2010) 239-264.

[4] D. Mark, S. Häberle, G. Roth, F. von Stetten, R. Zengerle, Chem. Soc. Rev. 39 (2010) 1153-1182.

[5] J.R. Kraly, R.E. Holcomb, Q. Guan, C.S. Henry, Anal. Chim. Acta 653 (2009) 23-35.

[6] K. Gupta, D.-H. Kim, D. Ellison, C. Smith, A. Kundu, J. Tuan, K.-Y. Suh, A. Levchenko, Lab Chip 10 (2010) 2019-2031.

[7] A. Arora, G. Simone, G.B. Salieb-Beugelaar, J.T. Kim, A. Manz, Anal. Chem. 82 (2010) 4830-4847.

[8] J.F. Dishinger, R.T. Kennedy, Electrophoresis 29 (2008) 3296-3305.

[9] K. Uchiyama, H. Nakajima, T. Hobo, Anal. Bioanal. Chem. 379 (2004) 375-382.

[10] J. Lee, S.A. Soper, K.K. Murray, J. Mass Spectrom. 44 (2009) 579-593.

[11] T. Sikanen, S. Franssila, T.J. Kauppila, R. Kostiainen, T. Kotiaho, R.A. Ketola, Mass Spectrom. Rev. 29 (2010) 351-391.

[12] S. Koster, E. Verpoorte, Lab Chip 7 (2007) 1394-1412.

[13] I.M. Lazar, J. Grym, F. Foret, Mass Spectrom. Rev. 25 (2006) 573-594.

[14] S. Khirevich, A. Höltzel, D. Hlushkou, U. Tallarek, Anal. Chem. 79 (2007) 934-9349.

[15] M. Prudent, H.H. Girault, Analyst 134 (2009) 2189-2203.

[16] P. Kebarle, U.H. Verkerk, Mass Spectrom. Rev. 28 (2009) 898-917.

[17] M. Cloupeau, B. Prunet-Foch, J. Aerosol Sci. 25 (1994) 1021-1036.

[18] R. Kostiainen, T.J. Kauppila, J. Chromatogr. A 1216 (2009) 685-699.

[19] R.T. Kelly, K. Tang, D. Irimia, M. Toner, R.D. Smith, Anal. Chem. 80 (2008) 3824-3831.

[20] I. Marginean, R.T. Kelly, R.J. Moore, D.C. Prior, B.L. LaMarche, K. Tang, R.D. Smith, J. Am. Soc. Mass Spectrom. 20 (2009) 682-688.

[21] I. Marginean, R.T. Kelly, D.C. Prior, B.L. LaMarche, K. Tang, R.D. Smith, Anal. Chem. 80 (2008) 6573-6579.

[22] G.A. Valaskovic, J.P. Murphy, M.S. Lee, J. Am. Soc. Mass Spectrom. 15 (2004) 1201-1215.

[23] H. Yin, K. Killeen, J. Sep. Sci. 30 (2007) 1427-1434.

[24] P. Hoffmann, M. Eschner, S. Fritzsche, D. Belder, Anal. Chem. 81 (2009) 7256-7261.

[25] S.L.S. Freire, H. Yang, A.R. Wheeler, Electrophoresis 29 (2008) 1836-1843.

[26] A. Jaworek, A. Krupa, J. Aerosol Sci. 30 (1999) 873-893.

[27] R. Juraschek, F.W. Röllgen, Int. J. Mass Spectrom. 177 (1998) 1-15.

[28] I. Marginean, L. Parvin, L. Heffernan, A. Vertes, Anal. Chem. 76 (2004) 4202-4207.

[29] P. Nemes, I. Marginean, A. Vertes, Anal. Chem. 79 (2007) 3105-3116.

[30] L. Parvin, M.C. Galicia, J.M. Gauntt, L.M. Carney, A.B. Nguyen, E. Park, L. Heffernan, A. Vertes, Anal. Chem. 77 (2005) 3908-3915.

[31] K.-G. Reinsberg, U. Effelsberg, U. Tallarek, Lab Chip 9 (2009) 2914.

[32] A. Gapeev, A. Berton, D. Fabris, J. Am. Soc. Mass Spectrom. 20 (2009) 1334-1341.

[33] R. Ramanathan, R. Zhong, N. Blumenkrantz, S.W. Chowdhury, K.B. Alton, J. Am. Soc. Mass Spectrom. 18 (2007) 1891-1899.

[34] G.O. Staples, H. Naimy, H. Yin, K. Kileen, K. Kraiczek, C.E. Costello, J. Zaia, Anal. Chem. 82 (2010) 516-522.

[35] S. Ehlert, L. Trojer, M. Vollmer, T. van de Goor, U. Tallarek, J. Mass Spectrom. 45 (2010) 313-320.

[36] S. Jung, A. Höltzel, S. Ehlert, J.-A. Mora, K. Kraiczek, M. Dittmann, G.P. Rozing, U. Tallarek, Anal. Chem. 81 (2009) 10193-10200.

[37] A.M. Gañán-Calvo, J. Dávila, A. Barrero, J. Aerosol Sci. 28 (1997) 249-275.

[38] I. Marginean, R.T. Kelly, J.S. Page, K. Tang, R.D. Smith, Anal. Chem. 79 (2007) 8030-8036.

[39] J. Fernández de la Mora, I.G. Loscertales, J. Fluid Mech. 260 (1994) 155-184.

[40] M. Cloupeau, B. Prunet-Foch, J. Electrostat. 22 (1989) 135-159.

[41] A. Schmidt, M. Karas, T. Dülcks, J. Am. Soc. Mass Spectrom. 14 (2003) 492-500.

[42] L. de Juan, J. Fernández de la Mora, J. Colloid Interface Sci. 186 (1997) 280-293.

[43] W.R. Melander, Cs. Horváth, High Performance Liquid Chromatography – Advances and Perspectives, Academic Press, New York, 1980.

[44] C. Moreau, G. Douhéret, Thermochim. Acta 13 (1975) 385-392.

[45] C. Moreau, G. Douhéret, J. Chem. Thermodyn. 8 (1976) 403-410.

[46] J.M. López-Herrera, A. Barrero, A. Boucard, I.G. Loscertales, M. Márquez, J. Am. Soc. Mass Spectrom. 15 (2004) 253-259.

[47] H. Colin, J.C. Diez-Masa, G. Guiochon, T. Czajkowska, I. Miedziak, J. Chromatogr. 167 (1987) 41-65.

[48] G. Vázquez, E. Alvarez, J.M. Navaza, J. Chem. Eng. Data 40 (1995) 611-614.

[49] G. Åkerlöf, J. Am. Chem. Soc. 54 (1932) 4125-4139.

[50] S.Z. Mikhail, W.R. Kimel, J. Chem. Eng. Data 6 (1961) 533-537.

Chapter III – Part B

Microchip electrospray: Improvements in spray and signal stability during gradient elution by an inverted post-column make-up flow

5.5 Introduction

High performance liquid chromatography (HPLC) coupled to mass spectrometry (MS) can be regarded as one of the most powerful workflows in chemical and biochemical analysis [1-3]. HPLC-MS provides high selectivity and high sensitivity together with short run times. Electrospray ionization (ESI) can easily be utilised with a flowing liquid and has become a routine tool for on-line coupling of HPLC with MS [4,5]. The necessity of manipulating small sample volumes in peptide and protein analysis led to an enormous progress in developing microfabricated fluidic devices [6]. Recent research focused on integrated ESI interfaces to spray directly from the microchip [7,8]. In any mass spectrometric analysis signal stability is critical to achieve high quality spectral data and good reproducibility for quantification. Ideally, the ion source should be capable of sustaining maximal ion production throughout the detection duty cycle. In ESI, the ion production rate is directly correlated to the spray stability, which in turn is influenced by the interplay of many factors including the applied voltage, emitter geometry, distance between emitter and MS inlet, flow rate, and solvent composition [9-15].

In general, most of the experimental conditions like flow rate and solvent composition are dictated by the HPLC separation. Only the applied voltage and emitter position can be adjusted prior to the analysis. Typically, a constant voltage is applied to the emitter, often selected according to the manufacturer's recommendations or experience based on previous analysis. The optimisation of emitter voltage with respect to spray morphology, signal stability, and ion production rate occurs rarely. Further, routine gradient elution in HPLC-MS analysis is usually performed without performance feedback from the electrospray, and the voltage that ensures optimal electrospray conditions at the beginning of the separation may not be appropriate for the mobile phase composition at the end of the solvent gradient. Changes of the physicochemical properties of the eluent *(e.g.*, surface tension, permittivity, electrical conductivity, and viscosity) during gradient elution HPLC separations alter the

electrospray operation mode [16-18], resulting in a drift of the optimum emitter voltage. Only a few attempts to automatically control the electrospray mode during the analysis have been reported [18-20].

VALASKOVIC *et al*. [18] used a feedback loop in which a control algorithm adjusts the applied voltage. The optoelectronic system provides an image analysis of the electrospray mode with reflected and strobed light illumination and is capable to respond to changes in the flow rate and solvent composition by tuning the applied voltage. GAPEEV *et al*. [19] developed a feedback mechanism based on spray current measurements. The system adjusts the applied emitter voltage according to real-time readings of the electrospray current. MARGINEAN *et al*. [20] built a similar feedback circuit and evaluated algorithms that can maintain the electrospray voltage within the optimum operation range throughout HPLC gradient elution by interpreting spray current measurements.

A simpler approach requiring less electronic components is the implementation of a post-column mobile phase gradient *(i.e.*, behind the chromatographic separation) that behaves inverse with respect to the HPLC separation gradient. In capillary electrophoresis, the addition of a liquid enhancing the electrospray properties of the background electrolyte after the separation channel and prior the ESI tip is a common feature [21,22]. This technique is scarcely used in chromatography. RAMANATHAN *et al.* [23] used a so-called response-normalisation flow to the HPLC effluent to minimise the effect on the analyte response resulting from changes in solvent composition. They utilised two HPLC systems for solvent delivery which unite in a T-junction prior to the ESI source. A chip-based format working in a similar way was developed by Agilent Technologies and tested for the separation of heparinoids [24]. This novel HPLC microchip allows the introduction of a post-column make-up flow (MUF) to the effluent of the analytical separation column. STAPLES *et al.* [24] employed a neat organic MUF and optimised the ratio of analytical column flow rate and MUF rate, but did not determine the influences of the spray mode and MUF compensation with varying mobile phase composition (*e.g.*, by exactly inverted gradient conditions) on electrospray performance. Thus, the resulting flow after uniting the column effluent and MUF still undergoes a (small) change of mobile phase composition, which may influence the electrospray performance.

In the present work the electrospray characteristics of a HPLC/ESI-MS system equipped with this MUF chip are investigated. The ability of the MUF chip to eliminate the need for adapting the emitter voltage during HPLC gradient elution is studied, when dynamic changes in solvent composition can be compensated any time. Infusion experiments with a

small analyte in aqueous acetonitrile solutions containing formic acid were performed to record signal intensities for different electrospray modes and solvent compositions. Analyte peak parameters were determined at constant emitter voltage by injecting the analyte dissolved in eluents of different composition. Our results demonstrate significant improvements in spray and signal stability with this post-column MUF compensation over the entire range of solvent compositions, without compromising the achieved chromatographic separation efficiency.

5.6 Experimental section

5.6.1 Mobile phase compositions and analytes

Mobile phases consisted of water (W) and acetonitrile (ACN) and contained 0 – 100 vol% water and formic acid (FA). Acetonitrile of HPLC grade was purchased from Sigma-Aldrich Chemie GmbH (Taufkirchen, Germany) and formic acid (p.a.) came from Fluka Chemie GmbH (Buchs, Switzerland). HPLC grade water (5.5×10^{-6} S/m) was obtained from a Milli-Q gradient water purification system (Millipore, Billerica, MA, USA). The tetrapeptide analyte MRFA (Met-Arg-Phe-Ala) was bought from Sigma-Aldrich Chemie GmbH (Taufkirchen, Germany). A stock solution of c = 1.667 pmol/µL in 50/50 (v/v) W/ACN was used for sample preparation and stored in a freezer.

5.6.2 Microchip electrospray configuration

An Agilent HPLC-ChipCube-MS interface was used with a HPLC-MS microchip coupled to a 1200 LC/MSD XCT Ultra ion trap mass spectrometer (Agilent Technologies, Waldbronn, Germany). The polyimide-based microchip contained a 6-port valve for sample injection and solvent delivery, two particle-packed microchannels that served as sample enrichment column (U-shaped) and separation column (S-shaped), one empty microchannel that delivered the MUF, and a nanoelectrospray tip (Figure 5.8A). The electrospray current was measured through the electrical interface on the microchip using a custom-built transimpedance amplifier converting the incoming current into an outgoing potential difference at 100 nA/V. As illustrated by Figure 5.8B the transimpedance amplifier was connected to a 10 MHz digital pc-oscilloscope (PicoScope 2204, Pico Technology, St Neots, UK). The oscilloscope's FOURIER transformation tool was used for frequency analysis. The 500 nL enrichment column was coupled to an Agilent 1200 cap pump via port A5, the 15 cm long separation column with

a Gaussian cross-section [25] (channel height ~ 75 µm, channel base width ~ 100 µm) was connected to an Agilent 1200 nano pump *via* port A2, and the MUF was delivered by an additional Agilent 1200 nano pump to the MUF channel (overall volume ~ 30 nL) *via* port A4 (Figure 5.8C and 5.8D).

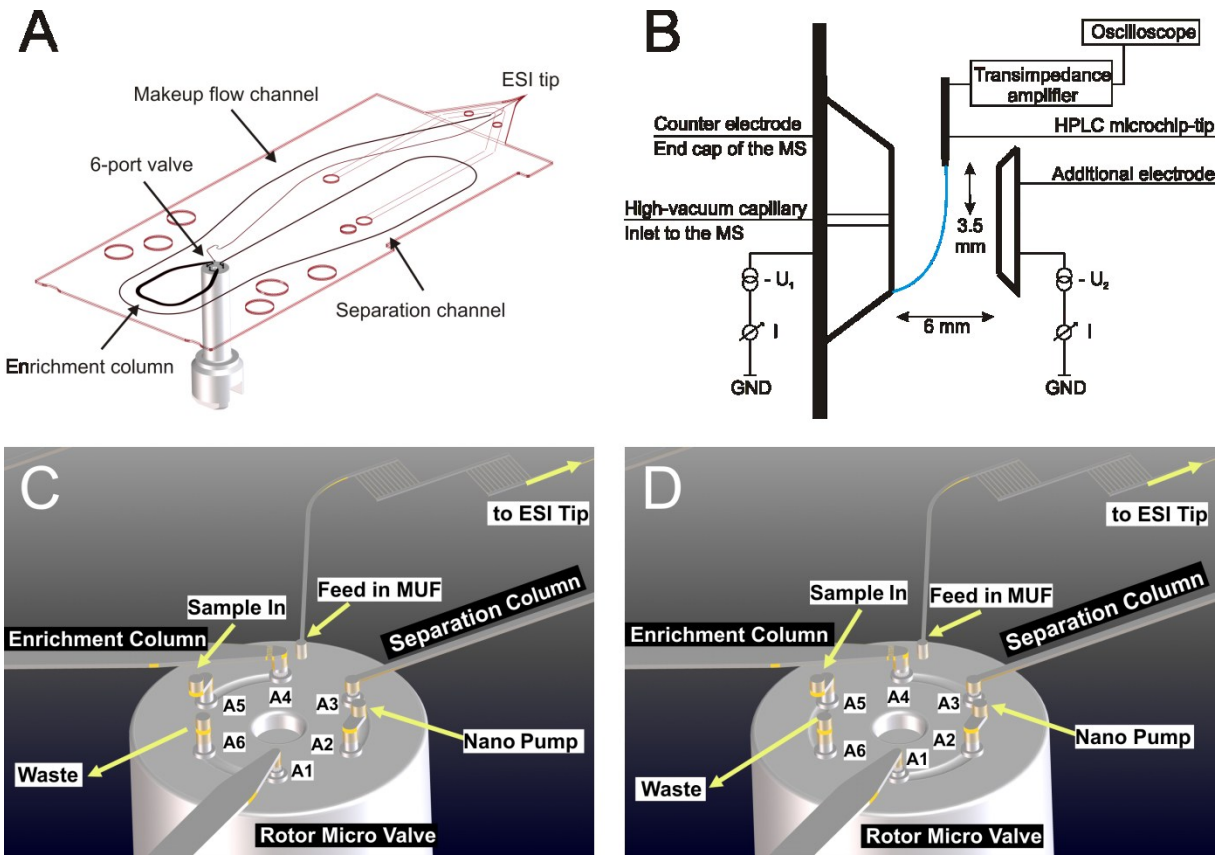

Figure 5.8: Layout of the microchip-HPLC/ESI-MS configuration. (A) Polyimide-based microchip with separation column (15 cm long), enrichment column (500 nL), MUF channel, and ESI tip. (B) Positioning of the microchip inside the ESI-MS interface. (C,D) Schematic of the 6-port valve on the microchip and its two configurations: (C) sample loading position prior to the analysis, and (D) separation position, where the sample is transferred onto the separation column by the nano pump.

Infusion experiments were made with an empty microchip, whereas in sample injection mode a microchip packed with 5 µm ZORBAX 300 SB-C18 particles (separation column and enrichment column) by Agilent Technologies was used. The microchip was positioned inside the ChipCube spray chamber between a counter electrode (end cap of the MS) and an additional electrode, 90° off-axis with respect to the MS inlet such that the ESI tip was *ca.* 3 mm away from the cone and *ca.* 3.5 mm above its axis (Figure 5.8B).

5.6.3 HPLC-MS analysis

All data were acquired in the positive-ion mode by applying ground potential to the liquid and negative potential to the end cap and additional electrode. A constant potential difference of 500 V between end cap (U_1) and additional electrode (U_2) made the end cap the part with the most negative potential in the system (Figure 5.8B). A drying gas flow rate of F = 4 L/min and a drying temperature of 320 °C were used. The potential difference between the emitter tip and end cap was varied *via* the TrapControl software (version 6.2), which allows changes in steps of minimal 50 V.

An Agilent 1200 cap pump at a flow rate of F = 4 µL/min attached to an Agilent 1100 µ-wellplate autosampler was used for sample injection. For the determination of peak parameters samples consisting of MRFA dissolved in running mobile phase were injected. In sample injection mode, the sample (injection volume: 0.5 µL) was loaded from the autosampler onto the enrichment column *via* the 6-port valve, whereas the separation column was equilibrated with mobile phase (Figure 5.8C). A rotor switch controlled by ChemStation software started sample elution from the enrichment column onto the separation column (Figure 5.8D). Infusion experiments were carried out with an empty MUF chip connected to a micro syringe (ILS GmbH, Stützerbach, Germany) installed on a syringe pump (Harvard Apparatus, Holliston, MA, USA). For post-column MUF compensation two syringes (one connected to the separation column *via* port A2, the other one connected to the MUF channel *via* port A4) were used, both installed on the double-barreled syringe pump to avoid flow rate fluctuations.

Signal intensities of infusion experiments were determined with DataAnalysis software (version 4.0). Peak parameters from sample injections were analysed with ChemStation software (Rev.B.01.03-SR2) after extracting the MS files. Each experiment was repeated four times and results were averaged.

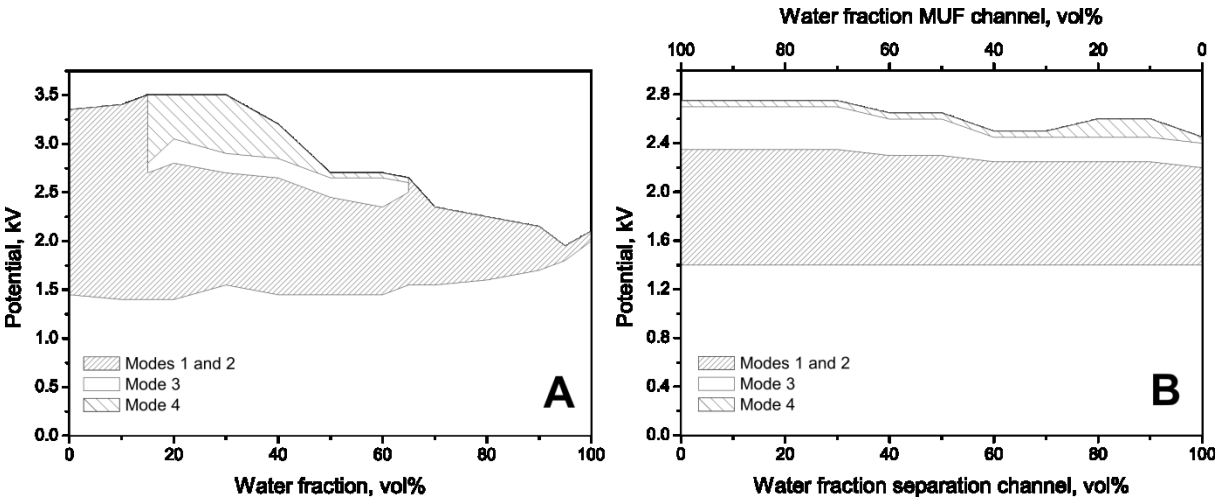

Figure 5.9: (A) Microchip electrospray characteristics for water-acetonitrile mixtures containing 0.05 vol% FA infused through the microchip's separation channel, F = 0.4 µL/min.
(B) Electrospray characteristics with the post-column MUF compensation. Separation channel: water-acetonitrile, 0.05 vol% FA, F = 0.2 µL/min; MUF channel: water-acetonitrile, 0.05 vol% FA, F = 0.2 µL/min.

5.7 Results and Discussion

5.7.1 Impact of the post-column MUF on the cone-jet stability island

Four distinct electrospray modes can be distinguished using criteria that were definable with the instrumental configuration based on a frequency analysis of the microchip emitter current combined with spray imaging [16,17]. This approach allowed detection of the different spray modes as well as their onset potentials precisely. A description of the four electrospray modes and their characteristics is given in Section 5.3.2 and Figure 5.3.

Figure 5.9A documents the four spray mode regimes (their "stability islands") for the full range of W/ACN mobile phases containing 0.05 vol% FA, which are infused (F = 0.4 µL/min) *via* the microchip's separation column. The potential difference between microchip emitter tip and end cap of the MS was stepwise increased, until a current limit of 100 nA (set by the manufacturer) was reached. The steady cone-jet mode, which is desirable because of a large and stable spray current and the production of smaller initial droplets [18,26-28], is reached only with water fractions of 15 – 65% at different emitter voltages (Figure 5.9A, mode 3). There is no single voltage which assures operation in the steady cone-jet mode over a complete W/ACN gradient run in HPLC-MS practice. The operation mode changes with the mobile phase composition due to the significant decrease in electrical conductivity, together with a decrease in surface tension, dielectric constant, viscosity, and density at increasing acetonitrile content [17]. At the start of a gradient run (water fraction ≥ 90%) mode 1 is the only stable electrospray configuration. Choosing a starting voltage of

2.0 kV, the established electrospray mode changes from mode 1 to mode 2 towards the end of the separation gradient (water fraction ~ 40%). Concomitantly, the spray appearance changes from a liquid stream to a less pronounced stream line of liquid surrounded by a distinct plume. To account for these differences the emitter voltage has to be reduced manually by about 300 V during a gradient run (1.7 kV corresponds to mode 1 at 40% water in the eluent). Although adapting the emitter voltage results in equal spray appearance, analyte signal response and spray current can still vary.

To overcome the disadvantages of spray mode instabilities and eventual spray mode transitions during HPLC-MS analysis, the changes in the eluent composition were compensated directly before the ESI tip with an additional solvent delivered by the MUF channel (*cf.* Figure 5.8A). At *any* time, the MUF channel provides an inverted solvent composition with respect to the actual composition in the separation column, *e.g.*, 30/70 (v/v) W/ACN in the MUF channel *vs*. 70/30 (v/v) W/ACN in the separation channel. Figure 5.9B shows the resulting spray mode regimes with this post-column MUF for the full range of W/ACN mobile phases. To account for the different mass transport properties (flow rates) that influence electrospray performance, solvent flow rates in the experiments with MUF compensation were halved (F = 0.2 µL/min in the separation column and MUF channel, Figure 5.9B). This provides the same volumetric flow rate as in the experiments without post-column MUF (F = 0.4 µL/min, Figure 5.9A). With MUF compensation the composition of the electrosprayed solution at the nozzle always adds up to 50/50 (v/v) W/ACN with 0.05 vol% FA, which ensures a steady cone-jet mode over the entire range of water fractions in the separation channel (Figure 5.9B). Smaller deviations in the onset of mode 4 (multi-jet mode) are caused by differences in the accuracy of the nano pumps and aging of the ESI tip. As a consequence of the inverted post-column MUF, relevant properties of the electrosprayed liquid (electrical conductivity, surface tension, dielectric constant, viscosity, and density) remain constant over a complete gradient run in HPLC-MS analysis.

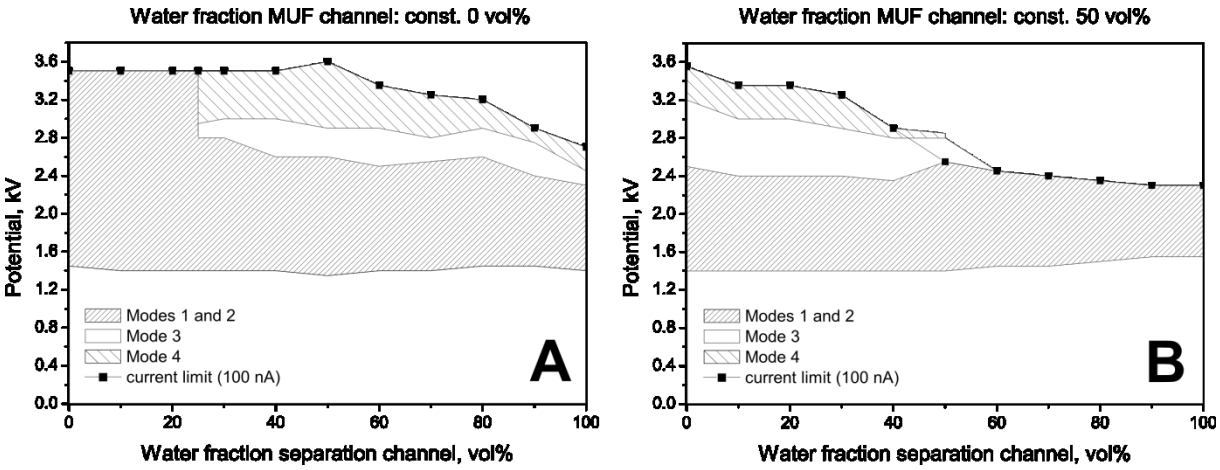

Figure 5.10: Microchip electrospray characteristics for post-column MUF with constant composition of the mobile phase supplied by the MUF channel. (A) Separation channel: water-acetonitrile, 0.05 vol% FA, F = 0.2 µL/min; MUF channel: neat acetonitrile, 0.05 vol% FA, F = 0.2 µL/min. The steady cone-jet mode is realised for 25 – 100% water in the separation channel, which translates to a water fraction of 12.5 – 50% in the electrospray. (B) Separation channel: water-acetonitrile, 0.05 vol% FA, F = 0.2 µL/min; MUF channel: 50/50 (v/v) W/ACN, 0.05 vol% FA, F = 0.2 µL/min. The steady cone-jet regime is realised for 0 – 60% water in the eluent passing the separation channel. The mobile phase in the ESI tip contains 25 – 55% water.

Another possibility to modulate the electrosprayed solution for improved MS operation during gradient elution is the delivery of a MUF with constant solvent composition, *e.g.,* 100% acetonitrile or a 50/50 (v/v) W/ACN mixture. Both modulations resulted in extended steady cone-jet regimes compared to the non-compensated electrospray behaviour in Figure 5.9A. In particular, the mobile phase composition at the ESI tip adds up to 50% water when 100% water passes the separation channel and 100% acetonitrile passes the MUF channel (Figure 5.10A). With 50% water in the separation channel, solvent at the ESI tip contains 25% water. The desirable steady cone-jet mode (mode 3) is realised for 25 – 100% water in the separation channel, which translates to a water fraction of 12.5 – 50% in the electrospray. The lower limit is very similar to the one for non-compensated electrospray (15% water) in Figure 5.9A. A constant liquid supply of 50/50 (v/v) W/ACN mixture *via* the MUF channel results in a steady cone-jet regime that ranges from 0 to 60% (Figure 5.10B), which corresponds to 25 – 55% water in the ESI tip. The upper limit without MUF was found at 65% water (Figure 5.9A), translating to 80% water in the separation channel with a MUF of 50/50 (v/v) W/ACN. The steady cone-jet regime with this MUF can probably be reached with 80% water, but at higher potential differences. However, the microchip's current limit of 100 nA is reached before the steady cone-jet mode sets in. Operating the microchip beyond

this current limit reduces its life time significantly, and was not increased the potential difference further.

In neither case of constant MUF solvent a steady cone-jet mode is reached over the entire range of solvent compositions at constant emitter voltage. An optimal balance of the electrospray behaviour in gradient HPLC-MS analysis is only achieved by applying an *inverted* solvent gradient through the MUF channel, as demonstrated by Figure 5.9B.

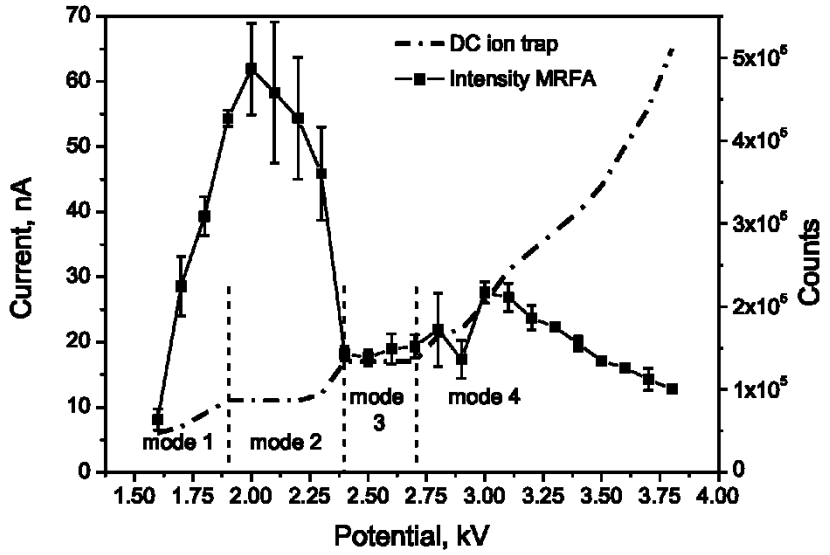

Figure 5.11: Microchip emitter current (dashed line) *vs.* the applied electrical potential at the end cap of the mass spectrometer's inlet. Changes in the slope indicate transitions between individual electrospray modes. Symbols illustrate the corresponding signal intensities recorded for the tetrapeptide analyte MRFA (Met-Arg-Phe-Ala), c = 8.34 fmol/µL. Mobile phase: 50/50 (v/v) W/ACN containing 0.001 vol% FA, F = 0.33 µL/min.

5.7.2 Impact of spray mode changes on analyte signal and emitter current

The impact of electrospray mode changes on the signal intensity of the tetrapeptide analyte MRFA (Met-Arg-Phe-Ala) is illustrated in Figure 5.11. To realise a wider range for mode 4 (multi-jet mode, Figure 5.3), the FA concentration was reduced to 0.001 vol% in the eluent (*cf.* Section 5.3.4). MRFA dissolved in 50/50 (v/v) W/ACN (c = 8.34 fmol/µL) with 0.001 vol% FA was infused (F = 0.33 µL/min) through the separation channel at varying potential differences between emitter and end cap (Figure 5.11). The dashed line denotes the corresponding DC current of the ion trap which helps to identify the electrospray modes. Signal intensity is reflected by the count rate of the MRFA peak at 524 m/z. With increasing potential difference the signal intensity increases in mode 1. At the transition to spray mode 2 the maximum count rate is reached. A further increase of the applied potential in mode 2

results in a decreasing signal intensity. Analyte ions generated by the ESI enter the ion trap and contribute to signal intensity, or collide with the wall in the transfer capillary and get lost for detection [14]. The latter scenario is more likely in the case of small droplets, which require less evaporation in order to produce ionised analyte molecules. Thus, the reduced droplet size at increasing emitter voltage [27] can result in a less efficient analyte transmission. In the steady cone-jet mode the signal intensity is quite low compared to mode 2, but the standard deviations are much smaller. The lower intensity yield is based on the smaller droplet size in the steady cone-jet mode [26,27] and the resulting higher probability of wall impacts. Due to the narrow size distribution of droplets produced in the steady cone-jet mode [27] the count rates are very similar to each other at different potentials within this spray mode (mode 3), which demonstrates good spray stability.

The general trend in spray mode 4 reveals decreasing signal intensities with increasing potential difference (> 3 kV) between emitter and end cap. It can be explained by the amount of solvent accelerated towards the additional electrode through the second jet (*cf*. Figure 5.3, panel E). Analyte ions in this jet do not enter the MS. The initial increase of counts in spray mode 4 (2.7 – 3.0 kV) results from the geometrical arrangement of the electrodes. Due to jet splitting, one jet faces the additional electrode, whereas droplets from the other jet are directed straight into the MS inlet. Thus, more and larger droplets compared with the steady cone-jet mode enter the MS and increase signal intensity. The curve progression in spray mode 4 is consistent with literature data [15,27]. At increasing emitter voltage the droplet size decreases, which results in a higher ion yield (2.7 – 3.0 kV) [27]. This trend is subject to changes as transport of ions becomes dominated by instrument parameters like the inlet length [14,15] or the geometrical configuration of the electrodes. In general, the results in Figure 5.11 emphasize the steady cone-jet mode (mode 3) as most desirable spray mode for stable and reproducible analyte signals.

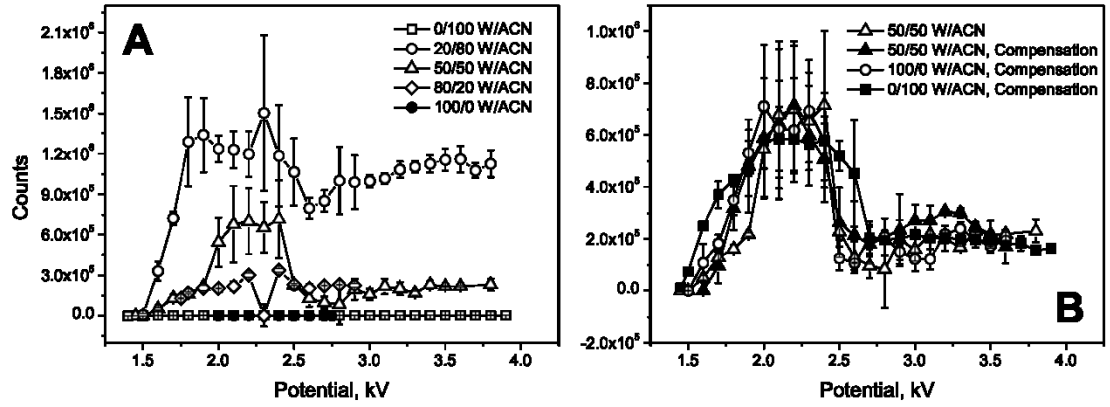

Figure 5.12: Signal intensities of the tetrapeptide analyte MRFA (Met-Arg-Phe-Ala). (A) MRFA in water-acetonitrile mixtures (c = 8.34 fmol/µL) containing 0.001 vol% FA infused via the separation channel, F = 0.4 µL/min. (B) Solvents passing the separation channel were compensated by the inverted post-column MUF, resulting in very similar MRFA intensities over the entire range of mobile phase compositions. A flow rate of 0.2 µL/min was applied to the separation channel (c = 16.68 fmol/µL) and the MUF channel.

5.7.3 Impact of the post-column MUF on analyte signal response

In Figure 5.12 the distributions of MRFA signal intensities for different W/ACN mobile phases are displayed as a function of the applied potential. To keep the amount of electrosprayed analyte constant, its concentration provided by the separation channel was adapted from c = 8.34 fmol/µL without post-column MUF to c = 16.68 fmol/µL with the MUF. Figure 5.12A shows count rates for the case of the non-compensated eluents (no MUF). Intensities vary widely with the water fraction in the mobile phase. For 0 and 100% water fraction count rates are very low, at a water fraction of 20% intensities go through a maximum, and values for intermediate water fractions reside in between. In contrast, with the post-column MUF compensation, such that the electrosprayed solution always contains a water fraction of 50%, the analyte's signal intensity curves for all mobile phase compositions provided by the microchip's separation channel become very similar (Figure 5.12B).

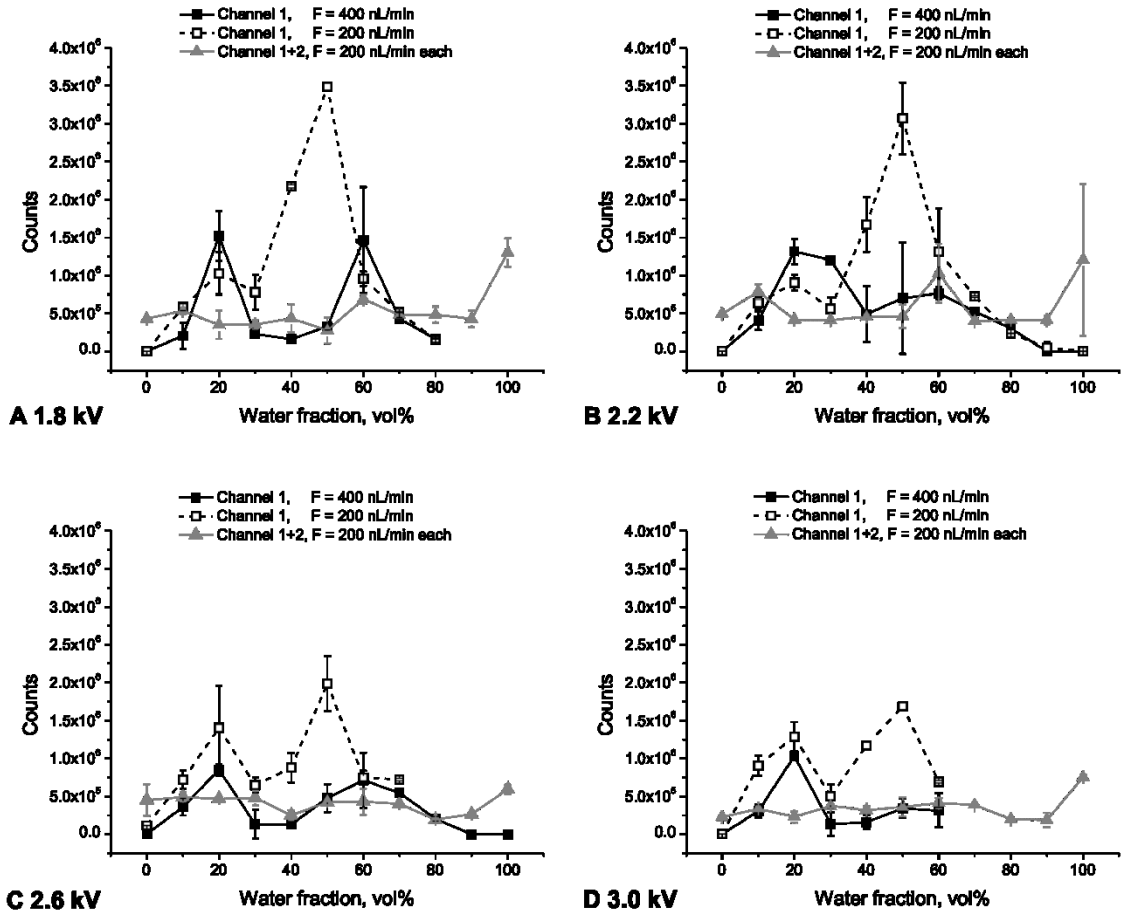

Figure 5.13: MRFA counts *vs.* the water fraction of the eluent at constant emitter voltage without MUF compensation using the separation channel only (channel 1) and with MUF compensation (channel 1 and 2). Solvents were doped with 0.001 vol% FA. Electrospraying of the analyte *via* channel 1 was performed at 0.4 and 0.2 µL/min (c = 8.34 fmol/µL). MUF compensation was realised by applying a flow rate of 0.2 µL/min to channel 1 (c = 16.68 fmol/µL) and channel 2.

(A) Emitter voltage: 1.8 kV; electrospray mode 1. (B) Emitter voltage: 2.2 kV, pulsating cone-jet mode; (C) Emitter voltage: 2.6 kV; mode 3 (steady cone-jet mode). (D) Emitter voltage: 3.0 kV; mode 4 (multi-jet mode).

The extent of variations in signal intensities during HPLC gradient elution at a constant potential difference between emitter and end cap is demonstrated by Figure 5.13A-D. In Figure 5.13B, a voltage of 2.2 kV was applied, a typical start condition in reversed-phase HPLC gradient elution with W/ACN mobile phases (water fraction ≥ 90%). The electrospray mode corresponding to this applied voltage is spray mode 2 (pulsating cone-jet mode). To compare electrospray properties, the flow rate without MUF compensation must equal the sum of the flow rates in both solvent channels (separation channel and MUF channel) with the MUF compensation, as in Figures 5.9 and 5.12, because the spray mode depends on the

amount of electrosprayed liquid, *i.e.*, on the actual volumetric flow rate in the ESI tip. On the other hand, chromatographic properties have to be compared for identical flow rates in the separation channel, because the flow rate affects chromatographic band broadening [29]. Thus, Figure 5.13 shows MRFA signal intensities with different W/ACN mobile phases for a volumetric flow rate of 0.4 µL/min in the separation channel (without MUF), and compares these data to those obtained for a flow rate of 0.2 µL/min in both channels (separation channel and MUF channel) with the MUF compensation. Signal intensities for a flow rate of 0.2 µL/min in the separation channel are shown to demonstrate the differences in ion yields without the MUF. To represent spray modes 1, 3, and 4 without MUF, potentials of 1.8 kV, 2.6 kV, and 3.0 kV were selected, which is illustrated in Figure 5.13A,C, and D, respectively. It shows that the signal intensities for a mobile phase of 50/50 (v/v) W/ACN are nearly identical for a non-compensated flow of F = 0.4 µL/min (channel 1) and compensated flow (F = 0.2 µL/min, channel 1 and 2) at 1.8 kV (mode 1, Figure 5.13A), 2.6 kV (mode 3, Figure 5.13C), and 3.0 kV (mode 4, Figure 5.13D). This result is not surprising as the electrosprayed solvents possess identical properties. The situation is similar at 2.2 kV (mode 2, Figure 5.13B), however, the signal intensity at a water fraction of 50% shows a remarkable standard deviation, which may be due to some unrecognised change in the test conditions. Count rates and scattering of the non-compensated data for modes 1 and 2 (Figure 5.13, panels A and B) are higher compared to modes 3 and 4 (Figure 5.14, panels C and D, respectively). It confirms the trend seen earlier in Figure 5.12. Signal intensities without MUF at different water fractions vary by as much as 600 times in mode 1, 1000 times in mode 2, 20 times in mode 3, and 250 times in mode 4. In all four electrospray modes the count rates with the MUF compensation are smaller, but the curves are smooth (scattering factor 3–5 only) and have small standard deviations due to the constant electrospray conditions realised with the inverted post-column solvent gradient throughout a complete gradient separation run. With the MUF, signal intensities are present even at high water fractions (no signal detectable for water fractions > 80% at 1.8 kV, > 70% at 2.6 kV, and > 60% at 3.0 kV without the MUF compensation). This is a significant improvement not only for quantitative but also qualitative analysis.

5.7.4 Impact of the post-column MUF on chromatographic performance

To investigate the impact of the MUF compensation on the chromatographic performance MRFA samples were injected in different W/ACN mobile phases and electrosprayed at 2300 V. This fits into the steady cone-jet mode (mode 3) with the employed microchip device and

the 50/50 (v/v) W/ACN mobile phase containing 0.001% FA resulting from the inverted post-column MUF at the ESI tip. Relevant peak parameters are summarised in Table 5.2.

Table 5.2.

Analyte peak characteristics without and with post-column MUF compensation.[1]

		Water fraction, vol%						
		30	**40**	**50**	**60**	**70**	**80**	**90**
Microchip separation channel only: F = 0.2 µL/min c = 8.34 fmol/µL	t_R, min	5.72 ± 0.33	3.74 ± 0.09	3.41 ± 0.06	4.49 ± 0.10	4.73 ± 0.07	5.78 ± 0.13	–
	Intensity, 10^6 counts	8.50 ± 5.03	2.76 ± 0.11	1.74 ± 0.04	0.99 ± 0.08	1.07 ± 0.03	1.03 ± 0.02	–
	Area, 10^6 counts min	2.72 ± 1.31	7.15 ± 0.28	4.71 ± 0.39	2.82 ± 0.02	3.40 ± 0.16	4.47 ± 0.17	–
	FWHM, min	1.54 ± 0.13	1.67 ± 1.34	1.38 ± 0.10	1.44 ± 0.21	1.46 ± 0.04	1.83 ± 0.07	–
	σ, min	0.65 ± 0.05	0.37 ± 0.57	0.59 ± 0.04	0.61 ± 0.09	0.62 ± 0.02	0.78 ± 0.03	–
	Tailing factor	0.79 ± 0.29	2.07 ± 0.49	0.733 ± 0.25	1.08 ± 0.57	1.08 ± 0.04	0.63 ± 0.05	–
Microchip separation channel only: F = 0.4 µL/min c = 8.34 fmol/µL	t_R, min	2.82 ± 0.30	1.71 ± 0.16	1.88 ± 0.12	2.31 ± 0.06	2.60 ± 0.09	2.92 ± 0.16	7.67 ± 0.04
	Intensity, 10^6 counts	3.17 ± 0.50	3.08 ± 0.72	1.97 ± 1.27	0.89 ± 0.15	0.40 ± 0.02	0.31 ± 0.43	0.24 ± 0.02
	Area, 10^6 counts min	8.93 ± 0.74	7.06 ± 1.31	4.31 ± 2.76	2.09 ± 0.39	1.08 ± 0.02	1.22 ± 0.17	1.58 ± 0.17
	FWHM, min	1.80 ± 0.23	1.29 ± 0.02	1.78 ± 0.05	1.07 ± 0.04	1.46 ± 0.04	1.98 ± 0.03	2.72 ± 0.43
	σ, min	0.48 ± 0.10	0.44 ± 0.01	0.44 ± 0.02	0.45 ± 0.02	0.50 ± 0.02	0.77 ± 0.01	1.06 ± 0.18
	Tailing factor	0.89 ± 0.30	0.53 ± 0.25	0.46 ± 0.60	0.96 ± 0.30	0.84 ± 0.04	0.99 ± 0.26	1.75 ± 0.61

With the MUF compensation **Separation channel:** F = 0.2 µL/min c = 16.68 fmol/µL **MUF channel:** F = 0.2 µL/min	t_R, min	5.59 ± 0.14	3.52 ± 0.29	3.34 ± 0.23	4.47 ± 0.16	4.56 ± 1.40	5.77 ± 0.34	13.40 ± 0.66
	Intensity, 10^6 counts	2.22 ± 0.02	2.33 ± 0.03	2.38 ± 0.08	2.22 ± 0.05	2.67 ± 1.0	3.61 ± 0.3	3.01 ± 1.2
	Area, 10^6 counts min	6.43 ± 0.09	6.79 ± 0.23	6.47 ± 0.23	5.64 ± 1.00	6.99 ± 0.28	6.85 ± 0.24	6.77 ± 0.85
	FWHM, min	1.80 ± 0.22	1.09 ± 0.42	1.58 ± 0.17	0.86 ± 0.12	1.26 ± 0.34	1.78 ± 0.73	2.52 ± 0.47
	σ, min	1.03 ± 0.09	0.53 ± 0.18	0.75 ± 0.07	0.44 ± 0.05	0.56 ± 0.14	0.83 ± 0.31	0.94 ± 0.20
	Tailing factor	0.79 ± 0.07	0.90 ± 0.31	1.08 ± 0.35	1.15 ± 0.18	1.09 ± 0.36	1.46 ± 0.79	3.24 ± 0.38

[1] The tetrapeptide analyte MRFA (Met-Arg-Phe-Ala) was electrosprayed in different water-acetonitrile mixtures containing 0.001 vol% FA. Potential difference between microchip emitter tip and end cap of the MS (Figure 5.8B): 2300 V; analyte concentration in the separation channel: c = 8.34 fmol/µL without MUF, c = 16.68 fmol/µL with MUF; injection volume: 0.5 µL.

No signal was available for water fractions of 10%, 20%, and 100% in the mobile phase without MUF compensation. Corresponding data with MUF compensation are not shown, but were similar to the data obtained with water fractions ≥ 30%. The retention times (t_R) with non-compensated and compensated mobile phases at F = 0.2 µL/min are very similar. Small differences are due to fluctuations in the nano pump performance. Peak intensities and peak areas for measurements without MUF compensation have higher standard deviations and depend on eluent composition. With increasing water fraction peak intensities decrease by a factor of ~ 8.6 and ~ 13.2 for F = 0.2 µL/min and F = 0.4 µL/min, respectively. Peak areas decrease by a factor of ~ 8.3 for F = 0.4 µL/min and scatter by up to 2.6 times for F = 0.2 µL/min. With the MUF compensation the MRFA analyte shows much steadier peak intensities as well as peak areas (variations by a factor of ~ 1.3 and ~ 1.6, respectively), indicating stable electrospray, which is independent of the water fraction in the mobile phase passing the separation column. This reduces the error in quantitative analysis significantly. Additionally, the similar values for peak areas provide evidence that no analyte discrimination due to solubility or sample injection on the enrichment column is present.

The chromatographic performance of the microchip-HPLC/ESI-MS configuration is hardly affected by the MUF compensation (Table 5.2). Tailing factors are similar for all experiments, indicating that both solvent flows (from the separation column and MUF

channel) are mixed regularly behind the T-junction, without peak distortion. Peak widths (full width at half maximum, FWHM) and variances (σ) were expected to be similar or slightly larger with the MUF compensation at identical separation flow rates, because additional band broadening can occur in the mixing chamber when the two solvent streams are united. However, a trend in the FWHM and σ cannot be observed, indicating that band broadening is governed by the quality of the chromatographic packing in the separation column, especially the packed bed's density, and external effects in the MS configuration [29]. To determine accurately the influence of the MUF compensation on the peak width all factors contributing to the performance of the whole setup have to be investigated separately. This is quite difficult given the limited life times of the ESI tip and microchip lamination. Our results already demonstrate that the impact of the MUF is negligible compared to the intrinsic chromatographic and extra-column contributions to band broadening in the studied microchip-HPLC/ESI-MS system.

5.8 Conclusions

A microchip-HPLC/ESI-MS configuration was used to analyse electrospray modes and study the MS response of the tetrapeptide MRFA in water-acetonitrile solutions. The focus of this study was on the microchip, equipped with enrichment column, separation column, and MUF channel, which was used for sample injection and infusion experiments. MS signal intensities were recorded for different mobile phase compositions and the dependency on the electrospray mode was determined. The steady cone-jet mode (mode 3), though the count rates are lower compared to the pulsating cone-jet mode (mode 2), guarantees a stable electrospray, resulting in small standard deviations of signal intensities. This emphasises the steady cone-jet mode as targeted electrospray condition for HPLC-MS analysis.

A routine HPLC gradient elution run is operated without performance feedback from the electrospray process. Thus, the changing mobile phase composition alters spray conditions and signal response at constant emitter voltage; peak parameters vary significantly with different water fractions in the eluent. The demonstrated application of a post-column MUF just before the ESI tip with exactly inverted mobile phase composition compensates for the eluent changes during gradient elution in the separation channel, because the resulting electrosprayed solution has identical composition throughout the gradient run. Variations in peak areas, which differ by a factor of up to 8.3 for non-compensated flow, reduce to a factor

of ~ 1.6. The better spray and signal stability with the MUF compensation results in smaller errors in quantification. The contribution to band broadening of the post-column mixing chamber turned out to be negligible compared to the influence of the microchip packing in the separation column (chromatographic bed) and external band broadening in the MS system. Thus, the post-column MUF improves detection without compromising chromatographic separation efficiency. It is easily integrated on flexible microchip platforms and will contribute to an increased HPLC/ESI-MS performance relevant for a wide range of applications.

References

[1] M. Bantscheff, A. Scholten, A.J.R. Heck, Drug Discov. Today 14 (2009) 1021-1029.

[2] T.A. Gillespie, B.E. Winger, Mass Spectrom. Rev. 30 (2011) 479-490.

[3] V. Viette, M. Fathi, S. Rudaz, D. Hochstrasser, J.-L. Veuthey, Clin. Chem. Lab. Med. 49 (2011) 1091-1103.

[4] D. Tao, L. Zhang, Y. Shan, Z. Liang, Y. Zhang, Anal. Bioanal. Chem. 399 (2011) 229-241.

[5] D.F. Cortes, J.L. Kabulski, A.C. Lazar, I.M. Lazar, Electrophoresis 32 (2011) 14-29.

[6] G.T. Roman, R.T. Kennedy, J. Chromatogr. A 1168 (2007) 170-188.

[7] J. Lee, S.A. Soper, K.K. Murray, J. Mass Spectrom. 44 (2009) 579-593.

[8] I.M. Lazar, R.S. Ramsey, S.C. Jacobson, R.S. Foote, J.M. Ramsey, J. Chromatogr. A 892 (2000) 195-201.

[9] M. Cloupeau, B. Prunet-Foch, J. Aerosol Sci. 25 (1994) 1021-1036.

[10] F. de la Mora, I.G. Loscertales, J. Fluid Mech. 260 (1994) 155-184.

[11] A. Schmidt, M. Karas, T. Dülcks, J. Am. Soc. Mass Spectrom. 14 (2003) 492-500.

[12] T. Sikanen, S. Franssila, T.J. Kauppila, R. Kostiainen, T. Kotiaho, R.A. Ketola, Mass Spectrom. Rev. 29 (2010) 351-391.

[13] I.M. Lazar, J. Grym, F. Foret, Mass Spectrom. Rev. 25 (2006) 573-594.

[14] J.S Page, I. Marginean, E.S. Baker, R.T. Kelly, K. Tang, R.D. Smith, J. Am. Soc. Mass Spectrom. 20 (2009) 2265-2272.

[15] I. Marginean, R.T. Kelly, D.C. Prior, B.L. LaMarche, K. Tang, R.D. Smith, Anal. Chem. 80 (2008) 6573-6579.

[16] S. Jung, U. Effelsberg, U. Tallarek, J. Chromatogr. A 1218 (2011) 1611-1619.

[17] K.-G. Reinsberg, U. Effelsberg, U. Tallarek, Lab Chip 9 (2009) 2914-2923.

[18] G.A. Valaskovic, J.P. Murphy, M.S. Lee, J. Am. Soc. Mass Spectrom. 15 (2004) 1201-1215.

[19] A. Gapeev, A. Berton, D. Fabris, J. Am. Soc. Mass Spectrom. 20 (2009) 1334-1341.

[20] I. Marginean, R.T. Kelly, R.J. Moore, D.C. Prior, B.L. LaMarche, K. Tang, R.D. Smith, J. Am. Soc. Mass Spectrom. 20 (2009) 682-688.

[21] F. Foret, H. Zhou, E. Gangl, B.L. Karger, Electrophoresis 21 (2000) 1363-1371.

[22] J. Li, P. Thibault, N.H. Bings, C.D. Skinner, C. Wang, C. Colyer, J. Harrison, Anal. Chem. 71 (1999) 3036-3045.

[23] R. Ramanathan, R. Zhong, N. Blumenkrantz, S.K. Chowdhury, K.B. Alton, J. Am. Soc. Mass Spectrom. 18 (2007) 1891-1899.

[24] G.O. Staples, H. Naimy, H. Yin, K. Killeen, K. Kraiczek, C.E. Costello, J. Zaia, Anal. Chem. 82 (2010) 516-522.

[25] S. Jung, A. Höltzel, S. Ehlert, J.-A. Mora, K. Kraiczek, M. Dittmann, G.P. Rozing, U. Tallarek, Anal. Chem. 81 (2009) 10193-10200.

[26] P. Kebarle, U.H. Verkerk, Mass Spectrom. Rev. 28 (2009) 898-917.

[27] P. Nemes, I. Marginean, A. Vertes, Anal. Chem. 79 (2007) 3105-3116.

[28] Z. Olumee, J.H. Callahan, A. Vertes, J. Phys. Chem. A 102 (1998) 9154-9160.

[29] S. Ehlert, L. Trojer, M. Vollmer, T. van de Goor, U. Tallarek, J. Mass Spectrom. 45 (2010) 313-320.

Conclusions

This work is concerned with different aspects of miniaturised HPLC and optimisation of the chromatographic performance. To achieve optimum separation efficiency in nano and microchip separation format reduction of peak dispersion, minimisation of the setup volume, optimisation of packing conditions to achieve low bed densities for particulate fixed beds, and optimisation of operating conditions are of great importance.

An important indicator for the quality and performance of a particle-packed separation column is the interparticle porosity ε_{inter}. Two independent chromatographic methods – based on inverse size-exclusion and DONNAN exclusion – for the determination of ε_{inter} are evaluated with a view to their applicability to a variety of chromatographic materials (Chapter I, Part A and B). In *Chapter I Part A – Determination of the interparticle void volume in packed beds via intraparticle DONNAN exclusion* – interparticle void volumes and porosities of particle-packed, 75 µm i.d. fused silica capillaries are determined by electrostatic (DONNAN) exclusion and inverse size-exclusion chromatography. Complete intraparticle DONNAN exclusion of a small, unretained co-ionic tracer – nitrate ions, with respect to the negative surface charge present on silica based separation materials – was established by careful adjustment of mobile phase's ionic strength. The application of the method has been studied for bare-silica (Nucleosil 100-5 and Nucleosil 1000-5), reversed-phase (Hypersil MOS 3 µm and Hypersil MOS 10 µm), and strong cation-exchange (Spherisorb SCX 3 µm) materials with different particle sizes and intraparticle pore sizes. Tris-HCl buffer was used to determine the intraparticle electric double layer (EDL) overlap and co-ion exclusion in dependence of the intraparticle pore size (Nucleosil 100-5 *versus* Nucleosil 1000-5 material) and the surface charge density (Hypersil MOS 3 µm *versus* Spherisorb SCX 3 µm) of the particles. Complementary, ε_{inter} was determined by the established method of inverse size-exclusion chromatography. A range of polymer standards of defined molecular weights were dissolved in dichloromethane and injected onto the columns. Elution volumes of the polymer standards reveal a bimodal distribution within the limits of total permeation and exclusion of the intraparticle pore space. For all investigated capillary columns values of ε_{inter} obtained by intraparticle DONNAN exclusion agreed well with those obtained by ISEC. Limitations to the use of DONNAN (electrostatic) exclusion and ISEC (mechanical exclusion) arise as either type of exclusion becomes noticeable also in the cusp regions between the particles, *i.e.*, the small particles are densely packed and EDL overlap exists between individual particles on the one

hand; and on the other, the interparticle flow through pores of the packing become too small for the polymer coils. Determination of ε_{inter} is also precluded by large intraparticle pores so that complete electrostatic and size-exclusion are difficult to realise.

In *Chapter I Part B – Fast, accurate, and convenient analysis of bed densities for columns packed with fine reversed-phase particles* – the DONNAN exclusion method was extended to determine ε_{inter} of commercially available analytical HPLC columns from Agilent Technologies packed with fine reversed-phase particles of different nominal sizes (1.8, 2.7, 3.5, and 5 µm) and construction (fully porous and core-shell). The experimental data demonstrate that the method is highly reproducible with a commercial chromatograph, and the small nitrate concentration inherent to the method was easily detected with a standard detection cell. A distinct plateau region in the elution curve at low buffer concentrations indicates EDL overlap in the intraparticle mesopores, so that small, co-ionic tracers are completely excluded from the intraparticle pore space and the elution volume of the tracer equals the interparticle void volume of the fixed bed. The DONNAN exclusion method worked well for all investigated commercial analytical columns including columns packed with 2.7 µm core-shell and 1.8 µm fully porous particles. In general, the DONNAN exclusion method proved to be a fast, accurate, and convenient procedure for the determination of interparticle void volumes and porosities, encompassing a variety of stationary phase chemistries (reversed-phase, bare-silica, and ion-exchange particles), particle construction (fully porous and core-shell particles), and particle sizes (1.8 – 5 µm).

At high buffer concentrations in the mobile phase, the elution volumes approach an asymptotic limit that is expected to denote the total column void volume. But due to the slow decrease of the EDL thickness over a wide range of ionic strengths, a noticeable exclusion from parts of the mesopores persists even at high buffer concentrations. These results confirm the statement that small ions are not suited for an accurate determination of the column void volume[4] without exact knowledge of the extent of possible electrostatic exclusion from the intraparticle pore space.

Separation efficiency in chromatography is determined by band broadening from hydrodynamic dispersion which in turn is governed by the packing microstructure. Microchip separation channels are inherently noncylindrical due to the fabrication processes. Noncylindrical conduit geometry influences axial dispersion which increases with increasing

[4] A detailed review of existing methods for the determination of column void volumes by C.A. Rimmer, C.R. Simmons, and J.G. Dorsey named "The measurement and meaning of void volumes in reversed-phase liquid chromatography" can be found in J. Chromatogr. A 965 (2002) 219-232.

deviation from cylindrical conduit geometry from circular *via* quadratic and rectangular to semicircular cross-sections.[5] Additionally, the corner regions of noncylindrical channels are more difficult to pack densely. The effects that lead to increased dispersion and flow maldistribution depend strongly on the packing density and particle-aspect (conduit-to-particle size) ratio of particulate microchip packings.[6] In *Chapter II – Impact of conduit geometry on the performance of typical particulate microchip packings* – axial dispersion in particulate microchip packings were determined chromatographically. The polyimide HPLC/UV microchips contained separation channels with trapezoidal, quadratic, and Gaussian cross-sectional geometry.

Dispersion in the empty separation channels reflects the symmetry of the respective channel cross-sections. The quadratic channel has the highest symmetry, resulting in a more symmetrical flow profile and a smaller flow maldistribution term. Flow maldistribution increases with decreasing symmetry due to the growing distance between different velocity zones over which exchange of solute molecules needs to occur by lateral diffusion to approach asymptotic dispersion in the long-time limit. The Gaussian cross-section shows the highest axial dispersion of the investigated microchips due to the continuous decrease in lateral diffusion length from bottom to top that leads to larger friction forces in the upper part of the channel and more pronounced velocity differences between top and bottom part.

The achieved packing densities of the microchip packings are determined by the particle-aspect ratio. In case of the 3 µm packings, dense beds could be achieved for all channel cross-sections. Interparticle porosities of the 5 µm packings are rather loose (ε_{inter} values increase from 0.40 for Gaussian over 0.41 for trapezoidal 0.42 for quadratic cross-sections, respectively). This is most likely related to the quantity and shape of the corners in the different channels, *i.e.*, corners with angles $\leq 45°$ are expected to be partially unoccupied, whereas corners with angles $\geq 90°$ or "softened" corners (*e.g.*, from a creeping of glue like in the trapezoidal channel cross-sections) reveal little steric hindrance for the particles to access the corner regions.

[5] Hydrodynamic dispersion in pressure-driven flow through fixed beds of solid spherical particles was studied by quantitative numerical analysis for conduits with circular, quadratic, rectangular, and semicircular cross-sectional geometries. The authors found that axial dispersion increases with increasing deviation from cylindrical geometry due to the presence of corners that give rise to the formation of channels of advanced fluid flow and longer characteristic length for lateral equilibration of solute molecules [S. Khirevich, A. Höltzel, D. Hlushkou, U. Tallarek, Anal. Chem. 79 (2007) 9340-9349].

[6] HPLC/UV microchips of trapezoidal cross-section geometry were investigated experimentally with respect to packing density, pressure drop – flow rate relation, hydraulic permeability, and separation efficiency in a former publication: S. Jung, S. Ehlert, J.-A. Mora, K. Kraiczek, M. Dittmann, G.P. Rozing, U. Tallarek, J. Chromatogr. A 1216 (2009) 264-273.

Separation efficiency of the 3 µm packings reflects dispersion behaviour of the empty separation channels. Dispersion behaviour of the 5 µm packings reflects their respective packing densities. The performance of the Gaussian 5 µm packing is comparable to that of the trapezoidal 5 µm packing, because the higher packing density balances the dispersion disadvantage from the Gaussian conduit shape. Quadratic packings differ not too much from the other 5 µm packings around the minimum, but suffer from a significantly steeper slope of the H-u curve. Here, quadratic conduits lose their symmetry advantage because the particles are more difficult to pack densely into the channel. Thus, the study shows that the conduit geometry influences the performance of typical particulate microchip packings in various ways, but the effects cannot be isolated from the particle-aspect ratio of the packings.

In *Chapter III* the impact of a gradually changing bulk solvent composition (like it is found in gradient elution HPLC) of an electrosprayed liquid on the establishing electrospray mode and the corresponding electrospray performance was investigated. Electrospray ionisation (ESI) has become a routine tool for online coupling of HPLC to mass spectrometry (MS). Ideally, the ion source should be capable of sustaining maximal ion production throughout the detection duty cycle. In ESI, the ion production rate is directly correlated to spray stability, which in turn is influenced by the interplay of many factors including the applied voltage, distance between emitter and MS inlet, flow rate, and solvent composition. Routine gradient elution in HPLC-MS analysis is usually performed without performance feedback from the electrospray, and the voltage that ensures optimal ESI conditions at the beginning of the separation may not be appropriate for the mobile phase composition at the end of the solvent gradient. Changes of the physicochemical properties of the eluent during gradient elution HPLC separations alter the electrospray operation mode.

In *Chapter III Part A – Microchip electrospray: Cone-jet stability analysis for water–acetonitrile and water–methanol mobile phases* – the influences of dynamic changes in bulk conductivity on the cone-jet stability island for aqueous acetonitrile and aqueous methanol mobile phases commonly used in reversed-phase HPLC are analysed. Bulk conductivities of the electrosprayed solutions were varied by adding different amounts of formic acid. A commercial microchip HPLC/ESI-MS configuration from Agilent Technologies was modified to enable *in situ* electrospray diagnostics by frequency analysis of the microchip emitter current and spray imaging. Different spray modes, the steady cone-jet mode in particular, and their stability regimes were detected. The steady cone-jet is desired in MS analysis since it provides relatively large and stable spray current as well as smaller initial droplets.

At low water fractions in the eluent the stability regime is limited by the bulk conductivity: below a critical conductivity the droplet generation rate, which depends on charge separation, is too slow for a stable cone-jet. With increasing bulk conductivity of the mobile phase the cone-jet stability island is shifted towards larger amounts of organic modifier. Due to the higher conductivity of water-methanol mixtures compared to water-acetonitrile mixtures, the cone-jet stability islands of water-methanol eluents are larger and tolerate higher fractions of organic modifier as well as lower flow rates.

At high water fractions and conductivities, the attractive forces of the additional electrode in the ChipCube on the liquid jet gain influence so that the steady cone-jet mode is by-passed and the pulsating cone-jet mode transcends directly into the multi-jet mode. A water fraction > 85% in the mobile phase prevents the generation of a stable cone-jet mode even at moderate bulk conductivities, because of the increased surface tension of the electrosprayed liquid. To counteract at least the destabilising effect of permittivity, the cone volume can be enlarged by reducing the drying temperature and gas flow in the electrospray interface.

However, it is demonstrated that during a typical gradient elution HPLC/ESI-MS analysis the cone-jet stability island is easily crossed because of dynamic changes of bulk conductivity and surface tension of the electrosprayed liquid. In *Chapter III Part B – Microchip electrospray: Improvements in spray and signal stability during gradient elution by an inverted post-column make-up flow* – the impact of the eluent composition on electrospray stability and MS response was investigated by infusion and injection experiments. The employed microchip device was equipped with an enrichment column, a separation column, and a make-up flow (MUF) channel. One nano pump is connected to the separation column, while a second one delivers solvent of exactly inverted composition to the MUF channel. Both solvent streams are united behind the separation column, before the ESI tip, such that the resulting electrosprayed solution always has identical composition during a gradient elution. MS signal intensities were recorded for different mobile phase compositions, and the dependency on the electrospray mode without MUF was determined. The steady cone-jet mode, though the count rates are lower compared to the pulsating cone-jet mode, guarantees a stable electrospray, resulting in small standard deviations of signal intensities. This emphasizes the steady cone-jet mode as targeted electrospray condition for HPLC-MS analysis.

The changing mobile phase compositions during a gradient elution run alters spray conditions and signal response at constant emitter voltage; peak parameters were found to

vary significantly with different water fractions in the eluent. The application of post-column MUF just before the ESI tip with exactly inverted mobile phase composition compensates for the eluent changes during gradient elution in the separation channel. Variations in peak areas, which differ by a factor of up to 8.3 for noncompensated flow, reduce to a factor of ~ 1.6. The better spray and signal stability with the MUF compensation results in smaller errors in quantification. The contribution to band broadening of the post-column mixing chamber turned out to be negligible compared to the influence of the microchip packing in the separation column and external band broadening in the MS system.

Thus, to achieve optimum separation efficiency in microchip HPLC/ESI-MS it is not only important to generate densely packed beds by optimised packing procedures specific to HPLC microchips (*i.e.*, to account for the pressure limitation of the used materials and to ensure efficient filling of the noncylindrical separation channels), but to consider the impact of the electrospray conditions on separation performance. The electrospray mode significantly impacts the signal response. To overcome electrospray mode changes during a gradient elution run and associated signal variations a post-column MUF can be easily implemented on flexible microchip platforms. The post-column MUF improves detection without compromising chromatographic separation efficiency, and thus, contribute to an increased HPLC/ESI-MS performance relevant for a wide range of applications.

Curriculum vitae

Zur Person / Personal details

Stephanie Jung
geboren am 13.05.1983 in Dillenburg, Deutschland
Date of birth: 05/13/1983 in Dillenburg, Germany

Schulbildung / Education

1989 – 1993	Grundschule in Manderbach Primary school Manderbach, Germany
1993 – 2002	Wilhelm-von-Oranien Gymnasium und altsprachliches Gymnasium in Dillenburg, Abschluss: Abitur Gymnasium Dillenburg, Germany, degree: Abitur

Hochschulbildung / University education

2002 – 2008	Diplomstudiengang Chemie, Philipps-Universität Marburg 25. Juli 2008, Diplom Diploma in chemistry, 07/25/2008, Philipps-Universität Marburg
2008 – 2012	Promotion zum Thema: „Microchip HPLC: Experimental investigation of separation efficiency, column characteristics, and coupling with mass spectrometry", Fachbereich Chemie der Philipps-Universität Marburg, Analytische Chemie, Arbeitsgruppe Prof. Dr. Ulrich Tallarek Doctoral thesis: "Microchip HPLC: Experimental investigation of separation efficiency, column characteristics, and coupling with mass spectrometry", Department of Chemistry, Philipps-Universität Marburg, Analytical Chemistry, Group of Prof. Dr. Ulrich Tallarek

Publikationsverzeichnis / List of publications

Artikel / Articles

Jung, S.; Ehlert, S.; Mora, J.-A.; Kraiczek, K.; Dittmann, M.; Rozing, G.P.; Tallarek, U. *J. Chromatogr. A* **2007**, *1172*, 25–39. „Packing density, permeability, and separation efficiency of packed microchips at different particle-aspect ratios.“

Jung, S.; Höltzel, A.; Ehlert, S.; Mora, J.-A.; Kraiczek, K.; Dittmann, M.; Rozing, G.P.; Tallarek, U. *Anal. Chem.* **2009**, *81*, 10193–10200. „Impact of Conduit Geometry on the Performance of Typical Particulate Microchip Packings.“

Jung, S.; Ehlert, S.; Pattky, M.; Tallarek, U. *J. Chromatogr. A* **2010**, *1217*, 696–704. „Determination of interparticle void volume in packed beds via intraparticle Donnan exclusion.“

Jung, S.; Effelsberg, U.; Tallarek, U. *J. Chromatogr. A* **2011**, *1218*, 1611–1619. „Microchip electrospray: Cone-jet stability analysis for water-acetonitrile and water-methanol mobile phases.“

Jung, S.; Stoeckel, D.; Tallarek, U. *J. Sep. Sci.* **2011**, *34*, 800–805. „Fast, accurate, and convenient analysis of bed densities and for columns packed with fine reversed-phase particles.“

Jung, S.; Effelsberg, U.; Tallarek, U. *Anal. Chem.* **2011**, *83*, 9167–9173. „Microchip electrospray: Improvements in Spray and Signal Stability during Gradient Elution by an Inverted Postcolumn Makeup Flow.“

Vorträge / Oral presentations

„Separation efficiency of particle packed HPLC microchips“ 24.09.2008, ISC 2008 - 27th International Symmposium on Chromatography, Münster.

Posterpresentationen / Poster presentations

„Impact of the Particle-Aspect Ratio on Packing Density of HPLC Microchips“ HPLC 2009 - 32nd International Symposium on Chromatography and Related Techniques, Dresden, D.

„Impact of Conduit Geometry on Packing Density and Separation Efficiency of HPLC Microchips“ HPLC 2009 - 32nd International Symposium on Chromatography and Related Techniques, Dresden, D.

„Separation Efficiency of HPLC-Microchips with Different Cross-Sectional Geometries“ 8th Balaton Symposium on High-Performance Separation Methods and 15th International Symposium on Separation Sciences, Siofok, H.

„Determination of interparticle void volume in packed beds via intraparticle Donnan exclusion“ HPLC 2010 - 35th International Symposium on Chromatography and Related Techniques, Boston, USA.

Erklärung der Eigenleistung

Die vorliegende Arbeit entstand durch Mithilfe verschiedener Ko-Autoren, deren Beitrag im Folgenden ausgeführt wird.

Die in Kapitel 1, Teil A verwendete Packstation zur Herstellung der gepackten HPLC Kapillaren wurde von Steffen Ehlert aufgebaut. Die Agilent 1100 liquid chromatograph Anlage, aufgebaut von Steffen Ehlert, wurde in Zusammenarbeit mit Martin Pattky in Betrieb genommen und kalibriert. Die zur Messung der Porositäten verwendeten gepackten Kapillaren sowie die Probenlösungen und Eluenten wurden von Martin Pattky hergestellt. Die Daten der mit Spherisorb SCX Partikeln gefüllten Kapillare wurden von mir aufgenommen, alle weiteren chromatographischen Experimente wurden von Martin Pattky durchgeführt. Das Manuskript zur Publikation der Ergebnisse von Kapitel 1, Teil A „Determination of the interparticle void volume in packed beds *via* intraparticle DONNAN exclusion“ wurde von mir erstellt und von Prof. Dr. Ulrich Tallarek korrigiert und eingereicht.

Die Ergebnisse in Kapitel 1, Teil B wurden ebenfalls veröffentlicht unter dem Titel „Fast, accurate, and convenient analysis of bed densities for columns packed with fine reversed phase particles“. Die LC Anlage wurde von mir aufgebaut, in Betrieb genommen und kalibriert. Die Bestimmung der totalen Porosität mit reinem Acetonitril und die zugehörigen Vorbereitungen wurden von mir durchgeführt. Sämtliche anderen Experimente wurden von Daniela Stoeckel ausgeführt. Das Manuskript wurde von mir geschrieben. Alexandra Höltzel und Prof. Dr. Ulrich Tallarek halfen bei den Korrekturen.

Die Mikrochips, welche in Kapitel 2 gepackt und vermessen wurden, wurden von Jose-Angel Mora und Karsten Kraiczek von Agilent Technologies hergestellt. Sämtliche experimentelle Daten in diesem Kapitel wurden von mir aufgenommen. Die Mikrochips wurden nach einer von Steffen Ehlert optimierten Prozedur gepackt. Die Packstation und die Agilent 1100 liquid chromatograph Anlage wurden von Steffen Ehlert aufgebaut. Die Kalibration der Anlage wurde von mir vorgenommen. Das Manuskript „Impact of Conduit Geometry on the Performance of Typical Particulate Microchip Packings“ wurde von mir mit der Hilfe von Alexandra Höltzel erstellt. Prof. Dr. Ulrich Tallarek fügte Korrekturen hinzu und reichte das Manuskript in seiner Endfassung ein.

Die verwendeten HPLC/ESI-MS Mikrochips in Kapitel 3 kamen von Uwe Effelsberg (Agilent Technologies). Er war ebenfalls eine große Hilfe beim Anschließen des Oszilloskops an den ChipCube, wodurch die Aufnahme der Strom-Spannungs-Kurven erst möglich wurde. Sämtliche Daten wurden von mir aufgezeichnet und ausgewertet. Die verwendeten Probenlösungen und Eluenten wurden ebenfalls von mir angesetzt. Die Rohfassungen der Manuskripte mit den Titeln „Microchip electrospray: Cone-jet stability analysis for water-acetonitrile and water-methanol mobile phases“ und „Microchip electrospray: Improvements in Spray and Signal Stability during Gradient Elution by an Inverted Post-column Make-up Flow“ wurden von mir verfasst. Alexandra Höltzel war eine große Hilfe bei der sprachlichen Verbesserung. Die Korrekturen wurden von Prof. Dr. Ulrich Tallarek vorgenommen und die Endversionen im Anschluss daran von ihm eingereicht.

Erklärung

Ich versichere, dass ich die vorliegende Dissertation mit dem Titel

Microchip HPLC: Experimental investigation of separation efficiency, column characteristics, and coupling with mass spectrometry

selbständig, ohne unerlaubte Hilfe angefertigt und mich dabei keiner anderen als der von mir ausdrücklich bezeichneten Quellen und Hilfen bedient habe. Die Dissertation wurde in der jetzigen oder einer ähnlichen Form noch bei keiner anderen Hochschule oder Fachhochschule eingereicht und hat noch keinem sonstigen Prüfungszweck gedient.

Ort, Datum	Stephanie Jung